Title
Engineering New Functionalities at Open Metal Sites in Metal–Organic Frameworks for Gas Separations

Author
Reed, Douglas

Publication Date
2018

Peer reviewed|Thesis/dissertation

Engineering New Functionalities at Open Metal Sites in Metal–Organic Frameworks for Gas Separations

By

Douglas Andrew Reed

A dissertation submitted in partial satisfaction of the

requirements for the degree of

Doctor of Philosophy

in

Chemistry

in the

Graduate Division

of the

University of California, Berkeley

Committee in charge:

Professor Jeffrey R. Long, Chair
Professor Richard A. Andersen
Professor Alexander Katz

Summer 2018

Abstract

Engineering New Functionalities at Open Metal Sites in
Metal–Organic Frameworks for Gas Separations

By

Douglas Andrew Reed

Doctor of Philosophy in Chemistry

University of California, Berkeley

Professor Jeffrey R. Long, Chair

The work herein describes progress toward designing, synthesizing, and characterizing new metal–organic frameworks for gas separation applications. Metal–organic frameworks (MOFs) are a class of porous materials synthesized from molecular inorganic nodes and organic bridging linkers that can be designed to have very precise gas binding sites comprising of coordinatively unsaturated transition metal centers. These binding sites can be modified using standard coordination chemistry concepts to tune the metal site to selectively bind one gas from a given mixture, allowing for effective separations through selective adsorption. The research addresses improvements in selectivity for gas binding in several different examples and in reducing the energy input required for a separation cycle by engineering new functionalities at these transition metal binding sites in new metal–organic frameworks.

Chapter 1 details the current literature on using adsorbents for gas separation applications, with an emphasis on utilizing tunable metal–organic frameworks as high-capacity, highly selective adsorbents. Separations utilizing coordinatively unsaturated transition metals within these frameworks as selective binding sites for small molecules are highlighted, and the efficacy and mechanisms for a variety of gas separations are described. However, as shown, these metal sites generally operate through one type of mechanism in which the metal centers act as exposed, Lewis acidic cations. While effective for some separations, the types of separations that can be performed are limited. Additionally, this adsorption mechanism limits the energy efficiencies of the separation processes. As such, the performance of these materials can be improved with new design principles. The chapter concludes with describing proposed new functionalities at these open metal sites as basic design principles to either make frameworks that can perform new gas separations or design more energy efficient adsorbents.

Chapter 2 describes the design and synthesis of a new metal–organic framework containing exposed vanadium(II) sites that have been designed to contain metal centers that perform electron back-donation to π-acidic gases. This is the first example of such an electron-donating metal center with the proper electronic structure to effectively donate electrons to π* orbitals of gas molecules. This is demonstrated through the strong adsorption of N_2 and characterization of the adsorbed species. In assessing it for potential gas separation performance, particularly for N_2-based separations such as the removal of N_2 from CH_4, the material displays excellent capacity and record-setting selectivity for N_2. This mechanism for adsorption is also applied to ethylene/ethane separations, where this material shows excellent selectivity at high temperatures.

Chapter 3 discusses the rational design of highly ethylene-specific binding sites in a manganese(II)-based metal–organic framework for ethylene capture in the presence of ethane, CO_2, CO, CH_4, and H_2. In particular, this emphasizes creating a metal site with the proper ionic radius, electronegativity, and π-basicity to selectively adsorb ethylene from this complex mixture, which is produced through the oxidative coupling of methane as an alternative process to making ethylene from petroleum sources. By adsorbing ethylene selectively, several different separation steps required for this process can be eliminated, reducing the energy and capital cost significantly. In assessing a series of different materials, the choice of a high-spin Mn(II) ion to act as an effective ethylene adsorbent was demonstrated, and this material was evaluated under realistic process conditions to show very selective ethylene adsorption.

Chapter 4 focuses on a new metal–organic framework that performs selective and reversible adsorbate-induced spin state transitions at the framework metal sites. This allows for highly selective gas separations for strong field ligand gases and the reversible desorption of these gases for facile regeneration of the adsorbent. The compound features open, high-spin Fe(II) sites ligated by triazolate ligands that undergo a spin transition to low-spin Fe(II) when exposed to CO. Applying vacuum then allows the CO to be efficiently removed as the iron sites convert back to high-spin Fe(II). This allows for reversible capture of CO at very low pressures, enabling a reversible CO scrubber for purification of other gases, and also allows for the capture of highly pure CO for potential use as a reagent with some of the highest selectivity values ever reported for metal–organic frameworks.

Chapter 5 reports the realization of the first cooperative adsorbent featuring open metal sites by using a spin transition mechanism in two Fe(II)-based frameworks. Cooperative adsorption for selective adsorbents has recently been demonstrated to have several desirable energy-efficient properties in gas separation applications, but general guidelines currently do not exist for the design of such materials. This new mechanism uses communicating metal centers to perform cooperative adsorption using a concerted spin transition spin transition mechanism for highly efficient CO separations. The iron centers in these frameworks are situated in highly interconnected Fe–triazolate chains with open, high-spin Fe(II) sites, such that CO binding at one iron site prompts a spin transition that subsequently promotes adsorption at neighboring iron sites. While being selective, this adsorption process allows for high working capacities with small temperature swings, resulting in very low regeneration energies for use in gas separations. Ultimately, due to the highly tunable nature of these metal sites, we envision that this can be a broadly applicable design principle toward making next-generation, highly efficient adsorbents.

Table of Contents

List of Figures

Chapter 5: A Spin Transition Mechanism for Cooperative Adsorption in Metal–Organic Frameworks Bearing Open Metal Sites

Appendix A: Schematic of Organic Ligands

Acknowledgements

The work included in this thesis would not have been possible without the incredible amount of support I've received from my family, friends, and advisors. Graduate school has been one of the best times of my life, and the people involved along the way have made it very special for me. I have to thank several people for making my time here so rewarding.

I'd first like to thank Jeff. You've created an incredible lab atmosphere where everyone works hard, but also remains happy and friendly, and where people are always helping others. You're incredibly supportive of my and everyone's work, even when it's failing or taking longer than it should, which is very reassuring and gives people the willingness to try so many different things and perform very thorough analyses of what they do.

To my labmates, you are the people I've worked with every day, helping me to be a better and more thoughtful scientist. You've all provided so much inspiration for me and are probably the most important part of why this was such an enjoyable experience for me. The time we spend helping each other to overcome challenges, learn new things, brainstorm ideas, and work through everything that comes at us has made this the best group of people I've ever worked with. Thanks for being at various points my mentors, teachers, scientific partners, collaborators, softball teammates, hiking and backpacking companions, roadtrip navigators, fellow hitchhikers, concert buddies, food and beer critics, and most importantly, friends.

While there were too many people that I've met over the years to list everyone here, I would like to single out a few people who've really helped me improve as a scientist. The mentorship on scientific and professional topics I've received from Dianne, Keith, Eric, Jarad, Miguel, David, Phil, Phill, Julia, and Mike, among others, is immeasurable, and I thank you all immensely for teaching me everything. Working together with so many people has also really helped me grow, and I have to thank Dianne, Keith, David, Jon, Matt, Julia, Lucy, Miguel, Jarad, Tomce, Henry, Alex, Job, Kaipeng, and Maria, among others, for helping me with every project I've ever worked on and being so supportive in so many ways for every part of my work, I couldn't have done it without you. I also need to thank everyone I've overlapped with for being part of a great group environment, including Joe, Tom, Zoey, Brian, Eric, Katie, Xiaowen, Dana, Jarad, David, Jordan, Dianne, Miguel, Mike, Phil, Lucy, Matt, Mercedes, Jon, Julia, Rodi, Rebecca, Kristen, Colin, Mike, Job, Henry, Ari, Dan, Jesse, David, Kaipeng, Naomi, Ryan, Eugene, Ever, Maria, Alex, Adam, Surya, Kaitlyn, Ziting, Maryanne, Gygi, Raymond, Jo, Michael, JVH, Keith, Rob, Tae-Hyun, Paulina, Jiwoong, Zach, Gokhan, Phill, Martell, Mike, Brandon, Adam, Kathy, Shela, Kristin, and Kenna, and several others that I'm forgetting. I'd particularly like to thank my cohort, Phil, Lucy, and Matt for being there for everything we've gone through together, and just for being great people and friends.

Finally, I need to thank those people who've been there for everything, not just graduate school. My parents have been amazing. They've always encouraged me to do what I wanted, and they've fully supported me for anything that I've chosen to do. I'll always be grateful for what they've given me. My brother and sister have also been so great about providing friendship and support, and I couldn't have asked for better friends. Finally, my wife Dianne has been there for everything, and made all of this worth it. You give me the best advice on everything imaginable, helped me with so many things as a grad student and with everything else, and are always there for me. I couldn't have done it without you.

Chapter 1: Gas Separations in Metal–Organic Frameworks

1.1. Introduction

The separation of molecules from chemical feedstocks or from reaction mixtures is of critical importance industrially. In particular, the separation of industrially relevant species accounts for approximately 50% of industrial energy, which translates to 15% of the annual US energy consumption.[1] A large number of these separation processes involve the mixtures of two or more different gaseous species, as these are widely used commodity chemicals that act as precursors to several other compounds and materials.[2] In examining the separation processes utilized, the majority, approximately 80%, of these processes are performed using thermal-based methods, such as distillation, drying, and evaporation.[1] These are very mature technologies that are easy to scale and are generally quite optimized. However, when assessing the relative energy consumption used during various methods for separations, these separations involving phase changes are relatively energy intense due to the necessary thermal energy input required (Figure 1.1).[1,3] In particular, the use of distillation is the most energy intensive, as this is often done under cryogenic conditions, but encompasses 49% of all separation processes. With the demand for more efficient energy usage, reducing the energy consumption of large scale separations is a prime candidate for reducing overall industrial energy usage.

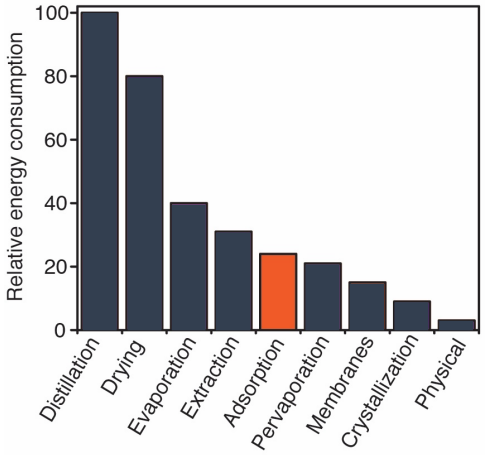

Figure 1.1. Relative energy consumption of different separation methods.[3] The relative energy cost of adsorption relative to commonly used methods such as distillation, drying, and evaporation is highlighted.

Among candidates for alternative separation methods, adsorption-based processes have the potential to be highly effective, particularly for gas-phase separations.[3] Typically, adsorbents are porous solids with binding sites for gas molecules.[4] When these adsorbents are either mesoporous, where a material has pores sizes of 2 to 50 nm, or even microporous, where a material has pore sizes of less than 2 nm, these materials can capture significant amounts of gas due to the large internal surface area associated with this porosity. When exposed to a gas mixture, the gas adsorbed onto the material is separated from the overall mixture. When done selectively, this method provides a very energy-efficient way to separate the gases in a mixture. Removing the adsorbed gas from the adsorbent can be accomplished by applying vacuum or heat to regenerate the adsorbent, allowing the material to be reused. If both selective adsorption and efficient

desorption can effectively occur at reasonable temperatures and pressures, this can dramatically reduce the energy costs associated with chemical separations.

An ideal adsorbent needs to consider several different factors when considering an industrial process:

(1) **Capacity**: The amount of the desired adsorbate that can be adsorbed by the material, which is often expressed gravimetrically. The higher the capacity, the less adsorbent is required, reducing the amount of material needed for an effective process.
(2) **Selectivity**: The ratio of the capacity of the desired adsorbate that is adsorbed versus the capacity of unwanted adsorbates that are adsorbed, when operating in a mixed gas environment with all adsorbates present to compete for binding sites. This value is dependent on the starting ratios of the partial pressures of different gases in a given mixture. An ideal adsorbent will have high selectivity for the desired adsorbate over others in a given gas mixture, even when the starting partial pressure of the desired adsorbate is substantially lower than the combined partial pressure of unwanted adsorbates, all while being effective at relevant pressures and temperatures. While important for all processes, this is particularly important when the desired adsorbate is valuable as a reagent.
(3) **Recyclability**: The performance of the adsorbent when used for successive separation cycles, typically measured as a comparison between the capacity in the first adsorption cycle to the capacity in subsequent adsorption cycles. In most cases, the adsorbent needs to be able to be used multiple times without losing any capacity, requiring the adsorbate-adsorbent interaction to be weak enough to be able to remove the adsorbent under mild conditions such as heating or applying vacuum. This is often in direct conflict with the selectivity described in item (2), as the stronger the adsorbate-adsorbent interaction, the worse the recyclability but better the selectivity.
(4) **Working capacity**: The actual amount that can be captured when using the adsorbent for multiple separation cycles. This is related to the total capacity described in item (1), but not all of this capacity is usable. Regeneration of the material after a separation cycle occurs primarily through temperature swing adsorption, where the material is heated up to remove the gas, or vacuum swing adsorption, where the pressure of the adsorbent bed is lowered to remove the gas through vacuum. When regenerating the material, some gas will be retained, and the difference in capacity between the total amount of gas adsorbed and the amount of gas retained under desorption conditions is the working capacity. A diagram is depicted in Figure 1.2. This working capacity is another factor when designing an adsorbent, and manipulating how temperature and pressure differences affect the adsorption properties needs to be considered to maximize the working capacity.
(5) **Regeneration energy**: The energy input required to regenerate the adsorbent. This value is related to the strength of the adsorbate-adsorbent interaction, as the stronger this is the more energy required to regenerate that adsorbent. The regeneration energy is also correlated to the working capacity and the heat capacity of the material.
(6) **Adsorption and desorption kinetics**: The diffusion of both adsorbed and desorbed species. Due to the small size of the pores, diffusion of the adsorbates within the pores of the adsorbent might limit the effectiveness of some materials on larger scales.

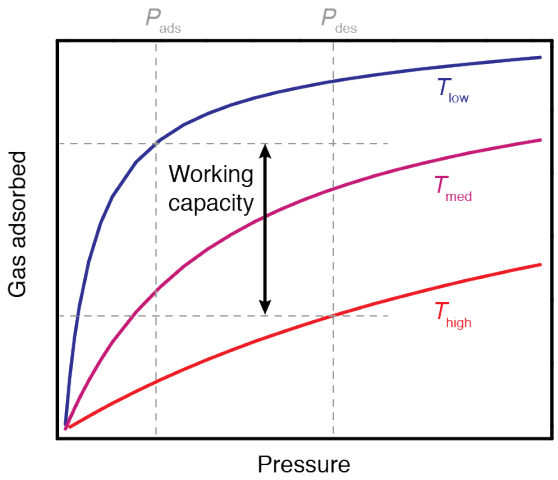

Figure 1.2. Working capacity in adsorbents. Typical adsorption isotherms shown for a standard adsorbent at three different temperatures, with the amount of gas adsorbed plotted as a function of pressure. In this case, the working capacity is demonstrated through a temperature swing process, with adsorption occurring at T_{low} and P_{ads}, with the amount adsorbed at this point denoted as the capacity. During regeneration, desorption occurs at higher temperatures and pressures T_{high} and P_{des}, where the adsorbent still retains some gas. The difference between these two values is the working capacity.

Traditional adsorbents such as zeolites and activated carbons have found niche applications for separations, but full scale industrial separations through adsorption are limited.[5] While cheap and very stable, these materials generally do not possess strong metrics in several of the categories listed above, and are often severely lacking in some categories, rendering them ineffective to replace thermal-based separations methods. As such, designing new adsorbates for every type of gas mixture for every separation is a difficult task, and a tunable set of materials should be the most effective in performing these processes.

1.2. Metal–organic frameworks as selective adsorbents

Metal–organic frameworks are a class of permanently porous materials consisting of organic bridging linkers that connect metal nodes to make extended networks, typically in three dimensions.[6] These materials can be synthesized in a variety of ways, with solvothermal synthesis in organic solvents being the primary method. The as-synthesized materials can then be desolvated, or activated, by applying heat or vacuum, yielding frameworks with high porosities and access to the internal pore environments that contains both organic and inorganic functional groups. Despite the sometimes large pore sizes, they are relatively chemically and thermally stable, especially when using linkers that produce strong metal–ligand bonds.[7] Due to their construction, by modifying the organic linker, the metal node, or coordination environment around the metal nodes, materials of several different topologies, pore sizes, pore shapes, and other variations can be made. As such, these have been explored for a variety of different applications, including selective gas sorption for potential gas separations.

Compared to more traditional adsorbents, the synthetic conditions and molecular precursors allow for the construction of highly crystalline materials.[8] These can be studied by traditional diffraction techniques to accurately study the framework structure and sometimes the interaction

of adsorbates on the binding sites of the framework. Additionally, common inorganic spectroscopy techniques, such as infrared spectroscopy and solid-state nuclear magnetic resonance spectroscopy, can be used to study interactions with a high degree of understanding of the sites that these techniques are probing. Finally, the transition metals and their coordination environments lead to facile characterization through electronic characterization such as X-ray adsorption spectroscopy, UV-Vis spectroscopy, magnetic susceptibility measurements, and even Mössbauer spectroscopy where applicable. Analysis using a wide range of these methods helps aid in probing the mechanisms for adsorption, and, combined with the great tunability, can to make new materials with improved properties for gas separations.

A wide range of mechanisms for separations are displayed in metal–organic frameworks to selectively adsorb one particular gas in a given mixture. The small size (in some cases < 1 nm) of the pores observed in metal–organic frameworks allows for size exclusion, where smaller adsorbates are selectively adsorbed over larger ones.[9] For example, a recent work that allows propylene to enter the pores of a material, but rejects propane, resulting in nearly perfect selectivity for propylene.[10] However, several disadvantages occur from this mechanism. Due to the obvious limitations in pore size relative to the size of the adsorbate, the diffusion of adsorbates into the material is relatively slow. As such, the performance under realistic conditions shows substantial decreases in separation capacities, indicating that most of the material is unutilized. Similar ideas invoking not just the size but the shape of the pores, invoking either the different shapes or flexibility of given adsorbates, have also been reported.[11] This has been shown to be highly effective for certain separations involving larger hydrocarbon isomers or specific mixtures involving rigid and flexible molecules, but the separations explored here lack this chemical handle.[12]

Selective chemisorption, where the gas molecule can react with some part of the framework, has also been explored.[13] This can typically allow for faster diffusion and is more applicable to some of the smaller gas phase substrates. If this reactivity is selective, then this can be another method used for separation purposes. For example, the acidity of CO_2 has been leveraged in amine-based chemistry to form carbamate or carbamic acid species selectively to separate it from either methane or nitrogen.[14] When reactivity is reversible under mild conditions, this method can then be used as the basis for industrial separations.

Physisorption, the use of weak adsorbent-adsorbate interactions, has also been investigated.[15] This can be due to a variety of organic and inorganic functionalities to selectively bind gas molecules typically quite weakly, allowing for reversibility. Of particular interest are frameworks exhibiting coordinatively unsaturated metal sites, as this site can be used as a binding site for gas molecules of interest (Figure 1.3). During the synthesis of the framework, these metal sites are initially ligated by solvent molecules. It was found that in several of these materials, replacing this solvent molecule with a relatively weak labile ligand such as methanol can be achieved. This methanol molecule can then be removed upon activation to make an open coordination site, or open metal site. The open metal site is a powerful tool that can be used as a tunable handle for selective gas binding to be highly effective for gas separations. Several examples of frameworks form with high densities of accessible, open metal sites, spanning a wide array of different transition metals and different coordination environments.[16] Additionally, even more methods have been developed to post-synthetically insert these open metal sites to already-synthesized frameworks bearing accessible metal coordination ligands.[17] As such, the gas binding sites can be precisely tuned to make a highly selective adsorbent for a variety of different gas mixtures.

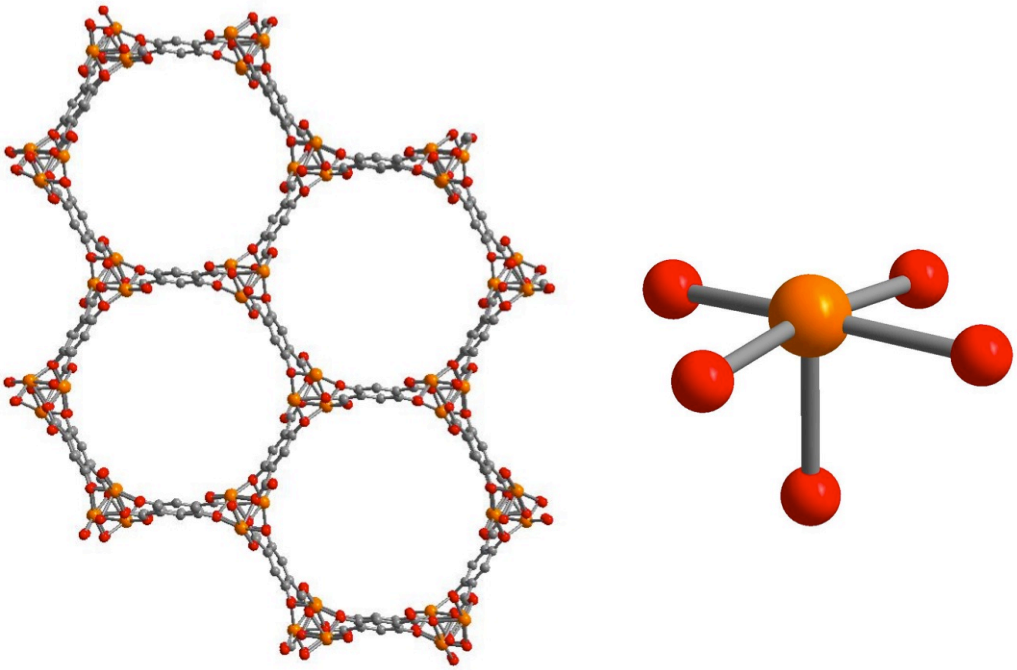

Figure 1.3. Representative structure of a metal–organic framework containing open metal sites, $Fe_2(dobdc)$ ($dobdc^{4-}$ = 2,5-dioxido-1,4-benzenedicarboxylate). (Left) Portion of the structure showing high accessibility to internal pore surfaces, in particular the exposed Fe(II) sites residing at the vertices of the hexagonal pores that can be used as selective binding sites. (Right) First coordination sphere of the iron centers, showing a very accessible open coordination site. Orange, red, and grey spheres represent Fe, O, and C, respectively; H atoms have been omitted.

1.3. Coordinatively unsaturated metal centers as selective gas binding sites

1.3.1. Current examples of coordinatively unsaturated metal centers for gas separations. Metal–organic frameworks containing these open metal sites have been shown to be highly effective for certain gas separations. Among the types of separations examined here, open metal sites functioning through this Lewis acidic mechanism have been shown to be highly effective for separations. This strategy of using Lewis acidic open metal sites as the primary method for separation selectivity leverages the typical metal centers and metal coordination environments observed in metal–organic frameworks. The majority of metal–organic frameworks are synthesized using late transition metals and carboxylate or aryl-oxide donors, rendering them quite electron poor and highly polarizing for this type of separation.

One of the earliest examples of using a metal–organic framework containing open metal sites for use in gas separations occurred was for CO_2-based separations. In 2008, Matzger and coworkers reported the ability to separate CO_2 from N_2 using a series of isotypic materials with exposed Mg(II), Co(II), or Ni(II) (analogous to the structure depicted in Figure 1.3).[18] All three metal sites were shown to be highly selective for CO_2, and showed > 25 wt % capacities at substantially less than 1 bar, while neither was able to adsorb more than 1 wt % of N_2 at 1 bar. The higher polarizability of CO_2 allows for very selective separations in this manner, and trends based on the identity of the metal center explained the differences in binding strength and selectivity for

CO_2 adsorption.[19] It was found that other materials featuring open metal sites could perform this separation, performing this selective adsorption in a similar manner.[20] Additionally, CO_2 separations from CH_4 and H_2 could also be performed with open metal sites, again leveraging the greater polarizability of CO_2.[21] The high density of open metal sites and the selectivity with which they bind CO_2 over other substrates make these materials extremely high performing for separations involving these particular gas mixtures.[22]

This open metal site and its ability to act as a Lewis acid was more thoroughly extended to separations not involving CO_2. It was shown that this property can be used to separate olefins and paraffins, particularly ethylene/ethane and propylene/propane mixtures.[23] In these cases, again the greater polarizability of the olefin molecule was used to produce selective binding of the olefin. This was confirmed through a variety of spectroscopic methods, including the structural characterization of a very long metal–olefin bond, showing minimal π -donation to the olefin that is typically observed in molecular transition metal–olefin interactions.[23a] Importantly, this interaction is highly reversible, making easily regenerable ethylene or propylene adsorbents. However, the relative polarizabilities of either ethane or propane makes this adsorption substantially less selective than that of separations involving CO_2, as these materials also adsorb a significant amount of the paraffin as well. To improve the ability of these sites using this adsorption mechanism, increasing the charge density on the metal sites and making the metal sites even more Lewis acidic was shown to increase the separation performance.[24] This strategy for separations involving other hydrocarbon mixtures has been achieved with various degrees of success based on the metal centers involved.[25]

Even for gaseous substrates that have other accessible chemical handles, such as CO and O_2, the majority of metal–organic frameworks use Lewis acidic sites for effective separations. Similar mechanisms for mixtures involving carbon monoxide, such as CO/N_2 and CO/H_2 separations, were also able to show good selectivity for binding CO over N_2 or H_2.[26] While most molecular examples of binding CO are often associated with changing electron structures due to the strong field character, in metal–organic frameworks this typically does not occur. This has been shown through a variety of different spectroscopic methods, which show that the metal–carbonyl interaction is non-classical, with unusual high-spin metal centers, long and non-linear metal–CO bonds, and blueshifted ν_{CO} stretching frequencies.[26,27] Similar to the ethylene example, the weak interaction allows for facile removal and thus good reversibility. The separation of N_2 from O_2 from air has also been investigated using this Lewis acidic mechanism, with materials that are typically slightly N_2 selective.[28] However, this trend is much less common, with some materials being slightly O_2 selective, even while retaining the Lewis acidic mechanism, indicating that metal identities and environments need to be carefully chosen for this separation to occur.[29] Finally, very recent work has shown that very Lewis acidic species with the right electronic structure can selectively adsorb N_2 over CH_4 under the right pressure and temperature conditions.[28]

1.3.2. Limitations of current adsorption mechanisms. While highly effective for certain separations, this mechanism of using the metal centers as polarizing, exposed cations do have some distinct limitations pertaining to gas separations. These disadvantages come from two main areas. First, due to the lack of exploiting different chemical handles, generally only substrates with differences in polarizability can be effectively separated, limiting the separations that can be performed. Second, when trying to design energy efficient regeneration conditions, standard adsorption behavior through these mechanisms generally encounters a trade-off where improving the selectivity for adsorption is generally associated with increasing the regeneration energy required for reactivation, limiting the overall effectiveness of these systems.

In addressing the first limitation, the restriction to one mechanism only utilizes one handle among several different types of gaseous species that require separation. As the selectivity of binding to metal sites is typically done through one mechanism, this limits the types of separations that can be performed. For example, types of separations involving gases that are not very polarizable, such as nitrogen and methane, are very difficult to make selective and difficult to create adsorbents with reasonable capacities (Figure 1.4).[21,22] Having both molecules bind too strongly can also be a problem, as is encountered with separations involving larger hydrocarbons.[30] Adsorbates that are relatively polarizable but easily reversible as well, such as ethylene, CO_2, and CO, are extremely common in gas mixtures but generally are not considered when designing new materials, rendering wildly different separation abilities.[18–26] While careful choice of cation-dependent properties such as ionic radii or electropositivity may be used to alleviate this problem, the use of different chemical handles, such as π-acidity, redox activity, ligand field strength, and others would be a more straightforward way to selectively adsorb certain gas molecules in a mixture.

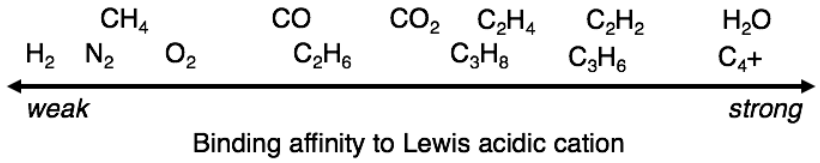

Figure 1.4. Typical relative binding strengths of common gas molecules to Lewis acidic cations. Molecules with similar polarizabilities often bind with similar affinities. While certain modifications to cation-dependent properties can influence the binding strength of a particular adsorbate, deviating from this mechanism for adsorption can potentially perform more difficult separations.

As an extension from this, application of selective adsorbents that have been studied for a binary gas mixture to more realistic mixtures that have other gases present may present additional problems. For example, if a desired selectivity of CO_2 over CH_4 is used in a realistic property such as natural gas purification, there generally exists small amounts of ethane, which could impact the selectivity for CO_2 as ethane can sometimes bind with similar binding enthalpies.[31] Another process, such as removal of CO from H_2, could also be hampered by the presence of the competitively-binding CO_2, as would exist after the production of H_2 through the water-gas shift reaction.[32] Overall, creating more chemical-specific handles could potentially be a way to make more applicable adsorbents for realistic applications.

Secondly, the types of isotherms that exist generally are classified as a type I adsorption isotherm, in which the gas uptake is initially very steep at low pressures and then gradually gets shallower as pressure is increased (Figure 1.2). This type of classical adsorption is highly effective for separations, as a high capacity can be quickly reached, even at low pressures. When comparing two isotherms, the steepness of the adsorption isotherm curve of the desired gas relative to the steepness of the undesired gas generally dictates the selectivity. As such, the steeper the isotherm, the more selective the material is for adsorbing that particular gas. However, the trade-off occurs when considered desorbing the gas to regenerate the material. This steep isotherm means that significantly higher temperatures or much lower pressures are required to remove the gas under real conditions and achieve reasonable working capacities. With this type of adsorption behavior

that results in these adsorption isotherm shapes, it is difficult to remove this correlation. Next generation adsorbents would ideally remove this correlation, and potentially the addition of phase-change like behavior could allow for different temperature and pressure dependences of the adsorption isotherms, resulting in different types of isotherm shapes for more energy efficient processes. Leveraging new techniques, we will investigate new methods of combing high selectivity and reasonable regeneration energies by using open metal sites in metal–organic frameworks.

These two limitations present major obstacles when envisioning adsorbent-based technologies as alternative separations methods. In addition, more minor implications related to practical usage of adsorbents also exist when using the metal centers as Lewis acidic cations. As these materials are meant to displace energetically costly cryogenic distillation, a key feature is the ability to perform these separations at higher temperatures than these distillation processes to reduce the amount of energy used in heating and cooling. However, the selectivity for the desired gas molecules that these systems exhibit are often highly temperature dependent, with these materials showing good selectivity at one temperature, but showing a gradual or even a substantial decrease in selectivity upon raising the temperature. In some cases, this completely removes the selectivity by raising the temperature just 20 °C (ref. 26c). As the Lewis acidic mechanism for adsorption generally promotes weak interactions and physisorption-like behavior, this negative response of selectivity to temperature is difficult to overcome. Using open metal sites in different ways can potentially help achieve improved selectivities at higher temperatures through formation of more bond-like interactions with adsorbate molecules.

1.4. Proposed new mechanisms for adsorption

As metal–organic frameworks can be synthesized using common inorganic and coordination chemistry concepts, we sought to envision ways that new materials can be designed with metal sites that have properties to take advantage of other chemical handles present in industrially relevant gas mixtures. We also wish to create materials that can leverage different materials properties that can result in new energy-efficient methods of separation. We propose five main deviations that can be made to the standard open metal site in metal–organic frameworks, and by doing so we can add new functionalities to these sites to perform new or more effective gas separations (Figure 1.5):

(1) **Electron-donating metal centers**: Simply switching from an electron-accepting metal center to an electron-donating metal center would allow for new types of separations. This has been proposed in theory, but due to the types of metals and weak field ligand environments typically encountered, actual implementation of this concept is limited. By switching to more electron donating ligands and more reducing metal centers, such as early first-row transition metals or second or third-row transition metals, this could potentially be achieved.[33] This could be used for potential donation to π-acidic gases, such as H_2, N_2, CO, olefins, and acetylene.

(2) **Redox-active metal centers**: Certain gaseous molecules can promote electronic responses at metal sites in molecular or biological compounds. In particular, some molecules are prone to redox activity, such as O_2, and designing new systems that selectively and reversibly oxidize in the presence of O_2 could be very effective for a separation. This has been shown for the selective adsorption of O_2 from N_2 through

installing redox active metal centers, such as Cr(II), Mn(II), Fe(II), and Co(II).[34] However, these systems either can only operate at low temperatures or face reversibility issues. As such, we can seek to more rationally install these sites to be more effective at these separations through controlling the coordination environment of these redox-active sites.

(3) **Spin transition metal centers**: Other gas molecules can promote spin transitions, such as turning an otherwise high-spin metal center to low-spin. This can be envisioned with certain strong field gas ligands such as CO, and would be highly selective for these substrates. If this process is reversible, it should allow for an easier release of the gas molecule for facile regeneration of the adsorbent. However, the rearrangements and flexibility required with this transition is difficult. A small amount of materials exhibit both spin transition properties and porosity, and none of them possess the required open metal sites necessary for this separation.[35] Designing a system that has open metal sites and the ability to perform spin transition could be a way to selectively capture these strong field ligands such as CO, but also potentially olefins and acetylene.

(4) **Multi-metal site interactions**: As all reported examples utilize these metal sties as isolated binding sites, moving to systems that use multiple metal sites could be advantageous. In practice, most metal–organic frameworks contain several metal centers that exist close to each other,[16] able to interact with one another if given the appropriate ligand environment. For example, the synergistic interaction between two different metal centers can be used to selectively adsorb molecules that can effectively bridge these centers versus molecules that are too small or too large. This can be used for separation of larger hydrocarbon isomers, such as xylene isomers.[36]

(5) **Cooperative adsorption**: Lastly, looking at systems where the metal centers communicate in some way, so that when binding occurs at one metal center the binding properties of neighboring sites change, this can impart many new effects. This can be used to leverage cooperative adsorption, a concept taken from biological systems such as hemoglobin where binding at one metal site promotes binding at neighboring sites.[37] This has been shown in synthetic systems to result in high working capacities with low temperature swings, resulting in low regenerations energies while retaining high selectivity.[38] As such, these materials have much higher energy efficiencies for separations than traditional adsorbents. However, current systems are highly chemically specific for CO_2, requiring insertion into metal–amine bonds and forming ammonium carbamate pairs, and extension to other substrates is difficult given these mechanisms. In theory, binding at an open metal site that promotes some rearrangement could impact nearby sites, causing this cooperative adsorption. In theory, the redox activity or spin transitions proposed in idea (2) or (3) could be the basis for this mechanism.[39] If cooperative adsorption is demonstrated for materials with open metal sites, this can be a generalizable design principle and a basis for more energy efficient adsorbents for several industrial separations.

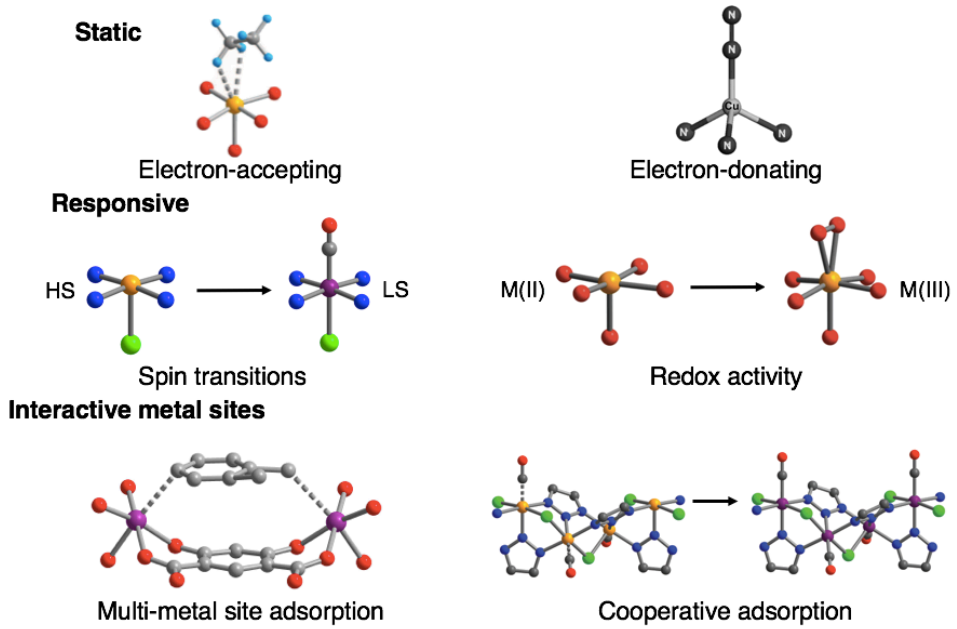

Figure 1.5. Proposed new mechanisms for gas adsorption at open metal sites.

This thesis studies several of these proposed mechanisms explicitly, including making advances in the Lewis acidic metal site adsorption mechanism for new separations. Ultimately, these can serve as new design principles for developing new adsorbent-based technologies for industrial applications.

1.5. Conclusions and outlook

As illustrated, metal–organic frameworks bearing open metal sites have shown impressive performance in gas separations. However, separations involving certain gas mixtures can be improved in terms of the selectivities of the adsorbent, and all adsorbents can be improved in terms of their energy efficiency. The tunable nature of metal–organic frameworks allows for the design of new metal sites that can take advantage of a whole range of basic inorganic coordination chemistry concepts and small molecule binding. Designing new frameworks to take advantage of these new proposed mechanisms could lead to more advanced materials properties for gas separations. In addition to the potential industrial applications, the concepts proposed here and the materials designed and synthesized can also eventually be used for applications in gas storage, sensing, conductivity, catalysis, and drug delivery, making them highly applicable and important fundamental works.

1.6. References

(1) Sholl, D. S.; Lively, R. P. *Nature* **2016**, *532*, 435–437.
(2) Kerry, F. G. *Industrial Gas Handbook: Gas Separation and Purification*; CRC: Boca Raton, FL, 2007.

(3) U.S. Department of Energy. *Materials Separation Technology: Energy and Emission Reduction Opportunities*. **2005**.
(4) Yang, R. T. *Gas Separations by Adsorption Process.* Ch. 7. Buttersworth: Boston, 1987.
(5) (a) Ackley, M. W.; Rege, S. U.; Saxena, H. *Microporous Mesoporous Mater.* **2003**, *61*, 25–42. (b) Moliner, M.; Martinez, C.; Corma, A. *Chem. Mater.* **2014**, *26*, 246–258. (c) Sircar, S.; Golden, T. C.; Rao, M. B. *Carbon* **1996**, *34*, 1–12.
(6) (a) Yaghi, O. M.; Li, H.; Eddaoudi, M.; O'Keefe, M. *Nature* **1999**, *402*, 276−279. (b) Kitagawa, S.; Kitaura, R.; Noro, S.-I. *Angew. Chem., Int. Ed.* **2004**, *43*, 2334−2375. (c) Matsuda, R.; Kitaura, R.; Kitagawa, S.; Kubota, Y.; Belosludov, R. V.; Kobayashi, T. C.; Sakamoto, H.; Chiba, T.; Takata, M.; Kawazoe, Y.; Mita, Y. *Nature* **2005**, *436*, 238− 241. (d) Millward, A. R.; Yaghi, O. M. *J. Am. Chem. Soc*. **2005**, *127*, 17998−17999. (e) Ferey, G. *Chem. Soc. Rev*. **2008**, *37*, 191−214. (f) Morris, R. E.; Wheatley, P. S. *Angew. Chem., Int. Ed*. **2008**, *47*, 4966−4981. (g) Czaja, A. U.; Trukhan, N.; Müller, U. *Chem. Soc. Rev*. **2009**, *38*, 1284−1293. (h) Chen, B.; Xiang, S.; Qian, G. *Acc. Chem. Res*. **2010**, *43*, 1115−1124. (i) Zhou, H.-C.; Long, J. R.; Yaghi, O. M. *Chem. Rev*. **2012**, *112*, 673−674. (j) Schneemann, A.; Henke, S.; Schwedler, I.; Fischer, R. A. *ChemPhysChem* **2014**, *15*, 823−839. (k) Evans, J. D.; Sumby, C. J.; Doonan, C. J. *Chem. Soc. Rev*. **2014**, *43*, 5933−5951.
(7) (a) Howarth, A. J.; Liu, Y.; Li, P.; Li, Z.; Wang, T. C.; Hupp, J. R.; Farha, O. K. *Nat. Rev. Mater.* **2016**, *1*, 1–15. (b) Bosch, M.; Zhang, M.; Zhou, H.-C. *Adv. Chem.* **2014**, 182327.
(8) Howarth, A. J.; Peters, A. W.; Vermeulen, N. A.; Wang, T. C.; Hupp, J. T.; Farha, O. K. *Chem. Mater.* **2017**, *29*, 26–39.
(9) (a) Ma, S. Q.; Wang, X. S.; Yuan, D. Q.; Zhou, H.-C. *Angew. Chem., Int. Ed.* **2008**, *47*, 4130–4133. (b) Loiseau, T.; Lecroq, L.; Volkringer, C.; Marrot, J.; Férey, G.; Haouas, M.; Taulelle, F.; Bourrelly, S.; Llewellyn, P. L.; Latroche, M. *J. Am. Chem. Soc.* **2006**, *128*, 10223–10230. (c) Xue, M.; Ma, S. Q.; Jin, Z.; Schaffino, R. M.; Zhu, G. S.; Lobkovsky, E. B.; Qiu, S. L.;Chen, B. L. *Inorg. Chem.* **2008**, *47*, 6825–6828 (d) Cui, X.; Chen, K.; Xing, H.; Yang, Q.; Krishna, R.; Bao, Z.; Wu, H.; Zhou, W.; Dong, X.; Han, Y.; Li, B.; Ren, Q.; Zaworotko, M. J.; Chen, B. *Science* **2016**, *353*, 141–144. (e) He, Y.; Xiang, S.; Zhang, Z.; Xiong, S.; Fronczek, F. R.; Krishna, R.; O'Keeffe, M.; Chen, B. *Chem. Commun*. **2012**, *48*, 10856.
(10) Cadiau, A.; Adil, K.; Bhatt, P. M.; Belmabkhout, Y.; Eddaoudi, M. *Science* **2016**, *353*, 137–140.
(11) Liao, P.-Q.; Huang, N.-Y.; Zhong, W.-X.; Zhang, J.-P.; Chen, X.-M. *Science* **2017**, *356*, 1193–1196.
(12) (a) Herm, Z. R.; Wiers, B. M.; Mason, J. A.; van Baten, J. M.; Hudson, M. R.; Zajdel, P.; Brown, C. M.; Masciocchi, N.; Krishna, R.; Long, J. R. *Science* **2013**, *340*, 960–964. (b) Warren, J. E.; Perkins, C. G.; Jelfs, K. E.; Boldrin, P.; Chater, P. A.; Miller, G. J.; Manning, T. D.; Briggs, M. E.; Stylianou, K. C.; Claridge, J. B.; Rosseinsky, M. J. *Angew. Chem., Int. Ed*. **2014**, *53*, 4592−4596.
(13) Sumida, K.; Rogow, D. R.; Mason, J. A.; McDonald, T. M.; Bloch, E. D.; Herm, Z. R.; Bae, T.-H.; Long, J. R. *Chem. Rev*. **2012**, *112*, 724− 781.
(14) (a) McDonald, T. M.; Lee, W. R.; Mason, J. A.; Wiers, B. M.; Hong, C. S.; Long, J. R. *J. Am. Chem. Soc.***2012**, *134*, 7056–7065. (b) Milner, P. J.; Siegelman, R. L.; Forse, A. C.; Gonzalez, M. I.; Runčevski, T.; Martell, J. D.; Reimer, J. A.; Long, J. R. *J. Am. Chem. Soc.* **2017**, *139*, 13541–13553. (c) Flaig, R. W.; Osborn Popp, T. M.; Fracaroli, A. M.;

Kapustin, E. A.; Kalmutzki, M. J.; Altamimi, R. M.; Fathieh, F.; Reimer, J. A.; Yaghi, O. M. *J. Am. Chem. Soc.* **2017**, *139*, 12125–12128.

(15) Li, J.-R.; Sculley, J.; Zhou, H.-C. *Chem. Rev*. **2012**, *112*, 869−932.

(16) (a) Rosi, N. L.; Kim, J.; Eddaoudi, M.; Chen, B.; O'Keeffe, M.; Yaghi, O. M. *J. Am. Chem. Soc*. **2005**, *127*, 1504. (b) Dietzel, P. D. C.; Panella, B.; Hirscher, M.; Blom, R.; Fjellvag, H. *Chem. Commun*. **2006**, 959. (c) Chui, S. S. Y.; Lo, S. M. F.; Charmant, J. P. H.; Orpen, A. G.; Williams, I. D. *Science* **1999**, *283*, 1148. (d) Horcajada, P.; Surble, S.; Serre, C.; Hong, D.-Y.; Seo, Y.-K.; Chang, J.-S.; Greneche, J.-M.; Margiolaki, I.; Ferey, G. *Chem. Commun*. **2007**, 2820. (e) Dincă, M.; Dailly, A.; Liu, Y.; Brown, C. M.; Neumann, D. A.; Long, J. R. *J. Am. Chem. Soc.* **2006**, *128*, 16876-16883.

(17) (a) Bloch, E. D.; Britt, D.; Doonan, C. J.; Uribe-Romo, F. J.; Furukawa, H.; Long, J. R.; Yaghi, O. M. *J. Am. Chem. Soc.* **2010**, *132*, 14382–14384. (b) Gonzalez, M. I.; Bloch, E. D.; Mason, J. A.; Teat, S. J.; Long, J. R. *Inorg. Chem.* **2015**, *54*, 2995–3005. (c) Feng, D.; Chung, W.-C.; Wei, Z.; Gu, Z.-Y.; Jiang, H.-L.; Chen, Y.- P.; Darensbourg, D. J.; Zhou, H.-C. *J. Am. Chem. Soc*. **2013**, *135*, 17105. (d) Shultz, A. M.; Sarjeant, A. A.; Farha, O. K.; Hupp, J. T.; Nguyen, S. T. *J. Am. Chem. Soc.* **2011**, *133*, 13252–13255.

(18) (a) Caskey, S. R.; Wong-Foy, A. G.; Matzger, A. J. *J. Am. Chem. Soc.* **2008**, *130*, 10870–10871. (b) Britt, D.; Furukawa, H.; Wang, B.; Glover, T. G.; Yaghi, O. M. *Proc. Natl. Acad. Sci. U.S.A*. **2009**, *106*, 20637–20640.

(19) (a) Dietzel, P. D. C.; Johnson, R. E.; Fjellvag, H.; Bordiga, S.; Groppo, E.; Chavan, S.; Blom, R. *Chem. Commun.* **2008**, 5125–5127. (b) Queen, W. L.; Hudson, M. R.; Bloch, E. D.; Mason, J. A.; Gonzalez, M. I.; Lee, J. S.; Gygi, D.; Howe, J. D.; Lee, K.; Darwish, T. A.; James, M.; Peterson, V. K.; Teat, S. J.; Smit, B.; Neaton, J. B.; Long, J. R.; Brown, C. M. *Chem. Sci*. **2014**, *5*, 4569–4581. (c) Gonzalez, M. I.; Mason, J. A.; Bloch, E. D.; Teat, S. J.; Gagnon, K. J.; Morrison, G. Y.; Queen, W. L.; Long, J. R. *Chem. Sci.* **2017**, *8*, 4387–4398.

(20) Ye, S.; Jiang, X.; Ruan, L.-W.; Liu, B.; Wang, Y.-M.; Zhu, J.-F.; Qiu, L.-G. *Microporous Mesoporous Mater.* **2013**, *179* 191–197. (b) Asgari, M.; Jawahery, S.; Bloch, E. D.; Hudson, M. R.; Flacau, R.; Vlaisavljevich, B.; Long, J. R.; Brown, C. M; Queen, W. L. *Chem. Sci.* **2018**, *9*, 4579–4588. (c) Mason, J. A.; McDonald, T. M.; Bae, T.-H.; Bachman, J. E.; Sumida, K.; Dutton, J. J.; Kaye, S. S.; Long, J. R. *J. Am. Chem. Soc.* **2015**, *137*, 4787–4803.

(21) (a) Herm, Z. R.; Swisher, J. A.; Smit, B.; Krishna, R; Long, J. R. *J. Am. Chem. Soc.* **2011**, *133*, 5664–5667. (b) Herm, Z. R.; Krishna, R.; Long, J. R. *Microporous Mesoporous Mater.* **2012**, *151*, 481–487.

(22) (a) Bae, Y.-S.; Mulfort, K. L.; Frost, H.; Ryan, P.; Punnathanam, S.; Broadbelt, L. J.; Hupp, J. T.; Snurr, R. Q. *Langmuir* **2008**, *24*, 8592. (b) Mu, B.; Li, F.; Walton, K. S. *Chem. Commun*. **2009**, 2493.

(23) (a) Bloch, E. D.; Queen, W. L.; Krishna, R.; Zadrozny, J. M.; Brown, C. M.; Long, J. R. *Science* **2012**, *355*, 1606–1610. (b) Geier, S. J.; Mason, J. A.; Bloch, E.D.; Queen, W. L.; Hudson, M. R.; Brown, C. M.; Long, J. R. *Chem. Sci.* **2013**, *4*, 2054–2061. (c) Bao, Z.; Alnemrat, S.; Yu, L.; Vasiliev, I.; Ren, Q.; Lu, X.; Deng, S. *Langmuir* **2011**, *27*, 13554–13562. (d) Bae, Y.-S.; Lee, C. Y.; Kim, K. C.; Farha, O. K.; Nickias, P.; Hupp, J. T.; Nguyen, S. T.; Snurr, R. Q. *Angew. Chem., Int. Ed.* **2012**, *51*, 1857–1860. (e) Wang, Q. M.; Shen, D. M.; Bülow, M.; Lau, M. L.; Deng, S. G.; Fitch, F. R.; Lemcoff, N. O.; Semanscin, J. *Microporous Mesoporous Mater*. **2002**, *55*, 217.

(24) Bachman, J. E.; Kapelewski, M. T.; Reed, D. A.; Gonzalez, M. I.; Long, J. R. *J. Am. Chem. Soc.* **2017**, *139*, 15363–15370.
(25) (a) Herm, Z. R.; Bloch, E. D.; Long, J. R. *Chem. Mater.* **2014**, *26*, 323–338. (b) Duan, X.; He, Y.; Cui, Y.; Yang, Y.; Krishna, R.; Chen, B.; Qian, G. *RSC Adv*. **2014**, *4*, 23058−23063. (c) He, Y.; Krishna, R.; Chen, B. *Energy Environ. Sci.* **2012**, *5*, 9107–9120.
(26) (a) Sato, H.; Kosaka, W.; Matsuda, R.; Hori, A.; Hijikata, Y.; Belosludov, R. V.; Sakaki, S.; Takata, M.; Kitagawa, S. *Science* **2014**, *343*, 167−170. (b) Bloch, E. D.; Hudson, M. R.; Mason, J. A.; Chavan, S.; Crocella, V.; Howe, J. D.; Lee, K.; Dzubak, A. L.; Queen, W. L.; Zadrozny, J. M.; Geier, S. J.; Lin, L.-C.; Gagliardi, L.; Smit, B.; Neaton, J. B.; Bordiga, S.; Brown, C. M.; Long, J. R. *J. Am. Chem. Soc*. **2014**, *136*, 10752−10761.
(27) (a) Chavan, S.; Vitillo, J. G.; Groppo, E.; Bonino, F.; Lamberti, C.; Dietzel, P. D. C.; Bordiga, S. *J. Phys. Chem. C* **2009**, *113*, 3292−3299. (b) Leclerc, H.; Vimont, A.; Lavalley, J.-C.; Daturi, M.; Wiersum, A. D.; Llwellyn, P. L.; Horcajada, P.; Ferey, G.; Serre, C. *Phys. Chem. Chem. Phys.* **2011**, *13*, 11748–11756.
(28) Yoon, J. W.; Chang, H.; Lee, S. J.; Hwang, Y. K.; Hong, D. Y.; Lee, S. K.; Lee, J. S.; Jang, S.; Yoon, T. U.; Kwac, K.; Jung, Y.; Pillai, R. S.; Faucher, F.; Vimont, A.; Daturi, M.; Férey, G.; Serre, C.; Maurin, G.; Bae, Y. S.; Chang. J. S. *Nat. Mater.* **2017**, *16*, 526–531.
(29) Sava Gallis, D. F.; Chapman, K. W.; Rodriguez, M. A.; Greathouse, J. A.; Parkes, M. V.; Nenoff, T. M. *Chem. Mater.* **2016**, *28*, 3327–3336.
(30) (a) Alaerts, L.; Kirschhock, C. E. A.; Maes, M.; van der Veen, M. A.; Finsy, V.; Depla, A.; Martens, J. A.; Baron, G. V.; Jacobs, P. A.; Denayer, J. F. M.; De Vos, D. E. *Angew. Chem., Int. Ed.* **2007**, *46*, 4293−4297. (b) Peralta, D.; Barthelet, K.; Perez-Pellitero, J.; Chizallet, C.;́ Chaplais, G.; Simon-Masseron, A.; Pirngruber, G. D. *J. Phys. Chem. C* **2012**, *116*, 21844−21855.
(31) Baker, R. W.; Lokhandwala, K. *Ind. Eng. Chem. Res.* **2008**, *47*, 2109–2121.
(32) Newsome, D. S. *Catal. Rev. Sci. Eng*. **1980**, *21*, 275–318.
(33) Lee, K.; Isley III, W. C.; Dzubak, A. L.; Verma, P.; Stoneburner, S. J.; Lin, L. C.; Howe, J. D.; Bloch, E. D.; Reed, D. A.; Hudson, M. R.; Brown, C. M.; Long, J. R.; Neaton, J. B.; Smit, B.; Cramer, C. J.; Truhlar, D. G.; Gagliardi, L. *J. Am. Chem. Soc.* **2014**, *136*, 698–704.
(34) (a) Murray, L. J.; Dincă, M.; Yano, J.; Chavan, S.; Bordiga, S.; Brown, C. M.; Long, J. R. *J. Am. Chem. Soc.* **2010**, *132*, 7856–7857. (b) Bloch, E. D.; Murray, L. M.; Queen, W. L.; Chavan, S.; Maximoff, S. N.; Bigi, J. P.; Krishna, R.; Peterson, V. K.; Grandjean, F.; Long, G. J.; Smit, B.; Bordiga, S.; Brown, C. M.; Long, J. R. *J. Am. Chem. Soc.* **2011**, *133*, 14814–14822. (c) Xiao, D. J.; Gonzalez, M. I.; Darago, L. E.; Vogiatzis, K. D.; Haldoupis, E.; Gagliardi, L.; Long, J. R. *J. Am. Chem. Soc.* **2016**, *138*, 7161–7170. (d) Bloch, E. D.; Queen, W. L.; Hudson, W. R.; Mason, J. A.; Xiao, D. J.; Murray, L. J.; Flacau, R.; Brown, C. M.; Long, J. R. *Angew. Chem. Int. Ed.* **2016**, *55*, 8605–8609. (e) Gallagher, A. T.; Lee, J. Y.; Kathiresan, V.; Anderson, J. S.; Hoffman, B. M.; Harris, T. D. *Chem. Sci.* **2018**, *9*, 1596–1603.
(35) (a) Halder, G. J.; Kepert, C. J.; Moubaraki, B.; Murray, K. S.; Cashion, J. D. *Science* **2002**, *298*, 1762−1765. (b) Bonhommeau, S.; Molnar, G.; Galet, A.; Zwick, A.; Real, J. A.; McGarvey, J. J.; Bousseksou, A. *Angew. Chem., Int. Ed*. **2005**, *44*, 4069−4073. (c) Quesada, M.; de la Pena-O'Shea, V. A.; Aromi, G.; Geremia, S.; Massera, C.; Roubeau, O.; Gamez, P.; Reedijk, J. *Adv. Mater*. **2007**, *19*, 1397−1402. (d) Neville, S. M.; Moubaraki, B.; Murray, K. S.; Kepert, C. J. *Angew. Chem., Int. Ed*. **2007**, *46*, 2059−2062.

(e) Neville, S. M.; Halder, G. J.; Chapman, K. W.; Duriska, M. B.; Southon, P. D.; Cashion, J. D.; Letard, J. F.; Moubaraki, B.; Murray, K. S.; Kepert, C. J. *J. Am. Chem. Soc*. **2008**, *130*, 2869−2876. (f) Halder, G. J.; Chapman, K. W.; Neville, S. M.; Moubaraki, B.; Murray, K. S.; Letard, J.-F.; Kepert, C. J. *J. Am. Chem. Soc*. **2008**, *130*, 17552−17652. (g) Ohba, M.; Yoneda, K.; Agusti, G.; Munoz, M. C.; Gaspar, A. B.; Real, J. A.; Yamasaki, M.; Ando, H.; Nakao, Y.; Sakaki, S.; Kitagawa, S. *Angew. Chem., Int. Ed*. **2009**, *48*, 4767−4771. (h) Southon, P. D.; Liu, L.; Fellows, E. A.; Price, D. J.; Halder, G. J.; Chapman, K. W.; Moubaraki, B.; Murray, K. S.; Letard, J. F.; Kepert, C. J. *J. Am. Chem. Soc*. **2009**, *131*, 10998−11009. (i) Ohtani, R.; Yoneda, K.; Furukawa, S.; Horike, N.; Kitagawa, S.; Gaspar, A. B.; Munoz, M. C.; Real, J. A.; Ohba, M. *J. Am. Chem. Soc*. **2011**, *133*, 8600−8605. (j) Salles, F.; Maurin, G.; Serre, C.; Llewellyn, P. L.; Knofel, C.; Choi, H. J.; Filinchuk, Y.; Oliviero, L.; Vimont, A.; Long, J. R.; Ferey, G. *J. Am. Chem. Soc*. **2010**, *132*, 13782−13788.

(36) Gonzalez, M. I.; Kapelewski, M. T.; Bloch, E. D.; Milner, P. J.; Reed, D. A.; Hudson, M. R.; Mason, J. A.; Barin, G.; Brown, C. M.; Long, J. R. *J. Am. Chem. Soc.* **2018**, *140*, 3412−3422.

(37) Perutz, M. F. *Mechanism of Cooperativity and Allosteric Regulation in Proteins*. Cambridge University Press, 1990.

(38) McDonald, T. M.; Mason, J. A.; Kong, X.; Bloch, E. D.; Gygi, D.; Dani, A.; Crocella, V.; Giordanino, F.; Odoh, S. O.; Drisdell, W.; Vlaisavljevich, B.; Dzubak, A. L.; Poloni, R.; Schnell, S. K.; Planas, N.; Lee, K.; Pascal, T.; Wan, L. F.; Prendergast, D.; Neaton, J. B.; Smit, B.; Kortright, J. B.; Gagliardi, L.; Bordiga, S.; Reimer, J. A.; Long, J. R. *Nature* **2015**, *519*, 303–308.

(39) (a) Kahn, O.; Martinez, C. J. *Science* **1998**, *279*, 44–48. (b) Niel, V.; Martinez-Agudo, J. M.; Munoz, M. C.; Gaspar, A. B.; Real, J. A. *Inorg. Chem.* **2001**, *40*, 3838–3839. (c) Foucher, D. A.; Honeyman, C. H.; Nelson, J. M.; Tang, B. Z.; Manners, I. *Angew. Chem., Int. Ed.* **1993**, *32*, 1709–1711.

Chapter 2: Backbonding-Based Gas Separations in a Metal–Organic Framework with Exposed Vanadium(II) Sites

2.1. Introduction

The effective utilization of solid adsorbents promises to be a central strategy toward mitigating the high energy and emission costs associated with current industrial chemical separations.[1,2] Implementation of this strategy relies on the design and development of porous materials with varying functionalities to affect selective capture for gas purification processes. While most industrial separations rely on relative volatility differences to impart selectivity, porous materials can separate gases based on various chemical properties, enabling operation at more relevant pressures and temperatures.[1] However, many industrially relevant gases interact weakly with adsorbates, and without substantial differences in common handles like polarizability or size, some separations remain challenging. Many of these gases, such as H_2, N_2, O_2, olefins, acetylene, and carbon monoxide, feature accessible π^* orbitals capable of accepting electron density. Therefore, if a material with exposed metal sites capable of backbonding to the adsorbate could be realized, π-acidity could be targeted as a means of imparting selectivity, enabling new separations of industrially relevant mixtures.

Metal–organic frameworks (MOFs), a class of crystalline and porous materials, have begun to rival the gas separation performance metrics of traditional solid adsorbents.[3–7] These frameworks, consisting of inorganic nodes connected by organic linkers, are amenable to precise tuning of surface functionality to control adsorption properties. A well-established strategy to realize high-performing adsorbents is the attainment of coordinatively unsaturated metal centers. Due to the typical metal ions and the weak ligand field linkers used, this approach results in exposed Lewis acidic metal sites that interact weakly with gases but are capable of polarizing and accepting electron density from various adsorbates, enabling effective polarizability-based separations.[8,9] However, this mechanism is not suitable for all mixtures, necessitating new methods for different separations.

A strategy to realize a generalizable π-acid selective adsorbent calls for exposed, electron-rich metal centers that can donate electron density into the adsorbate π^* orbitals. Specifically, a framework containing square pyramidal vanadium(II) centers has been predicted to be an excellent material for backbonding-based separations, as the d^3 configuration minimizes electron repulsion while allowing for strong electron donation into the adsorbate π^* LUMO.[10] Furthermore, the electropositive and diffuse vanadium *d*-orbitals result in an effective energy match and spatial overlap with the adsorbate frontier orbitals, creating a selective and reversible interaction over non π-acids. However, isolation of a framework with exposed vanadium(II) sites has remained elusive. While introducing vanadium(II) via postsynthetic metal exchange has been reported, it thus far is unsuitable for gas adsorption purposes as the best examples have very low loadings and only contain coordinatively saturated centers.[11] Due to the kinetic inertness, large thermodynamic driving force toward oxidation, and reactivity with carboxylate-containing ligands, the realization of a vanadium(II) MOF has remained a synthetic challenge.[12]

The need to overcome this synthetic challenge and access a π-acid selective adsorbent is highlighted by one of the most industrially expensive separations: the separation of N_2 from CH_4 for natural gas utilization.[13,14] These two gases have similar polarizabilities and kinetic diameters, rendering their separation remarkably difficult. Currently, capital- and energy-intensive cryogenic distillation is used. As the global energy market share of natural gas continues to increase, and as

more contaminated alternative sources of methane become more profitable, the development of an energy-efficient separation process is increasingly important.[15] While a few N_2-selective adsorbents exist, these either suffer from low equilibrium selectivity or a low N_2 adsorption capacity.[16–18] An adsorbent with a high density of square pyramidal vanadium(II) sites could overcome these limitations as it exploits the π-acidity difference between N_2 and CH_4. Importantly, it would also expand the molecular properties that can be targeted by solid adsorbents to impart selectivity. In particular, this backbonding functionality can be leveraged to separate olefins from paraffins, another energy demanding industrial separation.[2]

Herein, we report the initial results toward the synthesis and characterization of the first metal–organic framework with exposed vanadium(II) sites, $V_2Cl_{2.8}$(btdd) (H_2btdd = bis(1*H*-1,2,3-triazolo[4,5-*b*],[4′,5′-*i*])dibenzo[1,4]dioxin), which features a high density of square pyramidal vanadium(II) centers. We demonstrate its unique backbonding capabilities, thereby expanding the functionality available to rigid frameworks for gas separations beyond Lewis acidic behavior. We highlight its potential for selective capture of π-acids, such as N_2, CO, and ethylene. In particular, we demonstrate its remarkable performance for N_2/CH_4 separations, validating predictions form computational studies. Notably, this material exhibits record equilibrium selectivity for N_2 over CH_4, record N_2 uptake, and facile regeneration, qualifying it as a potential candidate for incorporation in an alternative natural gas purification process.

2.2. Materials and methods

2.2.1. General considerations. All synthetic procedures were performed under an Ar atmosphere using standard Schlenk techniques or in an N_2-filled VAC Atmospheres glove box. Methanol was purchased from EMD Millipore Corporation as DriSolv grade, dried over 3 Å molecular sieves, and sparged with Ar before use. *N,N*-dimethylformamide (DMF) was purchased from EMD Millipore Corporation as OmniSolv grade, sparged with Ar, and dried with an alumina column before use. The materials $VCl_2(tmeda)_2$ and H_2(btdd) were prepared according to previously reported procedures.[19,20] Dimethylformamidium trifluoromethanesulfonate was purchased from Sigma-Aldrich and dried under vacuum prior to use.

2.2.2. Synthesis of $V_2Cl_{2.8}$(btdd). A solution of $VCl_2(tmeda)_2$ (90.0 mg, 0.254 mmol) and dimethylformamidium trifluoromethanesulfonate (266 mg, 1.20 mmol) in DMF (10 mL) was added to a 20 mL borosilicate vial containing H_2(btdd) (20.0 mg, 0.0752 mmol). The solution was heated at 120 °C for 10 days. The resulting purple-red powder was collected by filtration, and soaked in 10 mL of DMF at 120 °C for 24 h. The solid was then collected by filtration, and soaked in another 10 mL of DMF at 120 °C for 24 h. This process was repeated five times so that the total time washing with DMF was 9 days. The solid was then collected by filtration, and soaked in 10 mL of methanol at 60 °C for 12 h. The solid was collected by filtration, and soaked in another 10 mL of methanol at 60 °C for 12 h. This process was repeated five times so that the total time washing with methanol was 3 days. The resulting solid was collected by filtration, and heated at a rate of 0.2 °C/min and held at 180 °C under dynamic vacuum for 36 h, affording 20 mg of product as a purple-red powder.

2.2.3. Gas adsorption measurements. Gas adsorption isotherms for pressures in the range 0–1 bar were measured by a volumetric method using a Micromeritics ASAP2020 or Micromeritics 3Flex gas sorption analyzer. A typical sample of ca. 100 mg of metal–organic framework was transferred in an N_2 filled glovebox to a pre-weighed analysis tube, which was capped with a Micromeretics TranSeal and evacuated by heating at 180 °C with a ramp rate of 0.5 °C/min under

dynamic vacuum until an outgas rate of less than 3 μbar/min was achieved. The evacuated analysis tube containing the degassed sample was then carefully transferred to an electronic balance and weighed again to determine the mass of sample. The tube was then transferred back to the analysis port of the gas adsorption instrument. The outgas rate was again confirmed to be less than 3 μbar/min. For all isotherms, warm and cold free space correction measurements were performed using ultra-high purity He gas (UHP grade 5.0, 99.999% purity); N_2, CH_4, CO, C_2H_4, and C_2H_6 isotherms at 298 to 348 K were measured in water baths equipped with a Julabo F32 circulator using UHP–grade gas sources. C_2H_4 and C_2H_6 isotherms at 353 to 373 K were measured using oil baths. N_2 isotherms collected at 77 K were measured in liquid nitrogen baths. Oil-free vacuum pumps and oil-free pressure regulators were used for all measurements to prevent contamination of the samples during the evacuation process or of the feed gases during the isotherm measurements. Langmuir surface areas were determined from N_2 adsorption data at 77 K using Micromeritics software.

2.2.4. Adsorption isotherm fitting. Adsorption isotherms were fit with a dual-site Langmuir–Freundlich equation (eq 2.1), where n is the total amount adsorbed in mmol/g, P is the pressure in bar, $n_{sat,i}$ is the saturation capacity in mmol/g, b_i is the Langmuir parameter in bar^{-1} defined in eq 2.2, and v is the Freundlich parameter for two sites 1 and 2.

$$n = \frac{n_{sat,1} b_1 P^{v_1}}{1+b_1 P^{v_1}} + \frac{n_{sat,2} b_2 P^{v_2}}{1+b_2 P^{v_2}} \tag{2.1}$$

$$b = e^{-S_1} e^{\frac{E_1}{RT}} \tag{2.2}$$

For eq 2.2, S is the entropy of adsorption at saturation in units of R, H is the enthalpy of adsorption in kJ/mol, for site 1. The fitted parameters for all gases for can be found in Tables 2.S2-2.S5.

2.2.5. Isosteric heat of adsorption calculations. Using the dual-site Langmuir-Freundlich fits, the isosteric heat of adsorption, $-Q_{st}$, was calculated for each compound as a function of the amount of CO adsorbed using the Clausius-Clapeyron relation (eq 2.3), where R is the ideal gas constant, P is the pressure, and T is the temperature.

$$-Q_{st} = RT^2 \left(\frac{\partial \ln P}{\partial T}\right)_n \tag{2.3}$$

For multi-site Langmuir-Freundlich models, it is necessary to calculate the loading dependence of the isosteric heat of adsorption. As written, multi-site Langmuir-Freundlich equations specify the amount adsorbed as a function of pressure, while the pressure as a function of the amount adsorbed is needed to use the Clausius-Clapeyron relation. To calculate the isosteric heat of adsorption for evenly spaced loadings, each multi-site Langmuir equation was solved for the pressures that correspond to specific loadings of a given gas at various 25–45 °C for N_2 and CH_4, and 60–80 °C for C_2H_4 and C_2H_6, and these calculated pressures were then used in eq 2.3 to determine the heat of adsorption as a function of the total amount of gas adsorbed.

2.2.6. Ideal adsorbed solution theory calculations. Since binary gas adsorption isotherms cannot be measured in a straightforward manner, it is often necessary to use an adsorption model, such as ideal adsorbed solution theory (IAST),[21] to predict mixed gas behavior from experimentally measured single–component isotherms. The accuracy of the IAST procedure has already been established for adsorption of a wide variety of different gases in zeolites and

metal−organic frameworks.[22] Here, IAST is used to estimate the selectivity of $V_2Cl_{2.8}$(btdd) for mixtures of N_2 and CH_4 at 25–45 °C, and C_2H_4 and C_2H_6 at 25–80 °C, with a total pressure of 1 bar for all calculations. The selectivity factor, *S*, is defined according to eq 2.4, where n_i is the amount adsorbed of each component as determined from IAST and x_i is the mole fraction of each component in the gas phase at equilibrium.

$$S = \frac{n_{CO}/n_{H_2}}{x_{CO}/x_{H_2}} \tag{2.4}$$

2.2.7. Powder X-ray diffraction. Microcrystalline powder samples of **1** (~5 mg) were loaded into two 1.0 mm boron-rich glass capillaries inside a glovebox under an N_2 atmosphere. The capillaries were attached to a gas cell, which was connected to the analysis port of a Micromeritics ASAP 2020 gas adsorption instrument. One capillary was fully evacuated at 180 °C for 12 h then flame-sealed, while the other capillary was dosed with N_2 to a pressure of 700 mbar, equilibrated for 2 h, then flame-sealed. Each capillary was placed inside a Kapton tube that was sealed on both ends with epoxy. This process was repeated for samples of **2**, with the exception that CO dosing was performed at a pressure of 700 mbar.

High-resolution synchrotron X-ray powder diffraction data for **2** and CO-dosed **2** were collected at beamline 17-BM at the APS. Diffraction patterns were collected at 298 K with a wavelength of 0.72768 Å. Discrete detectors covering an angular range from −6 to 16° in 2θ were scanned over a 34° range of 2θ, with data points collected every 0.001° and a scan speed of 0.01°/s. Note that due to the large number of data points collected, all diffraction patterns were rebinned to a step size of 0.005° in 2θ.

For all samples, a standard peak search, followed by indexing via the Single Value Decomposition approach,[23] as implemented in TOPAS-Academic V4.1,[24] allowed the determination of approximate unit cell dimensions. Using TOPAS-Academic, precise unit cell dimensions were determined by performing a structureless Le Bail refinement, and then Rietveld refinements were performed.

2.2.8. Infrared spectroscopy. Infrared spectra of $V_2Cl_{2.8}$(btdd) and gas-dosed $V_2Cl_{2.8}$(btdd) were collected *in situ* under UHP-grade N_2 and CO, and $^{15}N_2$ (98 atom % ^{15}N, Sigma-Aldrich) atmospheres on a Bruker Vertex 70 FTIR equipped with a Micromeritics ASAP 2020 for accurate gas dosing capabilities. Samples were prepared by mixing ~30 mg of MOF with KBr inside an N_2-filled glovebox, then evacuated at room temperature for 30 minutes. Measurements were collected at 80 mbar and room temperature. The samples were allowed to equilibrate for 30 minutes prior to data collection.

2.2.9. Solid state nuclear magnetic resonance spectroscopy. NMR spectra were collected for free $^{15}N_2$ and $^{15}N_2$-dosed $V_2Cl_{2.8}$(btdd). For gas-phase $^{15}N_2$, $^{15}N_2$ was dosed into an empty glass tube at 700 mbar, and then flame sealed. Gas dosing for $V_2Cl_{2.8}$(btdd) was performed on a custom gas dosing manifold described previously.[25] The rotor was packed with ~30 mg of MOF inside an N_2-filled glovebox, evacuated at room temperature for 30 minutes, and then dosed with 773 mbar of $^{15}N_2$ (98 atom % ^{15}N, Sigma-Aldrich) at room temperature with 30 minutes allowed for equilibration. For the measurement collection, all NMR spectra were recorded at 16.4 T using a DOTY magic angle spinning probe with a 4 mm silicon nitride rotor. For free $^{15}N_2$, the measurement was static, and $^{15}N_2$-dosed $V_2Cl_{2.8}$(btdd) was collected under magic-angle spinning at a rate of 15 kHz. All spectra were referenced to ^{15}N in glycine with a chemical shift of 33.4 ppm.[26]

2.3. Results and discussion

2.3.1. Synthesis and characterization. The M_2Cl_2(btdd) structure type (M = Mn, Fe, Co, Ni, Cu) served as a promising target to synthesize the first V(II) framework, as a nitrogen–based ligand is used, in contrast to the more common oxygen-based ligands, thereby obviating deleterious oxidation reactions.[27–29] Indeed, by combining $VCl_2(tmeda)_2$ (tmeda = *N*,*N*,*N*′,*N*′-tetramethylethylenediamine) and H_2btdd in dimethylformamide under acidic conditions, a microcrystalline purple-red powder can be isolated. This material can be desolvated, affording a Brunauer-Emmett-Teller surface area of 1930 m^2/g. Rietveld refinement of the powder X-ray diffraction data shows a hexagonal framework with 23 Å windows, decorated by vanadium sites at the vertices (Figure 2.1). The vanadium centers are ligated by bridging triazolates and chlorides, with equatorial V–N and V–Cl bond distances of 2.10(11) Å and 2.48(14) Å, respectively, consistent with vanadium(II) compounds.[30,31] Importantly, several of these vanadium centers contain one open coordination site that can be used for gas binding. Approximately 40% of these sites are occupied by terminal chloride ligands, likely due to *in situ* oxidation during the synthesis. Confirmation through elemental analysis suggests that a formula of $V_2Cl_{2.8}$(btdd) can accurately describe this new material, with coordinatively unsaturated vanadium(II) sites and coordinatively saturated vanadium(III) sites.

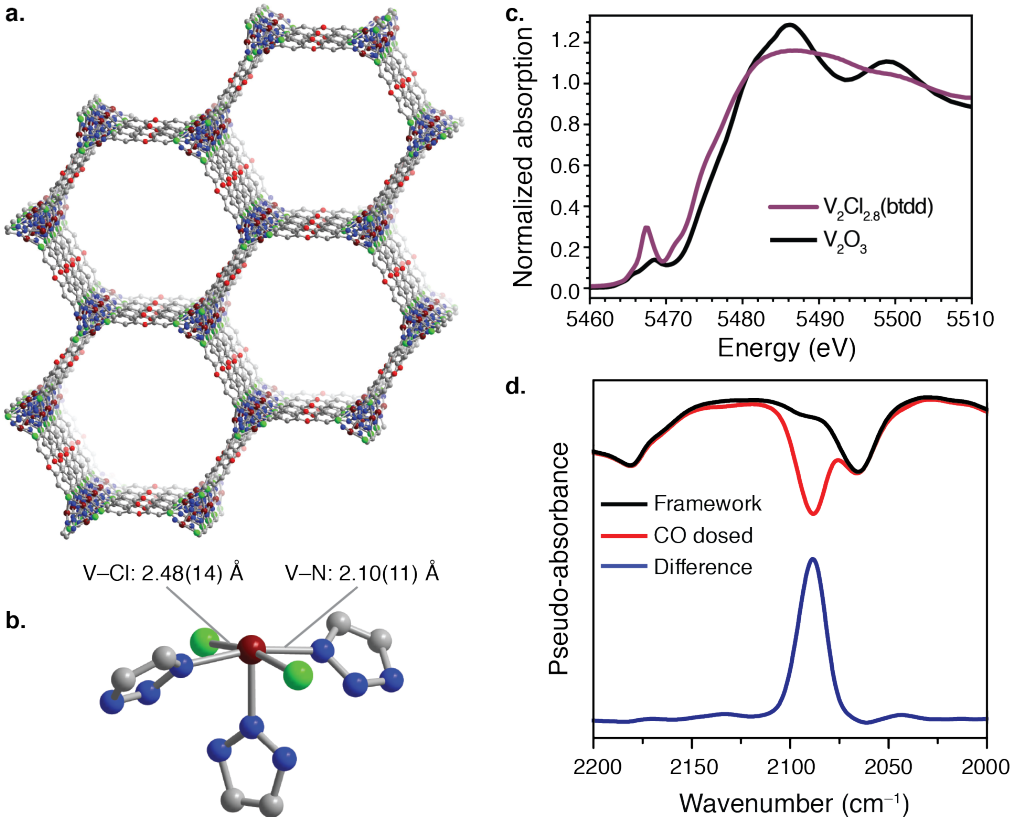

Figure 2.1. Structure and characterization of $V_2Cl_{2.8}$(btdd). A portion of the structure of $V_2Cl_{2.8}$(btdd) (**a**) and a single vanadium center and relevant bond lengths highlighted (**b**). Dark red, green, blue, light red, and grey represent V, Cl, N, O, and C, respectively. Terminal chloride ligands and H atoms have been omitted. X-ray adsorption spectra collected for $V_2Cl_{2.8}$(btdd) (purple) and V_2O_3 (black) (**c**). Infrared spectra for $V_2Cl_{2.8}$(btdd) (black) and CO-dosed $V_2Cl_{2.8}$(btdd) (red), with the difference shown in blue (**d**).

X-ray absorption spectroscopy was used to further probe the oxidation states of the vanadium centers (Figure 2.1). The vanadium *K*-edge absorption shows a sharp pre-edge and rising edge that are shifted by 1 and 1.2 eV, respectively, compared to the corresponding features for V_2O_3, suggesting that some amount of vanadium(II) is present.[32] Importantly, the *K*-edge X-ray absorption spectrum shows a pre-edge absorption feature with a relative intensity of 0.3, suggestive of non-centrosymmetric 5-coordinate vanadium centers.[32] Accordingly, this material is expected to possess open coordination sites at the vanadium centers. This was confirmed by monitoring *in situ* CO dosing by infrared spectroscopy, which gives rise to a single band at 2089 cm^{-1} (Figure 2.1). This band is redshifted relative to that of free CO, in contrast to the blueshift observed for other MOF adsorbents, wherein Lewis acidic behavior dominates.[9,17] Given this interaction, this material may be expected to selectively adsorb other target π-acidic substrates, including N_2.

2.3.2. N_2 adsorption. Gas adsorption isotherms of N_2 were collected at 25 °C, and excitingly the material adsorbs significant amounts of N_2 even at this elevated temperature (Figure 2.2). In contrast to typical N_2 adsorption isotherms, the isotherm for $V_2Cl_{2.8}$(btdd) shows an unprecedented steepness, rising initially to 1.5 mmol/g at just 50 mbar, before gradually rising to 1.9 mmol/g, or > 5 wt %. Analysis of adsorption isotherms collected at multiple temperatures indicates an isosteric heat of N_2 adsorption of –55 kJ/mol (Figure 2.2), the highest value reported amongst metal–organic frameworks, and consistent with theoretical data for square pyramidal V(II).[10] Notably, no hysteresis is observed upon desorption, indicative of fully reversible binding.

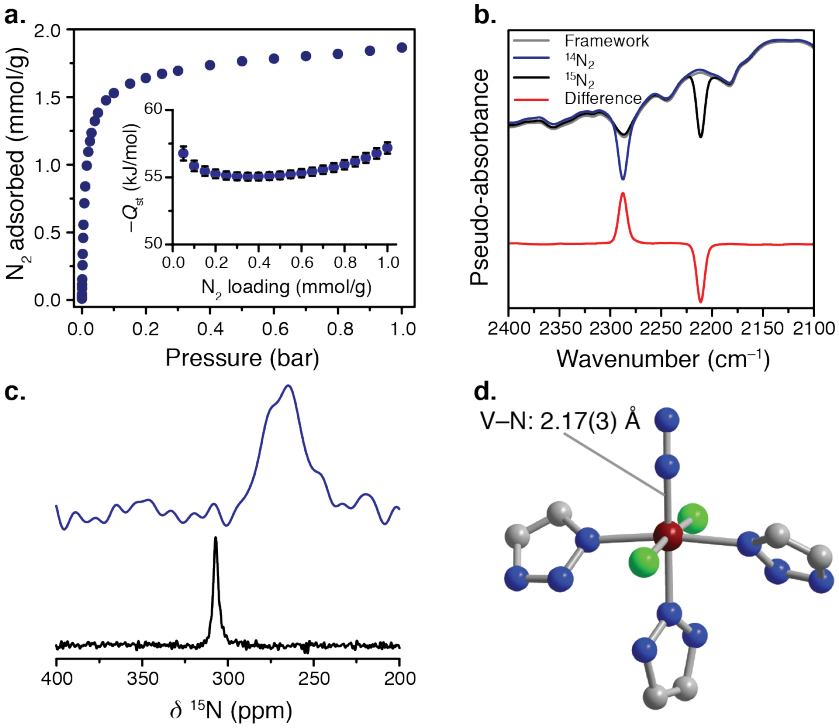

Figure 2.2. N_2 adsorption and characterization of N_2 binding. Adsorption isotherm of N_2 for collected at 25 °C, with the inset showing the isosteric heat of N_2 adsorption (error bars are shown in black) (**a**). Infrared spectra for $V_2Cl_{2.8}$(btdd) collected at 25 °C for the bare framework (grey), $^{14}N_2$-dosed sample (red), $^{15}N_2$-dosed sample (black), and the difference between $^{14}N_2$ and $^{15}N_2$ (red) (**b**). Solid-state ^{15}N nuclear magnetic resonance spectra collected for free $^{15}N_2$ (black) and $^{15}N_2$-dosed $V_2Cl_{2.8}$(btdd) (blue) at 20 °C (**c**). Structure of a single vanadium site in $V_2Cl_{2.8}$(btdd)·0.5N_2 (**d**). Dark red, green, blue, and grey represent V, Cl, N, and C, respectively.

The adsorption mechanism was probed in a variety of ways. Crystal structure of the N_2-dosed sample $V_2Cl_{2.8}(btdd)\cdot 0.5N_2$ was determined by analysis of powder X-ray diffraction data, and shows an end-on V–N_2 interaction (Figure 2.2). The V–N distance of 2.177(3) Å and a nearly linear V–N–N interaction are suggestive of a backbonding interaction from the vanadium to the orbitals of N_2. This is significantly shorter than other metal–organic frameworks that interact by polarizing the N_2.[10,33] Additionally, the N_2 adsorption was monitored through infrared spectroscopy. Upon dosing 80 mbar of N_2, a single feature is present at 2290 cm^{-1}, suggestive of a single type of vanadium open site. Dosing with $^{15}N_2$ confirms this as being associated with the V–N_2 interaction (Figure 2.2). The value is red-shifted with respect to gas-phase N_2, which is consistent with computational results for a weak field V(II)–N_2 interaction, free of solvent and cation effects.[10] This slight redshift confirms that the backbonding mechanism is operative. Additionally, solid-state magic-angle spinning (MAS) ^{15}N NMR spectroscopy was collected for a sample dosed with $^{15}N_2$. In contrast to most adsorbents, the signal is significantly broadened and shifted from free N_2, as expected when bound to a paramagnetic metal center. The value of 267 ppm is in agreement with other high-valent metal-dinitrogen complexes.[34] Taken together, the spectroscopic data confirm that the nitrogen is bound directly to the vanadium centers through the proposed backbonding mechanism.

2.3.3. N_2 separations. Due to this mechanism for N_2 adsorption, the exposed vanadium sites should allow for excellent performance in the adsorption of N_2 for industrial applications. For separations involving N_2, natural gas processing is the largest industrial process, with all inert gases required to be below a total of 4% and N_2 levels typically required to be lower than 2%.[14,15,35] Therefore, both capacity and selectivity over CH_4 need to be maximized at these low pressures. Comparing $V_2Cl_{2.8}(btdd)$ to previously reported materials for N_2 capture,[16–18] this new mechanism allows for the highest uptake across several pressures. Adsorption isotherms of N_2 collected at 25 °C show a very large uptake at low pressures, with 1.09 mmol/g adsorbed at 20 mbar and 1.32 mmol/g adsorbed at 40 mbar. This is substantially higher than all previously reported materials, as high-performing materials only adsorb ~0.25 mmol/g at 20 mbar at a much lower temperature of 10 °C.[17] Even more impressive, at 40 mbar the N_2 uptake in $V_2Cl_{2.8}(btdd)$ is higher than the amount adsorbed by any other material at 1 bar and the same temperature, highlighting its extraordinary performance for this separation.

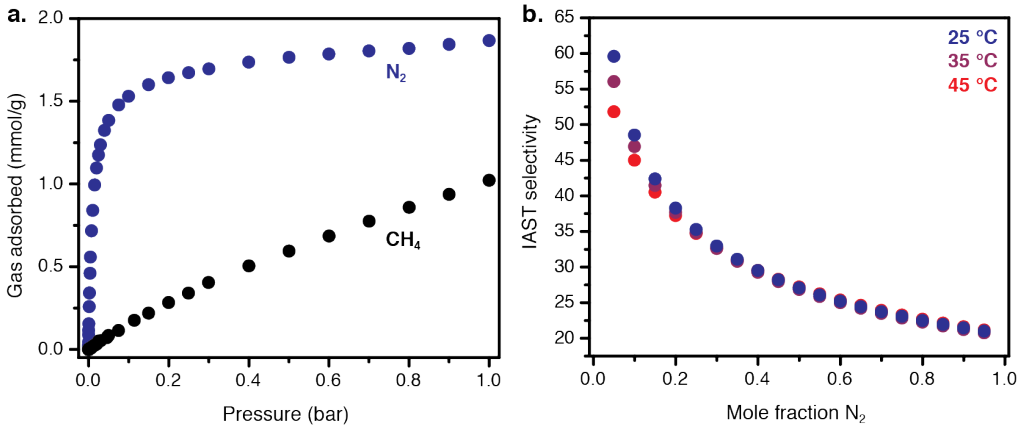

Figure 2.3. Selectivity for N_2 adsorption. Adsorption isotherms of N_2 (blue) and CH_4 (black) collected at 25 °C for $V_2Cl_{2.8}(btdd)$ (**a**). IAST selectivity values for multiple temperatures for varying N_2:CH_4 ratios with a total pressure of 1 bar (**b**).

In assessing the selectivity for N_2 adsorption, a comparison to the CH_4 adsorption isotherm collected at 25 °C shows that $V_2Cl_{2.8}$(btdd) adsorbs substantially more N_2 than CH_4 (Figure 2.3). While the compound adsorbs CH_4 with a considerable binding enthalpy of –35 kJ/mol, similar to that predicted computationally for other vanadium(II) frameworks,[10] this should still allow for considerable selectivity for N_2 adsorption. Using Ideal Adsorbed Solution Theory (IAST), selectivity values at low N_2 concentrations and 1 bar of total pressure are exceptional. Comparing to other materials, whose values are reported at a ratio of 20:80 N_2:CH_4, $V_2Cl_{2.8}$(btdd) shows a selectivity of 38 (Figure 2.3), substantially higher than the previous best-performing material, a Cr(III)-based metal–organic framework.[17] This material shows a selectivity of ~8 at a lower temperature of 10 °C, and which decreases substantially upon warming. Furthermore, because of the steepness of the N_2 adsorption isotherm, the IAST selectivity shows a considerable uptick towards higher selectivity at lower concentrations of N_2. This is in contrast to the expected performance of other materials with less steep adsorption isotherms. The IAST selectivity is 63 and 72 at 4% and 2% N_2 in CH_4, respectively, indicative of highly selective adsorption and for possible utility in real separation processes.

Importantly, N_2 adsorption isotherms at higher temperatures for $V_2Cl_{2.8}$(btdd) retain steep initial N_2 uptakes. Performing similar analyses at temperatures as high as 45 °C, the IAST selectivity values are similar to the values at 25 °C (Figure 2.3). Due to the strong orbital-mediated V–N_2 interaction relative to that with CH_4, the backbonding mechanism allows for this selectivity to remain constant with increasing temperature. This is similar to other materials that perform separations through more specific orbital interactions to form strong, chemisorptive interactions with target substrates, and in some cases these materials show greater selectivities at higher pressures.[36] In contrast, polarizability-driven mechanisms show negative dramatic temperature effects, where raising the temperature from 10 to just 20 °C lowers the IAST selectivity under standard conditions by over 20%.[17]

2.3.4 Ethylene separations. We sought to apply this impressive selectivity and temperature dependence to other separations involving π-acidic gases. Olefin separations from mixtures with paraffins is required at enormous scales that currently account for 0.3% of the world's energy consumption.[2] Similar to N_2 removal from natural gas, this separation currently exploits small volatility differences, resulting in an expensive and energy-demanding process. Metal–organic frameworks have been investigated as possible adsorption-based alternatives,[6,7,37,38] and in particular open metal site binding has emerged as an attractive method that combines relatively high selectivities with fast adsorption kinetics. However, while these materials are able to perform these separations at low temperatures, increasing the temperature results in significant decreases in selectivity. Because practical separations would be performed at higher temperatures to minimize energy penalties upon cooling, we sought to leverage the π-acidity of ethylene as a basis for separation.[39,40] Using this adsorption mechanism, the temperature dependence observed for N_2/CH_4 selectivity should apply to ethylene/ethane separations, allowing for selective separations at higher temperatures.

Ethylene adsorption isotherms collected at a variety of temperatures show an interaction of –66 kJ/mol, and as such the vanadium sites bind ethylene strongly at high temperatures. Indeed, the isotherm collected at 80 °C shows a steep uptake and notably remains highly reversible (Figure 2.4). Ethane adsorption isotherms, in contrast, are more shallow at all temperatures measured. IAST selectivity values for a 50:50 ethylene:ethane mixture at various temperatures were examined, and as predicted the selectivity rises as a function of temperature, reaching 6.9 at 80 °C. Compared to other materials, such as Fe_2(*m*-dobdc) (*m*-dobdc^{4-} = 4,6-dioxido-1,3-

benzenedicarboxylate), which has one of the highest reported selectivities at 25 °C,[37] $V_2Cl_{2.8}$(btdd) shows higher selectivity values at 80 °C. Importantly, $V_2Cl_{2.8}$(btdd) also retains high capacities at these temperatures. This mechanism is thus very applicable to realistic separation conditions for a variety of industrial processes.

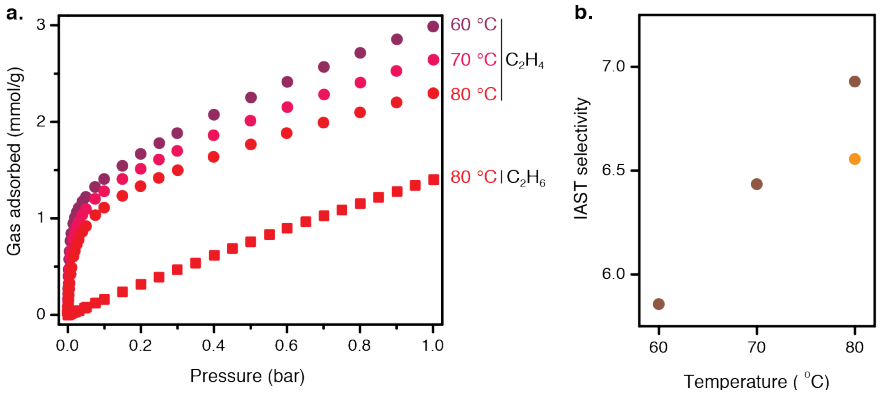

Figure 2.4. Ethylene adsorption and selectivity in $V_2Cl_{2.8}$(btdd). High-temperature adsorption isotherms for ethylene and ethane collected at various temperatures in $V_2Cl_{2.8}$(btdd) (**a**). IAST selectivity values collected at various temperatures for a 50:50 ethylene:ethane mixture at 1 bar total pressure in $V_2Cl_{2.8}$(btdd) (brown circles) and Fe_2(*m*-dobdc) (orange circle) (**b**).

2.4. Conclusions and outlook

The ability to design and incorporate new adsorption mechanisms is required for improving the properties of adsorbent materials. This was demonstrated through synthesizing a new metal–organic framework with synthetically challenging vanadium(II) centers to perform highly selective backbonding-based separations. Further optimization and targeting new materials based on triazolate-based frameworks to potentially stabilize these backbonding centers could result even higher densities for improved performances.[27–29,36] Additionally, the insights into selective small molecule binding provides further design principles for any adsorbent-based application including activation, sensing, and catalysis for a range of π-acidic species.

2.5. Acknowledgments

This research was supported through the Center for Gas Separations Relevant to Clean Energy Technologies, an Energy Frontier Research Center funded by the U.S. Department of Energy, Office of Science, Office of Basic Energy Sciences under Award DE-SC0001015. Powder X-ray diffraction data were collected at Beamline 17-BM at the APS, a DoE Office of Science User Facility, operated by Argonne National Laboratory under Contract DE-AC02-06CH11357. Beamlines. The National Science Foundation provided graduate fellowship support.

2.6. References and supplementary information

(1) U.S. Department of Energy. *Materials Separation Technology: Energy and Emission Reduction Opportunities*. **2005**.

(2) Sholl, D. S.; Lively, R. P. *Nature* **2016**, *532*, 435–437.

(3) Furukawa, H.; Cordova, K. E.; O'Keefe, M.; Yaghi, O. M. *Science* **2013**, *341***,** 1230444.
(4) Li, J. R.; Kuppler, R. J.; Zhou, H.-C. *Chem. Soc. Rev.* **2009**, *38*, 1477–1504.
(5) Bloch, E. D.; Queen, W. L.; Krishna, R.; Zadrozny, J. M.; Brown, C. M.; Long, J. R. *Science* **2012**, *355*, 1606–1610.
(6) Cadiau, A.; Adil, K.; Bhatt, P. M.; Belmabkhout, Y.; Eddaoudi, M. *Science* **2016**, *353*, 137–140.
(7) Herm, Z. R.; Wiers, B. M.; Mason, J. A.; van Baten, J. M.; Hudson, M. R.; Zajdel, P.; Brown, C. M.; Masciocchi, N.; Krishna, R.; Long, J. R. *Science* **2013**, *340*, 960–964.
(8) Caskey, S. R.; Wong-Foy, A. G.; Matzger, A. J. *J. Am. Chem. Soc.* **2008**, *130*, 10870–10871.
(9) Bloch, E. D.; Hudson, M. R.; Mason, J. A.; Chavan, S.; Crocella, V.; Howe, J. D.; Lee, K.; Dzubak, A. L.; Queen, W. L.; Zadrozny, J. M.; Geier, S. J.; Lin, L.-C.; Gagliardi, L.; Smit, B.; Neaton, J. B.; Bordiga, S.; Brown, C. M.; Long, J. R. *J. Am. Chem. Soc*. **2014**, *136*, 10752−10761.
(10) Lee, K.; Isley III, W. C.; Dzubak, A. L.; Verma, P.; Stoneburner, S. J.; Lin, L. C.; Howe, J. D.; Bloch, E. D.; Reed, D. A.; Hudson, M. R.; Brown, C. M.; Long, J. R.; Neaton, J. B.; Smit, B.; Cramer, C. J.; Truhlar, D. G.; Gagliardi, L. *J. Am. Chem. Soc.* **2014**, *136*, 698–704.
(11) Comito, R. J.; Wu, Z.; Zhang, G.; Lawrence III, J. A.; Korzyński, M. D.; Kehl, J. A.; Miller, J. T.; Dincă, M. *Angew. Chem., Int. Ed.* doi: 10.1002/anie.201803642.
(12) Cotton, F. A.; Extine, M. W.; Falvello, L. R.; Lewis, D. B.; Lewis, G. E.; Murillo, C. A.; Schwotzer, W.; Tomas, M.; Troup, J. M. *Inorg. Chem.* **1986**, *25*, 3505–3512.
(13) Caventi, S.; Grande, C. A.; Rodrigues, A. E. *Chem. Eng. Sci.* **2006**, *61*, 3893–3906.
(14) Lokhandwala, K. A.; Pinnau, I.; He, Z.; Amo, K. D.; DaCosta, A. R.; Wijmans, J. G.; Baker, R. W.; *J. Membr. Sci*. **2010**, *346*, 270–279.
(15) Saha, D.; Grappe, H. A.; Chakraborty, A.; Orkoulas, G. *Chem. Rev.* **2016**, *116*, 11436–11499.
(16) Kuznicki, S. M.; Bell, V. A.; Nair, S.; Hillhouse, H. W.; Jacubinas, R. M.; Braunbarth, C. M.; Toby, B. H.; Tsapatsis, M. *Nature* **2004**, *412*, 720–724.
(17) Yoon, J. W.; Chang, H.; Lee, S. J.; Hwang, Y. K.; Hong, D. Y.; Lee, S. K.; Lee, J. S.; Jang, S.; Yoon, T. U.; Kwac, K.; Jung, Y.; Pillai, R. S.; Faucher, F.; Vimont, A.; Daturi, M.; Férey, G.; Serre, C.; Maurin, G.; Bae, Y. S.; Chang. J. S. *Nat. Mater.* **2017**, *16*, 526–531.
(18) Denysenko, D.; Grzywa, M.; Jelic, J.; Reuter, K.; Volkmer, D.; *Angew. Chem., Int. Ed.* **2014**, *53*, 5832–5836.
(19) Edema, J. J. H.; Stauthamer, W.; Van Bolhuis, F.; Gambarotta, S.; Smeets, W. J. J.; Spek, A. L. *Inorg. Chem.* **1990**, *29*, 1302–1306.
(20) Denysenko, D.; Grzywa, M.; Tonigold, M.; Streppel, B.; Krkljus, I.; Hirscher, M.; Mugnaioli, E.; Kolb, U.; Hanss, J.; Volkmer, D. *Chem. Eur. J.* **2011**, *17*, 1837–1848.
(21) Myers, A. L.; Prausnitz, J. M. *AIChE J*. **1965**, *11*, 121−127.
(22) (a) Krishna, R.; Calero, S.; Smit, B. *Chem. Eng. J*. **2002**, *88*, 81− 94. (b) Krishna, R.; van Baten, J. M. *Chem. Eng. J.* **2007**, *133*, 121. (c) Krishna, R.; van Baten, J. M. *Phys. Chem. Chem. Phys*. **2011**, *13*, 10593−10616.
(23) Coelho, A. A. *J. Appl. Crystallogr.* **2003**, *36*, 86–95.
(24) Coelho, A. A. *TOPAS-Academic*, *Version 4.1*. Coelho Software, 2007.
(25) Milner, P. J.; Siegelman, R. L.; Forse, A. C.; Gonzalez, M. I.; Runčevski, T.; Martell, J. D.; Reimer, J. A.; Long, J. R. *J. Am. Chem. Soc.* **2017**, *139*, 13541–13553.

(26) Bertani, P.; Raya, J.; Bechinger, B. *Solid State Nucl. Magn. Reson.* **2014**, *61*, 15–18.
(27) Reed, D. A.; Keitz, B. K.; Oktawiec, J.; Mason, J. A.; Runčevski, T.; Xiao, D. J.; Darago, L. E.; Crocella, V.; Bordiga, S.; Long, J. R. *Nature* **2017**, *550*, 96–100.
(28) Reith, A. J.; Tulchinsky, Y.; Dincă, M. *J. Am. Chem. Soc.* **2016**, *138*, 9401–9404.
(29) Park, S. S.; Tulchinsky, Y.; Dincă, M. *J. Am. Chem. Soc.* **2017**, *139*, 13260–13263.
(30) Bechlars, B.; D'Alessandro, D. M.; Jenkins, D. M.; Iavarone, A. T.; Glover, S. D.; Kubiak, C. P.; Long, J. R. *Nat. Chem.* **2010**, *2*, 362–368.
(31) Cotton, F. A.; Duraj, S. A.; Extine, M. W.; Lewis, G. E.; Roth, W. J.; Schmulbach, C. D.; Schwotzer, W. *J. Chem. Soc., Chem. Commun.* **1983**, *23*, 1377–1378.
(32) Wong, J.; Lytle, F. W.; Messmer, R. P.; Maylotte, D. H. *Phys. Rev. B.* **1984**, *30*, 5596–5610.
(33) Gonzalez, M. I.; Mason, J. A.; Bloch, E. D.; Teat, S. J.; Gagnon, K. J.; Morrison, G. Y.; Queen, W. L.; Long, J. R. *Chem. Sci*. **2017**, *8*, 4387–4398.
(34) Donovan-Mtunzi, S.; Richards, R. L.; Mason, J. *J. Chem. Soc., Dalton Trans.* **1984**, 469–474.
(35) Rufford, T. E.; Smart, S.; Watson, G. C.; Graham, B. F.; Boxall, J.; Da Costa, J. D.; May, E. F. *J. Pet. Sci. Eng.* **2012**, *94*, 123–154.
(36) Reed, D. A.; Xiao, D. J.; Gonzalez, M. I.; Darago, L. E.; Herm, Z. R.; Grandjean, F.; Long, J. R. *J. Am. Chem. Soc.* **2016**, *138*, 5594–5602.
(37) Bachman, J. E.; Kapelewski, M. T.; Reed, D. A.; Gonzalez, M. I.; Long, J. R. *J. Am. Chem. Soc.* **2017**, *139*, 15363–15370.
(38) Li, B.; Zhang, Y.; Krishna, R.; Yao, K.; Han, Y.; Wu, Z.; Ma, D.; Shi, Z.; Pham, T.; Space, B.; Liu, J.; Thallapally, P. K.; Liu, J.; Chrzanowski, M.; Ma, S. *J. Am. Chem. Soc.* **2014**, *136*, 8654–8660.
(39) Eldridge, R. B. *Ind. Eng. Chem. Res.* **1993**, *32*, 2208–2212.
(40) Ren, T.; Patel, M.; Blok, K. *Energy* **2006**, *31*, 425–451.

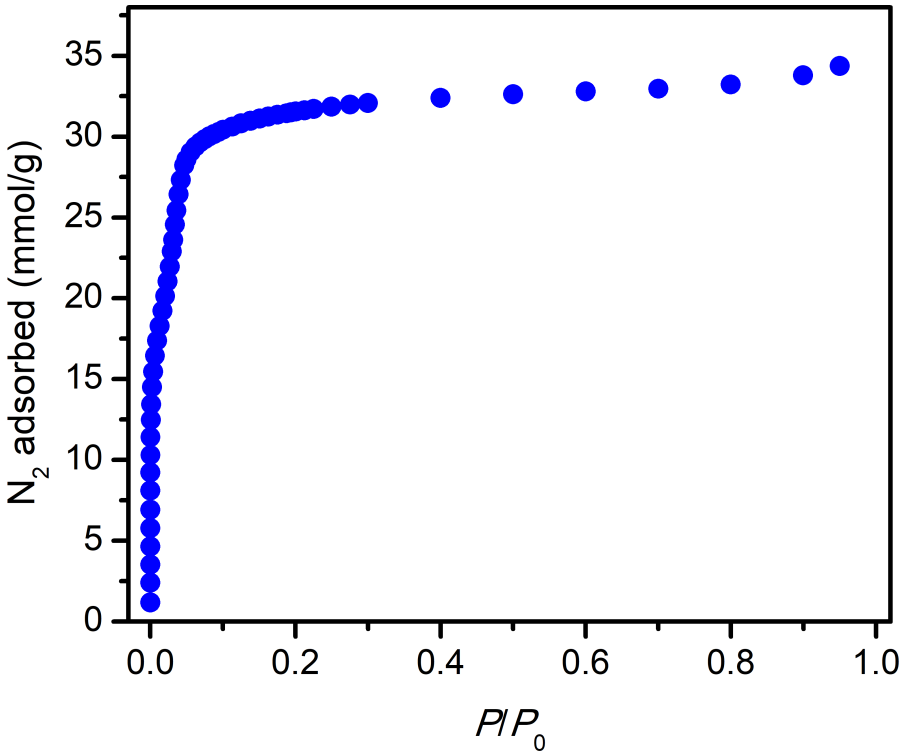

Figure 2.S1. Adsorption isotherm of N_2 collected at 77 K for $V_2Cl_{2.8}$(btdd)

Table 2.S1. Langmuir and BET surface areas of $V_2Cl_{2.8}$(btdd). The pressure region chosen is consistent with analogous frameworks.[27,28]

$SA_{Langmuir}$ (m^2/g)	SA_{BET} (m^2/g)	slope	y-int	P_{low} (bar)	P_{high} (bar)	q_{sat} (mmol/g)	C
3293	1932	5.05E–2	2.17E–6	2.31E–5	2.42E–2	19.8	2321

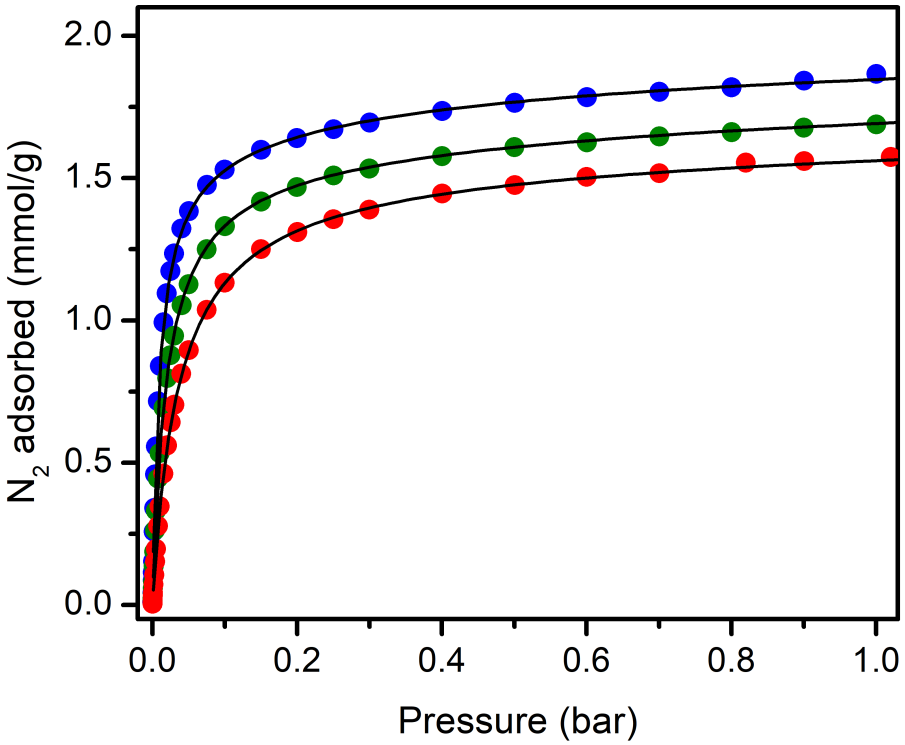

Figure 2.S2. Adsorption isotherms of N_2 collected at 25 (blue), 35 (green), and 45 °C (red) with fits to the dual-site Langmuir-Freundlich equation (eq 2.1) shown in black. Fitting parameters are shown in Table 2.S2.

Table 2.S2. Fitting parameters to the dual-site Langmuir-Freundlich equation (eq 2.1 and eq 2.2) for N_2 adsorption at 25–45°C.

Parameter	Value
$n_{sat,1}$ (mmol/g)	1.48
E_1 (–kJ/mol)	52.4
S_1 (–R)	16.5
v_1	0.997
$n_{sat,2}$ (mmol/g)	0.667
E_2 (–kJ/mol)	66.1
S_2 (–R)	26.4
v_2	0.571

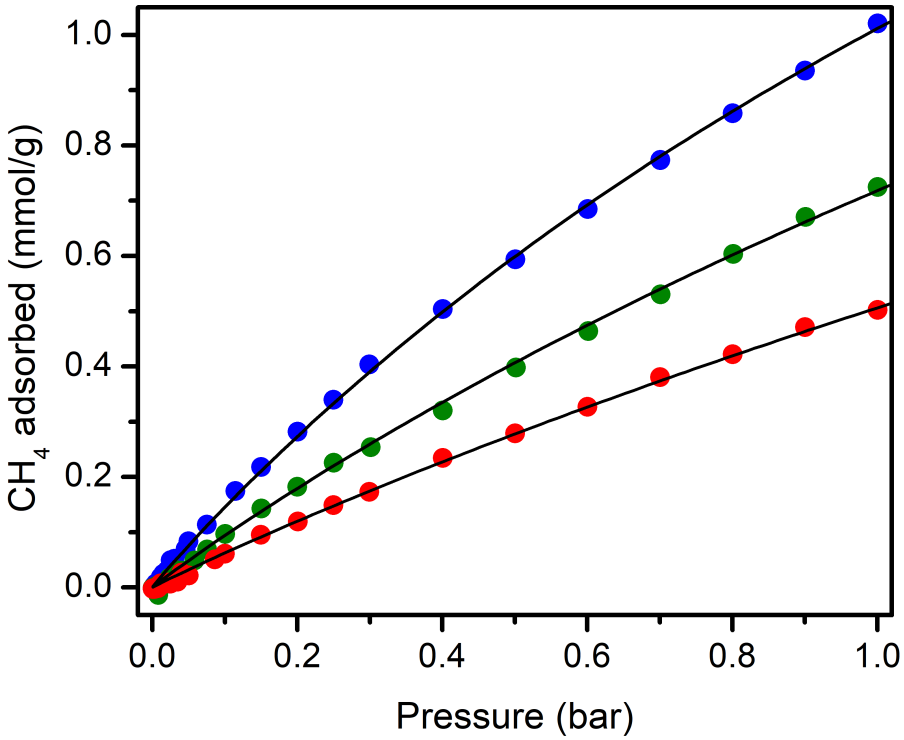

Figure 2.S3. Adsorption isotherms of CH_4 collected at 25 (blue), 35 (green), and 45 °C (red) with fits to the dual-site Langmuir-Freundlich equation (eq 2.1) shown in black. Fitting parameters are shown in Table 2.S3.

Table 2.S3. Fitting parameters to the dual-site Langmuir-Freundlich equation (eq 2.1 and eq 2.2) for CH_4 adsorption at 25–45°C.

Parameter	Value
$n_{sat,1}$ (mmol/g)	3.64
E_1 (–kJ/mol)	34.2
S_1 (–R)	14.8
v_1	0.967
$n_{sat,2}$ (mmol/g)	0.401
E_2 (–kJ/mol)	38.7
S_2 (–R)	40.1
v_2	1

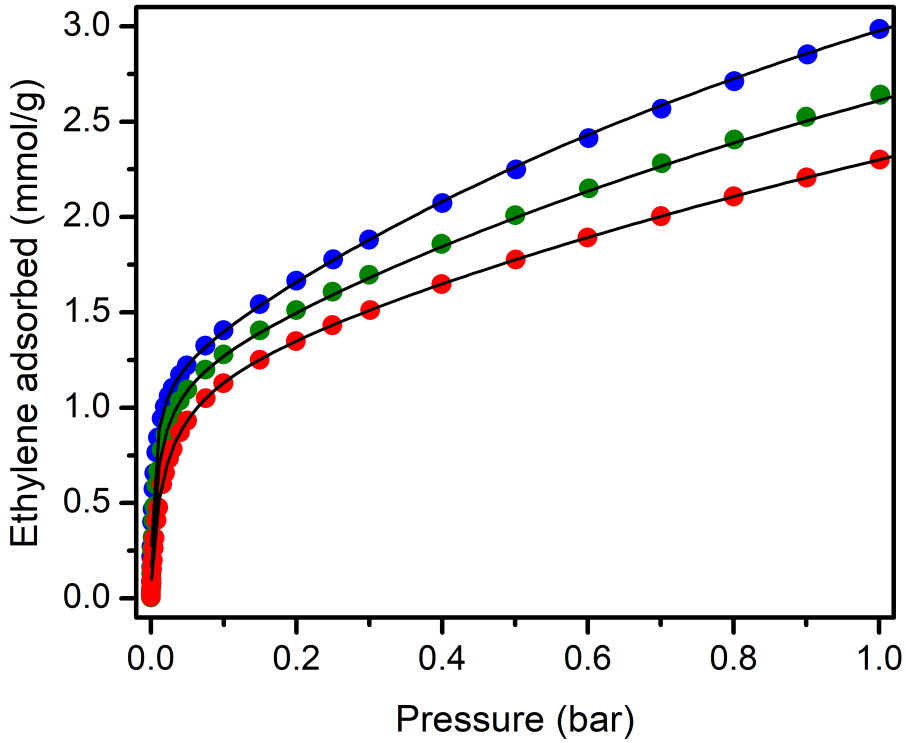

Figure 2.S4. Adsorption isotherms of ethylene collected at 60 (blue), 70 (green), and 80 °C (red) with fits to the dual-site Langmuir-Freundlich equation (eq 2.1) shown in black. Fitting parameters are shown in Table 2.S4.

Table 2.S4. Fitting parameters to the dual-site Langmuir-Freundlich equation (eq 2.1 and eq 2.2) for ethylene adsorption at 60–80°C.

Parameter	Value
$n_{sat,1}$ (mmol/g)	1.26
E_1 (–kJ/mol)	58.0
S_1 (–R)	16.4
v_1	0.839
$n_{sat,2}$ (mmol/g)	4.72
E_2 (–kJ/mol)	32.5
S_2 (–R)	12.3
v_2	1.06

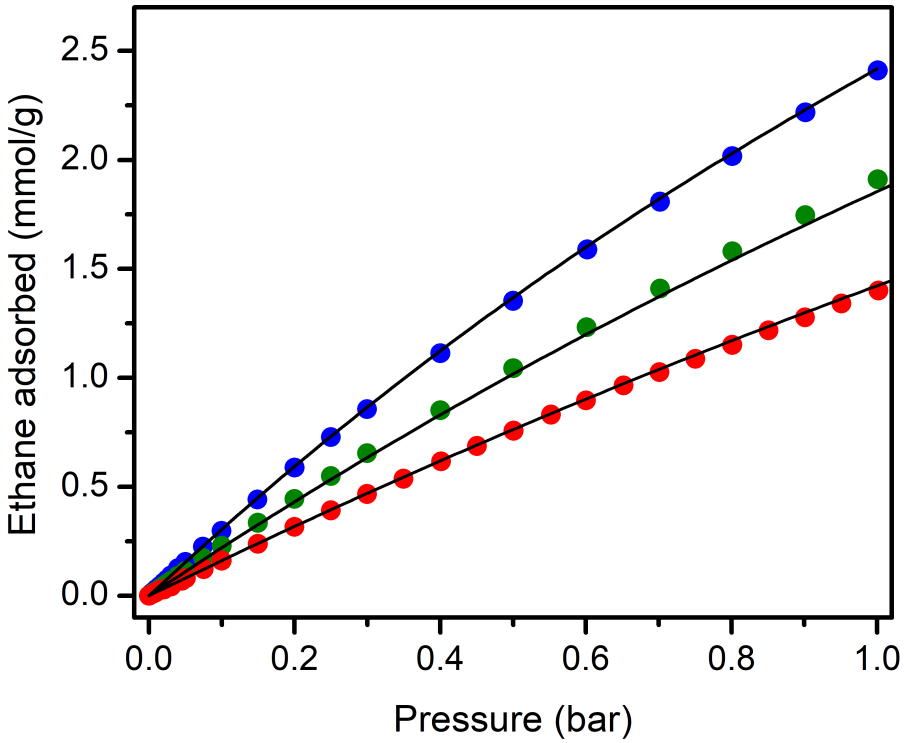

Figure 2.S5. Adsorption isotherms of ethane collected at 60 (blue), 70 (green), and 80 °C (red) with fits to the dual-site Langmuir-Freundlich equation (eq 2.1) shown in black. Fitting parameters are shown in Table 2.S5.

Table 2.S5. Fitting parameters to the dual-site Langmuir-Freundlich equation (eq 2.1 and eq 2.2) for ethane adsorption at 60–80°C.

Parameter	Value
$n_{sat,1}$ (mmol/g)	2.89
E_1 (–kJ/mol)	29.2
S_1 (–R)	12.5
v_1	1.00
$n_{sat,2}$ (mmol/g)	8.10
E_2 (–kJ/mol)	32.3
S_2 (–R)	12.7
v_2	1.01

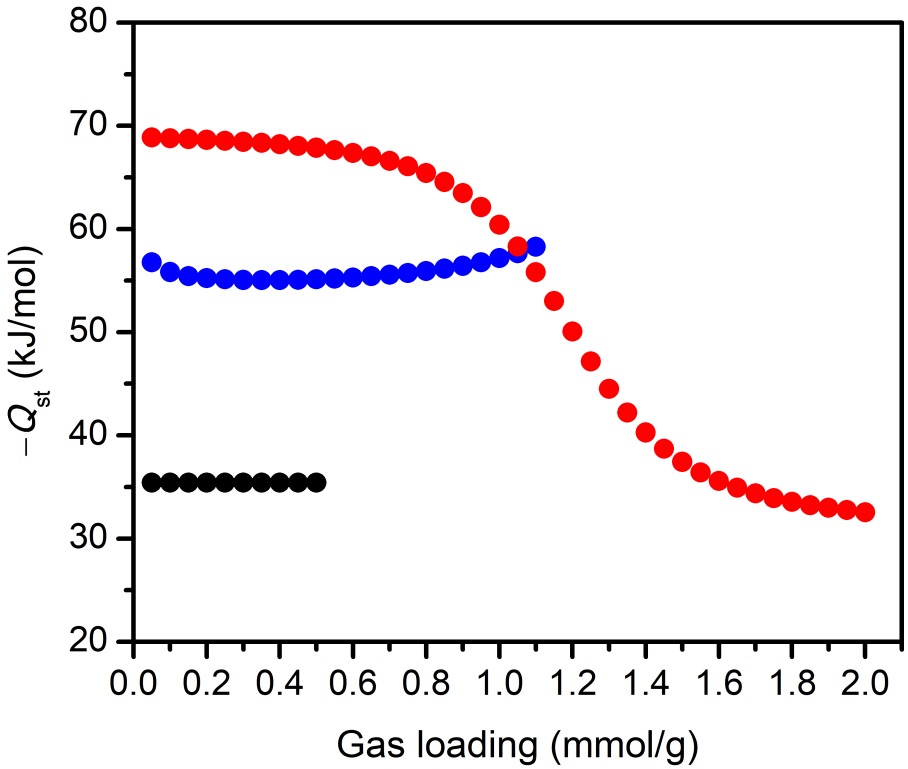

Figure 2.S6. Isosteric heats of adsorption for ethylene (red), N_2 (blue), and CH_4 (black) expressed as a function of gas loading calculated using the Clausius-Clapeyron relation (eq 2.3) for isotherm fits in tables 2.S2-2.S4.

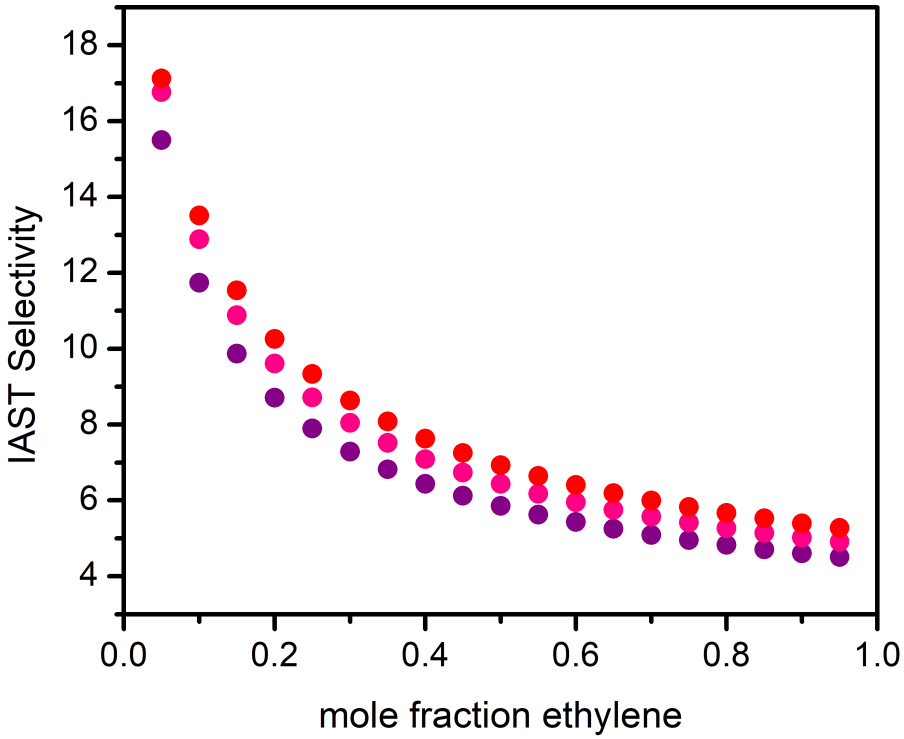

Figure 2.S7. Ethylene/ethane IAST selectivity values for various ethylene concentrations at a total pressure of 1 bar, calculated at 60 (purple), 70 (pink), and 80 °C (red).

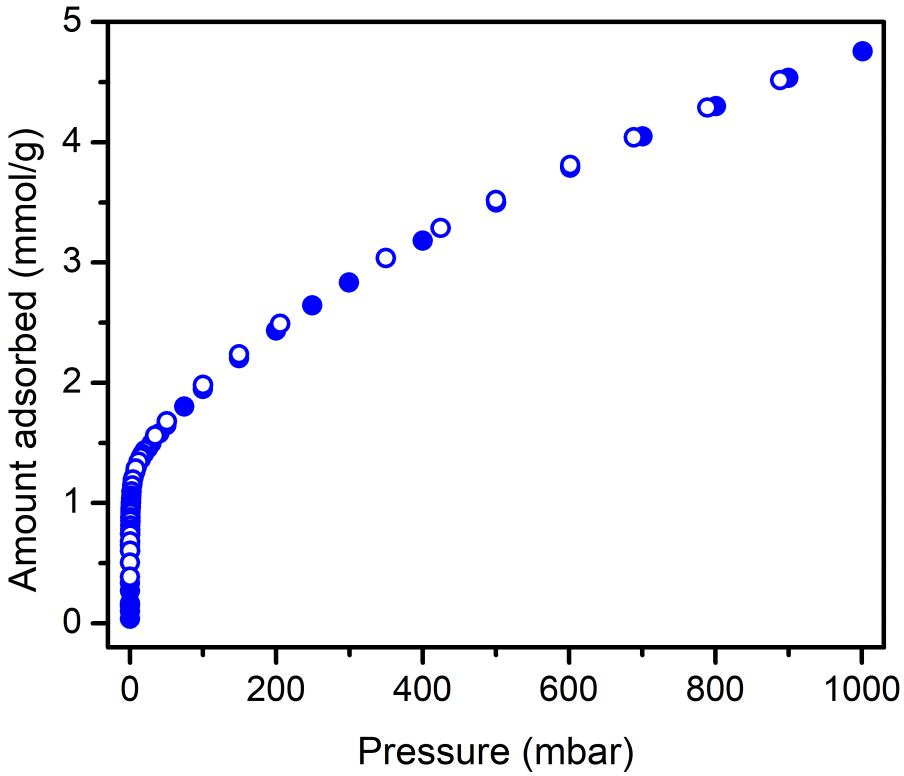

Figure 2.S8. Ethylene adsorption (solid circles) and desorption (open circles) isotherms collected in $V_2Cl_{2.8}$(btdd) at 25 °C, showing the very reversible nature of the ethylene adsorption.

Chapter 3: Selective Ethylene Adsorption from Complex Gas Mixtures with a Manganese(II) Metal–Organic Framework

3.1. Introduction

The pursuit of renewable raw materials and processes for the production of global commodity chemicals is a challenging yet critical enterprise toward a more sustainable energy future, alongside a transition away from fossil fuels to renewable energy sources. Ethylene is one ubiquitous raw material that is currently produced on massive scales—exceeding 150 million tonnes/year—and is primarily derived from cracking of naphtha and ethane.[1] In considering alternative routes to ethylene that do not rely on these fossil resources, significant attention has been given to the oxidative coupling of methane (OCM)[2–15] and the conversion of methanol-to-olefins (MTO).[16–21] Methanol itself is commonly derived from syngas generated by coal gasification or other petrochemical routes and therefore it is not an efficient precursor to renewable ethylene. Alternatively, the OCM process uses methane as a feedstock for ethylene production. Methane is an important intermediary as both an energy carrier and feedstock in the transition away from a fossil fuel-based economy to one primarily supplied through alternative energy; and with the advent of hydraulic fracturing, the displacement of coal with natural gas has been the primary driver for reduced CO_2 emissions in the United States in recent years.[22] Further, methane can be produced through a variety of renewable means, such as from biomass sources including agricultural waste,[23] wastewater,[24] landfills,[25] or via electrochemical CO_2 reduction.[26] Using methane to replace petroleum sources as a raw material for the production of ethylene would also ease a transition from fossil fuels to a more sustainable economy.

Large-scale implementation of OCM currently has limited viability, however, because methane–to–ethylene conversion is low and ethylene is generated together with several other products, including ethane, CO_2, CO, and H_2 (Figure 3.1). It is difficult to separate these components through a conventional scrubbing and distillation cascade, in which a high volume of methane and other products would need to be recycled in order to maximize carbon efficiency. Additionally, the OCM catalyst and reactor conditions dictate product stream composition, such that it is challenging to adopt a general solution to this separation. Finally, the OCM purification process is associated with high energy and capital costs that often make it infeasible in practice.

One avenue to address this separations challenge is through the use of an adsorbent that can selectively capture ethylene over the other OCM product stream components, eliminating the need for multiple separation operations in series. Upon inspection of the kinetic diameter, boiling point, dipole moment, quadrupole moment, and polarizability for each gas, it is clear, however, that ethylene has no single physical or thermodynamic property that can be used as a handle to separate it from this complex mixture in a single unit operation using traditional distillation or conventional adsorbents (Table 3.1).

Alternatively, we considered that metal–organic frameworks—a class of permanently porous, highly-tunable adsorbents—could offer an intriguing solution to this separations challenge. Consisting of metal nodes connected by organic linkers,[27–36] metal–organic frameworks have been studied extensively and found to show great promise for various CO_2 and hydrocarbon gas separations.[37–53] However, the separation of any one component from a complex mixture of molecules exhibiting similar physicochemical properties, as is needed here, requires a level of selectivity that has not yet been demonstrated. Certain techniques have been devised that facilitate selective adsorption of a single component over a variety of species; however, these methods typically require the target adsorbate to possess a chemical or physical handle—such as the Lewis acidity of CO_2 or the distinct sizes and shapes of different hydrocarbons—that differentiates it from the other molecules and facilitates tailored framework design.[54–56] Because ethylene lacks such distinguishing

handles relative to the other gases in the OCM product mixture, we sought to utilize a framework with open metal sites, pursuing an approach that involves balancing the electropositivity and π-backbonding ability of the coordinating metal site for achieving selectivity.

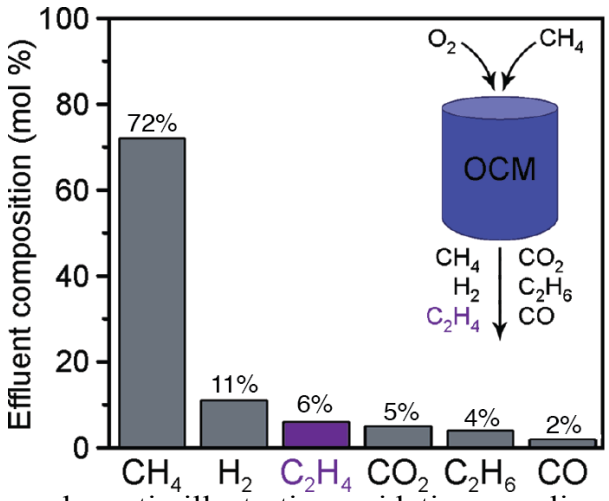

Figure 3.1. Block-flow schematic illustrating oxidative coupling of methane (OCM) and effluent composition. The reactants O_2 and CH_4 are fed into the OCM reactor and undergo coupling and cracking reactions to produce an effluent stream comprising CH_4, H_2, C_2H_4, CO_2, C_2H_6, CO, and other minor impurities.

Table 3.1. Physical and thermodynamic parameters of the primary small molecules composing the effluent in the oxidative coupling of methane, including the kinetic diameter, boiling point, dipole moment (μ), quadrupole moment (Θ), and polarizability (α).

	Kinetic Diameter (Å)	Boiling Point (K)	μ (10^{30} C·M)	Θ (10^{-40} C·m^2)	α (10^{-25} cm^3)
CH_4	3.758	111	0	0	25.93
H_2	2.89	20.3	0	2.21	8.042
C_2H_4	4.163	169.4	0	5.00	42.52
CO_2	3.300	216.55	0	14.33	29.11
C_2H_6	4.444	184.5	0	2.17	44.7
CO	3.690	81.66	0.329	8.33	19.5

In choosing a suitable framework, it was of paramount importance to find a material capable of selectively adsorbing ethylene from the given mixture. Furthermore, given the substantial amounts of adsorbent required in an industrial process, we sought a material with a high capacity for ethylene that could in part offset the associated materials costs. An ideal material would also undergo rapid adsorption and facile regeneration, allowing the ethylene to be collected and the material bed regenerated without the need for large swings in temperature or pressure. In the context of this study, we identified the M_2(*m*-dobdc) family of frameworks (M = Mg, Mn, Fe, Co, and Ni) as promising candidates meeting the above design criteria, with advantages including reasonable regeneration conditions and

low production costs that render them particularly attractive materials for commercial applications.[53] These materials exhibit ~11 Å-wide channels lined with a high concentration of Fe^{2+} ions, each featuring a single open coordination site that can selectively bind ethylene, resulting in a high ethylene uptake capacity and fast adsorption kinetics. Most importantly, framework–guest interactions can be finely tuned by varying the metal center, governing metal–ethylene, –ethane, $–CO_2$, and –CO interactions.

Here, we characterize the ability of M_2(*m*-dobdc) (M = Mg, Mn, Fe, Co, Ni) framework materials to selectively adsorb ethylene in a model OCM product stream, and compare this data to that obtained for zeolite CaX, which is commercially used for CO_2 separations and has also been shown to selectively adsorb ethylene over ethane.[57,58] Further, experimental breakthrough data obtained on these materials using a realistic OCM product mixture. Our results demonstrate that the M_2(*m*-dobdc) materials are generally superior to CaX in the separation of ethylene from the OCM mixture, with Mn_2(*m*-dobdc) displaying an electronic structure that is most conducive to the selective adsorption of ethylene.

3.2. Materials and methods

The M_2(*m*-dobdc) (M = Mg, Mn, Fe, Co, Ni) materials were synthesized and prepared for adsorption experiments according to previously reported methods.[53,59] Zeolite CaX was purchased from Tosoh Corporation in the form of 1.5-mm spherical pellets with 9 Å pores and was activated at 180 °C under dynamic vacuum in a pre-weighed sample tube. Its activated mass was recorded as a basis for adsorption experiments.

3.2.1. Single-component equilibrium adsorption isotherms. Single-component equilibrium gas adsorption data were collected at pressures ranging from 0 to 1.1 bar using a Micromeritics 3Flex instrument, which employs a volumetric method to determine the amount of gas adsorbed at equilibrium pressure. Activated samples were transferred under a dry N_2 atmosphere into pre-weighed sample tubes and capped with a Micromeritics Transeal. Samples were then evacuated at 180 °C under a dynamic vacuum ($<10^{-5}$ bar), until the off-gas rate was $<10^{-7}$ bar/s. The evacuated tubes and samples were then weighed to determine the mass of the activated sample, typically 30–100 mg. The free-space of each sample was then measured using UHP He (99.999%) prior to adsorption isotherm collection. Gas adsorption isotherm data for ethylene, ethane, CO, CO_2, and CH_4 were collected at 25, 35, and 45 °C, using a water circulator for temperature control. Between each isotherm measurement, samples were reactivated by heating at 180 °C under dynamic vacuum for at least 2 h. Oil-free vacuum pumps and oil-free pressure regulators were used for all sample preparations and measurements.

3.2.2. Adsorption isotherm fitting. The single-component gas adsorption isotherms were fit using a dual-site Langmuir–Freundlich equation, given by eqn 3.1:

$$n = \frac{q_{\mathrm{sat,a}} b_{\mathrm{a}} P^{v_{\mathrm{a}}}}{1+b_{\mathrm{a}} P^{v_{\mathrm{a}}}} + \frac{q_{\mathrm{sat,b}} b_{\mathrm{b}} P^{v_{\mathrm{b}}}}{1+b_{\mathrm{b}} P^{v_{\mathrm{b}}}} \qquad (3.1)$$

where n is the absolute amount of gas adsorbed in mmol/g, $q_{\mathrm{sat,I}}$ are the saturation capacities in mmol/g, b_i are the Langmuir parameters in bar^{-1}, P is the gas pressure in bar, and v_i are the dimensionless Freundlich parameters for sites *a* and *b*. These parameters were determined using a least-squares fitting method, and are given in Tables 3.S1-3.S10.

3.2.3 Differential enthalpy calculations. The differential enthalpy of adsorption for each gas was extracted from the temperature dependence of the isotherms using the Clausius–Clapyron relationship.[60] The adsorption isotherm fits were numerically inverted and solved as $P(n)$. The differential enthalpy, h, can then be determined at a constant loading using eqn 3.2:

$$h = -R\, d(lnP)/d(1\ /\ T) \tag{3.2}$$

where R is the ideal gas constant, P is the pressure at a given loading, and T is the data collection temperature (298.15, 308.15, or 318.15 K).

3.2.4. Ideal adsorbed solution theory calculations. Single-component equilibrium adsorption isotherm data can be employed to simulate adsorbed-phase compositions in the presence of gases containing multiple species, using Ideal Adsorbed Solution Theory (IAST).[61,62,63] In the simplest case, binary selectivities can be calculated as the ratio of the adsorbed phase mole fractions relative to the ratio of gas phase mole fractions of two components, given by eqn 3.3:

$$S = \ (x_1\ /\ x_2\ )/(y_1\ /\ y_2\ ) \tag{3.3}$$

where S is the ideal selectivity for component 1 over component 2, x is the adsorbed phase mole fraction, and y is the gas phase mole fraction. This theory can also be extended to multicomponent mixtures to predict equilibrium compositions under a given OCM mixture.

3.2.5. Transient breakthrough experiments. Breakthrough experiments were performed using a custom-built apparatus constructed of primarily 1/8″ copper tubing fitted with Swagelok fittings and valves to control the flow of the gas either through the sample holder or to bypass the sample holder and flow directly to a gas chromatograph (GC) used to monitor outflow composition. Cylinders of premixed 1:1 ethane:ethylene, CO_2, and CH_4 were attached to the breakthrough manifold via MRS mass flow controllers to control gas flow. The Mn_2(*m*-dobdc) sample was pelletized using a 5 mm evacuatable pellet die and broken into pieces using a 20-40 mesh sieve, and ~0.555 g of sample was then loaded into one vertical component (13.335 cm long, 0.4572 cm inner diameter) of a U-shaped sample holder comprised of 1/4″ tubing and fitted with Swagelok VCR fittings with fritted (0.5 μm) gaskets to prevent sample escaping from the bed. The U-shaped tubing was immersed in a water bath and connected to the breakthrough manifold. The Mn_2(*m*-dobdc) sample was activated in the sample holder by heating it with heating tape at 180 °C under flowing He. The sample was then cooled to 25 °C for the breakthrough experiments using a total flow rate of 3–4 mL/min. Prior to flowing through the packed Mn_2(*m*-dobdc) sample, the gas mixture outflow was monitored using the GC to ensure the expected composition and separation. The mixture was then flowed through the packed bed of Mn_2(*m*-dobdc) and the outflow was recorded by the GC every 2 min for each gas mixture. The outflow composition was analyzed by gas chromatography using a SRI Instruments 8610 V GC equipped with a 6′ HayeSep D column, which was kept at 90 °C. The GC effluent was then fed into a flow meter to instantaneously monitor the volumetric flow rate of the gas through the column. The flow rate of each individual component was then calculated using eqn 3.4:

$$F_i(t) = y_i(t) * F^{\mathrm{tot}}(t) \tag{3.4}$$

where $F_i(t)$ is the flow rate of species i at time t in mL/min, y_i is the fraction of component i measured from the peak areas in the gas chromatogram, and $F^{tot}(t)$ is the instantaneous total flow rate of gas at the time the sample was injected into the GC, in mL/min. The quantity $F_i(t)/F_0$ is the flow of component i in the outlet stream relative to the total flow rate after breakthrough of all components.

In a given experiment, after all components had broken through the packed Mn_2(*m*-dobdc) bed, the flow was switched to He or another purge gas and the sample heated to 180 ˚C using heating tape to fully desorb adsorbed components from the column. All data were recorded and analyzed using PeakSimple software.

3.3. Results and discussion

3.3.1. Gas adsorption isotherms. Temperature-dependent equilibrium gas adsorption measurements can reveal a great deal of information about how a molecule interacts with an adsorbent. In the case of the raw data for ethylene, ethane, CO, CO_2, and methane adsorption in M_2(*m*-dobdc), it is possible to gauge relative binding strength and the adsorption capacity for each gas (Figure 3.2). The differential enthalpies for adsorption for each of these gases are shown in Figure 3.3 and compared across a constant loading of 0.5 mmol/g. For M_2(*m*-dobdc), the principle interaction with all adsorbates is electrostatic, in which the metal sites act as exposed cationic charges that can polarize proximal gas molecules. As such, all of these materials bind the highly-polarizable ethylene with binding enthalpies ranging from –44.1 ± 1.2 for Mg_2(*m*-dobdc) to –52.8 ± 1.0 kJ/mol for Fe_2(*m*-dobdc). This electrostatic interaction is well-illustrated by the previously reported single crystal X-ray diffraction structure of ethylene bound to Co_2(*m*-dobdc), which reveals a side-on binding interaction with metal–carbon distances of 2.630(18) Å and 2.685(17) Å.[53] However, a combination of cationic charge density, ionic radius, and π-back donation character will all subtly influence the binding of ethylene relative to the other gases in this study. As will be outlined further below, both Mn_2(*m*-dobdc) and Fe_2(*m*-dobdc) possess the ideal combination of these properties to display highly selective ethylene adsorption over the other measured gases.

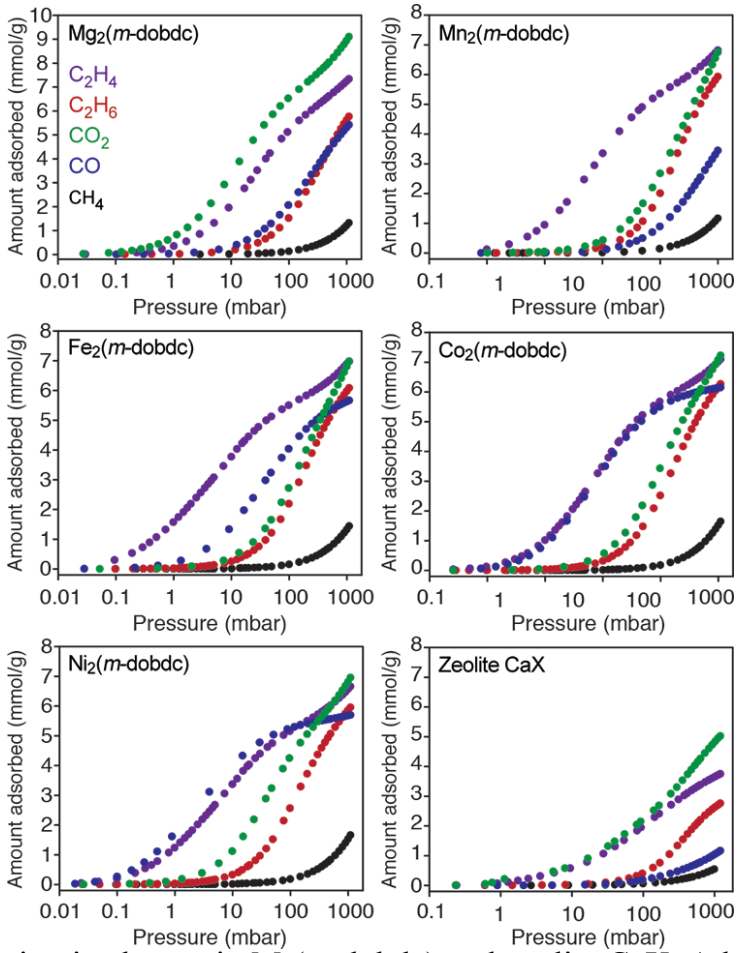

Figure 3.2. Adsorption isotherms in M_2(*m*-dobdc) and zeolite CaX. Adsorption isotherms of ethylene, ethane, CO_2, CO, and CH_4 in M_2(*m*-dobdc) (M = Mg, Mn, Fe, Co, Ni) and in zeolite CaX collected at 25 ˚C.

The binding of H_2 in M_2(*m*-dobdc) materials has been thoroughly investigated under both sub-ambient and elevated pressures for H_2 storage.[64] Under the partial pressures of interest for an OCM effluent gas separation, the isosteric heat of H_2 adsorption is on the order of –10 to –12.5 kJ/mol, and thus this molecule cannot compete for adsorption sites with the other, much more strongly interacting species in the mixture.[64]

Among the frameworks, methane adsorbs most strongly in Mg_2(*m*-dobdc), with a binding enthalpy of –22.7 ± 2.4 kJ/mol. However, zeolite CaX has significantly stronger interactions with CH_4 overall, and the methane adsorption enthalpy in this material is –35.0 ± 0.4 kJ/mol. These relative magnitudes coincide with the fact that Mg^{2+} is the most electropositive cation within the metal–organic framework series while Ca^{2+} in CaX is the most electropositive cation overall. The relative electropositivity of the binding sites in Mg_2(*m*-dobdc) and CaX is even more apparent upon considering the isosteric heats for CO_2 adsorption in these materials, which are –44.0 ± 3.1 and –54.9 ± 5.2 kJ/mol, respectively. These values are substantially larger than those measured for CO_2 binding in the transition metal frameworks, and thus these two materials would not be capable of selecting for ethylene over CO_2 out of the OCM reaction effluent mixture.

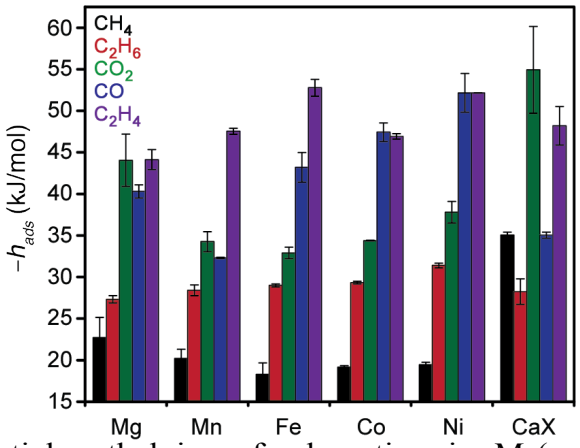

Figure 3.3. Differential enthalpies of adsorption in M_2(*m*-dobdc) and zeolite CaX. Differential enthalpies of adsorption of CH_4, C_2H_6, CO_2, CO, and C_2H_4, in M_2(*m*-dobdc) (M = Mg, Mn, Fe, Co, Ni) and zeolite CaX. Enthalpies were calculated at a constant loading of 0.5 mmol/g in each adsorbent.

While the electropositivity of the M^{2+} centers is the dominant factor influencing CH_4 and CO_2 adsorption in M_2(*m*-dobdc) and CaX, the trends in adsorption and binding enthalpy observed for CO are better understood by invoking the ionic radii and associated metal cationic charge density and some slight π-back donation ability. Carbon monoxide binds most strongly in Ni_2(*m*-dobdc) and Co_2(*m*-dobdc), with adsorption enthalpies of –52.0 ± 4.8 and –47.4 ± 1.1 kJ/mol, respectively, followed by the Fe, Mg, and Mn frameworks. This trend also matches that characterized previously for CO binding in the isomeric M_2(dobdc) (M = Mg, Mn, Fe, Co, Ni, Zn; $dobdc^{4-}$ = 2,5-dioxido-1,4-benzenedicarboxylate) frameworks,[65] including through the use of *in situ* gas dosing during neutron diffraction and FT-IR experiments. The infrared spectra reveal that upon adsorption of CO to the divalent metal cation, the C–O stretching frequency is blue-shifted, consistent with non-classical metal-CO interactions.[44] Given their strong interaction with CO, Co_2(*m*-dobdc) and Ni_2(*m*-dobdc) are poorly suited for selectively separating ethylene from the OCM effluent mixture.

In contrast to the other materials, Mn_2(*m*-dobdc) and Fe_2(*m*-dobdc) do not exhibit an exceptionally strong affinity for CH_4, CO_2, or CO, and they show the greatest relative

affinity for ethylene. Accordingly, these two frameworks were further evaluated for their ethylene separation performance under more realistic conditions. Finally, relative to other materials, Mn_2(*m*-dobdc) and Fe_2(*m*-dobdc) exhibit significantly higher ethylene adsorption capacity at the relevant partial pressure. For an ethylene partial pressure of 400 mbar at a temperature of 25 ˚C, the capacities of Mn_2(*m*-dobdc) and Fe_2(*m*-dobdc) are 6.12 and 6.19 mmol/g, respectively. These are substantially higher than in Ag-exchanged zeolite A (2.2 mmol/g) or zeolite ITQ-55 (1.3 mmol/g).[66,67]

3.3.2. Ideal selectivities. Binary selectivities for ethylene and each additional major species in the OCM effluent were calculated by fitting the equilibrium gas adsorption isotherms with a dual-site Langmuir-Freundlich equation and applying the Ideal Adsorbed Solution Theory (IAST) model.[61-63] The resulting selectivities at 25 ˚C are plotted in Figure 3.4 as a function of ethylene mole fraction in the gas phase relative to the competing species, since the selectivity will be dependent on the OCM gas composition. The ethylene/ethane ratio in the OCM reaction effluent is ~1.25:1. At this value, Fe_2(*m*-dobdc) shows the highest selectivity of 24.6 at 25 °C, followed by Mn_2(*m*-dobdc) with a selectivity of 17.0 (Figure 3.4a). Notably, these selectivities are much higher than any measured thus far for other adsorbents that utilize a rapid, reversible, and physisorptive mechanism.[53] A similar trend exists for the ethylene/CO_2 selectivities at an ethylene mole fraction of 0.5, reflecting the ~1:1 ethylene:CO_2 ratio present in the OCM reaction effluent. Notably, Fe_2(*m*-dobdc) displays the highest selectivity of 11.0, followed by Mn_2(*m*-dobdc) with a selectivity of 7.7. In contrast, both Mg_2(*m*-dobdc) and zeolite CaX exhibit near-zero ethylene/CO_2 selectivity, as expected from the adsorption enthalpies. In agreement with the adsorption isotherms and differential enthalpies of adsorption, all frameworks are highly selective for ethylene over CH_4, binding only one molecule of CH_4 for every 1000 or more ethylene molecules adsorbed.

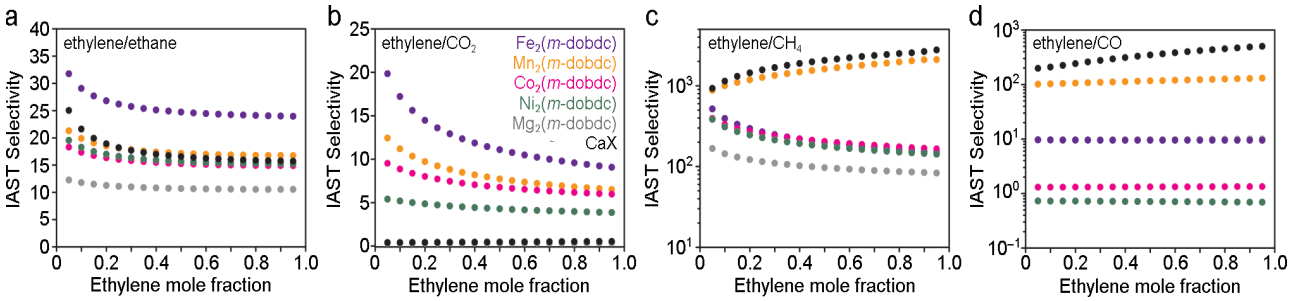

Figure 3.4. Selectivities for ethylene adsorption over other gases in the OCM effluent mixture. Selectivities for ethylene over other gases as calculated by the ideal adsorbed solution theory. The IAST selectivities for (**a**) ethylene/ethane, (**b**) ethylene/CO_2, (**c**) ethylene/CH_4, and (**d**) ethylene/CO were determined for M_2(*m*-dobdc) (M = Mg, Mn, Fe, Co, Ni) and zeolite CaX.

This series of adsorbents varies most in their ability to separate ethylene from CO. For example, Ni_2(*m*-dobdc) binds CO with a selectively over ethylene that is orders of magnitude greater than that exhibited by the other frameworks and CaX. As such, CO would remain a substantial component of the OCM effluent if the Ni framework were used in a purification process—a detrimental result if the ethylene is to be used later for polymerization. While Fe_2(*m*-dobdc) exhibits the highest ethylene/ethane selectivity across the series, it displays only a modest ethylene/CO selectivity of ~10 compared to that of Mn_2(*m*-dobdc), which is an order of magnitude higher at 125 for a 3:1 mixture of ethylene:CO. The Fe compound is also significantly less stable in air than the other frameworks, and therefore based on equilibrium adsorption and thermodynamic analysis, Mn_2(*m*-dobdc) is clearly the best material out of those examined here for the purification of the OCM effluent.

Beyond binary IAST calculations, the theory can be extended to include a more complex mixture of gases. Similar to a distillation, the composition of the mixture can be determined under a series of equilibrium stages, wherein the adsorbed phase at one stage is used as a feed to the subsequent stage (Figure 3.5). Through this type of simulation, we found that only three theoretical equilibrium stages would be necessary to obtain a 99.9% ethylene product using Mn_2(*m*-dobdc) as the adsorbent and starting with the OCM effluent composition as the initial feed (Figure 3.1). When compared with conventional cryogenic distillation, which utilizes more than 50 stages for ethylene/ethane separation alone, it is clear that an optimized adsorption process can vastly improve the outcome of a purification process.[1]

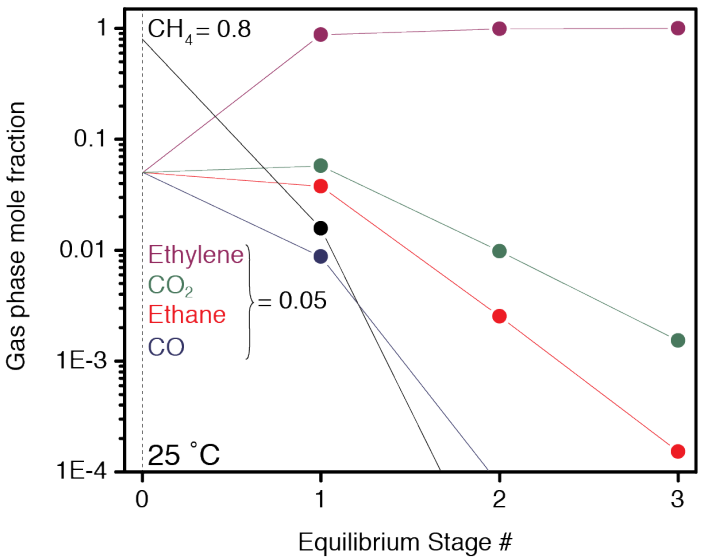

Figure 3.5. 5-Component IAST simulation of an equilibrium stage separation. Initial feed composition, corresponding to stage 0, is 80% CH_4, and 5% of ethylene, ethane, CO_2, and CO. Subsequent equilibrium stage compositions represent the adsorbed phase mole fraction in equilibrium with a gas phase containing the composition from the previous equilibrium stage. After three equilibrium stages, the adsorbed phase is >99.9% ethylene.

3.3.3. Transient breakthrough experiments. Transient breakthrough experiments were conducted on Mn_2(*m*-dobdc) to examine the performance of this material under more realistic process conditions. Under a single-component gas flow, Mn_2(*m*-dobdc) exhibits breakthrough capacities of 6.8, 6.3, 4.7, and 0.1 mmol/g for ethylene, ethane, CO_2, and CH_4, respectively (Figures 3.S1–3.S4). These values are in good agreement with the equilibrium adsorption measurements, indicating that gas transport is relatively rapid. Slight differences in the adsorptive capacities determined from breakthrough experiments and equilibrium measurements are likely the result of non-isothermal adsorption, associated with a large exothermic release during gas adsorption that increases the temperature of the bed during measurement.

The single component breakthrough curves were used in conjunction with equilibrium adsorption data to determine mass transfer coefficients (Table 3.S11). Interestingly, the mass transfer coefficients are most closely correlated with the adsorption enthalpy of a particular gas, as opposed to physical characteristics such as molecular weight. For example, methane has a smaller kinetic diameter and lower mass than ethylene, and thus gas-phase and mesopore diffusion of methane is expected to be faster than that of ethylene. However, the mass transfer coefficients for ethylene and methane were found to be 0.0125 and 0.004 s^{-1}, respectively, indicating that diffusion within the metal–organic framework

pores may be the dominating factor determining the kinetics, wherein a steeper concentration gradient exists for more strongly adsorbing gases.

To assess preliminary selectivity for ethylene adsorption, multi-component breakthrough measurements were then collected. Under a flowing equimolar mixture of ethylene and ethane, steep breakthrough of ethane occurs first, followed by ethylene (Figure 3.S6). These sharp breakthrough curves suggest that the mass transfer zone is small relative to the size of the bed, implying that the majority of the bed is useful in conducting the separation. The experiment was repeated with a mixture of ethylene, ethane, and CO_2, resulting in a breakthrough pattern in which ethane was once again observed first, followed by CO_2, and finally ethylene (Figure 3.S7). The breakthrough curves of each gas remain steep, indicating retention of fast adsorption kinetics.

Upon testing a mixture of ethylene, ethane, CH_4, and CO_2 at a total pressure of 6.2 bar (representing partial pressures of 0.45, 0.45, 0.65, and 4.65 bar for ethylene, ethane, CO_2 and CH_4, respectively), a clean separation of ethylene was again observed. Consistent with the equilibrium adsorption isotherms, differential enthalpy trends, IAST calculations, and pure-component breakthrough measurements, CH_4 breaks through first, followed by ethane, CO_2, and finally ethylene (Figure 3.6).

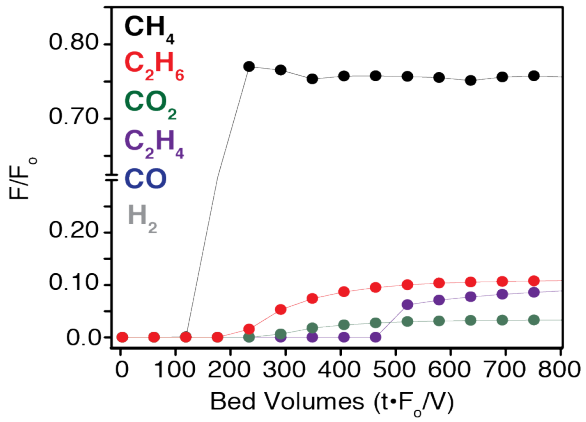

Figure 3.6. Experimental breakthrough curves for a OCM gas mixture in Mn_2(*m*-dobdc). Experimental breakthrough curves collected in a transient breakthrough experiment for a simplified OCM gas mixture in Mn_2(*m*-dobdc) at 25 °C and a total pressure of 6.2 bar.

Taken together, the experimental and simulated transient breakthrough experiments demonstrate the exceptional ability of Mn_2(*m*-dobdc) to purify ethylene from a simulated OCM effluent mixture. Significantly, this is the first adsorbent reported to cleanly separate ethylene from this complex mixture of gases.

3.4. Conclusions and outlook

The use of methane as an alternative feedstock for ethylene production via the oxidative coupling of methane represents a promising energy- and cost-effective alternative to the derivation of ethylene from fossil fuels. However, implementation of this process on a large-scale is hindered by the co-production of a complex mixture of other gases including ethane, CO_2, CO, and CH_4, which are prohibitively challenging to separate from ethylene using a conventional distillation approach. We have evaluated the M_2(*m*-dobdc) family of frameworks (with M = Mg, Mn, Fe, Co, and Ni) as candidate materials for the separation of ethylene in an adsorbent-based process, and compared their performance to that of the commercial adsorbent zeolite CaX. A suite of adsorption data as well as experimental and simulated breakthrough results indicate that Mn_2(*m*-dobdc)—which displays a high

selectivity for ethylene over CO_2, CO, and CH_4, large ethylene capacities, and fast adsorption kinetics—is the most promising out of these materials for the separation of ethylene from the oxidative coupling of methane effluent mixture. In addition to identifying Mn_2(*m*-dobdc) as an outstanding adsorbent for separating ethylene from this specific mixture, our data suggest that Mg_2(*m*-dobdc) may be useful as an adsorbent that can co-capture ethylene and CO_2, while Ni_2(*m*-dobdc) or Co_2(*m*-dobdc) may be used effectively for processing effluent streams where CO is absent or where it is desirable to isolate both ethylene and CO. These results show that metal–organic framework adsorbents can be used to dramatically improve the efficiency of the OCM effluent separation, potentially supporting the large-scale deployment of this ethylene production process and offering a competitive alternative to the decades-old fossil-based ethylene production routes.

3.5. Acknowledgements

We gratefully acknowledge Siluria Technologies for financial support of this research. This material is based upon work supported by the Department of Energy, Office of Energy Efficiency and Renewable Energy (EERE), under Award Number DE-EE0005769. The National Science Foundation provided graduate fellowship support.

3.6. References and supplementary information

(1) Eldridge, R. B. *Ind. Eng. Chem. Res.* **1993**, *32*, 2208–2212.
(2) Farrell, B. L.; Igenegbai, V. O.; Linic, S. *ACS Catal.* **2016**, *6*, 4340–4346.
(3) Farrell, B. L.; Linic, S. *Catal. Sci. Technol.* **2016**, *6*, 4370–4376.
(4) Kondratenko, E. V.; Baerns, M. Oxidative Coupling of Methane. *Handbook of Heterogeneous Catalysis;* Wiley: New York, 2008.
(5) Keller, G. E.; Bhasin, M. M. *J. Catal.* **1982**, *73*, 9–19.
(6) Otsuka, K.; Jinno, K.; Morikawa, A. J. *Catal.* **1986**, *100*, 353–359.
(7) Mleczko, L.; Baerns, M. *Fuel. Proc. Tech.* **1995**, *42*, 217–248.
(8) Lunsford, J. H. *Catal. Today* **1990**, *6*, 235–259.
(9) Lunsford, J. H. *Catal. Today* **2000**, 2, 165–174.
(10) Sofranko, J. A.; Leonard, J. J.; Jones, A. J. *Catal.* **1987**, *103*, 302–310.
(11) Elshof, J. E.; Bouwmeester, H. J. M.; Verweij, H. *Appl. Catal. A.* **1995**, *130*, 195–212.
(12) Nishiyama, T.; Aika, K.-I. *J. Catal.* **1990**, *122*, 346–351.
(13) Beck, B.; Fleischer, V.; Arndt, S.; Hevia, M. G.; Urakawa, A.; Hugo, P; Schomacker, R. *Catal. Today*, **2014**, *228*, 212–218.
(14) Bhatia, S.; Thien, C. Y.; Mohamed, A. R. *Chem Eng. J.* **2009**, *148*, 525–532.
(15) Su, Y. S.; Ying, J. Y.; Green, W. H. *J. Catal.* **2003**, *218*, 321–333.
(16) McCann, D. M.; Lesthaeghe, D.; Kletnieks, P. W.; Guenther, D. R.; Mayman, M. J.; Speybroeck, V. V.; Waroquier, M.; Haw, J. F. *Agnew. Chemie* **2008**, *120*, 5257–5260.
(17) Hereijgers, B. P. C.; Bleken, F.; Nilsen, M. H.; Svelle, S.; Lillerud, K.-P; Bjorgen, M.; Weckhuysen, B. M.; Olsbye, U. *Catal.* **2009**, *264*, 77–87.
(18) Blaken, F.; Bjorgen, M.; Palumbo, L.; Bordiga, S.; Svelle, S.; Lillerud, K.-P.; Olsbye, U. *Top. Catal.* **2009**, *52*, 218–228.
(19) Dubois, D. R.; Obrzut, D. L.; Liu, J.; Thudimadathil, J.; Adekkanattu, P. M.; Guin, J. A.; Punnoose, A.; Seehra, M. S.; *Fuel Proc. Technol.* **2003**, *83*, 203–218.
(20) Chang, C. D.; Chu, C. T.-W.; Socha, R. F. *J. Catal.* **1984**, *86*, 289–296.
(21) Tian, P.; Wei, Y.; Ye, M.; Liu, Z. *ACS Catal.* **2015**, *5*, 1922–1938.

(22) Feng, K.; Davis, S. J.; Sun, L.; Hubacek, K. *Nat. Commun.* **2015**, *6*, 7714.
(23) Nasir, I. M.; Gazhi, T. I.; Omar, R. *Eng. Life Sci.* **2012**, *12*, 258–269.
(24) Barber, W. P.; Stuckey, D. C. *Water Res.* **1999**, *33*, 1559–1578.
(25) U.S. Department of Agriculture. *Biogas Opportunities Roadmap* (2014).
(26) Lin, S.; Diercks, C. S.; Zhang, Y.; Kornienko, N.; Nichols, E. M.; Zhao, Y.; Paris, A. R.; Kim, D.; Yang, P.; Yaghi, O. M.; Chang, C. J. *Science* **2015**, *346*, 1208–1213.
(27) Yaghi, O. M.; Li, H.; Eddaoudi, M.; O'Keefe, M. *Nature* **1999**, *402*, 276−279.
(28) Kitagawa, S.; Kitaura, R.; Noro, S.-I. *Angew. Chem., Int. Ed*. **2004**, *43*, 2334−2375.
(29) Matsuda, R.; Kitaura, R.; Kitagawa, S.; Kubota, Y.; Belosludov, R. V.; Kobayashi, T. C.; Sakamoto, H.; Chiba, T.; Takata, M.; Kawazoe, Y.; Mita, Y. *Nature* **2005**, *436*, 238− 241.
(30) Millward, A. R.; Yaghi, O. M. *J. Am. Chem. Soc*. **2005**, *127*, 17998−17999.
(31) Ferey, G. *Chem. Soc. Rev*. **2008**, *37*, 191−214.
(32) Czaja, A. U.; Trukhan, N.; Müller, U. *Chem. Soc. Rev*. **2009**, *38*, 1284−1293.
(33) Chen, B.; Xiang, S.; Qian, G. Acc. *Chem. Res*. **2010**, *43*, 1115−1124.
(34) Zhou, H.-C.; Long, J. R.; Yaghi, O. M. *Chem. Rev*. **2012**, *112*, 673−674.
(35) Li, J.-R.; Sculley, J.; Zhou, H.-C. *Chem. Rev.* **2012**, *112*, 869−932.
(36) Schneemann, A.; Henke, S.; Schwedler, I.; Fischer, R. A. *ChemPhysChem* **2014**, *15*, 823−839.
(37) Yazaydin, A. O.; Snurr, R. Q.; Park, T.-H.; Koh, K.; Liu, J.; LeVan, M. D.; Benin, A. I.; Jakubczak, P.; Lanuza, M.; Galloway, D. B.; Low, J. J.; Willis, R. R. *J. Am. Chem. Soc.* **2009**, *131*, 18198–18199.
(38) Yazaydin, A. O.; Benin, A. I.; Faheem, S. A.; Jakubczak, P.; Low, J. J.; Willis, R. R.; Snurr, R. Q. *Chem. Mater.* **2009**, *21*, 1425–1430.
(39) Caskey, S. R.; Wong-Foy, A. G.; Matzger, A. J. *J. Am. Chem. Soc.* **2008**, *130*, 10870−10871.
(40) Dinca, M.; Long, J. R. *Angew. Chem., Int. Ed.* **2008**, *47*, 6766−6779.
(41) Dietzel, P. D. C.; Besikiotis, V.; Blom, R. *J. Mater. Chem.* **2009**, *19*, 7362−7370.
(42) Herm, Z. R.; Swisher, J. A.; Smit, B.; Krishna, R.; Long, J. R. *J. Am. Chem. Soc.* **2011**, *133*, 5664−5667.
(43) Mason, J. A.; Sumida, K.; Herm, Z. R.; Krishna, R.; Long, J. R. *Energy Environ. Sci.* **2011**, *4*, 3030−3040.
(44) Bloch, E. D.; Murray, L. M.; Queen, W. L.; Chavan, S.; Maximoff, S. N.; Bigi, J. P.; Krishna, R.; Peterson, V. K.; Grandjean, F.; Long, G. J.; Smit, B.; Bordiga, S.; Brown, C. M.; Long, J. R. *J. Am. Chem. Soc.* **2011**, *133*, 14814−14822.
(45) Bloch, E. D.; Queen, W. L.; Krishna, R.; Zadrozny, J. M.; Brown, C. M.; Long, J. R. *Science* **2012**, *335*, 1606−1610.
(46) Geier, S. J.; Mason, J. A.; Bloch, E. D.; Queen, W. L.; Hudson, M. R.; Brown, C. M.; Long, J. R. *Chem. Sci.* **2013**, *4*, 2054−2061.
(47) Sumida, K.; Rogow, D. R.; Mason, J. A.; McDonald, T. M.; Bloch, E. D.; Herm, Z. R.; Bae, T.-H.; Long, J. R. *Chem. Rev.* **2012**, *112*, 724− 781.
(48) Herm, Z. R.; Krishna, R.; Long, J. R. *Microporous Mesoporous Mater.* **2012**, *151*, 481−487.
(49) Peng, Y.; Krungleviciute, V.; Eryazici, I.; Hupp, J. T.; Farha, O. K.; Yildirim, T. *J. Am. Chem. Soc.* **2013**, *135*, 11887−11894.
(50) Mason, J. A.; Veenstra, M.; Long, J. R. *Chem. Sci.* **2014**, *5*, 32−51.
(51) Herm, Z. R.; Bloch, E. D.; Long, J. R. *Chem. Mater.* **2014**, *26*, 323−338.

(52) Duan, X.; He, Y.; Cui, Y.; Yang, Y.; Krishna, R.; Chen, B.; Qian, G. *RSC Adv.* **2014**, *4*, 23058−23063.
(53) Bachman, J. E.; Kapelewski, M. T.; Reed, D. A.; Gonzalez, M. I.; Long, J. R. *J. Am. Chem. Soc.* **2017**, *139*, 15363–15370.
(54) McDonald, T. M.; Mason, J. A.; Kong, X.; Bloch, E. D.; Gygi, D.; Dani, A.; Crocella, V.; Giordanino, F.; Odoh, S. O.; Drisdell, W.; Vlaisavljevich, B.; Dzubak, A. L.; Poloni, R.; Schnell, S. K.; Planas, N.; Lee, K.; Pascal, T.; Wan, L. F.; Prendergast, D.; Neaton, J. B.; Smit, B.; Kortright, J. B.; Gagliardi, L.; Bordiga, S.; Reimer, J. A.; Long, J. R. *Nature* **2015**, *519*, 303–308.
(55) Reed, D. A.; Xiao, D. J.; Gonzalez, M. I.; Darago, L. E.; Herm, Z. R.; Grandjean, F.; Long, J. R. *J. Am. Chem. Soc*. **2016**, *138*, 5594–5602.
(56) Herm, Z. R.; Wiers, B. M.; Mason, J. A.; van Baten, J. M.; Hudson, M. R.; Zajdel, P.; Brown, C. M.; Masciocchi, N.; Krishna, R.; Long, J. R. *Science* **2013**, *340*, 960–964.
(57) Hosseinpour, S.; Fatemi, S.; Mortazavi, Y.; Gholamhoseini, M.; Ravanchi, M. T. *Sep. Sci. Technol*. **2010**, *46*, 349–355.
(58) Li, Y.; Yi, H.; Tang, X.; Li, F.; Yuan, Q. *Chem. Eng. J.* **2013**, *229*, 50–56.
(59) Kapelewski, M. T.; Geier, S. J.; Hudson, M. R.; Stuck, D.; Mason, J. A.; Nelson, J. N.; Xiao, D. J.; Hulvey, Z.; Gilmour, E.; FitzGerald, S. A.; Head-Gordon, M.; Brown, C. M.; Long, J. R. *J. Am. Chem. Soc.* **2015**, *136*, 12119–12129.
(60) Rudzinski, W.; Everett, D. H. *Adsorption of Gases on Heterogeneous Surfaces*; Academic Press, Inc: CA, 1992.
(61) Myers, A. L.; Prausnitz, J. M. *AIChE Journal* **1965**, *11*, 121–127.
(62) LeVan, M. D.; Vermeulen, T. *J. Phys. Chem.* **1981**, *85*, 3247–3250.
(63) Richter, E.; Wilfried, S.; Myers, A. L. *Chem. Eng. Sci.* **1989**, *44*, 1609–1616.
(64) Kapelewski, M. T.; Runčevski, T.; Tarver, J. D.; Jiang, H. Z. H.; Hurst, K. E.; Parilla, P. A.; Ayala, A.; Gennett, T.; FitzGerald, S. A.; Brown, C. M.; Long, J. R. *Submitted.*
(65) Bloch, E. D.; Hudson, M. R.; Mason, J. A.; Chavan, S.; Crocella, V.; Howe, J. D.; Lee, K.; Dzubak, A. L.; Queen, W. L.; Zadrozny, J. M.; Geier, S. J.; Lin, L.-C.; Gagliardi, L.; Smit, B.; Neaton, J. B.; Bordiga, S.; Brown, C. M.; Long, J. R. *J. Am. Chem. Soc*. **2014**, *136*, 10752−10761.
(66) Aguado, S.; Bergeret, G.; Daniel, C.; Farrusseng, D. *J. Am. Chem. Soc.* **2012**, *134*, 14635–14637.
(67) Bereciartua, P. J.; Cantín, A.; Corma, A.; Jordá, J. L.; Palomino, M.; Rey, F.; Valencia, S.; Corcoran, E. W.; Kortunov, P.; Ravikovitch, P. I.; Burton, A.; Yoon, C.; Wang, Y.; Paur, C.; Guzman, J.; Bishop, A. R.; Casty, G. L. *Science* **2017**, *358*, 1068–1071.

Table 3.S1. Dual-site Langmuir-Freundlich equation fits for CH_4, CO, and CO_2 in Mn_2(*m*-dobdc).

	CH_4			CO_2			CO		
T (°C)	25	35	45	25	35	45	25	35	45
$q_{sat,a}$ (mmol/g)	4.513	6.498	5.555	7.019	6.527	6.232	5.565	5.264	5.103
b_a (1/bar)	0.342	0.188	0.157	5.772	4.322	2.883	1.610	1.228	0.912
v_a	1.036	1.003	1.001	0.977	1.003	0.995	0.925	0.949	0.968
$q_{sat,b}$ (mmol/g)	0	0	0	3.491	3.244	3.099	0	0	0
b_b (1/bar)	n/a	n/a	n/a	0.280	0.274	0.281	n/a	n/a	n/a
v_b	n/a	n/a	n/a	1.761	1.404	1.088	n/a	n/a	n/a

Table 3.S2. Dual-site Langmuir-Freundlich equation fits for ethylene and ethane in Mn_2(*m*-dobdc)

	Ethylene			Ethane		
T (°C)	25	35	45	25	35	45
$q_{sat,a}$ (mmol/g)	5.603	5.451	5.421	6.854	7.727	6.700
b_a (1/bar)	73.02	48.25	30.43	6.228	4.080	2.606
v_a	0.854	0.868	0.876	1.170	1.173	1.153
$q_{sat,b}$ (mmol/g)	23.94	10.72	9.560	0	0	0
b_b (1/bar)	0.057	0.116	0.109	n/a	n/a	n/a
v_b	0.727	0.646	0.632	n/a	n/a	n/a

Table 3.S3. Dual-site Langmuir-Freundlich equation fits for CH_4, CO, and CO_2 in Fe_2(*m*-dobdc)

	CH_4			CO_2			CO		
T (°C)	25	35	45	25	35	45	25	35	45
$q_{sat,a}$ (mmol/g)	4.812	14.00	14.90	10.06	7.126	6.921	5.656	5.749	5.435
b_a (1/bar)	0.235	0.083	0.022	0.324	4.227	2.825	0.207	10.65	7.912
v_a	1.073	0.963	0.847	0.691	1.020	1.019	0.410	0.866	0.895
$q_{sat,b}$ (mmol/g)	9.740	0	0	4.723	1.606	1.540	4.842	0.794	1.125
b_b (1/bar)	0.044	n/a	n/a	11.25	0.336	0.342	29.03	0.233	0.343
v_b	0.843	n/a	n/a	1.138	1.885	1.477	0.967	1.405	1.079

Table 3.S4. Dual-site Langmuir-Freundlich equation fits for ethylene and ethane in Fe_2(*m*-dobdc)

	Ethylene			Ethane		
T (°C)	25	35	45	25	35	45
$q_{sat,a}$ (mmol/g)	5.657	5.288	5.479	4.907	4.250	3.485
b_a (1/bar)	59.52	48.99	28.01	9.727	6.895	4.924
v_a	0.735	0.771	0.776	1.254	1.295	1.344
$q_{sat,b}$ (mmol/g)	3.841	4.255	7.464	3.274	3.703	4.049
b_b (1/bar)	0.503	0.500	0.173	0.876	0.947	1.004
v_b	0.790	0.593	0.576	0.700	0.761	0.818

Table 3.S5. Dual-site Langmuir-Freundlich equation fits for CH_4, CO, and CO_2 in Co_2(*m*-dobdc)

	CH_4			CO_2			CO		
T (°C)	25	35	45	25	35	45	25	35	45
$q_{sat,a}$ (mmol/g)	9.874	9.035	8.270	7.162	3.286	2.354	6.078	3.614	3.324
b_a (1/bar)	0.182	0.157	0.137	10.21	14.20	9.258	71.42	94.97	85.06
v_a	0.990	0.998	0.999	1.041	1.214	1.249	0.877	0.953	0.996
$q_{sat,b}$ (mmol/g)	0	0	0	2.079	5.354	5.958	0.909	2.659	2.868
b_b (1/bar)	n/a	n/a	n/a	0.370	1.822	1.816	0.207	13.46	10.94
v_b	n/a	n/a	n/a	2.357	0.841	0.889	0.878	0.807	0.918

Table 3.S6. Dual-site Langmuir-Freundlich equation fits for ethylene and ethane in Co_2(*m*-dobdc)

	Ethylene			Ethane		
T (°C)	25	35	45	25	35	45
$q_{sat,a}$ (mmol/g)	5.968	5.983	5.850	5.756	3.409	0.178
b_a (1/bar)	79.89	45.60	29.82	8.88	0.362	82.65
v_a	0.869	0.866	0.876	1.133	0.707	2.270
$q_{sat,b}$ (mmol/g)	4.917	9.454	3.615	3.724	5.561	6.697
b_b (1/bar)	0.293	0.108	0.321	0.362	5.767	2.725
v_b	0.838	0.760	0.719	0.684	1.130	1.033

Table 3.S7. Dual-site Langmuir-Freundlich equation fits for CH_4, CO, and CO_2 in Ni_2(*m*-dobdc)

	CH_4			CO_2			CO		
T (°C)	25	35	45	25	35	45	25	35	45
$q_{sat,a}$ (mmol/g)	9.215	8.715	8.335	5.763	5.872	6.072	4.750	5.538	4.083
b_a (1/bar)	0.199	0.165	0.137	29.39	16.74	9.459	217.3	59.31	87.44
v_a	0.996	1.011	1.010	1.036	1.024	1.017	0.879	0.784	0.869
$q_{sat,b}$ (mmol/g)	0	0	0	3.796	1.706	1.679	1.084	0.224	1.577
b_b (1/bar)	n/a	n/a	n/a	0.489	0.942	0.400	6.149	6.924	14.01
v_b	n/a	n/a	n/a	1.357	1.692	2.037	0.617	2.105	0.910

Table 3.S8. Dual-site Langmuir-Freundlich equation fits for ethylene and ethane in Ni_2(*m*-dobdc).

	Ethylene			Ethane		
T (°C)	25	35	45	25	35	45
$q_{sat,a}$ (mmol/g)	5.496	5.304	5.631	6.666	6.510	6.321
b_a (1/bar)	52.14	38.07	21.79	6.824	4.804	3.460
v_a	0.755	0.777	0.776	1.046	1.063	1.075
$q_{sat,b}$ (mmol/g)	5.558	6.990	1.003	0	0	0
b_b (1/bar)	0.267	0.192	1.784	n/a	n/a	n/a
v_b	0.866	0.727	1.774	n/a	n/a	n/a

Table 3.S9. Dual-site Langmuir-Freundlich equation fits for CH_4, CO, and CO_2 in zeolite CaX.

	CH_4			CO_2			CO		
T (°C)	25	35	45	25	35	45	25	35	45
$q_{sat,a}$ (mmol/g)	2.761	2.532	1.933	6.011	6.573	7.009	1.275	1.256	1.290
b_a (1/bar)	0.302	0.281	0.299	3.211	2.047	1.380	0.923	0.817	0.670
v_a	0.876	0.902	0.936	0.674	0.620	0.597	1.088	1.037	0.991
$q_{sat,b}$ (mmol/g)	n/a	n/a	n/a	0.485	0.285	0.203	0.568	0.480	0.410
b_b (1/bar)	n/a	n/a	n/a	1522	1573	1466	23.91	21.84	17.00
v_b	n/a	n/a	n/a	1.326	1.233	1.265	0.933	0.977	1.007

Table 3.S10. Dual-site Langmuir-Freundlich equation fits for ethylene and ethane in zeolite CaX.

	Ethylene			Ethane		
T (°C)	25	35	45	25	35	45
$q_{sat,a}$ (mmol/g)	2.845	3.353	3.873	2.858	0.348	0.327
b_a (1/bar)	2.498	2.040	1.701	3.793	0.079	0.074
v_a	0.604	0.534	0.477	1.269	0.481	0.672
$q_{sat,b}$ (mmol/g)	1.051	0.644	0.287	0.377	4.198	4.460
b_b (1/bar)	28.59	52.25	1488	42.10	1.301	0.904
v_b	0.477	0.513	0.848	0.979	0.861	0.860

Table 3.S11. Mass transfer coefficients determined from breakthrough data for Mn_2(*m*-dobdc).

Gas	Value
Ethylene	0.0125 s^{-1}
Ethane	0.0037 s^{-1}
CO_2	0.01 s^{-1}
CO	0.0125 s^{-1}
Methane	0.004 s^{-1}

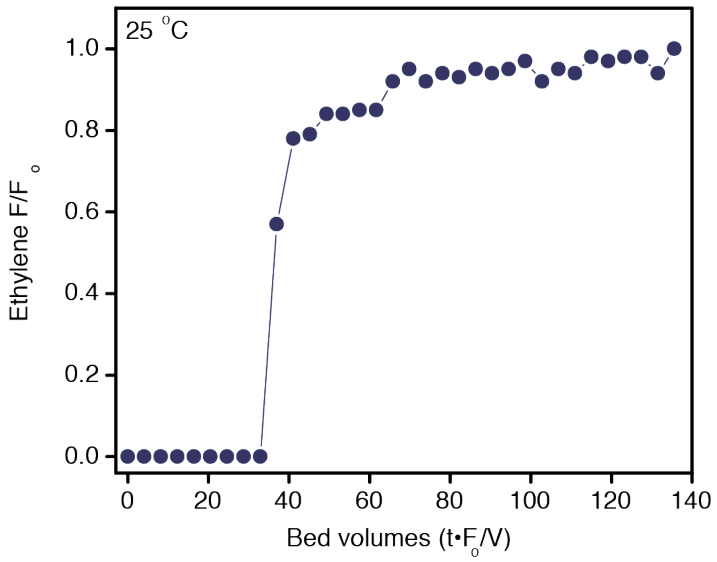

Figure 3.S1. Single-component transient breakthrough curve of ethylene in Mn_2(*m*-dobdc). Breakthrough capacity was determined to be 6.81 mmol/g.

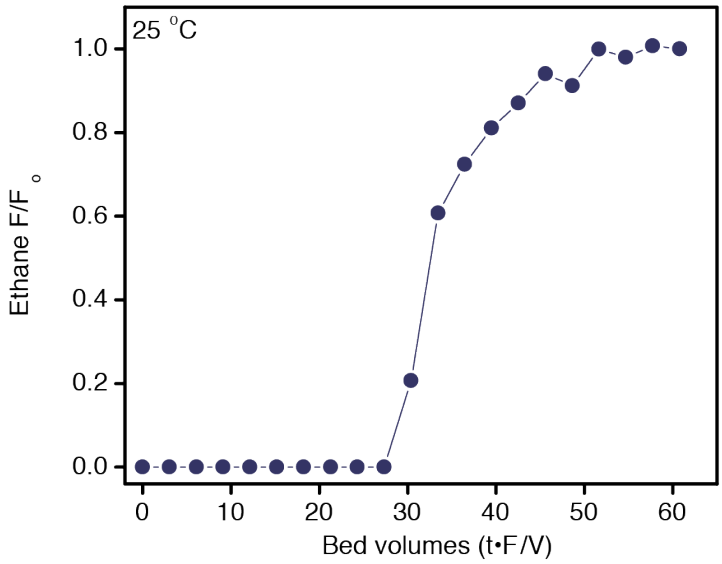

Figure 3.S2. Single-component transient breakthrough curve of ethane in Mn_2(*m*-dobdc). Breakthrough capacity was determined to be 6.31 mmol/g.

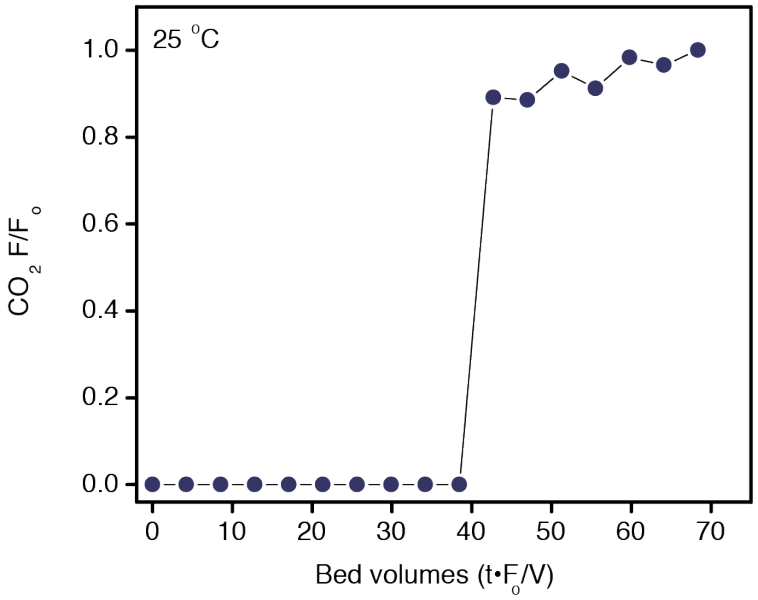

Figure 3.S3. Single-component transient breakthrough curve of CO_2 in Mn_2(*m*-dobdc). Breakthrough capacity was determined to be 4.67 mmol/g.

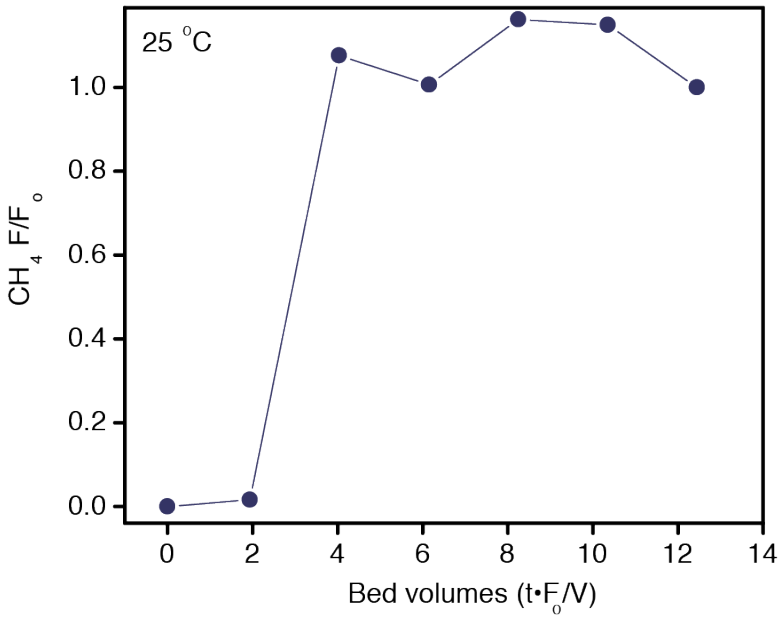

Figure 3.S4. Single-component transient breakthrough curve of CH_4 in Mn_2(*m*-dobdc). Breakthrough capacity was determined to be 0.09 mmol/g.

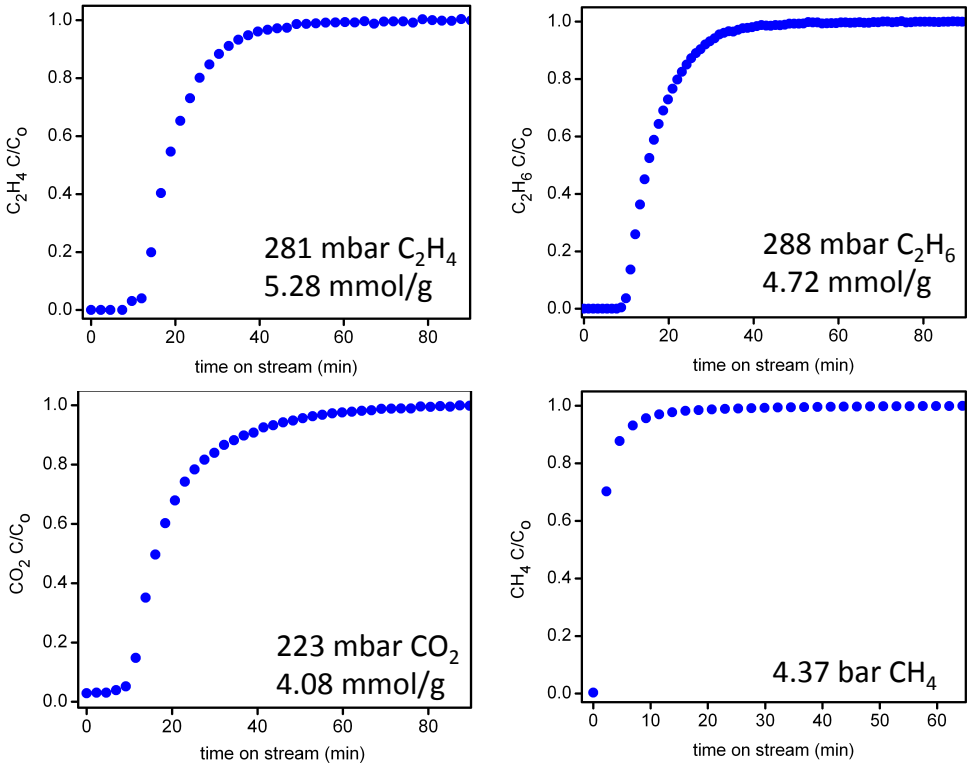

Figure 3.S5. Elevated pressure, single-component transient breakthrough curves for Mn_2(*m*-dobdc), including the partial pressure of each gas and the corresponding breakthrough capacity. Total pressure is 6.2 bar, with the remainder of the gas being He. Total flow rate is 40 sccm. Temperature is 25 ˚C.

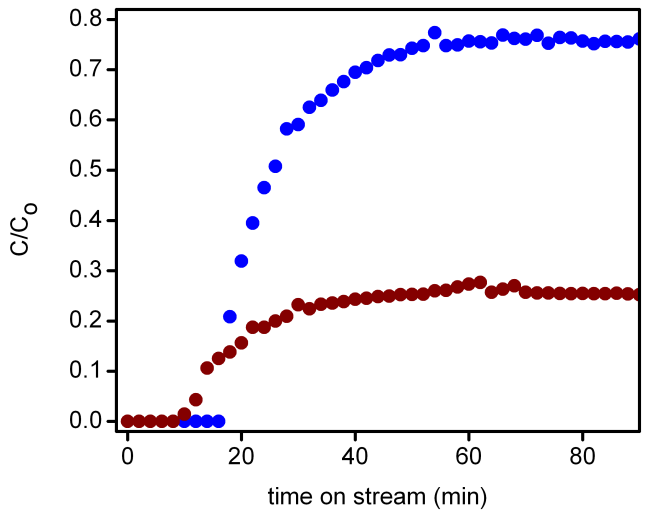

Figure 3.S6. Binary transient breakthrough curves of 3:1 ethylene:ethane in Mn_2(*m*-dobdc). Blue and red circles correspond to ethylene and ethane, respectively. Total pressure is 6.2 bar. Total flow rate is 40 sccm. Temperature is 25 ˚C.

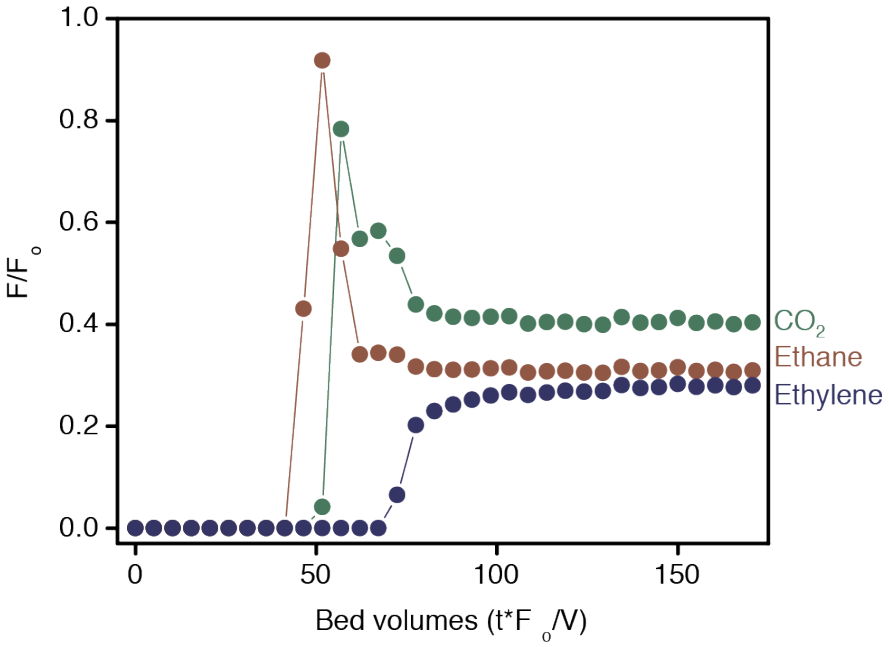

Figure 3.S7. Transient breakthrough curve of a CO_2/ethylene/ethane mixture in Mn_2(*m*-dobdc) at a total pressure of 1 bar and 25 ˚C.

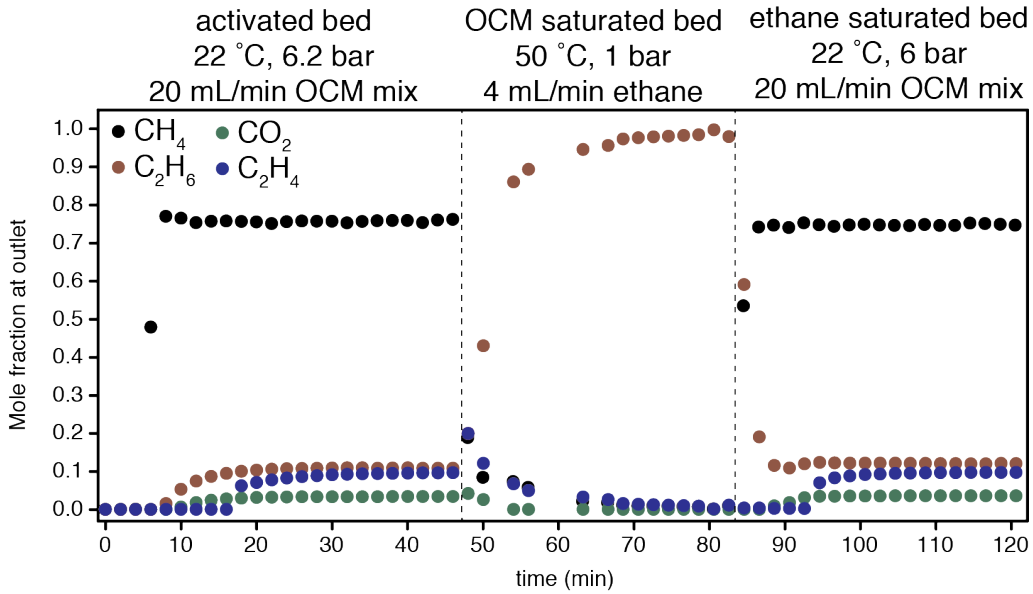

Figure 3.S8. Bed cycling experiment using an ethane purge and elevated temperature to regenerate the bed. The experiment is broken into three parts. The first section corresponds to the breakthrough of an OCM effluent gas stream on an activated bed at a total pressure of 6.2 bar and 22 ˚C. The second section corresponds to the gas phase being switched to an ethane purge and the temperature is raised to 50 ˚C. Correspondingly, ethylene and the other adsorbed components are purged from the bed. In the third section, the gas phase was returned to the OCM effluent composition. Ethylene selectivity is maintained after the purge phase.

Chapter 4: Adsorbate-Induced Spin State Transitions for Reversible CO Scavenging in an Iron(II)–Triazolate Metal–Organic Framework

4.1. Introduction

Metal–organic frameworks are a class of permanently porous materials exhibiting tremendous chemical tunability and high internal surface areas.[1] An important subset of these materials features high densities of exposed metal cation sites (*i.e.*, metal centers that preserve open coordination sites upon desolvation of the framework). These exposed metal sites typically act as Lewis acids that can accept electron density from easily polarized gas molecules such as CO_2. This electrostatic interaction is the underlying basis for a wide variety of potential applications in gas storage and separations.[2] However, many gas molecules can behave as π-acids in addition to σ-donors, and developing frameworks that take advantage of this additional property could lead to new adsorbents displaying unprecedented selectivities in separations involving carbon monoxide, unsaturated hydrocarbons, and other small molecules with low-lying π* orbitals. In order to bind such species strongly, a material needs to possess exposed transition metal centers that function not just as exposed partial positive charges, but as sites capable of π back-donation.[3] Unfortunately, this feature has been difficult to realize in practice, since the majority of frameworks with open metal sites are ligated by weak-field carboxylate or aryl-oxide ligands, resulting in electron-poor, high-spin metal centers that are only weakly π-donating. As a result, only a small number of metal–organic frameworks feature exposed electron-rich, low-spin first-row transition metal centers suitable for π back-donation.[4]

An important application of porous materials containing π-donating exposed metal sites is in the area of carbon monoxide separations, and new adsorbent-based technologies can be envisioned for both CO removal as well as CO purification. For example, trace CO removal from H_2 is relevant to both ammonia production and fuel cell technologies, as even ppm levels (often <10 ppm) of CO can poison the catalysts used in these applications.[5] Aside from CO scrubbing, CO is produced in large quantities from processes such as iron and steel production, coke production and coal gasification, partial oxidation processes, and steam reforming of methane, appearing in mixtures containing H_2, N_2, CO_2, and various hydrocarbons. Carbon monoxide is a valuable chemical precursor used in the production of several commodity chemicals, including alcohols, monomers and polymers, and acetic acid, and the efficient separation of pure CO from these gas mixtures would allow for the use of CO as a versatile carbon synthon.[6] Currently, CO separations are achieved via cryogenic distillation, although membrane,[7] adsorption,[8] and liquid adsorption[9] based processes have also been investigated. While some metal–organic frameworks or similar materials have been studied for CO adsorption,[10] most of these materials do not bind CO strongly enough to remove trace amounts or leverage the π-acidity of CO to selectively adsorb it over a variety of gas molecules. Other frameworks bind CO so strongly that adsorption is irreversible, limiting their use in practical applications.[11]

In order to achieve highly selective CO binding while retaining good reversibility, we envisioned a material in which the exposed metal center could interconvert between high-spin and low-spin configurations. A low-spin metal center would afford an elusive electron donating metal species capable of strong CO interactions for trace CO removal and selective CO adsorption over polarizable gas molecules that are typically adsorbed strongly by metal–organic frameworks, while the ability to convert back to high-spin would also allow for facile desorption of CO due to the much weaker metal–carbonyl interaction. To date, only a small number of metal–organic

frameworks display the ability to undergo reversible spin transitions and retain their porosity,[12] and none feature accessible, coordinatively-unsaturated metal sites. We hypothesized that a framework with exposed Fe^{II} centers in a triazolate-based coordination environment would be a promising material, due to the large number of spin-crossover Fe^{II}–triazole and Fe^{II}–triazolate complexes.[13] Specifically, an iron analogue of a triazolate-based copper framework previously synthesized in our laboratory, $H[(Cu_4Cl)_3(BTTri)_8]$ (Cu-BTTri, H_3BTTri = 1,3,5-tris(1*H*-1,2,3-triazol-5-yl)benzene)), was targeted due to its high concentration of open metal sites coordinated by triazolates.[14] Herein, we report the new metal–organic framework, $Fe_3[(Fe_4Cl)_3(BTTri)_8]_2$•$18CH_3OH$ (Fe-BTTri), featuring coordinatively-unsaturated Fe^{II} centers that can indeed reversibly convert from a high-spin to a low-spin electron configuration upon exposure to carbon monoxide. As a result, the material shows unprecedented selectivity for the adsorption of CO over H_2, especially at low concentrations of CO, while also displaying preferential adsorption of CO over N_2, CO_2, ethylene, and a variety of other molecules.

4.2. Materials and methods

4.2.1. General Information. All manipulations were performed under an N_2 atmosphere in a VAC Atmospheres glovebox or using standard Schlenk techniques. The compound H_3BTTri was prepared according to a previously reported procedure.[14] $FeCl_2$ was purchased from Sigma-Aldrich and used as received. Dimethylformamidium trifluoromethanesulfonate was purchased from Sigma-Aldrich and dried under vacuum prior to use. Methanol was purchased from EMD Millipore Corporation as DriSolv grade, dried over 3 Å sieves, and sparged with Ar prior to use. Dimethylformamide (DMF) was purchased from EMD Millipore Corporation as OmniSolv grade, sparged with Ar, and dried with an alumina column prior to use.

4.2.2. Synthesis of $Fe_3[(Fe_4Cl)_3(BTTri)_8]_2$•$18CH_3OH$ (Fe-BTTri). To a 25 mL Schlenk flask charged with a stir bar and a solution of H_3BTTri (50 mg, 1.0 eq, 0.18 mmol) and dimethylformamidium trifluoromethanesulfonate (180 mg, 4.5 eq, 0.81 mmol) in DMF (8 mL) was added a solution of $FeCl_2$ (230 mg, 10 eq, 1.8 mmol) in 2 mL of methanol. The yellow solution was stirred at 120 °C for 10 days. The resulting yellow powder was collected by filtration, rinsed with DMF, and soaked in 10 mL of DMF at 120 °C for 12 h. The supernatant solution was decanted, and 10 mL of fresh DMF was added. This process was repeated nine times so that the total time washing with DMF was 5 days. The yellow powder was collected by filtration, rinsed with methanol, and soaked in 10 mL of methanol at 60 °C for 12 h. The supernatant solution was decanted, and 10 mL of fresh methanol was added. This process was repeated nine times so that the total time washing with methanol was 5 days. The resulting yellow powder was collected by filtration, and heated at 180 °C under dynamic vacuum (<0.01 mbar) for 2 days, affording 50 mg (66%) of product as a tan powder. Elemental analysis of bulk sample ($C_{210}H_{168}Cl_6Fe_{27}N_{144}O_{18}$): Found: C 37.40 H 2.20 N 30.05. Calculated: C 37.53 H 2.52 N 30.03.

4.2.3. Synthesis of single crystals of Fe-BTTri. To a stainless steel bomb charged with a solution of H_3BTTri (12 mg, 2.2 eq, 0.043 mmol) and dimethylformamidium trifluoromethanesulfonate (24 mg, 5.4 eq, 0.11 mmol) in DMF (8 mL) was added a solution of $FeCl_2$ (2.5 mg, 1.0 eq, 0.020 mmol) in methanol (2 mL). The solution was heated at 160 °C for 3 days. Small yellow crystals were isolated by decanting the supernatent solution, rinsed with DMF, and soaked in 10 mL of DMF at 120 °C for 12 h. The supernatant solution was decanted, and 10 mL of fresh DMF was added. This process was repeated four times so that the total time washing with DMF was 5 days. The yellow crystals were collected by filtration, rinsed with methanol, and

soaked in 10 mL of methanol at 60 °C for 12 h. The supernatant solution was decanted, and 10 mL of fresh methanol was added. This process was repeated nine times, so that the total time washing with methanol was 5 days. The yellow crystals were collected by filtration, and heated at 150 °C under dynamic vacuum (<0.01 mbar) for 2 days, affording ~ 2 mg of pale red crystals of Fe-BTTri.

4.2.4. Gas adsorption measurements. Gas adsorption isotherms for pressures in the range 0–1 bar were measured by a volumetric method using a Micromeritics ASAP2020 or Micromeritics 3Flex gas sorption analyzer. A typical sample of ca. 100 mg of metal–organic framework was transferred in an N_2 filled glovebox to a pre-weighed analysis tube, which was capped with a Micromeretics TranSeal and evacuated by heating at 180 °C with a ramp rate of 0.5 °C/min under dynamic vacuum until an outgas rate of less than 3 μbar/min was achieved. The evacuated analysis tube containing the degassed sample was then carefully transferred to an electronic balance and weighed again to determine the mass of sample. The tube was then transferred back to the analysis port of the gas adsorption instrument. The outgas rate was again confirmed to be less than 3 μbar/min. For all isotherms, warm and cold free space correction measurements were performed using ultra-high purity He gas (UHP grade 5.0, 99.999% purity); CO, H_2, N_2, CH_4, CO_2, C_2H_4, and C_2H_6 isotherms at 298 to 348 K were measured in water baths using UHP–grade gas sources. CO isotherms at 373 to 423 K were measured using a sandbath. N_2 isotherms collected at 77 K were measured in liquid nitrogen baths. Oil-free vacuum pumps and oil-free pressure regulators were used for all measurements to prevent contamination of the samples during the evacuation process or of the feed gases during the isotherm measurements. Langmuir surface areas were determined from N_2 adsorption data at 77 K using Micromeritics software.

4.2.5. Adsorption isotherm fitting. Adsorption isotherms were fit with either a single-, dual-, triple-, or quadruple-site Langmuir–Freundlich equation (eq 4.1), where n is the total amount adsorbed in mmol/g, P is the pressure in bar, $n_{sat,i}$ is the saturation capacity in mmol/g, b_i is the Langmuir parameter in bar^{-1}, and v is the Freundlich parameter for up to four sites 1, 2, 3, and 4.

$$n = \frac{n_{sat,1} b_1 P^{v_1}}{1+b_1 P^{v_1}} + \frac{n_{sat,2} b_2 P^{v_2}}{1+b_2 P^{v_2}} + \frac{n_{sat,3} b_3 P^{v_3}}{1+b_3 P^{v_3}} + \frac{n_{sat,4} b_4 P^{v_4}}{1+b_4 P^{v_4}} \quad (4.1)$$

The fitted parameters for CO adsorption can be found in Table 4.S1, the parameters for H_2, N_2, or CO_2 can be found in Table 4.S2, with alternate H_2 parameters found in Table 4.S3, the parameters for C_2H_6 and CH_4 can be found on table S4, and the parameters for C_2H_4 can be found on table S5. Plots of the adsorption isotherms with the corresponding single-, dual-, triple-, or quadruple-site Langmuir-Freundlich fits can be found in Figures 4.S6, 4.S10, 4.S12, or 4.S14.

4.2.6. Isosteric heat of adsorption calculations. Using the quadruple-site Langmuir-Freundlich fits, the isosteric heat of adsorption, $-Q_{st}$, was calculated for each compound as a function of the amount of CO adsorbed using the Clausius-Clapeyron relation (eq 4.2), where R is the ideal gas constant, P is the pressure, and T is the temperature.

$$-Q_{st} = RT^2 \left(\frac{\partial \ln P}{\partial T}\right)_n \quad (4.2)$$

For multi-site Langmuir-Freundlich models, it is necessary to calculate the loading dependence of the isosteric heat of adsorption. As written, multi-site Langmuir-Freundlich equations specify the amount adsorbed as a function of pressure, while the pressure as a function of the amount adsorbed is needed to use the Clausius-Clapeyron relation. To calculate the isosteric heat of adsorption for evenly spaced loadings, each multi-site Langmuir equation was solved for the

pressures that correspond to specific loadings of CO at 65, 75, and 100 °C, and these calculated pressures were then used in eq 4.2 to determine the heat of adsorption as a function of the total amount of CO adsorbed.

4.2.7. Ideal adsorbed solution theory calculations. Since binary gas adsorption isotherms cannot be measured in a straightforward manner, it is often necessary to use an adsorption model, such as ideal adsorbed solution theory (IAST),[15] to predict mixed gas behavior from experimentally measured single–component isotherms. The accuracy of the IAST procedure has already been established for adsorption of a wide variety of different gases in zeolites and metal−organic frameworks.[16] Here, IAST is used to estimate the selectivity, S_{ads}, of Fe–BTTri for mixtures of CO and H_2 at 25 °C, CO and N_2 at 25 °C, CO and CH_4 at 25 °C, CO and CO_2 at 25 and 45 °C, CO and C_2H_4 at 25 and 45 °C, and CO and C_2H_6 at 25 and 45 °C and a total pressure of 1 bar for all calculations. The selectivity factor, S, is defined according to eq 4.3, where n_i is the amount adsorbed of each component as determined from IAST and x_i is the mole fraction of each component in the gas phase at equilibrium.

$$S = \frac{n_{CO}/n_{H_2}}{x_{CO}/x_{H_2}} \tag{4.3}$$

4.2.8. Infrared spectroscopy. Infrared spectra were collected on a PerkinElmer Avatar Spectrum 400 FTIR spectrophotometer equipped with a Pike attenuated total reflectance accessory (ATR) accessory equipped with a N_2-filled glove bag. CO-dosed Fe–BTTri was prepared by placing activated Fe-BTTri under an atmosphere of 1.0 mbar of CO at room temperature, and then transferring the sample in an N_2 atmosphere. The measurement for CO-dosed Fe-BTTri was collected under an N_2 atmosphere, however no appreciable change in intensity of the ν_{CO} band was observed after sitting in an N_2 atmosphere overnight.

4.2.9. Single-crystal X-ray diffraction. Single-crystal X-ray diffraction data for $[Fe(CH_3OH)_6]_3[(Fe_4Cl(DMF)_4)_3(BTTri)_8]_2$ and $[Fe(CH_3OH)_6]_3[(Fe_4Cl(CO)_4)_3(BTTri)_8]_2$ were collected at Beamline 11.3.1 at the Advanced Light Source at Lawrence Berkeley National Laboratory using synchrotron radiation (λ = 0.7749 Å) with a Bruker PHOTON 100 CMOS detector on a Bruker AXS D8 diffractometer through a combination of 4° phi and 1° phi and omega scans. Data were collected from single crystals mounted on a MiTeGen loop with Paratone-N oil and frozen at 100 K by an Oxford Cryosystems Cryostream 700 Plus. CO-dosed single crystals were prepared by dosing CO on a Micromeritics ASAP2020 gas adsorption analyzer and adding Paratone-N oil in an N_2 atmosphere. Bruker AXS SAINT software[17] was used to integrate the raw data and correct for Lorentz and polarization effects, and SADABS[18] was used to apply absorption corrections. Space group assignment was made by examination of systematic absences, E-statistics, and successive structure refinement. SHELXT[19,20] was used to solve the structure using direct methods, and SHELXL[21] was used for refinement as implemented within the OLEX2[22] interface. Thermal parameters for all non-hydrogen atoms were refined anisotropically. Hydrogen atoms were placed in ideal positions and a riding model was used to refine their positions. Residual electron density in the pores of both structures could not be modeled and is likely due to disordered extra-framework Fe^{II} cations and solvent molecules. Consequently, a solvent mask was applied as implemented in OLEX2.[8]

4.2.10. Powder X-ray diffraction. Microcrystalline powder samples of Fe-BTTri (~5 mg) were loaded into 1.0 mm boron-rich glass capillaries inside a glovebox under an N_2 atmosphere. The capillaries were attached to a gas cell, which was connected to the analysis port of a Micromeritics ASAP 2020 gas adsorption instrument. The capillaries of activated Fe-BTTri were

fully evacuated at room temperature for one hour and then flame-sealed and placed inside a Kapton tube that was sealed on both ends with epoxy. To prepare CO-dosed Fe-BTTri, the capillaries were fully evacuated at room temperature for one hour, then placed under a 200 mbar atmosphere of CO for two hours. The capillary was then flame-sealed with a 200 mbar atmosphere of CO, and placed inside a Kapton tube that was sealed on both ends with epoxy.

High-resolution synchrotron powder X-ray diffraction data were subsequently collected at Beamline 17-BM at the Advanced Photon Source (APS) at Argonne National Laboratory. Diffraction patterns were collected at 100 K with a wavelength of 0.72959 Å.

4.2.11. Mössbauer spectroscopy. Mössbauer spectra of Fe-BTTri, DMF-solvated Fe-BTTri, and CO-dosed Fe-BTTri were measured at various temperatures between 100 and 290 K with a constant acceleration spectrometer, which utilized a rhodium matrix cobalt–57 source. Isomer shifts are reported relative to 27 μm α–iron foil at 295 K. The absorber contained ca. 40 mg/cm^2 of powder. CO-dosed Fe-BTTri was prepared by loading activated Fe-BTTri in an N_2-filled glovebox and placed in a Schlenk flask. The flask was removed from the glovebox, evacuated, and filled with 0.1 mbar of CO at 298K for two hours. The sample was then cooled to 77 K with liquid nitrogen and inserted into a precooled cryostat under dry helium. The Mössbauer spectra were fit with a sum of symmetric Lorentzian doublets. In some cases, some spectral parameters were constrained and they are reported without error bars in Table 4.S6.

4.2.12. Magnetic susceptibility measurements. Samples were prepared by adding crystalline powder of Fe–BTTri (21.9 mg, 20.6 mg, and 21.6 mg for Fe-BTTri, Fe-BTTri–$(CO)_{3.2}$, and Fe-BTTri–$(CO)_{10.6}$, respectively) to a 5 mm inner diameter quartz tube containing a raised quartz platform. Sample powders were restrained with a plug of compacted glass wool that prevented crystallite torqueing, but enabled gas-dosing with CO. Preparation of the CO-loaded samples was accomplished by attaching the quartz tubes containing activated Fe-BTTri to a Micromeritics ASAP 2020 Surface Area and Porosity Analyzer. Adsorption isotherms were then run until the pressure of the atmosphere of CO gas in the sample tubes reached exactly 13.4% (3.2 molar equivalents of CO per mole of Fe-BTTri) and 44.3% (10.6 molar equivalents of CO per mole of Fe-BTTri) loading of CO in the sample, respectively, at which point the measurements were terminated. The quartz tubes were then cooled in liquid N_2 and flame-sealed. Magnetic susceptibility measurements were performed using a Quantum Design MPMS2 SQUID magnetometer. Dc magnetic susceptibility measurements were collected in the temperature range 2-300 K under applied magnetic fields of 0.1 T, 0.5 T, and 1 T. Diamagnetic corrections were applied to the data using Pascal's constants to give χ_D = –0.00300606 emu/mol (Fe-BTTri), χ_D = –0.00303988 emu/mol (Fe-BTTri–$(CO)_{3.2}$), and χ_D = –0.00311842 emu/mol (Fe-BTTri–$(CO)_{10.6}$). Prior to fitting of the magnetic data (H_{dc} = 1 T), $\chi_M T$ data for Fe-BTTri (formula unit $[Fe(CH_3OH)_6]_3[(Fe_4Cl)_3(BTTri)_8]_2$) was simplified by subtracting the $\chi_M T$ product expected for the extra framework cations (3 S = 2 centers with g = 2.00) and dividing the resultant $\chi_M T$ data by six, the number of $Fe_4(\mu_4\text{-Cl})$ clusters present in the formula unit. The resulting data set reflected the $\chi_M T$ behavior for a single $Fe_4(\mu_4\text{-Cl})$ cluster within the framework. This data was fit across the temperature range 2–300 K using the program PHI[23] using the simplex method.

4.3. Results and discussion

4.3.1. Synthesis of Fe-BTTri. A solvated form of the new metal–organic framework $Fe_3[(Fe_4Cl)_3(BTTri)_8]_2$•$18CH_3OH$ (Fe-BTTri) was isolated as a yellow, microcrystalline powder from the reaction between $FeCl_2$ and H_3BTTri in DMF and methanol. The compound can be mostly desolvated by first soaking in methanol to remove DMF, followed by heating at 180 °C under dynamic vacuum to yield activated Fe-BTTri as a tan powder. The powder is microcrystalline and retains its crystallinity through activation, as assessed by powder X-ray diffraction measurements (Figure 4.S1). The resulting X-ray diffraction pattern indicates a framework structure type analogous to that of Cu-BTTri.[14] The activated material retains a small amount of methanol, as seen by elemental analysis, and the majority of these methanol molecules are postulated to be bound to the extra-framework Fe^{II} cations. Adsorption of N_2 at 77 K revealed a Langmuir surface area of 1930 m^2/g and a Brunauer–Emmett–Teller (BET) surface area of 1630 m^2/g (Figure 4.S3). These values are in good agreement with results obtained for Cu-BTTri, which displays Langmuir and BET surface areas of 1900 and 1770 m^2/g, respectively.[14]

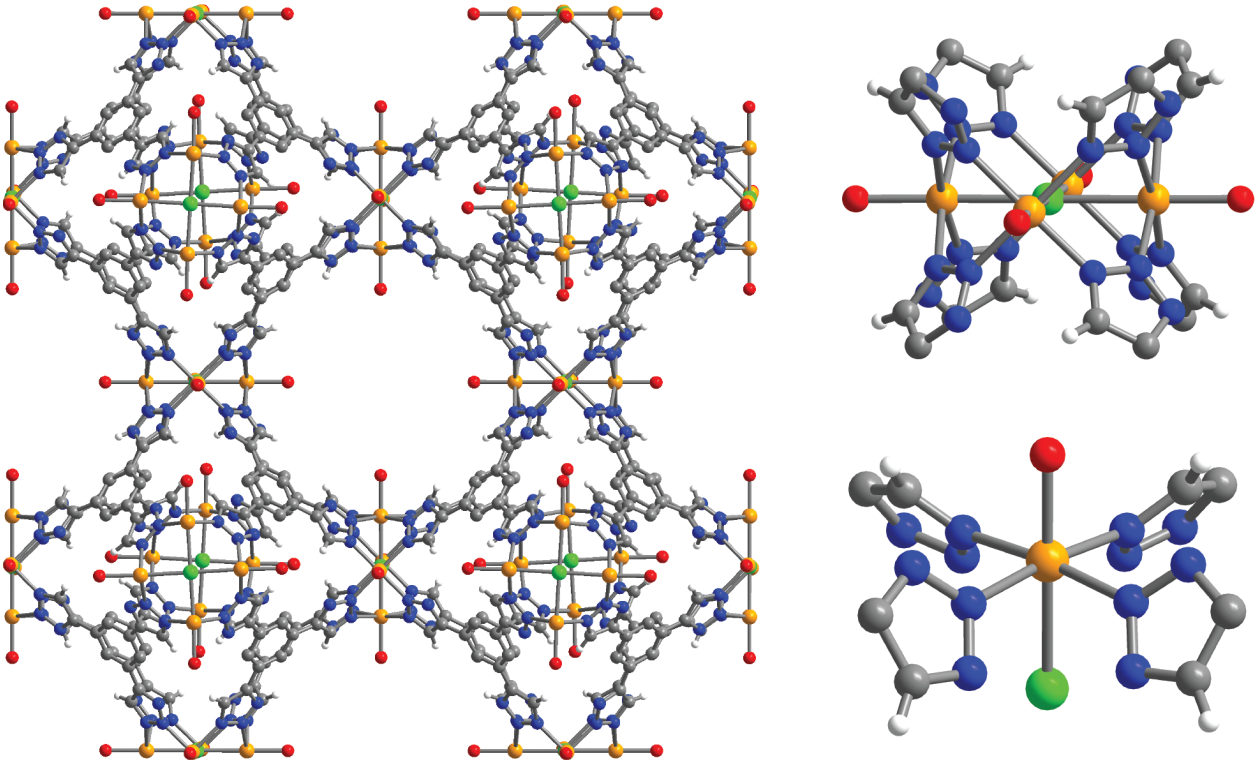

Figure 4.1. Structure of Fe-BTTri. A portion of the structure of DMF-solvated Fe-BTTri (left) as determined by analysis of single-crystal X-ray diffraction data. Structures of $[Fe_4Cl]^{7+}$ (upper right) and a single iron site (lower right) of DMF-solvated Fe-BTTri. Orange, grey, blue, red, green, and white spheres represent Fe, C, N, O, Cl, and H atoms, respectively; some H atoms and C and N atoms on iron-bound DMF molecules are omitted for clarity.

Cubic single crystals suitable for X-ray diffraction can be grown under similar conditions using more dilute iron and ligand concentrations and more acidic conditions. The DMF solvated form of

a Fe-BTTri crystal displays $Fm\bar{3}c$ symmetry, composed of six square, chloride-centered $[Fe_4Cl]^{7+}$ units and eight trigonal $BTTri^{3-}$ ligands that combine to form truncated octahedra, creating a sodalite-like cage (Figure 4.1). Numerous frameworks of this type, commonly referred to as M-BTT (M = Mn, Fe, Co, Ni, Cu, Cd), have been realized using the analogous tetrazolate ligand 1,3,5-benzenetristetrazolate (BTT^{3-}).[24] Interestingly, the less symmetric triazolate groups are well ordered within Fe-BTTri, with the H atoms of each triazolate unit oriented in the same direction around a crystallographic four-fold rotation axis on which the $[Fe_4Cl]^{7+}$ unit resides. This ordering is likely a result of the framework connectivity disfavoring steric repulsion between H atoms on adjacent triazolates. The resulting arrangement creates a slight twist of the triazoles around the $[Fe_4Cl]^{7+}$ unit, which is not observed in M-BTT structures, and causes opposite squares on each truncated octahedron to be offset by approximately 6°. The location of the charge balancing extra-framework Fe^{II} cations within the pores of the framework could not be determined from the electron difference map obtained from the X-ray diffraction data. Structural characterization of the activated material could not be achieved under standard single crystal experimental conditions, as ambient solvent rapidly binds to the open iron sites prior to data collection. However, the single crystals retain their crystallinity upon heating to 150 °C, indicating that the material is thermally stable.

4.3.2. Gas adsorption. The compound Fe-BTTri was investigated for selected gas adsorption properties. In particular, adsorption isotherms for CO were collected at various temperatures. As shown in Figure 4.2, the CO adsorption isotherm at 25 °C shows an extremely steep initial rise, reaching a value of 1.49 mmol/g adsorbed at just 102 μbar. The sharp initial uptake ends at 2.2 mmol/g at 157 μbar, and subsequent uptake more gradually increases to 2.7 mmol/g at 268 mbar, corresponding to a maximum total adsorption of CO at 75% of the iron sites (excluding extra-framework Fe^{II} cations). The steep rise in the isotherm suggests an initial strong interaction with CO for some of the iron sites, whereas the gradual rise afterwards represents weak interactions with the framework. The remaining iron sites are likely blocked by solvent or remain inaccessible, as has been observed previously for Fe-BTT.[24c] This sharp uptake of CO adsorption is also seen at higher temperatures, with significant adsorption of CO still observable at 100 °C, reaching 1.08 mmol/g at 1.06 mbar.

The adsorption of CO at different temperatures was examined to evaluate the strength of its binding within the framework. Isotherms collected from 25 to 150 °C all displayed significant low-pressure adsorption relative to other CO adsorbing materials (Figure 4.2). By fitting isotherms collected from 65 °C to 100 °C with a Langmuir-Freundlich equation and employing the Clausius-Clapeyron relation, an isosteric heat of adsorption (Q_{st}) of –65 kJ/mol can be calculated (Figure S7). This value is greater in magnitude than those previously reported for metal–organic frameworks examined for CO adsorption, which have isosteric heats of adsorption ranging from –19 to –52 kJ/mol.[10] The isosteric heat of adsorption, combined with a high capacity for CO at low pressures, suggests that Fe-BTTri is a promising candidate for extracting and removing very low concentrations of CO from gas mixtures. Indeed, its CO adsorption capacity of 0.75 mmol/g at just 0.05 mbar is unprecedented for these materials, representing a two orders of magnitude improvement relative to the previous best material, Ni_2(dobdc) ($dobdc^{4-}$ = 2,5-dioxido-1,4-benzene-dicarboxylate) (Figure 4.S8).[10d] It should be noted, however, that the adsorption capacity of Fe-BTTri at pressures greater than 268 mbar is lower than that of Ni_2(dobdc) and several related materials because of its lower concentration of accessible open metal sites.[10d]

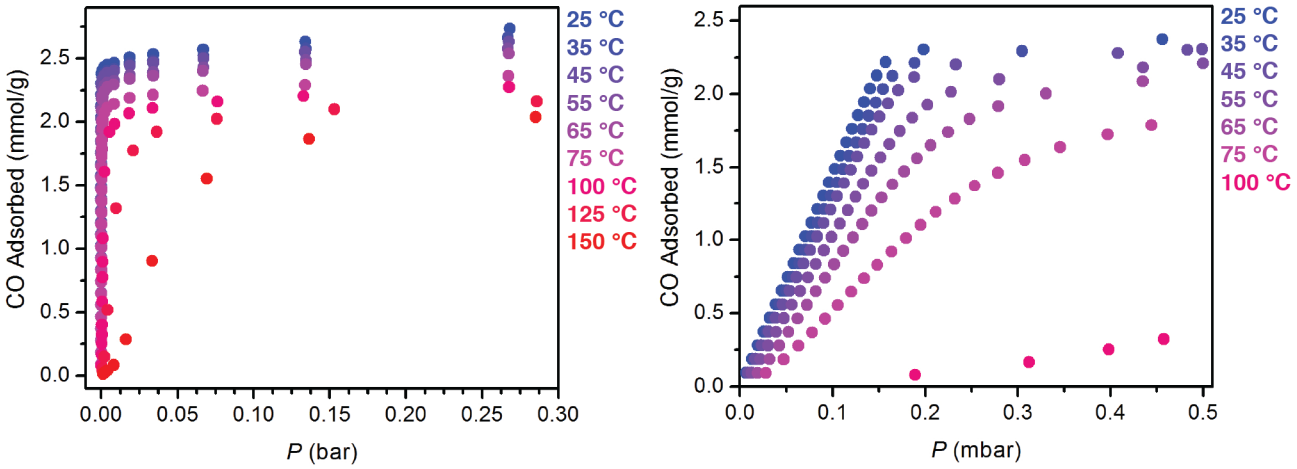

Figure 4.2. Carbon monoxide adsorption in Fe-BTTri. Excess carbon monoxide isotherms measured at various temperatures in Fe-BTTri (left). Detail of low-pressure region (right).

Remarkably, despite the strong binding of CO, ready desorption of the adsorbed CO can be accomplished by heating CO-dosed Fe-BTTri under dynamic vacuum at 150 °C for as little as 5 min. No loss in CO capacity is observed even after 10 cycles (Figure 4.3). At lower temperatures, full reactivation can be achieved by using slightly longer activation times (*e.g.*, 30 min at 100 °C) (Figure 4.S9). Thus, Fe-BTTri offers the possibility of serving as a readily regenerable scavenger for removing CO from gas mixtures.

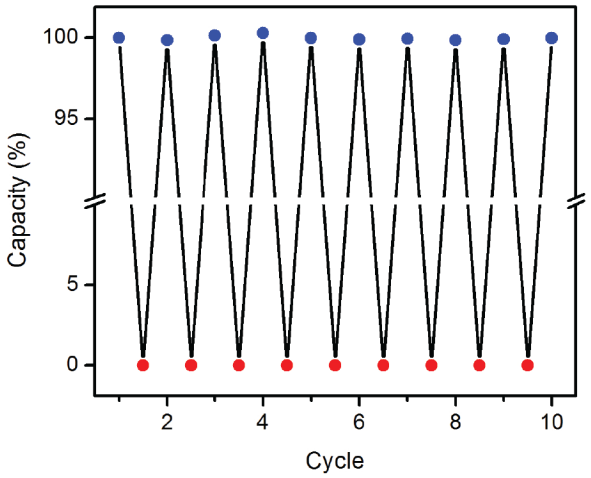

Figure 4.3. Carbon monoxide adsorption reversibility in Fe-BTTri. Cycling data of successive adsorption and desorption of carbon monoxide in Fe-BTTri, with adsorption expressed in terms of percentage of the capacity observed for cycle 1. Adsorption (blue circles) occurred within 10 min upon dosing CO at 25 °C at 10 mbar, and complete desorption (red circles) was accomplished by heating the sample at 150 °C under dynamic vacuum for 5 min.

To assess the ability of Fe-BTTri to separate CO from mixed CO/H_2 gas streams for the purification of hydrogen, H_2 adsorption isotherms were also collected. At 25 °C, only a very minor uptake of H_2 is observed, with the isotherm rising gradually to reach a value of 0.05 mmol/g at 1.0 bar (Figure 4.4). Indeed, at all of the pressures evaluated, Fe-BTTri was found to adsorb significantly more CO than H_2, suggesting its application in the selective adsorption of CO during hydrogen purification.

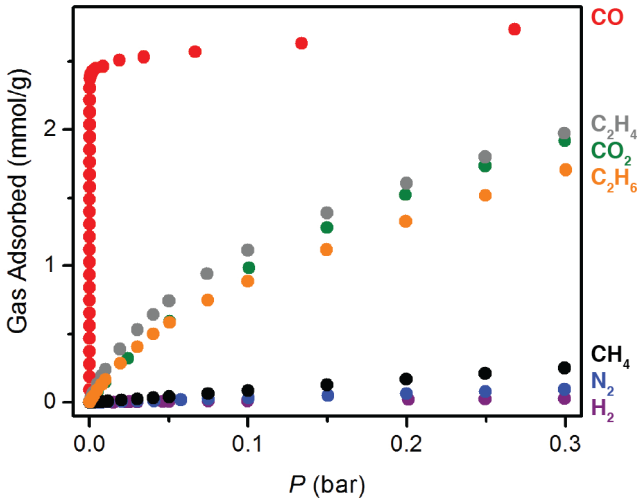

Figure 4.4. Gas adsorption isotherms of several gases in Fe-BTTri. Excess gas adsorption isotherms for CO, C_2H_4, CO_2, C_2H_6, CH_4, N_2, and H_2 collected at 25 °C for Fe-BTTri.

In order to evaluate the separation capabilities, Ideal Adsorbed Solution Theory (IAST) was used to calculate selectivity factors for a hypothetical mixed gas stream containing a variety of different gas compositions at a total pressure of 1 bar at 25 °C.[15] For all calculated CO/H_2 mixtures, Fe-BTTri shows very high IAST selectivity values. At low concentrations of CO in a mixture with H_2 (5% CO at a total pressure of 1 bar), IAST predicts a selectivity of 7400 for CO over H_2, over 40% higher than the value calculated for Ni_2(dobdc), and among the best values for any mixed gas separation with a metal–organic framework (Figure 4.5).[10d] CO concentrations in H_2 streams can be as low as 1-3%, and at these concentrations for 1 bar total pressure, IAST predicts even higher selectivities of 10900 at 3% CO and 24800 at 1% CO. Importantly, the strong upward trend towards lower concentrations of CO suggests Fe-BTTri is a very promising CO scrubbing material. For fuel cell technologies and other applications sensitive to even ppm levels of CO, one can envision performing these separations at higher pressures or different temperatures to achieve nearly complete CO removal. It should be noted that these values are particularly sensitive to the accuracy of the H_2 isotherm fit, and fitting the isotherm with different saturation capacities changes these selectivity values slightly (Figure 4.S11). However, these IAST values remain significantly higher than all previously reported CO adsorbing materials for several different isotherm fits for H_2.

The purity of the adsorbed phase in these separations was also examined, as the adsorbed CO can also be used as a feedstock in a variety of industrial processes. The IAST values for CO/H_2 mixtures suggest that Fe-BTTri could be used to obtain very pure CO, with purities ranging from 99.6% at the very lowest concentration of CO (1% CO in a CO/H_2 mixture at 1 bar total pressure), to 99.99% at higher CO concentrations. In examining the ability of Fe-BTTri to separate CO from other gas streams, such as mixtures with N_2, CO_2, CH_4, C_2H_6, and C_2H_4, additional adsorption

isotherms were measured (Figure 4.4). For CH_4 and N_2 at 25 °C, the isotherms rise gradually to 0.69 and 0.26 mmol/g at 1.0 bar, respectively. For all pressures measured Fe-BTTri adsorbs significantly more CO, leading to high calculated IAST selectivities. For mixtures with N_2, these values are as high as 1750 for a 1 bar mixture containing 0.05 mol fraction of CO (Figure 4.5), corresponding to 98.9% pure CO in the adsorbed phase at room temperature. Importantly, this is much more practical than the very low temperature (120 K) required for other frameworks that exhibit this selectivity.[10c] Notably, this IAST value is also over 200% higher than that calculated for Ni_2(dobdc), which also exhibits the ability to separate CO and N_2 at room temperature.[10d] Selectivities are similarly high for mixtures with CH_4, with IAST values approaching as high as 650 for a 0.05 mol fraction of CO in a 1 bar total CO/CH_4 mixture, corresponding to 97.1% adsorbed CO. Both CO/N_2 and CO/CH_4 selectivities in Fe-BTTri approach 99.9% CO on the adsorbed phase at higher concentrations of CO in hypothetical CO/N_2 and CO/CH_4 mixtures, indicating the significant promise of this material for collecting pure CO from gas streams.

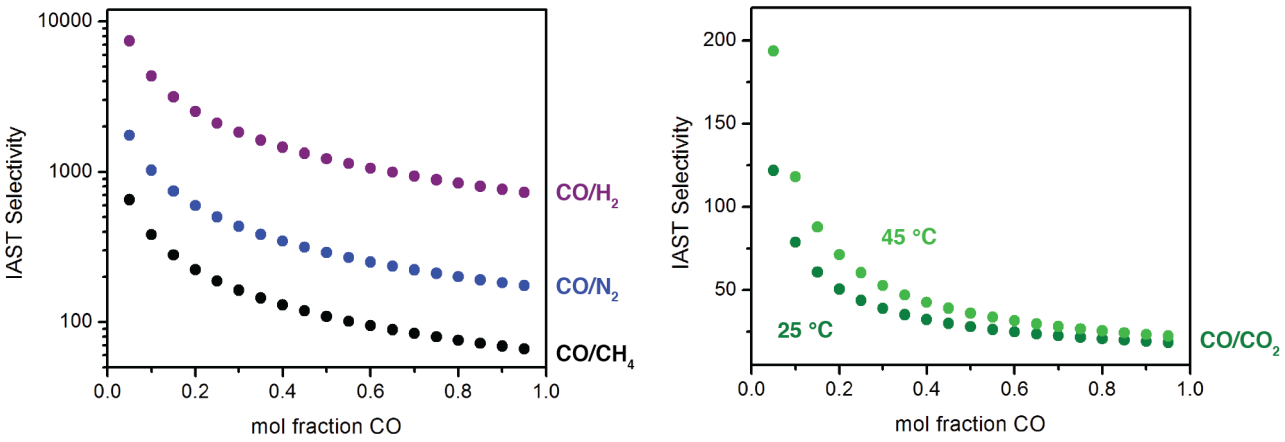

Figure 4.5. Selectivity for CO adsorption in Fe-BTTri. Ideal adsorbed solution theory (IAST) selectivities for mixtures of CO/H_2 (purple), CO/N_2 (blue) and CO/CH_4 (black) at varying concentrations at 25 °C and 1 bar of total pressure in Fe-BTTri (upper). IAST selectivites for mixtures of CO/CO_2 at varying concentrations and 1 bar total pressure at 25 °C (dark green) and 45 °C (light green) (lower).

For CO_2, C_2H_6, and C_2H_4, the 25 °C isotherms rise gradually to 3.52, 3.83, and 3.64 mmol/g at 1.0 bar, respectively (Figure 4.4). While the uptake is significant, the low-pressure (<300 mbar) uptake is much more gradual than that observed for CO adsorption, suggesting that useful selectivities can be achieved. Indeed, for Fe-BTTri, an IAST selectivity of 121 is calculated for a 0.05 mol fraction of CO in a 1 bar mixture with CO_2 at 25 °C (Figure 5). In addition, because of the strong binding of CO relative to CO_2, raising the temperature from 25 to 45 °C increases the IAST selectivity significantly, going from 121 to 193 for a 5:95 CO:CO_2 mixture at 1 bar total pressure. This temperature dependence of the IAST selectivity is also observed in CO/C_2H_4 and CO/C_2H_6 mixtures, with calculated selectivity values similar to those observed for CO/CO_2 separations (Figures 4.S13 and 4.S15). Importantly, these values still translate to very pure CO in the adsorbed phase, as 50% CO in mixtures of CO/C_2H_6, CO/CO_2, and CO/C_2H_4 at 25 °C at 1 bar total pressure are expected to result in 93.2-96.5% CO in the adsorbed phase, respectively, and increase upon raising the temperature, reaching 95.9-98.1% at 45 °C under the same conditions.

Indeed, Fe-BTTri shows the ability to separate CO from a variety of different gas mixtures, even in mixtures with ethylene and CO_2 that are very competitive in other metal–organic frameworks, and retains high purity CO in the adsorbed phase.

4.3.3. Infrared Spectroscopy. To understand the origin of the strong CO selectivity observed in Fe-BTTri, various spectroscopic methods were employed to probe the state of both the framework iron sites and the bound CO molecules. Infrared spectroscopy was used as an initial probe for the nature of the iron–carbonyl interaction. After exposure to 0.05 bar of CO, a sharp absorbance band at 2017 cm^{-1} arises (Figure 4.6). This C–O stretching frequency is red-shifted relative to free CO (2143 cm^{-1}), indicating π back-donation into the π* orbital of the carbonyl.

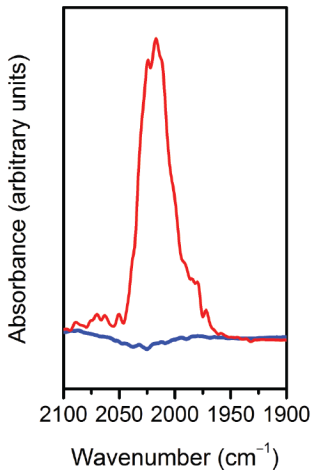

Figure 4.6. Infrared spectra for activated and CO-dosed Fe-BTTri. Infrared spectra collected at 25 °C for Fe-BTTri (blue) and CO-dosed Fe-BTTri (red).

To date, a red-shift in the carbonyl stretching frequency has only been observed for metal–organic frameworks that irreversibly bind CO.[11] Indeed, all metal–organic frameworks that have been characterized so far for reversible CO adsorption display blue-shifted stretching frequencies, with values ranging from 2160 to 2190 cm^{-1}, indicating a weak interaction with a high-spin metal center acting predominantly as a Lewis acid.[10b-d,25] In distinct contrast, the value observed for CO-dosed Fe-BTTri is more consistent with several known low-spin molecular Fe^{II} species in similar ligand environments, such as those observed in various CO-bound Fe^{II} porphyrins or other nitrogen-containing square-planar tetradentate ligands.[26] This indicates that upon binding CO the Fe^{II} sites of Fe-BTTri are low-spin, which to date has not been seen in a metal–organic framework with reversible CO adsorption.

4.3.4. Spin State Characterization. Since the CO stretching frequency suggested a conversion from high-spin to low-spin Fe^{II} upon adsorption of CO, Mössbauer spectroscopy and dc magnetic susceptibility were utilized to probe directly the metal spin states in the activated Fe-BTTri and the CO-dosed framework. For the activated material, the Mössbauer spectrum at 100 K (Figure 4.7) reveals several high-spin Fe^{II} species, with isomer shifts, δ, between 1.05 and 1.07 mm/s and quadrupole splitting values, ΔE_Q, between 1.80 and 3.06 mm/s. The existence of several slightly different iron sites is attributed to the distribution of residual solvent and extra-framework cations throughout the framework, which, as observed previously in related frameworks, can subtlely alter the environment of the Fe^{II} sites.[15c] While solvation with DMF did not increase the resolution for determination of distinct iron sites (Figure 4.S17), both the activated and DMF-solvated Fe-BTTri profiles are readily fit using standard high-spin parameters, thus confirming the high-spin ground

state for the Fe^{II} centers within the activated framework.[13c,d,24c,27] Upon increasing the temperature from 100 to 290 K, the isomer shifts and quadrupole splittings decrease as expected for high-spin Fe^{II} (Figure 4.S18).

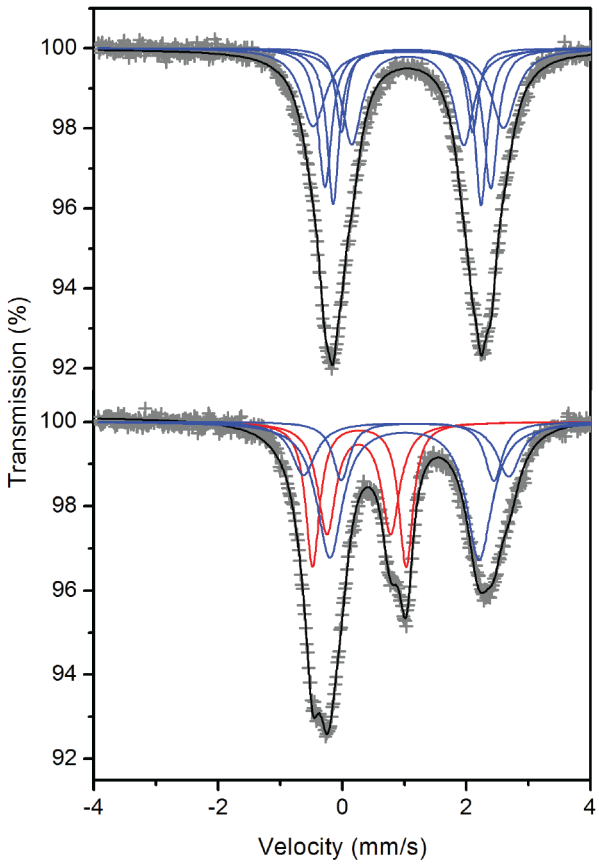

Figure 4.7. Mössbauer spectra of activated and CO-dosed Fe-BTTri. Mössbauer spectra collected at 100 K for Fe-BTTri (upper) and CO-dosed Fe-BTTri (lower), with the experimental data in grey plusses and the total fit in black. In both spectra, the blue components are assigned to high-spin Fe^{II}. In CO-dosed Fe-BTTri, the red components are assigned to low-spin Fe^{II}. The parameters for all components are listed in Table 4.S6.

Activated Fe-BTTri was then dosed *ex situ* with 0.1 mbar of CO, and the 100 K Mössbauer spectrum exhibits a significantly different profile (Figure 4.7). Again, multiple different Fe^{II} components are required to reproduce the observed profile, however both high-spin and low-spin Fe^{II} species are observed. Here, high-spin Fe^{II} components, shown in blue, represent 58(3)% of the total absorption area and exhibit high-spin Fe^{II} with δ between 1.00 and 1.21 mm/s and ΔE_Q between 2.42 and 3.31 mm/s. These components are assigned to five-coordinate framework Fe^{II} sites and the extra-framework cations, which are not involved in CO binding. In contrast, a new set of doublets shown in red, representing 42(4)% of the total absorption area, exhibit significantly different hyperfine parameters, with both smaller δ of 0.26 and 0.27 mm/s and ΔE_Q between 1.03 and 1.50 mm/s. These hyperfine parameters are consistent with low-spin Fe^{II},[13c,d,27] strongly suggesting that upon binding CO the electron configuration of the Fe^{II} ions change from high-spin to low-spin. Remarkably, the total conversion to low-spin closely matches the uptake observed in the CO isotherm data at 0.1 mbar. Upon increasing the temperature from 100 to 290 K, the usual

decrease in isomer shifts and quadrupole splittings is observed, but the percent area of the low-spin CO-bound Fe^{II} of 46(4) % remains constant within the accuracy of the measurements (Figure 4.S19).

Magnetic measurements were also used to probe the spin state of the iron ions in Fe-BTTri. Dc magnetic susceptibility measurements performed under an applied magnetic field of 1 T were conducted for activated Fe-BTTri as well as samples dosed with various amounts of CO (Figure 4.8). For activated Fe-BTTri, the 300 K $\chi_M T$ value is expected to be 81 emu·K/mol for all high–spin Fe^{II} centers with $S = 2$ and $g = 2.00$. The observed $\chi_M T$ value at 300 K is 82.9 emu·K/mol, in good agreement with the calculated spin-only value. In order to confirm the high-spin nature of these iron sites in the bare framework, the data between 2 and 300 K was fit using the Hamiltonian shown in eq 4.4, which includes two isotropic coupling parameters and zero-field splitting and Zeeman terms.

$$\hat{H} = -2J\left(\hat{S_1}\cdot\hat{S_2} + \hat{S_2}\cdot\hat{S_3} + \hat{S_3}\cdot\hat{S_4} + \hat{S_1}\cdot\hat{S_4}\right) - 2J'\left(\hat{S_1}\cdot\hat{S_3} + \hat{S_2}\cdot\hat{S_4}\right) + \sum_{i=1}^{4}\{D_i S_{iz}^2 + E_i(S_{ix}^2 + S_{iy}^2) + \mu_B g_i \hat{S}_i \cdot \hat{B}\} \quad (4.4)$$

Magnetic coupling between nearest-neighbor Fe^{II} ions is represented by J, while the coupling between Fe^{II} sites located 180º from one another (*i.e.*, coupling across the μ_4-Cl) is represented by J'. The Hamiltonian provided a good fit to the magnetic data in the temperature range 2-300 K using the parameters $|D_i| = 27$ cm^{-1}, $|E_i| = 0.01$ cm^{-1}, and $g_i = 2.40$, all for $i = 1$-4, and coupling constants of $J = -5.8$ cm^{-1} and $J' = -5.8$ cm^{-1}. High-spin square pyramidal Fe^{II} systems have been predicted to exhibit significant magnetic anisotropy,[28] and similar $|D|$ values and g values greater than 2 have been observed for a number of high-spin square planar Fe^{II} complexes.[29] Although the coupling constants J and J' were expected to be different, coincidentally these values were found to be equivalent in the best fit of the data. This behavior has been seen in a similar molecular, pyrazolate bridged $Co^{II}{}_4(\mu_4\text{-Cl})$ square.[30] The magnetic analysis confirms that the Fe^{II} sites in Fe-BTTri can reasonably be classified as high-spin Fe^{II}.

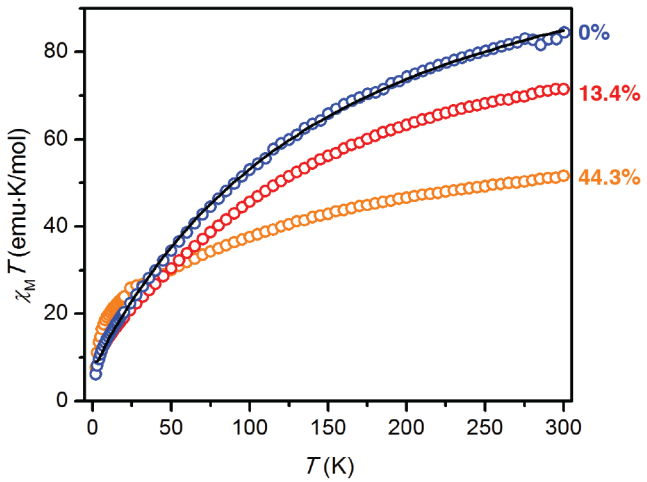

Figure 4.8. Magnetic susceptibility of activated and CO-dosed Fe-BTTri. Variable-temperature magnetic susceptibility times temperature data collected under $H_{dc} = 1$ T for Fe-BTTri (blue), Fe-BTTri–$(CO)_{3.2}$ (13.4% CO-loaded, red), and Fe-BTTri–$(CO)_{10.6}$ (44.3% CO-loaded, orange). The

black line represents a fit to the data employing a Hamiltonian and the parameters described in the text.

Samples of Fe-BTTri loaded *ex situ* with CO were also investigated using magnetic susceptibility measurements. Materials with precisely-dosed loadings of 13.4% and 44.3% of carbon monoxide per framework iron site were prepared using a gas adsorption analyzer. These materials, Fe-BTTri–$(CO)_{3.2}$ and Fe-BTTri–$(CO)_{10.6}$, respectively, exhibit decreased $\chi_M T$ values at 300 K compared to activated Fe-BTTri. The predicted $\chi_M T$ values for these loadings, assuming a spin state transition from $S = 2$ (high-spin) to $S = 0$ (low-spin) upon binding of CO to Fe^{II}, are 71.4 and 50.8 emu·K/mol for 13.4% and 44.3% CO loading, respectively. The observed values of 71.5 and 51.6 emu·K/mol are in good agreement with these predictions. Overall, both Mössbauer spectral and dc magnetic susceptibility measurements completely agree with the conversion of high-spin Fe^{II} to low-spin Fe^{II} upon CO binding.

4.3.5. Structural Characterization. Single-crystal X-ray diffraction data were collected for the DMF-solvated and CO-dosed forms of the Fe-BTTri. Owing to the conditions needed to collect and mount the crystals, a structure of the activated material could not be obtained, as ambient solvent was taken up at the vacant metal site prior to data collection. However, due to the high-spin nature of both the bare and DMF-solvated material, the structure of the activated material is likely similar to that of the DMF-solvated material, and comparisons to the CO-dosed structure can be made.

Ligated by DMF, the bond lengths associated with the metal centers are consistent with a high-spin Fe^{II} species. The Fe–O_{DMF} and the average Fe–N distances are 2.116(2) and 2.1424(14) Å, respectively, indicative of high-spin Fe^{II}.[31] These values are expected to be similar for activated Fe-BTTri, and are consistent with other high-spin Fe^{II} centers in metal–organic frameworks.[12a-i,24c]

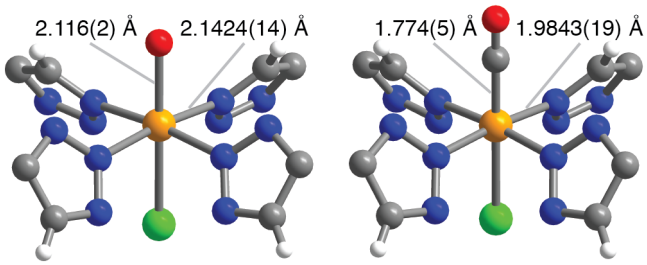

Figure 4.9. Structures of DMF-solvated and activated Fe-BTTri. A portion of the structure of DMF-solvated Fe-BTTri (left) and CO-dosed Fe-BTTri–$(CO)_{24}$ (right), as determined by analysis of single-crystal X-ray diffraction data, with selected bond lengths highlighted. Numbers in parentheses give the estimated standard deviation in the final digits of the number. Orange, grey, red, blue, green, and white spheres represent Fe, C, O, N, Cl, and H atoms, respectively.

Upon *ex situ* dosing with CO, a significant structural change was observed (Figure 4.9). In Fe-BTTri–$(CO)_{24}$, the distances between the iron centers and the triazolate ligands contract to an average Fe–N distance of 1.9843(19) Å, a value that is consistent with low-spin Fe^{II}.[12a-i,13] In addition, the observed Fe–C_{CO} distance of 1.774(5) Å is very similar to reported literature values of octahedral low-spin Fe^{II}–CO complexes, such as the porphyrin complex Fe(TPP)CO(Py) (TPP = 5,10,15,20-tetraphenylporphyrin dianion, Py = pyridine), which exhibits a bond length of 1.77(2) Å, as well as other low-spin Fe^{II}-CO species.[31] Finally, the Fe–C–O linkage is essentially linear

with an angle of 179.7(4)°, indicating a large degree of π orbital overlap. This is in contrast to structurally characterized high-spin (S = 2) Fe^{II}–CO adducts, which display non-linear Fe–C–O linkages.[10d] These structural data, together with the infrared, Mössbauer, and magnetic results, confirm beyond any doubt that upon binding CO, the Fe^{II} centers undergo a conversion from high- to low-spin, which to our knowledge has not previously been observed within a porous material.

4.4. Conclusions and outlook

The foregoing results demonstrate that Fe-BTTri engages in an unprecedented spin state change mechanism for the highly selective yet reversible binding of CO over H_2, N_2, CO_2, and various hydrocarbons. Indeed, IAST selectivity factors for these separations are among the highest values reported for any adsorbent-based gas separation, indicating the promise of this material for scavenging CO from various industrially relevant gas mixtures. Importantly, by leveraging the π-acidity of CO, Fe-BTTri is able to show preferential binding of CO over CO_2, ethylene, and other highly-polarizable gas molecules that typically interact with Lewis-acidic open metal sites, as present in current metal–organic frameworks. The possibility of extending this spin-change mechanism to related frameworks and other gas molecules that might also have a strong interaction with low-spin Fe^{II}, such as olefins in olefin/paraffin separations, O_2 in O_2/N_2 separations, and N_2 in N_2/CH_4 separations, is now being investigated. Finally, since exposure to just trace amounts of CO induces changes in the structural, electronic, and spectral properties of Fe-BTTri, chemical identification and sensing are also promising avenues of exploration for this new type of material.

4.5. Acknowledgements

This research was supported through the Center for Gas Separations Relevant to Clean Energy Technologies, an Energy Frontier Research Center funded by the U.S. Department of Energy, Office of Science, Office of Basic Energy Sciences under Award DE-SC0001015. Single-crystal X-ray diffraction experiments were performed at Beamline 11.3.1 at the Advanced Light Source, a DoE Office of Science User Facility operated by Lawrence Berkeley National Laboratory under contract no. DE-AC02-05CH11231. Powder X-ray diffraction data were collected at Beamline 17-BM at the APS, a DoE Office of Science User Facility, operated by Argonne National Laboratory under Contract DE-AC02-06CH11357. The National Science Foundation provided graduate fellowship support.

4.6. References and supplementary information

(1) (a) Yaghi, O. M.; Li, H.; Eddaoudi, M.; O'Keefe, M. *Nature* **1999**, *402*, 276−279. (b) Kitagawa, S.; Kitaura, R.; Noro, S.-I. *Angew. Chem., Int. Ed*. **2004**, *43*, 2334−2375. (c) Matsuda, R.; Kitaura, R.; Kitagawa, S.; Kubota, Y.; Belosludov, R. V.; Kobayashi, T. C.; Sakamoto, H.; Chiba, T.; Takata, M.; Kawazoe, Y.; Mita, Y. *Nature* **2005**, *436*, 238− 241. (d) Millward, A. R.; Yaghi, O. M. *J. Am. Chem. Soc*. **2005**, *127*, 17998−17999. (e) Ferey, G. *Chem. Soc. Rev*. **2008**, 37, 191−214. (f) Morris, R. E.; Wheatley, P. S. *Angew. Chem., Int. Ed*. **2008**, *47*, 4966−4981. (g) Czaja, A. U.; Trukhan, N.; Müller, U. *Chem. Soc. Rev*. **2009**, *38*, 1284−1293. (h) Chen, B.; Xiang, S.; Qian, G. *Acc. Chem. Res*. **2010**, *43*, 1115–1124. (i) Zhou, H.-C.; Long, J. R.; Yaghi, O. M. *Chem. Rev*. **2012**, *112*, 673−674. (j) Li, J.-R.; Sculley, J.; Zhou, H.-C. *Chem. Rev*. **2012**, *112*, 869−932. (k) Schneeman, A.; Henke,

S.; Schwedler, I.; Fischer, R. A. *ChemPhysChem* **2014**, *15*, 823–839. (l) Evans, J. D.; Sumby, C. J.; Doonan, C. J. *Chem. Soc. Rev*. **2014**, *43*, 5933−5951.

(2) (a) Caskey, S. R.; Wong-Foy, A. G.; Matzger, A. J. *J. Am. Chem. Soc*. **2008**, *130*, 10870−10871. (b) Dincă, M.; Long, J. R. *Angew. Chem., Int. Ed.* **2008**, *47*, 6766–6779. (c) Dietzel, P. D. C.; Besikiotis, V.; Blom, R. *J. Mater. Chem*. **2009**, *19*, 7362−7370. (d) Herm, Z. R.; Swisher, J. A.; Smit, B.; Krishna, R.; Long, J. R. *J. Am. Chem. Soc*. **2011**, *133*, 5664−5667. (e) Mason, J. A.; Sumida, K.; Herm, Z. R.; Krishna, R.; Long, J. R. *Energy Environ. Sci*. **2011**, *4*, 3030−3040. (f) Bloch, E. D.; Murray, L. M.; Queen, W. L.; Chavan, S.; Maximoff, S. N.; Bigi, J. P.; Krishna, R.; Peterson, V. K.; Grandjean, F.; Long, G. J.; Smit, B.; Bordiga, S.; Brown, C. M.; Long, J. R. *J. Am. Chem. Soc.* **2011**, *133*, 14814–14822. (g) Bloch, E. D.; Queen, W. L.; Krishna, R.; Zadrozny, J. M.; Brown, C. M.; Long, J. R. *Science* **2012**, *335*, 1606−1610. (h) Geier, S. J.; Mason, J. A.; Bloch, E. D.; Queen, W. L.; Hudson, M. R.; Brown, C. M.; Long, J. R. *Chem. Sci*. **2013**, *4*, 2054−2061. (i) Sumida, K.; Rogow, D. R.; Mason, J. A.; McDonald, T. M.; Bloch, E. D.; Herm, Z. R.; Bae, T.-H.; Long, J. R. *Chem. Rev*. **2012**, *112*, 724−781. (j) Herm, Z. R.; Krishna, R.; Long, J. R. *Microporous Mesoporous. Mater.* **2012**, *151*, 481–487. (k) Peng, Y.; Krungleviciute, V.; Eryazici, I.; Hupp, J. T.; Farha, O. K.; Yildirim, T. *J. Am. Chem. Soc*. **2013**, *135*, 11887−11894. (l) Mason, J. A.; Veenstra, M.; Long, J. R. *Chem. Sci*. **2014**, *5*, 32−51. (m) Herm, Z. R.; Bloch, E. D.; Long, J. R. *Chem. Mater*. **2014**, *26*, 323−338. (n) Duan, X.; He, Y.; Cui, Y.; Yang, Y.; Krishna, R.; Chen, B.; Qian, G. *RSC Adv.* **2014**, *4*, 23058–23063.

(3) Lee, K.; Isley, W. C., III; Dzubak, A. L.; Verma, P.; Stoneburner, S. J.; Lin, L.–C.; Howe, J. D.; Bloch, E. D.; Reed, D. A.; Hudson, M. R.; Brown, C. M.; Long, J. R.; Neaton, J. B.; Smit, B.; Cramer, C. J.; Truhlar, D. G.; Gagliardi, L. *J. Am. Chem. Soc*. **2014**, *136*, 698–704.

(4) (a) Colombo, V.; Galli, S.; Choi, H. J.; Han, G. D.; Maspero, A.; Palmisano, G.; Masciocchi, N.; Long, J. R. *Chem. Sci.* **2011**, *2*, 1311–1319. (b) Anderson, J. S.; Gallagher, A. T.; Mason, J. A.; Harris, T. D. *J. Am. Chem. Soc.* **2014**, *136*, 16489–16492.

(5) (a) Baschuk, J. J.; Li, X. *Int. J. Energy Res.* **2001**, *25*, 696–713. (b) Cheng, X.; Shi, Z.; Glass, N.; Zhang, L.; Zhang, J.; Song, D.; Liu, Z.-S.; Wang, H.; Shen, J. *J. Power Sources*. **2007**, *165*, 739–756. (c) Hooper, C. W. *Catalytic Ammonia Synthesis: Fundamentals and Practice*; Jennings, J. R., Ed.; Springer: New York, NY, 1991.

(6) (a) Dutta, N. N.; Patil, G. S. *Gas Sep. Purif.* **1995**, *9*, 277–283. (b) Kerry, F. G. *Industrial Gas Handbook: Gas Separation and Purification*; CRC: Boca Raton, FL, 2007.

(7) (a) McCandless, F. P. *Ind. Eng. Chem. Process Des. Dev*. **1972**, *11*, 470−478. (b) DiMartino, S. P.; Glazer, J. L.; Houston, C. D.; Schott, M. E. *Gas Sep. Purif.* **1988**, *2*, 120–125.

(8) (a) Tamon, H.; Kitamura, K.; Okazaki, M. *AIChE J*. **1996**, *42*, 422. (b) Golden, T. C.; Guro, D. E.; Kratz, W. C.; Sabram, T. E. *Fundamentals of Adsorption*; Meunier, F., Ed.; Elsevier: Amsterdam, The Netherlands, 1998. (c) Miyajima, H.; Kodama, A.; Goto, M.; Hirose, T. *Adsorption* **2005**, *11*, 625−630.

(9) (a) Kohl, A. L.; Reisenfeld, F. C. *Gas Purification*, 3rd ed.; Gulf Publishing: Houston, TX, 1979. (b) Haase, D. J.; Walker, D. G. *Chem Eng. Prog*. **1974**, *70*, 74.

(10) (a) Manusamy, K.; Sethia, G.; Patil, D. V.; Somayajulu Rallapalli, P. B.; Somani, R. S.; Bajaj, H. C. *Chem. Eng. J.* **2012**, *195*, 359–368. (b) Chavan, S.; Vitillo, J. G.; Groppo, E.; Bonino, F.; Lamberti, C.; Dietzel, P. D. C.; Bordiga, S. *J. Phys. Chem. C* **2009**, *113*, 3292–3299. (c) Sato, H.; Kosaka, W.; Matsuda, R.; Hori, A.; Hijikata, Y.; Belosludov, R. V.;

Sakaki, S.; Takata, M.; Kitagawa, S. *Science* **2014**, *343*, 167–170. (d) Bloch, E. D.; Hudson, M. R.; Mason, J. A.; Chavan, S.; Crocella, V.; Howe, J. D.; Lee, K.; Dzubak, A. L.; Queen, W. L.; Zadrozny, J. M.; Geier, S. J.; Lin, L.-C.; Gagliardi, L.; Smit, B.; Neaton, J. B.; Bordiga, S.; Brown, C. M.; Long, J. R. *J. Am. Chem. Soc.* **2014**, *136*, 10752–10761. (e) Peng, J.; Xian, S.; Xiao, J.; Huang, Y.; Xia, Q.; Wang, H.; Li, W. *Chem. Eng. J.* **2015**, *270*, 282–289.

(11) (a) Denysenko, D.; Grzywa, M.; Jelic, J.; Reuter, K.; Volkmer, D. *Angew. Chem., Int. Ed.* **2014**, *53*, 5832–5836. (b) Gonzalez, M. I.; Bloch, E. D.; Mason, J. A.; Teat, S. J.; Long, J. R. *Inorg. Chem.* **2015**, *54*, 2995–3005.

(12) (a) Halder, G. J.; Kepert, C. J.; Moubaraki, B.; Murray, K. S.; Cashion, J. D. *Science* **2002**, *298*, 1762–1765. (b) Bonhommeau, S.; Molnar, G.; Galet, A.; Zwick, A.; Real, J. A.; McGarvey, J. J.; Bousseksou, A. *Angew. Chem., Int. Ed.* **2005**, *44*, 4069–4073. (c) Quesada, M.; de la Pena-O'Shea, V. A.; Aromi, G.; Geremia, S.; Massera, C.; Roubeau, O.; Gamez, P.; Reedijk, J. *Adv. Mater.* **2007**, *19*, 1397–1402. (d) Neville, S. M.; Moubaraki, B.; Murray, K. S.; Kepert, C. J. *Angew. Chem., Int. Ed.* **2007**, *46*, 2059–2062. (e) Neville, S. M.; Halder, G. J.; Chapman, K. W.; Duriska, M. B.; Southon, P. D.; Cashion, J. D.; Letard, J. F.; Moubaraki, B.; Murray, K. S.; Kepert, C. J. *J. Am. Chem. Soc.* **2008**, *130*, 2869–2876. (f) Halder, G. J.; Chapman, K. W.; Neville, S. M.; Moubaraki, B.; Murray, K. S.; Letard, J.-F.; Kepert, C. J. *J. Am. Chem. Soc.* **2008**, *130*, 17552–17652. (g) Ohba, M.; Yoneda, K.; Agusti, G.; Munoz, M. C.; Gaspar, A. B.; Real, J. A.; Yamasaki, M.; Ando, H.; Nakao, Y.; Sakaki, S; Kitigawa, S. *Angew Chem., Int. Ed.* **2009**, *48*, 4767–4771. (h) Southon, P. D.; Liu, L.; Fellows, E. A.; Price, D. J.; Halder, G. J.; Chapman, K. W.; Moubaraki, B.; Murray, K. S.; Letard, J. F.; Kepert, C. J. *J. Am. Chem. Soc.* **2009**, *131*, 10998–11009. (i) Ohtani, R.; Yoneda, K.; Furukawa, S.; Horike, N.; Kitigawa, S.; Gaspar, A. B.; Munoz, M. C.; Real, J. A.; Ohba, M. *J. Am. Chem. Soc.* **2011**, *133*, 8600–8605. (j) Salles, F.; Maurin, G.; Serre, C.; Llewellyn, P. L.; Knofel, C.; Choi, H. J.; Filinichuk, Y.; Oliviero, L.; Vimont, A.; Long, J. R.; Ferey, G. *J. Am. Chem. Soc.* **2010**, *132*, 13782–13788.

(13) (a) Garcia, Y.; Niel, V.; Munoz, M. C.; Real, J. A. *Top. Curr. Chem.* **2004**, *233*, 229–257. (b) Van Koningsbruggen, P. J. *Top. Curr. Chem.* **2004**, *233*, 123–149. (c) Kitchen, J. A.; Brooker, S. *Coord. Chem. Rev.* **2008**, *252*, 2072–2092. (d) Kitchen, J. A.; White, N. G.; Jameson, G. N. L.; Tallon, J. L.; Brooker, S. *Inorg. Chem.* **2011**, *50*, 4586–5497. (e) Krober, J.; Audiere, J. P.; Claude, R.; Codjovi, E.; Kahn, O.; Haasnoot, J. G.; Groliere, F.; Jay, C.; Bousseksou, A.; Linares, J.; Varret, F.; Gonthier-Vassal, A. *Chem. Mater.* **1994**, *6*, 1404–1412. (f) Schneider, C. J.; Cashion, J. D.; Chilton, N. F.; Etrillard, C.; Fuentealba, M.; Howard, J. A. K.; Letard, J.-F.; Milsmann, C.; Moubaraki, B.; Sparkes, H. A.; Batten, S. R.; Murray, K. S. *Eur. J. Inorg. Chem.* **2013**, 850–864.

(14) Demessence, A.; D'Alessandro, D. M.; Foo, M. L.; Long, J. R. *J. Am. Chem. Soc.* **2009**, *131*, 8784–8786.

(15) Myers, A. L.; Prausnitz, J. M. *AIChE J.* **1965**, *11*, 121−127.

(16) (a) Krishna, R.; Calero, S.; Smit, B. *Chem. Eng. J.* **2002**, *88*, 81− 94. (b) Krishna, R.; van Baten, J. M. *Chem. Eng. J.* **2007**, *133*, 121. (c) Krishna, R.; van Baten, J. M. *Phys. Chem. Chem. Phys.* **2011**, *13*, 10593−10616.

(17) *SAINT and APEX 2 Software for CCD Diffractometers*, Bruker Analytical X-ray Systems Inc., Madison, WI, USA, 2014.

(18) Sheldrick, G. M. SADABS, Bruker Analytical X-ray Systems Inc., Madison, WI, USA, 2014.
(19) Sheldrick, G. M. SHELXT, University of Göttingen, Germany, 2015.
(20) Sheldrick, G. M. *Acta Crystallogr*., *A, Found. Crystallogr*. **2008**, *64*, 112–122.
(21) Sheldrick, G. M. SHELXL, University of Göttingen, Germany, 2014.
(22) Dolomanov, O. V.; Bourhis, L. J.; Gildea, R. J.; Howard, J. A. K.; Puschmann, H. *J. Appl. Cryst*. **2009**, *42*, 339–341.
(23) Chilton, N. F.; Anderson, R. P.; Turner, L. D.; Soncini, A.; Murray, K. S. *J. Chem. Comput.* **2013**, *34*, 1164.
(24) (a) Dincă, M.; Dailly, A.; Liu, Y.; Brown, C. M.; Neumann, D. A.; Long, J. R. *J. Am. Chem. Soc.* **2006**, *128*, 16876–16883. (b) Dincă, M.; Han, W. S.; Liu, Y.; Dailly, A.; Brown, C. M.; Long, J. R. *Angew. Chem. Int. Ed.* **2007**, *46*, 1419–1422. (c) Sumida, K.; Horike, S.; Kaye, S. S.; Herm, Z. R.; Queen, W. L.; Brown, C. M.; Grandjean, F.; Long, G. J.; Dailly, A.; Long, J. R. *Chem. Sci.* **2010**, *1*, 184–191. (d) Biswas, S.; Maes, M.; Dhakshinamoorthy, A.; Feyand, M.; De Vos, D. E.; Garcia, H.; Stock, N. *J. Mater. Chem.* **2012**, *22*, 10200–10209. (e) Liao, J. H.; Chen, W. T.; Tsai, C. S.; Wang, C. C. *CrystEngComm*. **2013**, *15*, 3377–3384.
(25) (a) Bordiga, S.; Regli, L.; Bonino, F.; Groppo, E.; Lamberti, C.; Xiao, B.; Wheatley, P. S.; Morris, R. E.; Zecchina, A. *Phys. Chem. Chem. Phys*. **2007**, *9*, 2676–2685. (b) Yoon, J. W.; Seo, Y.-K.; Hwang, Y. K.; Chang, J.-S.; Leclerc, H.; Wuttke, S.; Bazin, P.; Vimont, A.; Daturi, M.; Bloch, E.; Llewellyn, P. L.; Serre, C.; Horcajada, P.; Greneche, J.-M.; Rodrigues, A. E.; Ferey, G. *Angew. Chem., Int. Ed*. **2010**, *49*, 5949–5952.
(26) (a) Yoshida, Z.; Sugimoto, H.; Ogoshi, H. *Ada Chem. Ser*. **1980**, *191*, 307. (b) Strauss, S. H.; Holm, R. H. *Inorg. Chem.* **1982**, *21*, 863–868. (c) Klose, A.; Hesschenbrouck, J.; Solari, E.; Latronico, M.; Floriani, C.; Re, N.; Chiesi-Villa, A.; Rizzoli, C. *J. Organomet. Chem.* **1999**, *591*, 45. (d) Benito-Garagorri, D.; Lagoja, I.; Veiros, L. F.; Kirchner, K. A. *Dalton Trans.* **2011**, *40*, 4778–4792.
(27) Gütlich, P.; Bill, E.; Trautwein, A. X. *Mossbauer Spectroscopy and Transition Metal Chemistry*. Springer-Verlag: Berlin, 2007.
(28) Neese, F.; Pantazis, D. A. *Faraday Discuss.* **2011**, *148*, 229–238.
(29) (a) Cantalupo, S. A.; Fiedler, S. R.; Shores, M. P.; Rheingold, A. L.; Doerrer, L. H. *Angew. Chem., Int. Ed.* **2011**, *51*, 1000–1005. (b) Pascualini, M. E.; Di Russo, N. V.; Thuijs, A. E.; Ozarowski, A.; Stoian, S. A.; Abboud, K. A.; Christou, G.; Veige, A. S. *Chem. Sci.* **2015**, *6*, 608–612.
(30) Sachse, A.; Demeshko, S.; Meyer, F. *Dalton Trans*. **2009**, 7756–7764.
(31) (a) Peng, S.-M.; Ibers, J. A. *J. Am. Chem. Soc.* **1976**, *98*, 8032–8036. (b) Goedkin, V. L.; Peng, S.-M.; Molin-Norris, J.; Park, Y. *J. Am. Chem. Soc.* **1976**, *98*, 8391–8400.
(32) Walton, K. S.; Snurr, R. Q. *J. Am. Chem. Soc*. **2007**, *129*, 8552.

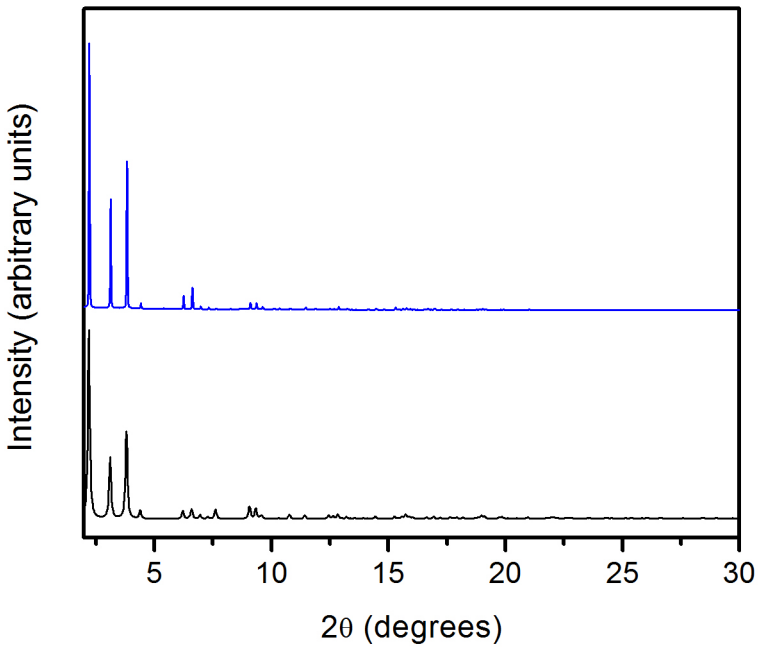

Figure 4.S1. Powder X-ray diffraction data collected at 100 K with λ = 0.72959 Å of activated Fe-BTTri (blue). Calculated powder pattern (black) is from single crystal X-ray diffraction data of DMF-solvated Fe-BTTri.

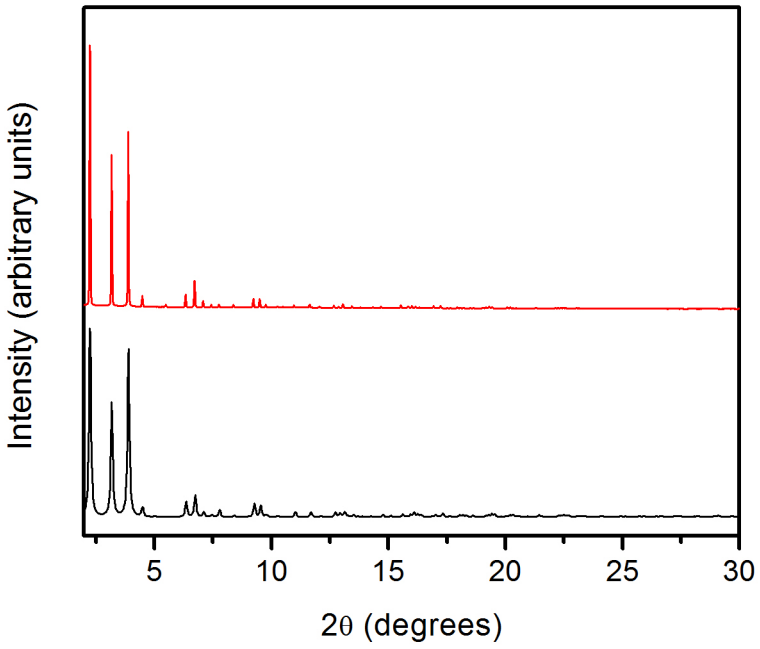

Figure 4.S2. Powder X-ray diffraction data collected at 100 K with λ = 0.72959 Å of Fe-BTTri under a 200 mbar atmosphere of CO (red). Calculated powder pattern (black) is derived from single crystal X-ray diffraction data of CO-dosed Fe-BTTri.

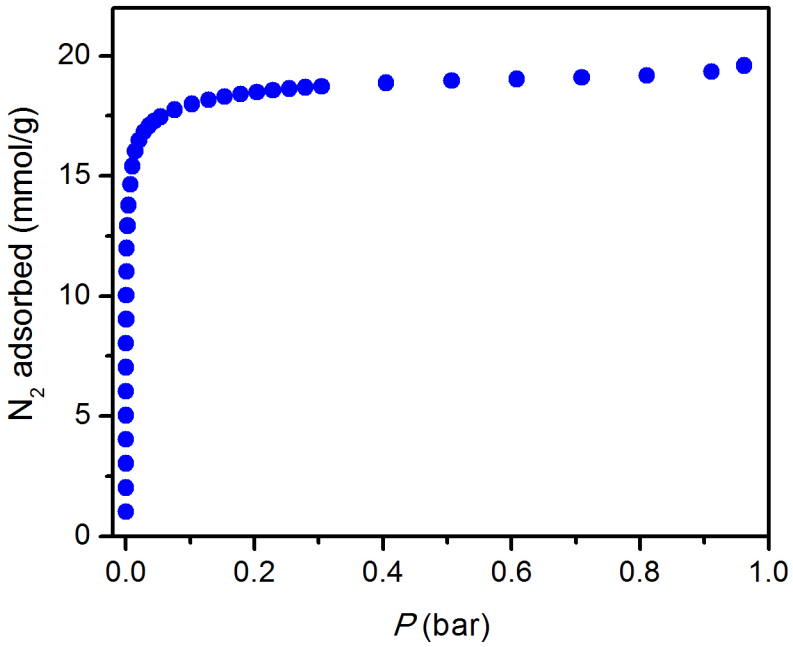

Figure 4.S3. N_2 isotherm collected at 77 K for Fe-BTTri.

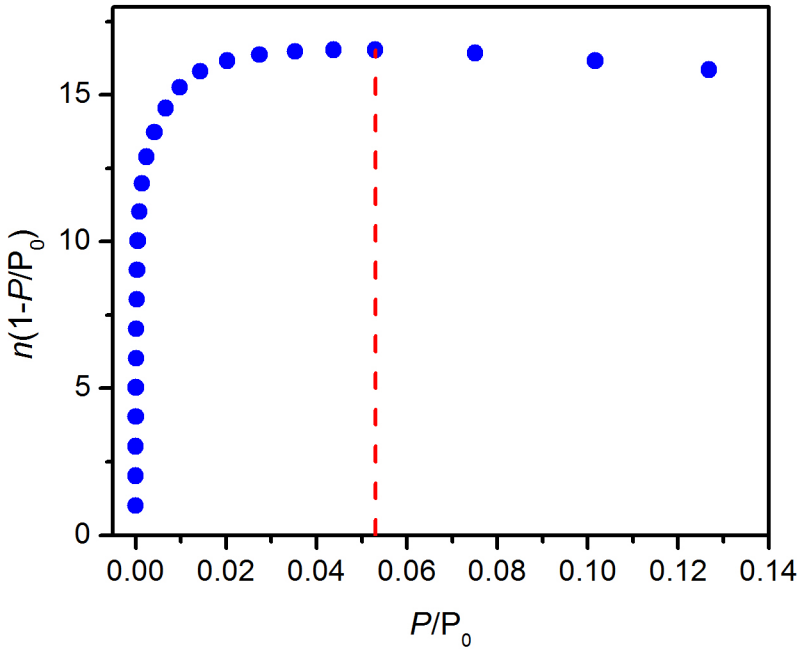

Figure 4.S4. Plot of n•(1-p/p_0) vs. p/p_0 to determine the maximum p/p_0 used in the linear BET fit of Fe-BTTri according to the first BET consistency criterion.[32]

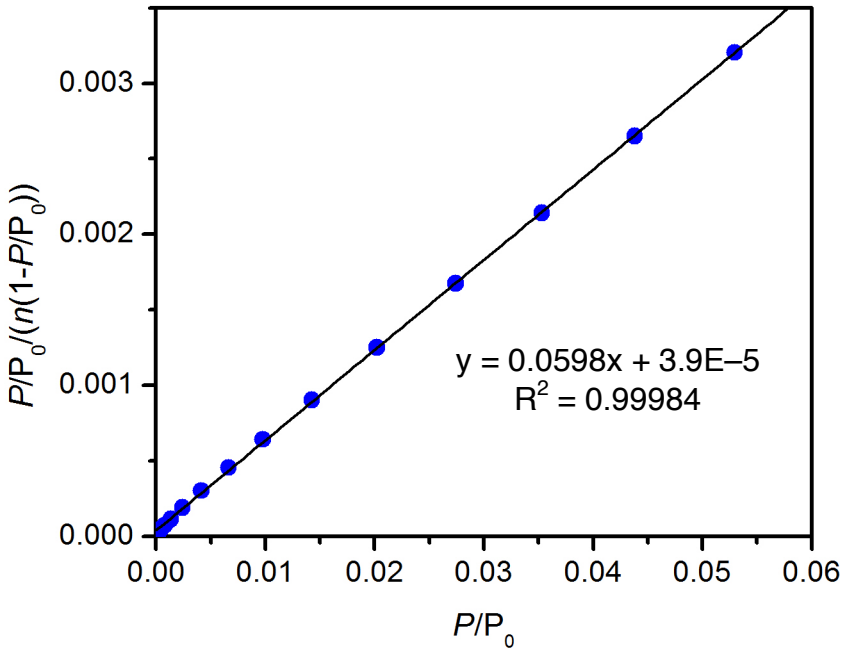

Figure 4.S5. Plot of $p/p_0/(n\bullet(1-p/p_0))$ vs. p/p_0 to determine the BET surface area. The slope of the best fit line for $p/p_0 < 0.055$ is 0.0598, and the y-intercept is 3.851×10^{-5}, which satisfies the second BET consistency criterion. This results in a saturation capacity of 16.7 mmol/g and a BET surface area of 1630 m^2/g.[32]

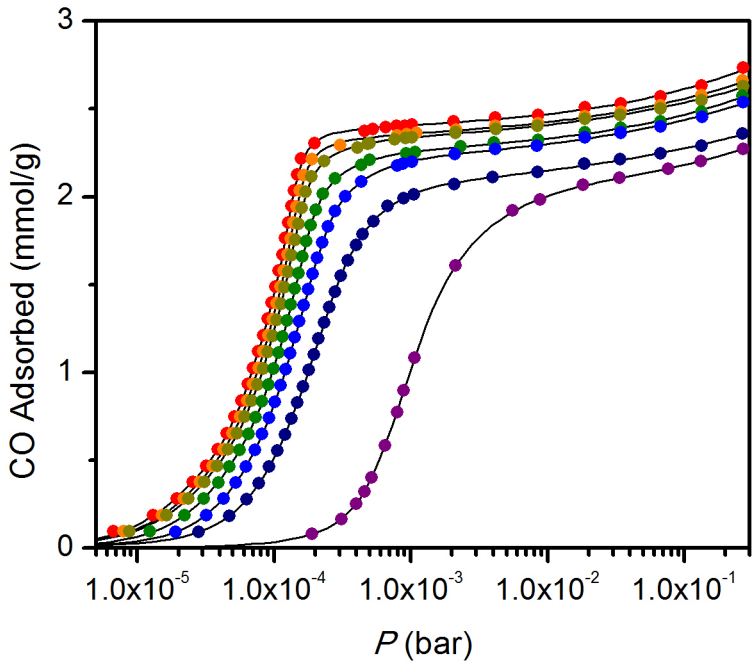

Figure 4.S6. Carbon monoxide isotherms collected at various temperatures for Fe-BTTri. Black lines represent fits to a quadruple-site Langmuir-Freundlich equation, with the parameters listed in Table 4.S1. Red, orange, yellow, green, light blue, dark blue, and purple circles correspond to isotherms collected at 25, 35, 45, 55, 65, 75, and 100 °C, respectively.

Table 4.S1. Quadruple-site Langmuir-Freundlich parameters for CO isotherms in Fe-BTTri, with the Freundlich parameter defined in eq 4.1. Note that these fits represent the best possible fit for each isotherm in order to accurately calculate isosteric heats of adsorption and ideal adsorbed solution theory (IAST) selectivities, and not necessarily the most physically realizable parameters.

	25 °C	35 °C	45 °C	55 °C	65 °C	75 °C	100 °C
$q_{sat,1}$ (mmol/g)	0.88675	0.86711	0.80989	0.73508	0.58948	0.38571	0.99077
b_1 (bar^{-1})	7.26782 $*10^{15}$	7.25442 $*10^{15}$	5.97967 $*10^{15}$	5.02067 $*10^{15}$	2.44942 $*10^{15}$	1.25296 $*10^{14}$	1.00761 $*10^{9}$
v_1	3.86037	3.90644	3.93724	4.01811	4.03749	3.86439	2.95955
$q_{sat,2}$ (mmol/g)	0.82623	0.87233	1.04370	1.25245	1.48253	1.61133	0.97433
b_2 (bar^{-1})	1.15355 $*10^{7}$	1.13698 $*10^{7}$	2.92724 $*10^{6}$	2.91986 $*10^{6}$	5.80034 $*10^{6}$	3.45154 $*10^{6}$	4.27708 $*10^{3}$
v_2	1.56208	1.59091	1.49981	1.55727	1.70263	1.73417	1.28399
$q_{sat,3}$ (mmol/g)	0.65579	0.56787	0.43661	0.24370	0.10093	0.01593	0.07226
b_3 (bar^{-1})	9.09203 $*10^{33}$	9.07239 $*10^{33}$	4.4044 $*10^{33}$	5.3714 $*10^{33}$	1.93111 $*10^{33}$	1.5997 $*10^{29}$	7.28842 $*10^{21}$
v_3	8.71723	8.78618	8.75936	8.92421	9.05801	7.36274	6.64970
$q_{sat,4}$ (mmol/g)	17.8286	16.9732	19.1364	20.7822	5.20312	1.88381	2.08321
b_4 (bar^{-1})	0.03388	0.03232	0.02681	0.02694	0.11353	0.33507	0.25457
v_4	0.38591	0.33238	0.31467	0.3712	0.32601	0.31341	0.52352

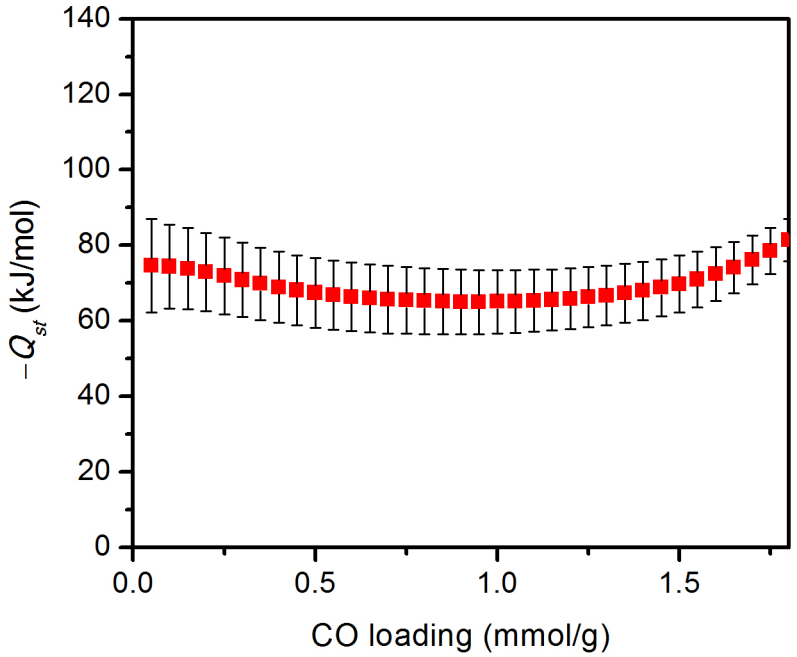

Figure 4.S7. Isosteric heats of CO adsorption in Fe-BTTri, calculated from isotherms collected at 65, 75, and 100 °C.

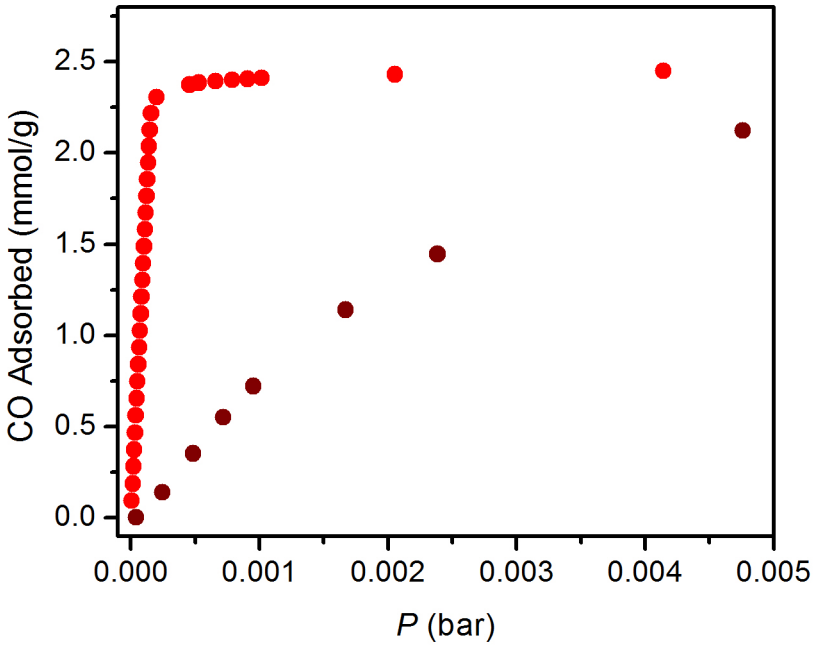

Figure 4.S8. CO isotherms collected at 25 °C for Fe-BTTri (red) and Ni_2(dobdc) (brown), showing a remarkable increase in low-pressure CO capacity in Fe-BTTri.[10d]

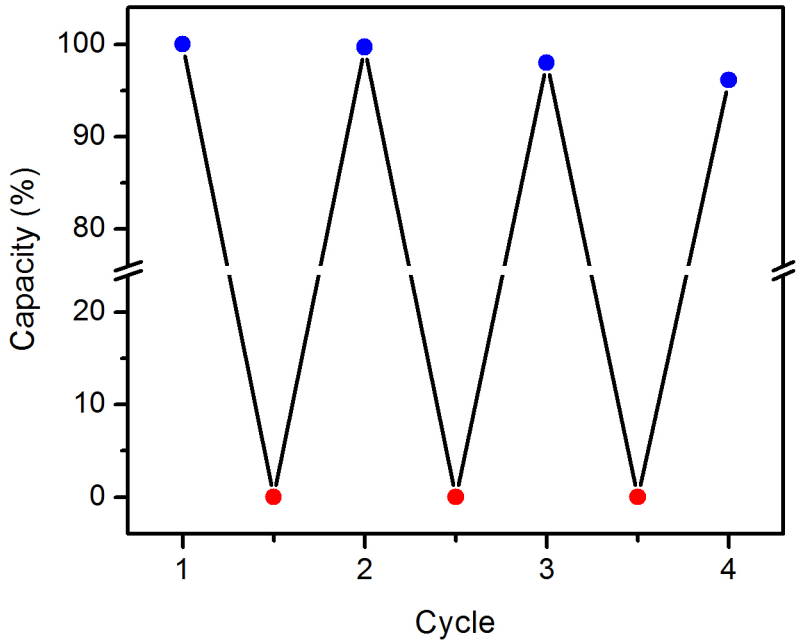

Figure 4.S9. Cycling data for successive CO adsorption and desorption in Fe-BTTri, varying the temperature of desorption. Adsorption capacities are expressed in terms of percentage of the capacity observed for cycle 1. Adsorption (blue circles) occurred within 10 min upon dosing CO at 25 °C at 10 mbar with the exception of cycle 4, which occurred at 9 mbar under otherwise similar conditions. Desorption (red circles) occurred under dynamic vacuum for the following temperatures and durations: Cycle 2, 140 °C, 10 min; Cycle 3, 115 °C, 15 min; Cycle 4, 100 °C, 30 min. Note that the lower pressure of adsorption for cycle 4 likely accounts for some of the loss in capacity.

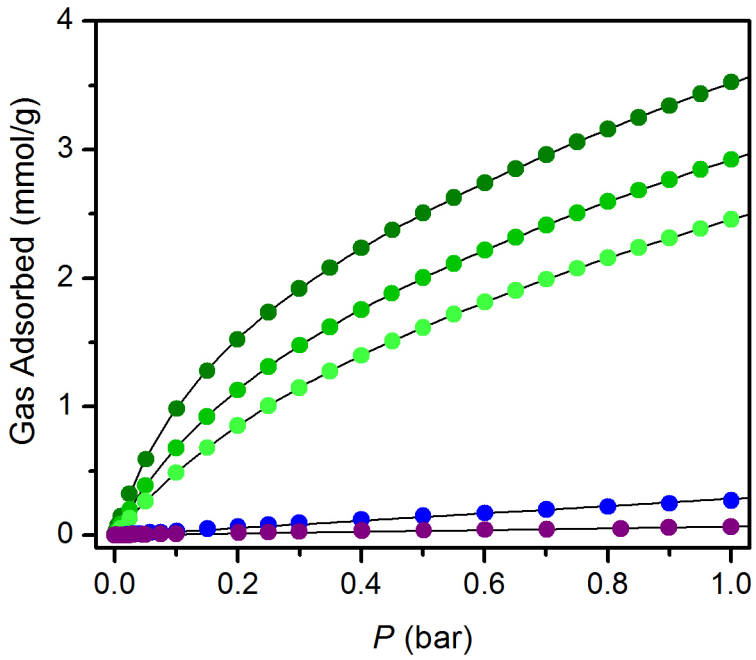

Figure 4.S10. Single-component CO_2 (green), N_2 (blue), and H_2 (purple) isotherms collected at various temperatures. CO_2 isotherms were collected at 25, 35, and 45 °C (from dark to light), and N_2 and H_2 isotherms were collected at 25 °C. Black lines represent fits to either a single- or dual-site Langmuir equation with the parameters listed in Table 4.S2.

Table 4.S2. Single- or dual-site Langmuir parameters for CO_2, H_2, and N_2 isotherms collected at various temperatures.

	$q_{sat,1}$ (mmol/g)	b_1 (bar^{-1})	$q_{sat,2}$ (mmol/g)	b_2 (bar^{-1})
CO_2 (25 °C)	1.86734	6.67618	8.55299	0.28431
CO_2 (35 °C)	1.78361	3.94927	9.23874	0.19372
CO_2 (45 °C)	1.9873	2.30927	18.0022	0.0632
H_2 (25 °C)	20	0.00338	-	-
N_2 (25 °C)	20	0.01422	-	-

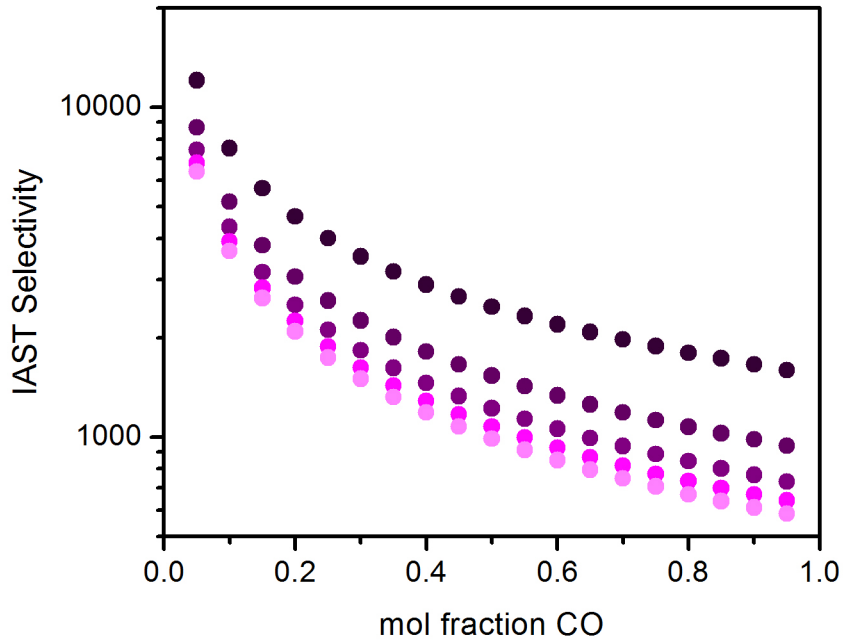

Figure 4.S11. Comparison of different values of ideal adsorbed solution theory (IAST) selectivities for CO/H_2 mixtures at 25 °C and 1 bar total pressure by fitting the H_2 isotherm with different saturation capacities, q_{sat}, in the single-site Langmuir equation, with the parameters listed in Table 4.S3. From light to dark, q_{sat} =30, 25, 20, 15, 10 mmol/g. All IAST selectivities, even when using q_{sat} = 10 mmol/g, suggest Fe-BTTri will be a highly selective material for CO/H_2 separations.

Table 4.S3. Single-site Langmuir parameters for 25 °C H_2 isotherms using different q_{sat} parameters for Figure 4.S11.

$q_{sat,1}$ (mmol/g)	b_1 (bar^{-1})
10	0.00677
15	0.00451
20	0.00338
25	0.0027
30	0.00225

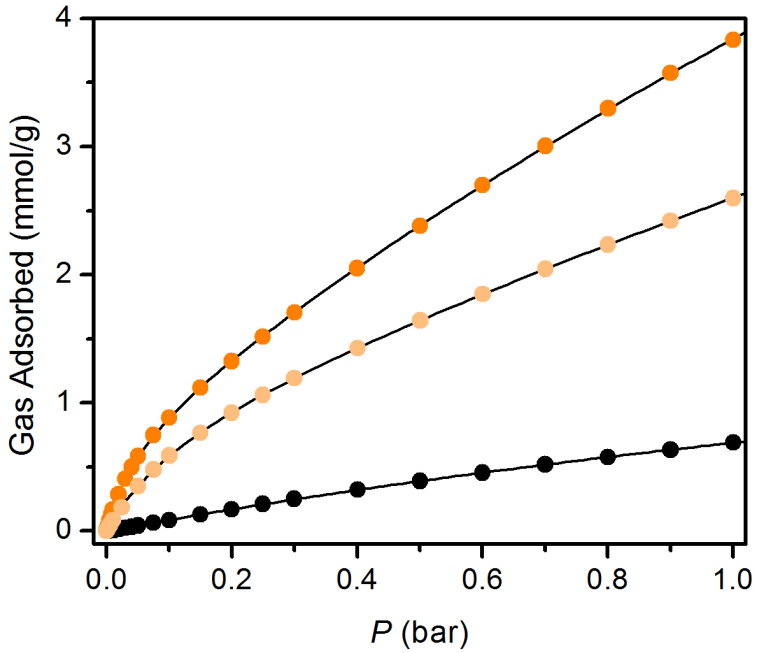

Figure 4.S12. Single-component C_2H_6 (orange) and CH_4 (black) isotherms collected at various temperatures. C_2H_6 isotherms were collected at 25 (dark) and 45 °C (light), and CH_4 isotherms were collected at 25 °C. Black lines represent fits to either a single- or dual-site Langmuir equation with parameters listed in Table 4.S4.

Table 4.S4. Single- or dual-site Langmuir parameters for C_2H_6 and CH_4 isotherms collected at various temperatures.

	$q_{sat,1}$ (mmol/g)	b_1 (bar^{-1})	$q_{sat,2}$ (mmol/g)	b_2 (bar^{-1})
C_2H_6 (25 °C)	0.77218	20.9313	20.4725	0.17859
C_2H_6 (45 °C)	0.88578	7.9759	30.417	0.06336
CH_4 (25 °C)	20	0.03761	-	-

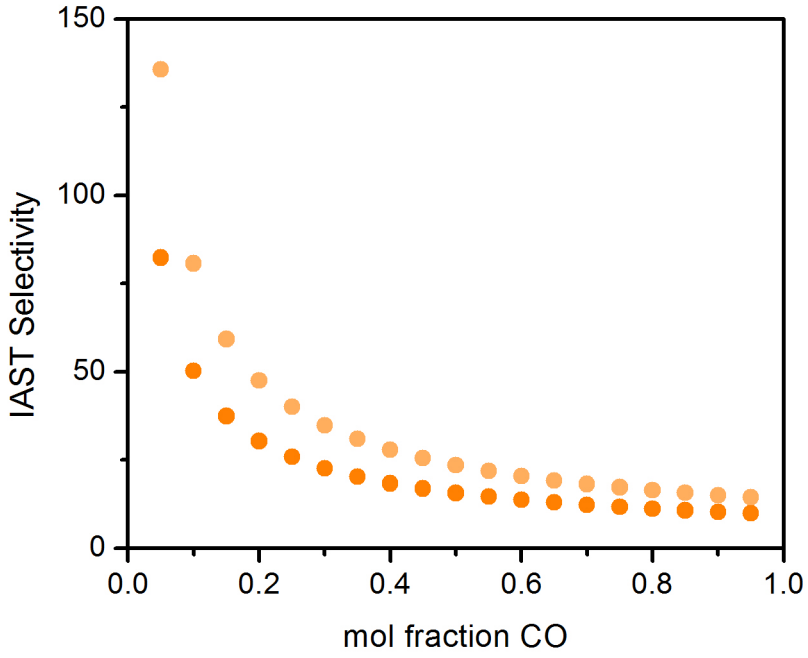

Figure 4.S13. Ideal Adsorbed Solution Theory values for CO/C_2H_6 mixtures at 25 (dark) or 45 (light) °C at 1 bar total pressure.

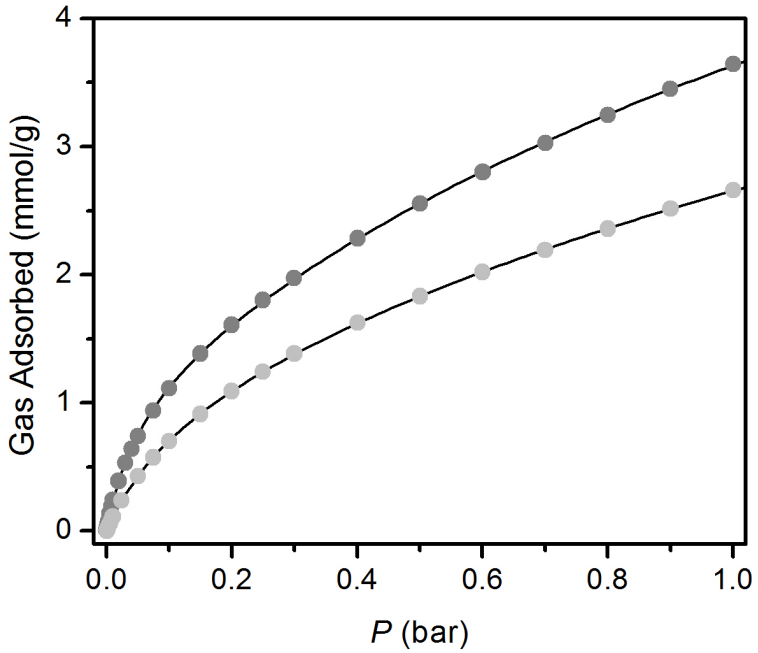

Figure 4.S14. Single-component C_2H_4 isotherms collected at 25 (dark) and 45 °C (light). Black lines represent fits to a dual-site Langmuir equation with the parameters listed in Table 4.S5.

Table 4.S5. Dual-site Langmuir parameters for C_2H_4 isotherms collected at various temperatures.

	$q_{sat,1}$ (mmol/g)	b_1 (bar^{-1})	$q_{sat,2}$ (mmol/g)	b_2 (bar^{-1})
C_2H_4 (25 °C)	1.16712	19.2807	7.99987	0.46058
C_2H_4 (45 °C)	1.04808	8.60521	6.8752	0.33266

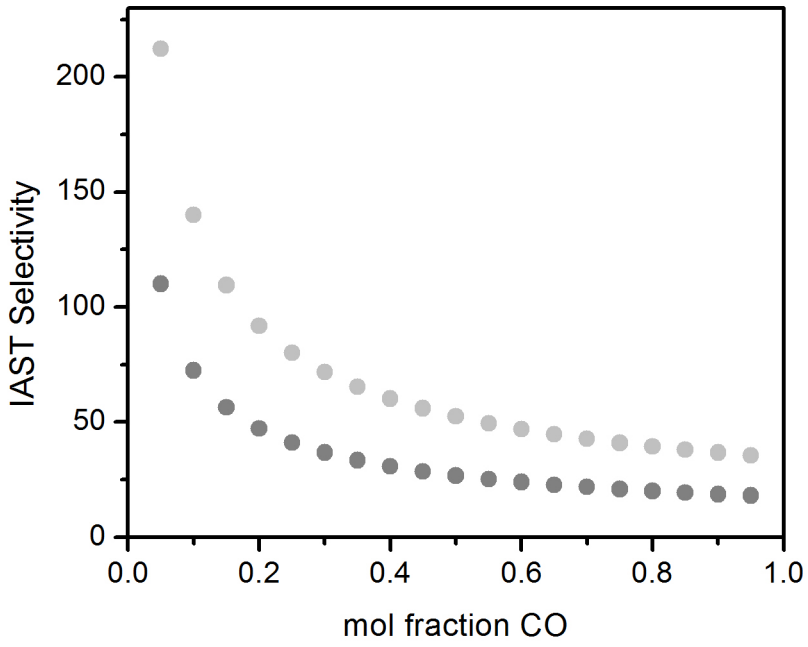

Figure 4.S15. Ideal Adsorbed Solution Theory values for CO/C_2H_4 mixtures at 25 (dark) or 45 °C (light) at 1 bar total pressure.

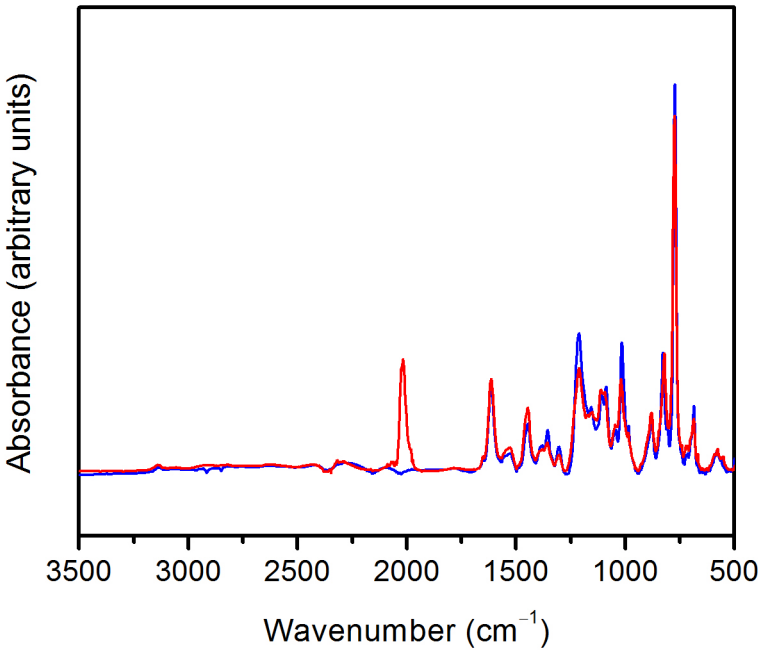

Figure 4.S16. Full infrared spectra of Fe-BTTri (blue) and CO-dosed Fe-BTTri (red).

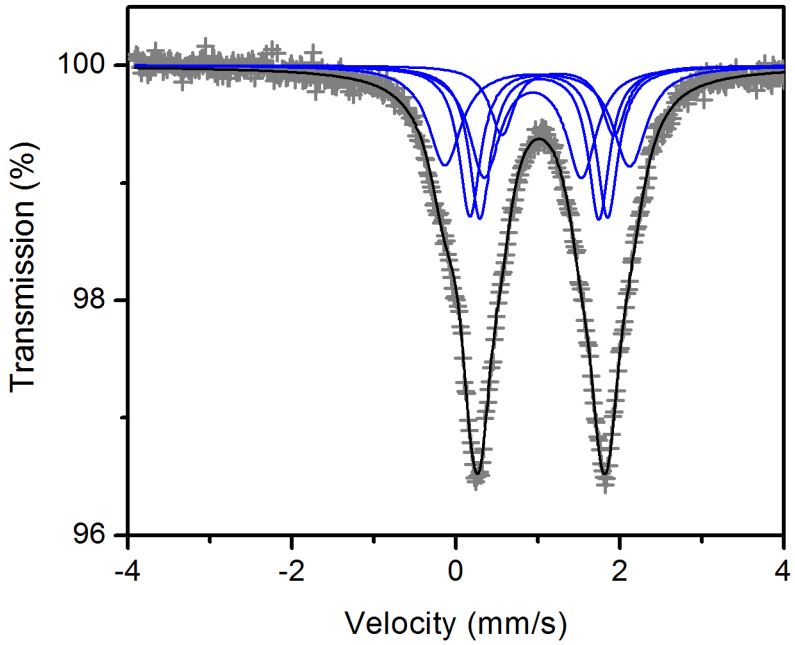

Figure 4.S17. Mössbauer spectra collected at 290 K for DMF-solvated Fe-BTTri, with the experimental data in grey crosses and the total fit in black. The blue components are assigned to high-spin Fe^{II}. The parameters for all components are listed in Table 4.S6.

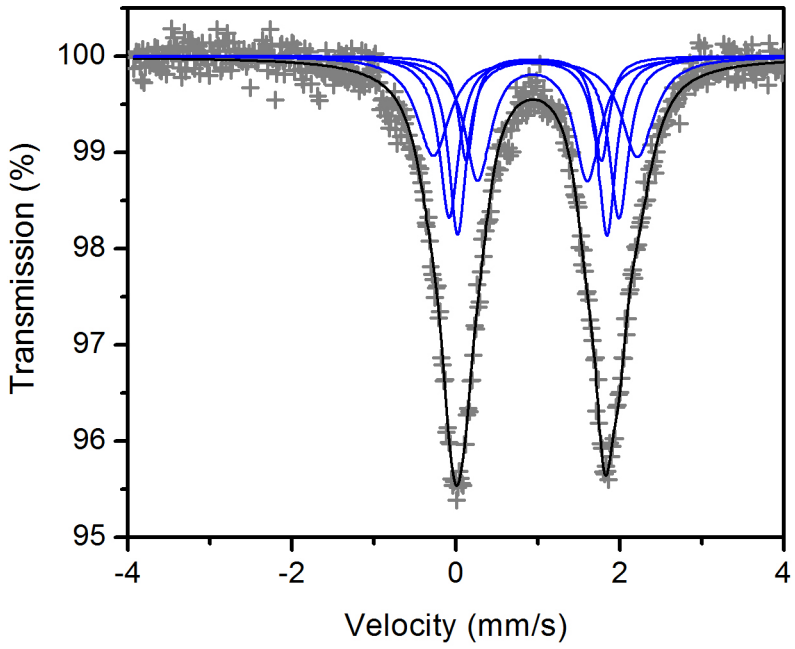

Figure 4.S18. Mössbauer spectra collected at 290 K for Fe-BTTri, with the experimental data in grey plusses and the total fit in black. The blue components are assigned to high-spin Fe^{II}. The parameters for all components are listed in Table 4.S6.

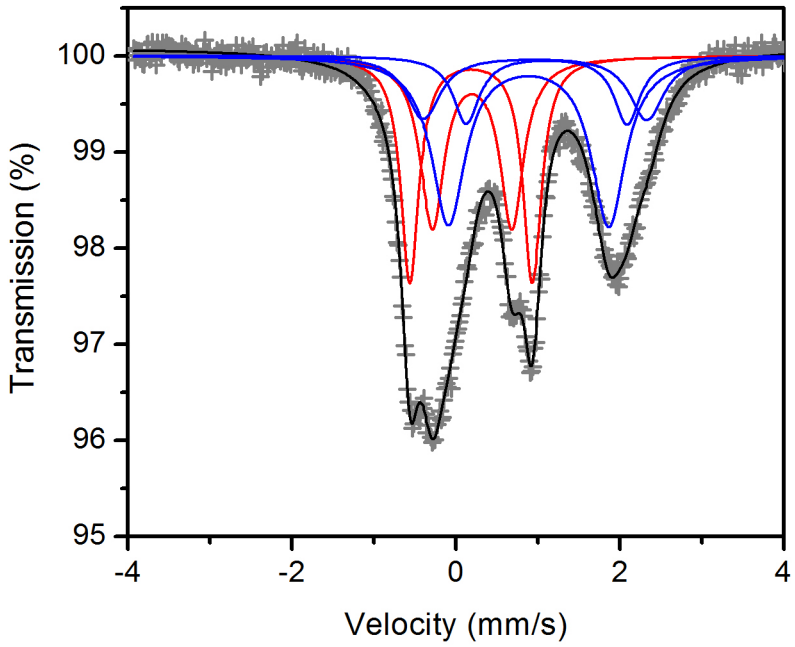

Figure 4.S19. Mössbauer spectra collected at 290 K for DMF-solvated Fe-BTTri, with the experimental data in grey plusses and the total fit in black. The blue components are assigned to high-spin Fe^{II}, while the red components are assigned to low-spin Fe^{II}. The parameters for all components are listed in Table 4.S6.

Table 4.S6. Mössbauer parameters. [a]HS = high-spin, LS= low-spin

Sample	δ (mm/s)	ΔE_Q (mm/s)	Γ (mm/s)	Area (%)	Assignment[a]
Fe-BTTri	1.06(2)	1.80(2)	0.39(2)	22	Fe^{2+} (HS)
100 K	1.05(1)	2.38(1)	0.23(1)	22	Fe^{2+} (HS)
	1.06(1)	2.67(3)	0.26(3)	22	Fe^{2+} (HS)
	1.07(1)	3.06(3)	0.48(2)	22	Fe^{2+} (HS)
	1.05(1)	2.11(3)	0.22(4)	11	Fe^{2+} (HS)
Fe-BTTri	0.94(4)	1.34(6)	0.38(5)	22	Fe^{2+} (HS)
290 K	0.93(3)	1.82(6)	0.26(7)	22	Fe^{2+} (HS)
	0.95(1)	2.07(5)	0.29(4)	22	Fe^{2+} (HS)
	0.97(4)	2.50(7)	0.48(4)	22	Fe^{2+} (HS)
	0.95(4)	1.65(11)	0.22(7)	11	Fe^{2+} (HS)
Fe-BTTri – DMF	0.94(4)	1.18(8)	0.45(4)	22	Fe^{2+} (HS)
solvated	1.02(2)	1.45(6)	0.32(4)	22	Fe^{2+} (HS)
290 K	1.10(2)	1.68(5)	0.32(4)	22	Fe^{2+} (HS)
	0.99(1)	2.26(3)	0.49(2)	22	Fe^{2+} (HS)
	1.25(7)	1.37(13)	0.35(7)	11	Fe^{2+} (HS)
CO-Dosed Fe-BTTri	0.26(2)	1.03(4)	0.35(3)	21(4)	Fe^{2+} (LS)
100 K	0.27(1)	1.50(2)	0.27(3)	21(4)	Fe^{2+} (LS)
	1.03(2)	3.31(6)	0.47(5)	13(3)	Fe^{2+} (HS)
	1.00(2)	2.42(4)	0.50(2)	34(3)	Fe^{2+} (HS)
	1.21(2)	2.46(5)	0.38(3)	11	Fe^{2+} (HS)
CO-dosed Fe-BTTri	0.20(1)	0.97(3)	0.35(4)	23(4)	Fe^{2+} (LS)
290 K	0.19(1)	1.50(1)	0.27(3)	23(3)	Fe^{2+} (LS)
	0.96(4)	2.73(10)	0.50(5)	12(5)	Fe^{2+} (HS)
	0.89(1)	1.96(4)	0.50(3)	31(5)	Fe^{2+} (HS)
	1.11(5)	1.96(7)	0.39(6)	11	Fe^{2+} (HS)

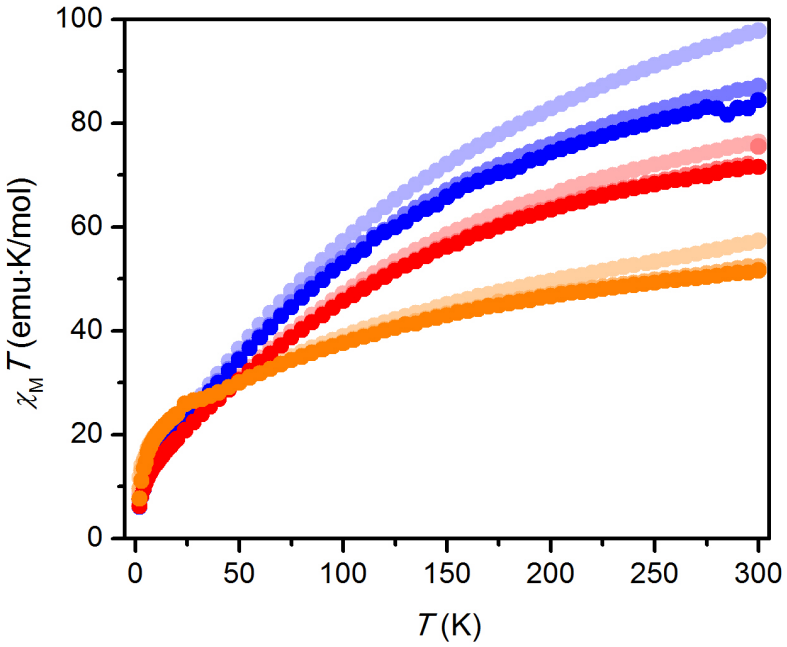

Figure 4.S20. Variable-temperature magnetic susceptibility data collected under multiple H_{dc} for Fe-BTTri (blue), Fe-BTTri–$(CO)_{3.2}$ (13.4% CO-loaded, red), and Fe-BTTri–$(CO)_{10.6}$ (44.3% CO-loaded, orange). From light to dark, H_{dc} = 0.1, 0.5, and 1 T.

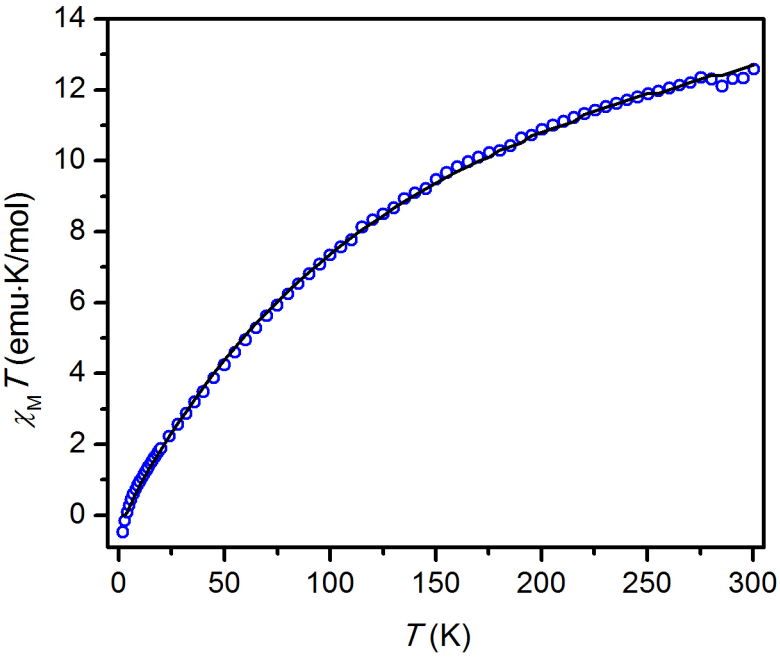

Figure 4.S21. Variable-temperature magnetic susceptibility data collected under H_{dc} = 1 T for Fe-BTTri, adjusted per $[Fe_4Cl]^{7+}$ cluster. Each cluster has an expected $\chi_M T$ of 12emu•K/mol at 300 K, with an experimentally observed value of 12.6 emu•K/mol, showing good agreement. The black line represent the fit to the data employing a Hamiltonian and parameters described in eq 4.4.

Table 4.S7. Crystallographic Data

	DMF-solvated Fe-BTTri, $Fe_3[(Fe_4Cl(DMF)_4)_3(BTTri)_8]_2$	CO-dosed Fe-BTTri, $Fe_3[(Fe_4Cl(CO)_4)_3(BTTri)_8]_2$
Formula	$C_{264}H_{240}Cl_6Fe_{27}N_{168}O_{24}$	$C_{216}H_{96}Cl_6Fe_{27}N_{144}O_{24}$
Crystal System	Cubic	Cubic
Space Group	*Fm-3c*	*Fm-3c*
a, b, c (Å)	38.0680(11)	37.2012(9)
α, β, γ (°)	90	90
V, (Å^3)	55167(5)	51484(4)
Z	4	4
Radiation, λ (Å)	Synchrotron, 0.7749	Synchrotron, 0.7749
R1[a], wR2[b] (I>2σ(I))	0.0505, 0.1595	0.0405, 0.1272
R1[a], wR2[b] (all data)	0.0556, 0.1651	0.0439, 0.1292

[a] $R1 = \sum||F_o| - |F_c||/\sum|F_o|$. [b] $wR2 = \{\sum[w(F_o^2 - F_c^2)^2]/\sum[w(F_o^2)^2]\}^{1/2}$.

Chapter 5: A Spin Transition Mechanism for Cooperative Adsorption in Metal–Organic Frameworks Bearing Open Metal Sites

5.1. Introduction

Cooperative binding, whereby an initial binding event facilitates the uptake of additional substrate molecules, is common in biological systems such as hemoglobin.[1,2] It was recently shown that porous solids that exhibit cooperative binding have substantial energetic benefits over traditional adsorbents,[3] but few guidelines currently exist for the design of such materials. In principle, metal–organic frameworks that contain coordinatively unsaturated metal centers could act as both selective[4–7] and cooperative adsorbents if guest binding at one site were to trigger an electronic transformation that subsequently altered the binding properties at neighboring metal sites.[8–10] Here we illustrate this concept through the selective adsorption of carbon monoxide (CO) in a series of metal–organic frameworks featuring coordinatively unsaturated iron(II) sites. Functioning via a mechanism by which neighbouring iron(II) sites undergo a spin-state transition above a threshold CO pressure, these materials exhibit large CO separation capacities with only small changes in temperature. The very low regeneration energies that result may enable more efficient Fischer–Tropsch conversions and extraction of CO from industrial waste feeds, which currently underutilize this versatile carbon synthon.[11] Ultimately, the electronic basis for the cooperative adsorption demonstrated here could provide a general strategy for designing efficient and selective adsorbents suitable for various separations.

Metal–organic frameworks are highly porous, chemically tunable solids that have been investigated as selective adsorbents for gas separation applications.[12–14] These systems typically exhibit classical, type I adsorption isotherms (Figure 5.1a). However, a trade-off between selectivity and working capacity is encountered, as steeper isotherms are generally associated with greater selectivity but consequently require harsher regeneration conditions. A more energetically favorable separation method involves cooperative adsorption, wherein little adsorption is observed until a sharp rise, or step, occurs, where the majority of gas is adsorbed over a narrow pressure region (Figure 5.1b). Owing to the temperature dependence of the step pressure, such adsorbents combine high working capacities with modest temperature swings, as moving the step between the adsorption and desorption pressures recovers large quantities of adsorbed gas.

Although step-shaped isotherms are well established, the vast majority occur in pressure-responsive flexible frameworks[15,16] or arise when adsorbate–adsorbate interactions become important.[17] Although useful for other applications, the responsive nature of these systems does not substantially contribute to selective gas adsorption. Thus far, the only reported mechanism for selective cooperative adsorption in rigid metal–organic frameworks involves rearrangement of amines to form ammonium carbamate chains upon CO_2 adsorption.[3] However, this mechanism is specific to CO_2, and designing cooperative adsorbents for other industrially relevant gases requires a different strategy.

In nature, cooperative binding is accomplished by transition metals in enzymes, with an initial binding event inducing an electronic response at the active site and a corresponding structural change throughout the system. This promotes subsequent substrate binding at neighboring active sites, as observed with O_2 or CO uptake in hemoglobin.[1,2] Metal–organic frameworks that feature coordinatively unsaturated metal sites have been studied for applications involving selective gaseous substrate binding[4–7], but these adsorption sites are often treated as isolated centers that

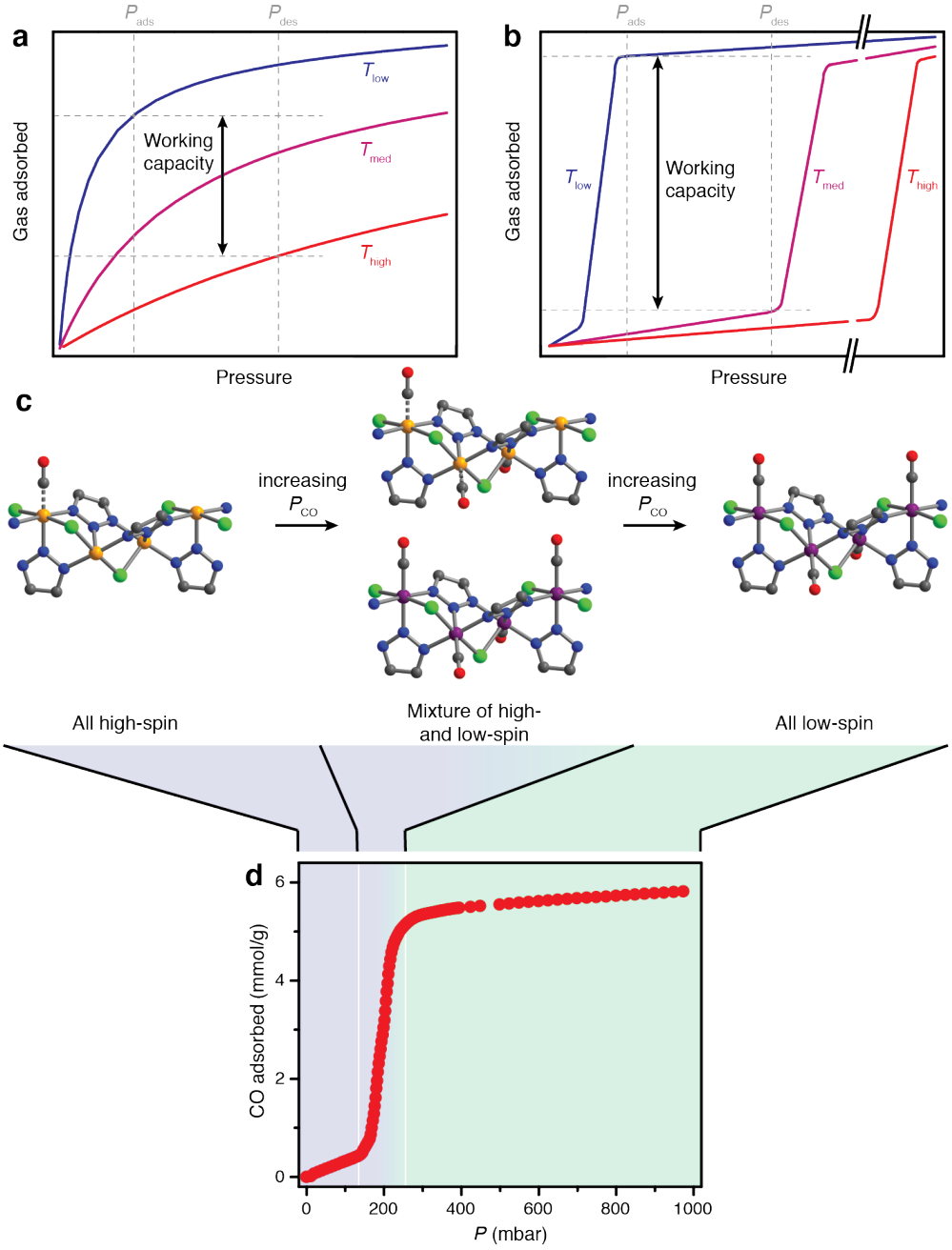

Figure 5.1. Idealized adsorption isotherms and the cooperative spin transition mechanism. Comparison of working capacities for idealized gas adsorption isotherms of classical (**a**) and cooperative (**b**) adsorbents, highlighting the increased working capacity for a cooperative adsorbent using a smaller temperature swing. Schematic of the cooperative spin transition mechanism, starting at an all high-spin Fe^{II} (orange spheres) phase before the step region of the isotherm, and during the step pressure converting to low-spin Fe^{II} (purple spheres) upon increasing pressure, with full conversion to a low-spin phase complete after the step (**c**). Relevant regions are indicated on the CO adsorption isotherm of **1** collected at 25 °C (**d**).

operate independently from one another. With an appropriate design, the electronic properties of a transition metal situated within an extended network can influence the binding properties of neighboring metal sites.[8–10] By combining these strategies, a framework that contains coordinatively unsaturated metal sites that are closely linked, such that electronic properties change in a concerted fashion upon gas binding, might be expected to behave as a cooperative and selective adsorbent, mimicking the cooperative electronic and subsequent structural transitions observed in biological systems.

We selected carbon monoxide (CO) as a sorbate to test this hypothesis because, as the quintessential strong-field ligand, its coordination induces spin transitions in otherwise high-spin molecular species.[18] Spin transitions are highly dependent on the proximity of neighboring spin transition centres,[8,9] and provide an appropriate electronic transformation for potential cooperative adsorption. In addition, industrial CO separations are widely implemented, and a selective and easily regenerable CO adsorbent would be immediately applicable.[11] A triazolate-based metal–organic framework was recently reported with iron(II) centres that selectively convert from a high-spin to a low-spin electron configuration upon CO coordination.[19] However, no cooperative phase transition was observed due to the large distance between the tetranuclear iron nodes. We envisioned that a structure wherein iron(II) sites with a similar coordination environment were linked into chains would create a favorable environment for a cooperative spin transition upon CO adsorption. Here we report two such metal–organic frameworks, Fe_2Cl_2(bbta) (**1**; H_2bbta = 1*H*,5*H*-benzo(1,2-*d*:4,5-*d*)bistriazole) and Fe_2Cl_2(btdd) (**2**; H_2btdd = bis(1*H*-1,2,3-triazolo[4,5-*b*],[4′,5′-*i*])dibenzo[1,4]dioxin), which indeed adsorb CO through a cooperative spin-transition mechanism. This mechanism results in highly efficient CO separations and demonstrates that rational design of cooperative adsorbents can be achieved by controlling the electronic properties at open metal sites.

5.2. Materials and methods

5.2.1. General considerations. All synthetic procedures were performed under an Ar atmosphere using standard Schlenk techniques or in an N_2-filled VAC Atmospheres glove box. The compound $FeCl_2$ was purchased from Sigma-Aldrich and used as received. Methanol was purchased from EMD Millipore Corporation as DriSolv grade, dried over 3 Å molecular sieves, and sparged with Ar prior to use. DMF was purchased from EMD Millipore Corporation as OmniSolv grade, sparged with Ar, and dried with an alumina column prior to use. The linkers H_2bbta[20] and H_2btdd[21] were prepared according to previously reported procedures. Ultrahigh purity (99.999%) grade He, N_2, H_2, and CO_2, and research purity (99.99%) grade CO were used for all gas adsorption measurements and dosing. Elemental analyses for C, H, and N were performed at the Microanalytical Laboratory at the University of California, Berkeley.

5.2.2. Synthesis of Fe_2Cl_2(bbta) (1). A solution of $FeCl_2$ (200 mg, 1.58 mmol) and H_2bbta (125 mg, 0.781 mmol) in a mixture of DMF (40 mL) and methanol (10 mL) was added to a Schlenk flash charged with a magnetic stir bar. The solution was stirred at 100 °C for 24 h. The resulting orange powder was collected by filtration, and soaked in 10 mL of DMF at 120 °C for 12 h. The solid was then collected by filtration, and soaked in another 10 mL of DMF at 120 °C for 12 h. This process was repeated five times so that the total time washing with DMF was three days. The solid was then collected by filtration, and soaked in 10 mL of methanol at 60 °C for 12 h. The solid was collected by filtration, and soaked in another 10 mL of methanol at 60 °C for 12 h. This process was repeated five times so that the total time washing with methanol was three days. The resulting

orange solid was collected by filtration, and heated at a rate of 0.2 °C/min and held at 180 °C under dynamic vacuum for 7 days, affording 200 mg (75%) of product as a yellow powder. Anal. Calcd for $C_6H_2Cl_2Fe_2N_6$: C, 21.15; H, 0.59; N, 24.67. Found: C, 20.69; H, 0.61; N, 24.90.

5.2.3. Synthesis of Fe_2Cl_2(btdd) (2). A solution of $FeCl_2$ (200 mg, 1.58 mmol) and H_2btdd (100 mg, 0.376 mmol) in a mixture of DMF (20 mL) and methanol (20 mL) was added to a Schlenk flash charged with a magnetic stir bar. The solution was stirred at 100 °C for 4 days. The resulting brown powder was collected by filtration, and soaked in 10 mL of DMF at 120 °C for 8 h. The supernatant solution was decanted, and 10 mL of DMF was added. This process was repeated once more so that the total time washing with DMF at 120 °C was one day. The supernatant solution was decanted, and the solid was soaked in DMF at 140 °C for 8 h. The supernatant solution was decanted, and 10 mL of DMF was added. This process was repeated once more so that the total time washing with DMF at 140 °C was one day. The solid was collected by filtration, and soaked in 10 mL of methanol at 60 °C for 8 h. The supernatant solution was decanted, and 10 mL of methanol was added. This process was repeated five times so that the total time washing with methanol was two days. The resulting brown solid was collected by filtration, and heated at a rate of 0.2 °C/min and held at 100 °C under dynamic vacuum for 36 h, affording 140 mg (83%) of product as a brown powder. Anal. Calcd for $C_{12}H_4Cl_2Fe_2N_6O_2$: C, 32.26; H, 0.90; N, 18.81. Found: C, 32.51; H, 1.02; N, 18.61.

5.2.4. Gas adsorption measurements. Gas adsorption isotherms for pressures in the range 0–1 bar were measured by a volumetric method using a Micromeritics ASAP2020 or Micromeritics 3Flex gas adsorption analyzer. A typical sample of ~100 mg of metal–organic framework was transferred in an N_2 filled glovebox to a pre-weighed analysis tube, which was capped with a Micromeretics TranSeal and evacuated by heating to a specified temperature with a ramp rate of 0.5 °C/min under dynamic vacuum until an outgas rate of less than 3 μbar/min was achieved. The evacuated analysis tube containing the degassed sample was then carefully transferred to an electronic balance and weighed again to determine the mass of sample. The tube was then transferred back to the analysis port of the gas adsorption instrument. The outgas rate was again confirmed to be less than 3 μbar/min. For all isotherms, warm and cold free space correction measurements were performed using ultrahigh purity He gas. Isotherms collected at 15 to 45 °C were measured in water baths using a Julabo F32 water circulator, while N_2 isotherms collected at 77 K were measured in liquid nitrogen baths. Oil-free vacuum pumps and oil-free pressure regulators were used for all measurements to prevent contamination of the samples during the evacuation process or of the feed gases during the isotherm measurements. Langmuir surface areas were determined from N_2 adsorption data collected at 77 K using Micromeritics software.

5.2.5. Powder X-ray diffraction. Microcrystalline powder samples of **1** (~5 mg) were loaded into two 1.0 mm boron-rich glass capillaries inside a glovebox under an N_2 atmosphere. The capillaries were attached to a gas cell, which was connected to the analysis port of a Micromeritics ASAP 2020 gas adsorption instrument. One capillary was fully evacuated at room temperature for 15 min then flame-sealed, while the other capillary was dosed with CO to a pressure of 350 mbar, equilibrated for 2 h, then flame-sealed. Each capillary was placed inside a Kapton tube that was sealed on both ends with epoxy. This process was repeated for samples of **2**, with the exception that CO dosing was performed at a pressure of 700 mbar.

High-resolution synchrotron X-ray powder diffraction data for **1** and CO-dosed **1** were collected at beamline 11-BM at the Advanced Photon Source (APS) at Argonne National Laboratory. Diffraction patterns were collected at 295 K with a wavelength of 0.458996 Å. Discrete detectors covering an angular range from −6 to 16° in 2θ were scanned over a 34° range

of 2θ, with data points collected every 0.001° and a scan speed of 0.01°/s. Note that due to the large number of data points collected, all diffraction patterns were rebinned to a step size of 0.005° in 2θ.

High-resolution synchrotron X-ray powder diffraction data for **2** and CO-dosed **2** were collected at beamline 17-BM at the APS. Diffraction patterns were collected at 298 K with a wavelength of 0.72768 Å. Discrete detectors covering an angular range from −6 to 16° in 2θ were scanned over a 34° range of 2θ, with data points collected every 0.001° and a scan speed of 0.01°/s. Again, all diffraction patterns were rebinned to a step size of 0.005° in 2θ.

For all samples, a standard peak search, followed by indexing via the Single Value Decomposition approach,[22] as implemented in TOPAS-Academic V4.1,[23] allowed the determination of approximate unit cell dimensions. Using TOPAS-Academic, precise unit cell dimensions were determined by performing a structureless Le Bail refinement, and then Rietveld refinements were performed. For CO-dosed **2**, the precise unit cell dimensions were determined by performing a structureless Pawley refinement. After obtaining the precise unit cell dimensions for the activated phase pattern, a structural model constructed in Materials Studio (Materials Studio v. 5.0.0.0, 2009, Accelrys Software Inc.) was used in the Rietveld refinement where all profile and atomic parameters were set free (applying soft restrains on the bond lengths and angles).

For *in situ* powder X-ray diffraction measurements of **1**, a microcrystalline powder sample (~5 mg) was loaded into a 1.0 mm glass capillary inside a glovebox under an N_2 atmosphere. The capillary was attached to a gas cell, which was connected to the analysis port of a Micromeritics ASAP 2020 gas adsorption instrument and then evacuated. It was then dosed with CO to a pressure of 300 mbar, equilibrated for 2 h, and flame-sealed. High-resolution synchrotron X-ray powder diffraction data were subsequently collected at beamline 17-BM at the Advanced Photon Source (APS) at Argonne National Laboratory. Diffraction patterns were collected at various temperatures with a wavelength of 0.72768 Å. During the course of the experiment, the temperature was cycled between 273 and 353 K at rates varying from 3 K/min to 6 K/min. In total, four cycles were performed with patterns collected every minute. Qualitative phase data were obtained using simultaneous sequential Rietveld refinements.

5.2.6. Infrared spectroscopy. FTIR spectra were collected in transmission mode on a self-supported wafer of sample, in a controlled atmosphere using a custom-built infrared cell. The spectra were recorded at a 2 cm^{-1} resolution on a Bruker IFS 66 FTIR spectrometer, equipped with a MCT detector. Adsorption and desorption of CO were followed at 25 °C. Before CO was exposed to the sample, the sample was first activated at 150 °C for 15 min while flowing 30 mL/min of pure N_2 (heating ramp rate of 1 °C/min).

5.2.7. Mössbauer spectroscopy. Mössbauer spectra were measured at 100 K with a constant acceleration spectrometer, which utilized a rhodium matrix cobalt–57 source. Isomer shifts are reported relative to 27 μm α–iron foil at 295 K. The absorber contained ~40 mg/cm^2 of powdered sample. Preparation of the CO-loaded sample was accomplished by attaching a glass tube containing activated **1** to a Micromeritics ASAP 2020 Surface Area and Porosity Analyzer, dosing with 1 bar of CO at 295 K, and allowing the sample to equilibrate for 1 h. The sample was then cooled to 77 K and evacuated, and immediately transferred to the spectrometer.

5.2.8. Dc magnetic susceptibility measurements. Samples were prepared by adding crystalline powder (14 mg for **1**, 28 mg for **1**·2CO) to a 5 mm inner-diameter quartz tube containing a raised quartz platform. Sample powders were restrained with a plug of compacted glass wool that prevented crystallite torqueing, but enabled gas-dosing with CO. Preparation of the CO-loaded samples was accomplished by attaching the quartz tubes containing activated **1** to a Micromeritics

ASAP 2020 gas adsorption analyzer. Adsorption isotherms were then collected until the pressure of the atmosphere of CO gas in the sample tubes reached 300 mbar of CO, at which point the measurements were terminated. The quartz tubes were then cooled in liquid N_2 and flame-sealed. Magnetic susceptibility measurements were performed using a Quantum Design MPMS2 SQUID magnetometer. Dc magnetic susceptibility measurements were collected in the temperature range 2-300 K under applied magnetic fields of 1 T. Diamagnetic corrections were applied to the data using Pascal's constants to give χ_D = –0.00014752 emu/mol for **1** and χ_D = –0.00016872emu/mol for **1**·2CO.

5.2.9. Differential scanning calorimetry. Heat capacity measurements were collected on a TA Instruments Q200 differential scanning calorimeter (DSC) equipped with a refrigerated cooling system RSC90 under a He flow. Baseline data for the empty heating chamber was collected between the temperatures of –90 and 400 °C, followed by a temperature calibration using the melting point of an indium sample. A sample of **1** (5.5 mg) was hermetically sealed in an aluminum pan under an N_2 atmosphere. The heat flow data were collected by using a modulated DSC program with a temperature ramp rate of 2 °C/min in the temperature range of –20 to 150 °C, using a temperature modulation of ± 0.75 °C per 80 s using a standard modulated DSC method and TA Instruments software.

5.3. Results and discussion

5.3.1. Structure and properties of frameworks 1 and 2. We synthesized microcrystalline powders of **1** and **2**, and powder X-ray diffraction data show both materials to be isostructural to previously reported analogues.[20,24,25] In the desolvated forms of these compounds, helical chains of square pyramidal iron(II) centers, each ligated by three triazolates and two chlorides, are linked into a highly porous three-dimensional framework that features a hexagonal array of one-dimensional channels (Figure 5.2). Neighboring iron sites along the chains are 3.361(5) Å apart in **1** and 3.602(7) Å apart in **2** (the number in parentheses is the estimated standard deviation in the final digit) and are tightly interconnected, with each chloride and triazolate moiety bridging two and three separate iron sites, respectively.

The structure of the iron(II)–triazolate chains in **1** suggests that the coordination environment of one metal site will be highly sensitive to electronically induced structural changes at adjacent sites. Indeed, the CO adsorption isotherm of **1** collected at 25 °C has a prominent step, with a sharp rise occurring at 170 mbar (Figure 5.1c). Analysis of the isotherm data resulted in a Hill coefficient of 10.7 during the transition, suggesting a high degree of cooperativity (Figure 5.S17). The bound CO is readily released in a similar step-shaped isotherm upon decreasing CO pressure, with a hysteresis width of approximately 120 mbar (Figure 5.S11), and complete regeneration of the material is observed over successive adsorption/desorption cycles (Figure 5.S15).

5.3.2. Characterization of the spin transition mechanism. To investigate the mechanism for the unusual adsorption of CO, we analysed powder X-ray diffraction data for activated and CO-dosed samples of **1**. Unlike most materials that have step-shaped isotherms, in which unit-cell expansions are observed upon gas loading owing to a gate-opening mechanism,[15,16] adsorption of CO causes substantial structural contractions in **1** (Figure 5.3). Whereas the activated material has Fe–N and Fe–Cl bond lengths of 2.11(2) Å and 2.385(6) Å, respectively, the CO-bound material (**1**·2CO) has contracted Fe–N and Fe–Cl bond distances of 1.972(5) Å and 2.259(4) Å, respectively. These changes in bond length are consistent with a conversion from high-spin to low-

spin iron(II).[18,26] The assignment of low-spin iron(II) in **1**·2CO is further supported by a Fe–C_{CO} bond length of 1.76(4) Å and a nearly linear Fe–C–O bond angle.[18]

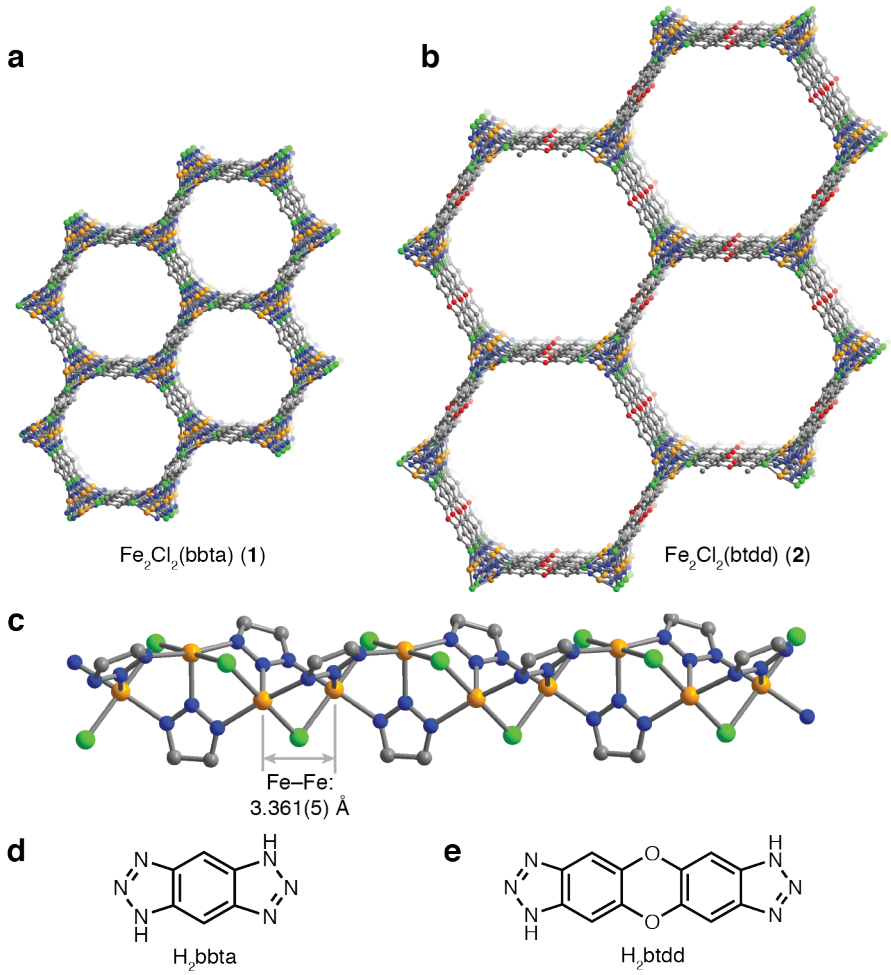

Figure 5.2. Solid state structures of **1** and **2**. Portions of the structures of **1** (**a**) and **2** (**b**) determined from analysis of powder X-ray diffraction data, showing the hexagonal array of one-dimensional channels, which are lined with a high concentration of coordinatively-unsaturated iron(II) sites. Structure of a helical iron–chloride–triazolate chain running along the *c* axis in **1**, with the proximity of adjacent iron centers highlighted (**c**). Structures of the linker precursors H_2bbta for **1** (**d**) and H_2btdd for **2** (**e**). For (**a**)-(**c**), grey, green, orange, blue, and red spheres represent C, Cl, Fe, N, and O atoms, respectively, and H atoms are omitted for clarity.

Remarkably, *in situ* powder X-ray diffraction studies performed on **1** revealed no detectable intermediates between the high- and low-spin phases, suggesting that the spin transition, once triggered, occurs simultaneously and cooperatively throughout an entire crystallite. A sample of **1** sealed under 300 mbar of CO was subjected to repeated heating and cooling cycles (Figure 5.3c). Above 52 °C, even in the presence of CO, we observed a single phase corresponding to all high-spin iron(II). Cooling resulted in the appearance of a distinct new phase with a smaller unit-cell volume, corresponding to the low-spin, CO-bound iron phase. By 25 °C, the conversion to low-spin was complete, as expected from the adsorption data.

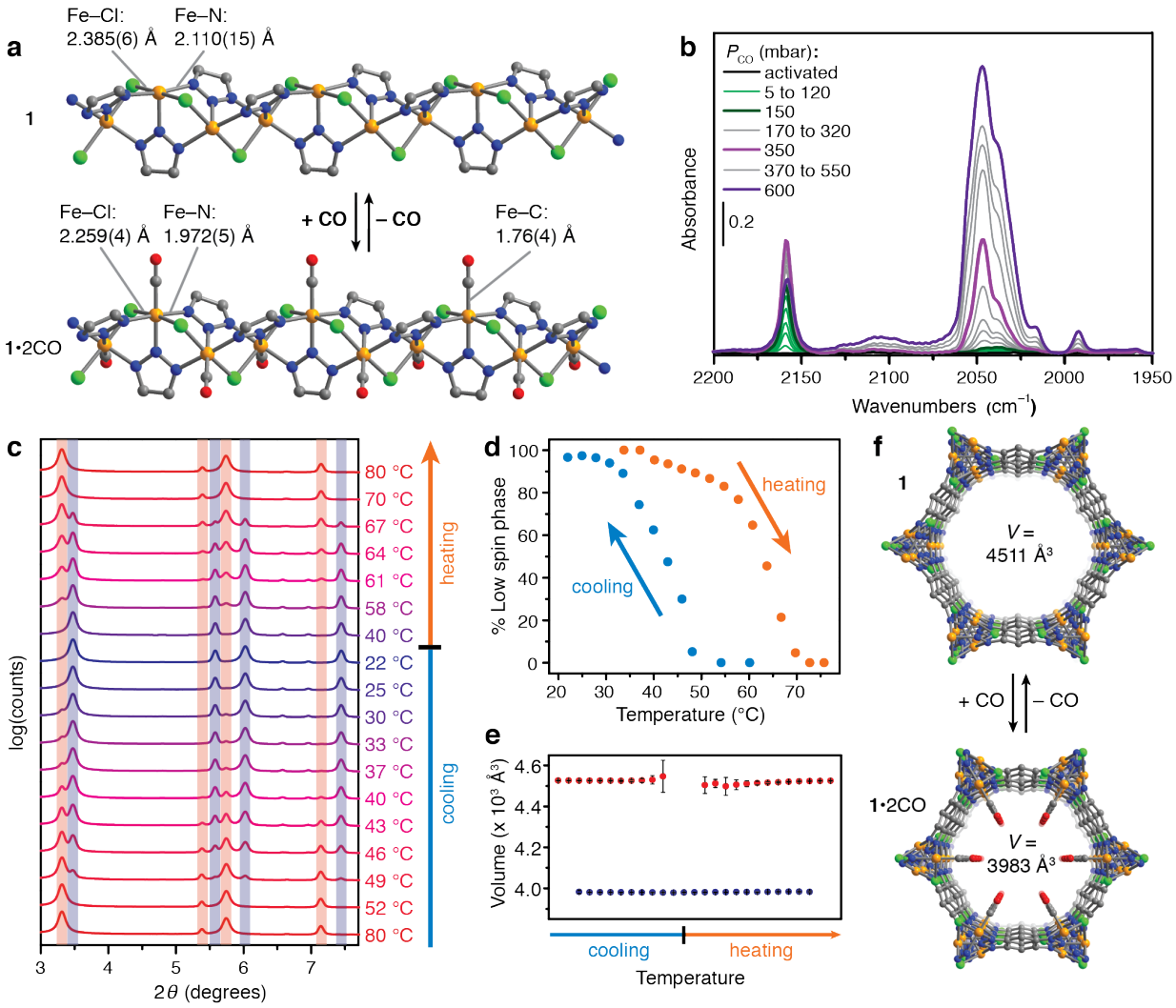

Figure 5.3. Characterization of the spin transition mechanism. Portions of the structures of **1** and **1**·2CO, with selected bond lengths indicated (**a**). Infrared spectra of **1** collected at 25 °C at various pressures of CO (**b**). All spectra are shown as the difference with respect to the spectrum of the activated sample, with the gas phase CO spectra subtracted. Powder X-ray diffraction data for **1** under 300 mbar of CO collected at various temperatures with a wavelength of 0.72768 Å (**c**). Peaks corresponding to the high-spin phase are shaded in red and peaks corresponding to the low-spin, CO-bound phase are shaded in blue (**c**). Weight fraction (%) of the low-spin phase, as determined from Rietveld refinements against the diffraction data, as a function of temperature upon heating (orange circles) and cooling (light blue circles) (**d**). Unit cell volume of the low-spin, CO-bound component (blue circles) and high-spin component (red circles) for each diffraction pattern collected during heating or cooling, with error bars shown in black, demonstrating the stability of each phase at all relevant temperatures (**e**). Unit cell volume comparison of the high-spin phase **1** and low-spin, CO-bound phase **1**·2CO (**f**). For (**a**) and (**f**), grey, green, orange, blue, and red spheres represent C, Cl, Fe, N, and O atoms, respectively, and H atoms are omitted for clarity.

Mössbauer spectra and dc magnetic susceptibility measurements corroborate the iron(II) spin transition from high- to low-spin, or $S = 2$ to $S = 0$. The Mössbauer spectrum of **1** obtained at 100 K showed one dominant iron site (Figure 5.S19), with an isomer shift of $\delta = 1.084(2)$ mm s^{-1} and a quadrupole splitting of $\Delta E_Q = 1.928(6)$ mm s^{-1}, typical of square pyramidal high-spin iron(II) species.[18,26] Upon *ex situ* dosing of CO, data collection at 100 K revealed a different species, with $\delta = 0.364(2)$ mm s^{-1} and $\Delta E_Q = 0.989(4)$ mm s^{-1}, consistent with low-spin iron(II). Before dosing with CO, we determined the molar magnetic susceptibility (χ_M) times temperature (T), $\chi_M T$, at 300 K to be 3.45 emu·K/mol Fe, consistent with all high-spin iron(II). After dosing with CO, this value was greatly diminished, reaching only 0.6 emu·K/mol Fe at 300 K (Figure 5.S20). This result again corroborates the spin transition from $S = 2$ to $S = 0$, with the slight residual magnetic moment attributed to incomplete saturation of CO during the experiment.

Infrared spectroscopy was used to probe the nature of the adsorbed CO in **1** at all pressures, including before the adsorption step (Figure 5.3b). Below 150 mbar, weakly bound CO with a stretching frequency of ν_{CO} = 2,157 cm^{-1} was observed. Compared to free CO, for which ν_{CO} = 2,143 cm^{-1}, this blue-shifted resonance is attributed to high-spin iron(II)–CO adducts.[27] Upon increasing the pressure past the expected step pressure of 170 mbar, new peaks appear at 2,048 cm^{-1} and 2,039 cm^{-1}, which closely match previously reported values for low-spin iron(II)–CO species.[19] These peaks quickly increase in intensity with increasing CO pressure, suggesting that the majority of the adsorbed CO is bound to low-spin iron(II) after the step.

Combining the structural, magnetic and spectroscopic studies, we propose the following mechanism for the step-shaped CO adsorption isotherm. The proximity and interconnectedness of the iron(II) sites in **1** creates a barrier to the structural rearrangements that are required for the spin-state conversion of a single iron center. Therefore, at low pressures of CO, the spin state of an individual iron site cannot convert and remains high-spin. However, once a threshold pressure of CO is reached, the transition becomes favorable, at which point all of the iron sites in a crystallite simultaneously convert to the low-spin state. This behavior is reminiscent of the pressure-induced phase transformations that are observed in flexible materials,[15,16] but involves a specific adsorbate-induced electronic response at an open metal site. This design allows **1** to behave similarly to responsive adsorbents in biological systems.

5.3.3. Gas adsorption. Having confirmed the cooperative nature of the spin transition and CO adsorption, we compared the working capacities, regeneration energies, and selectivities of **1** with other leading materials for CO separations. In an industrial context, CO is an intermediate in the conversion of natural gas, biomass, and other carbon feedstocks into valuable products, typically through the Fischer–Tropsch process.[11] However, adjusting the H_2:CO ratio in syngas produced from various sources and for every product is energetically costly. Other sources of CO, such as that produced during steel production or coal gasification, are contaminated with N_2, CO_2, and hydrocarbons. These vast resources are usually wasted, and in many instances are burned, accounting for a large portion of the 2.5 Gt of CO_2 produced annually from iron and steel production.[28] Current CO separations generally use energetically costly cryogenic distillation, and liquid- or membrane-based adsorption processes have not been widely implemented.[29] Porous materials, including metal–organic frameworks, have been investigated for CO separations, but face selectivity issues or need improvements in working capacity.[19,27,30,31]

Adsorption isotherms obtained at multiple temperatures show that the step pressure of **1** has a pronounced temperature dependence (Figure 5.4a). A change in temperature of only 5 °C (25 to 30 °C) results in an 80 mbar increase in step pressure (Figure 5.S11), and similar shifts occur in the desorption isotherms. Standard temperature swing adsorption processes should recover nearly

all of the CO adsorbed without the need for a purge gas if the desorption step pressure is above 1 bar, which occurs near 60 °C in **1**. As an example of a working process, adsorption at 200 mbar and 20 °C and desorption at 1 bar and 60 °C (a temperature swing of only 40 °C) corresponds to a CO removal capacity of 11.4 wt %. This is a much greater working capacity than has been achieved using the best non-cooperative adsorbents, which are estimated to require temperature swings in excess of 100 °C to achieve comparable working capacities (Figure 5.4b).[27] Notably, unlike classical adsorbents, **1** only requires the step position to be lower than the CO partial pressure to achieve these high working capacities, so higher adsorption temperatures can be used in gas mixtures with higher partial pressures of CO.

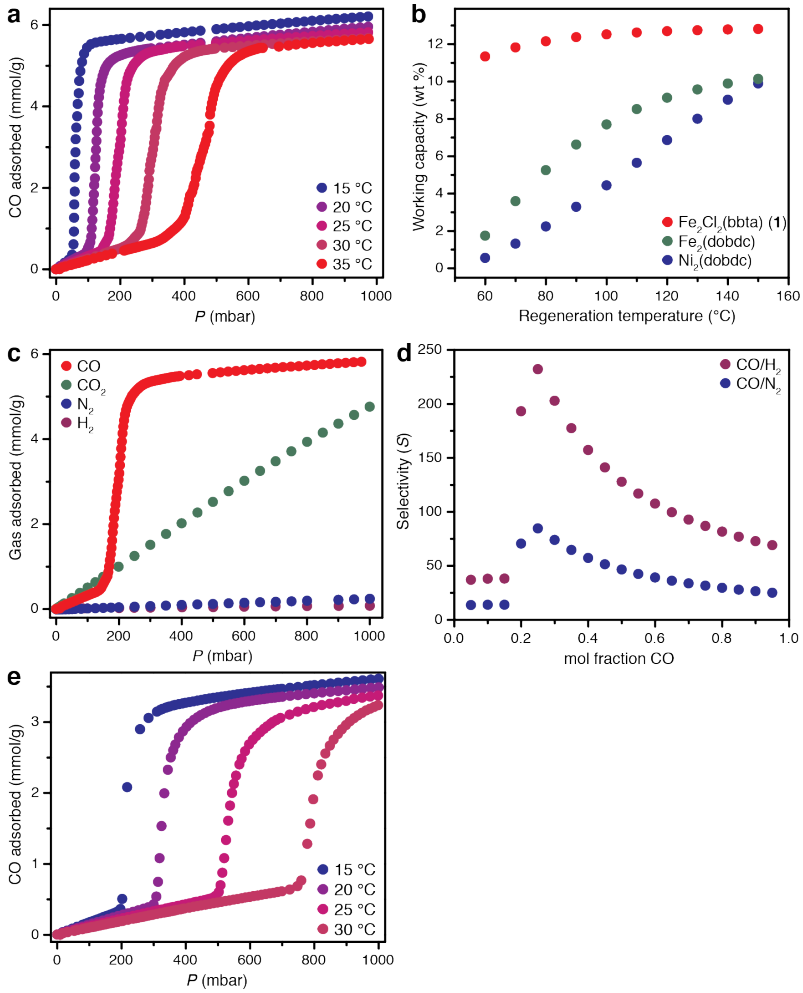

Figure 5.4. Gas adsorption isotherms, working capacities, and molar selectivity values. Adsorption isotherms of CO collected for **1** (**a**). Comparison of the working capacities for **1** with those calculated for the classical CO adsorbents Fe_2(dobdc) and Ni_2(dobdc) (dobdc^{4-} = 1,4-dioxido-2,5-benzenedicarboxylate), with adsorption at 0.2 bar and 20 °C and desorption at 1.0 bar and the specified temperatures (**b**). Single-component adsorption isotherms of CO, CO_2, N_2, and H_2 for **1** collected at 25 °C (**c**). Molar selectivity (*S*) values for mixtures of CO and selected gases at varying concentrations for 25 °C and 1.0 bar of total pressure in **1**, with the step position occurring at approximately 0.2 mol fraction CO (**d**). Adsorption isotherms of CO collected for **2** (**e**), demonstrating the different adsorption properties caused by the different ligand environment of the Fe^{II} centers compared to those in **1 (a)**.

The cooperative adsorption mechanism enables highly efficient regeneration of the adsorbent. Using differential scanning calorimetry data to calculate the heat capacities of **1** (Figure 5.S21) and the Clausius–Clapeyron relation to calculate the isosteric heats of CO adsorption (−66 kJ mol^{-1}, Figure 5.S14), regeneration energies as low as 2.66 MJ/kg CO were obtained, with adsorption at 20 °C at 200 mbar and desorption at 60 °C and 1 bar, and without using any purge gas. For comparison, the COSORB process, a leading alternative to cryogenic distillation, requires up to 8.31 MJ/kg CO for regeneration.[32]

To test the selectivity of **1** in CO separation applications, we measured the pure-component adsorption isotherms of other gases. At 25 °C, **1** adsorbs much less H_2 and N_2 than CO (Figure 5.4c). We calculated the molar selectivity from the pure component isotherms to be 232 for a 1:3 CO:H_2 ratio at 25 °C and 1.0 bar of total pressure, with similarly high selectivities obtained for CO/N_2 mixtures (Figure 5.4d). These high selectivity values demonstrate the utility of **1** for potential CO separations. Unlike most CO adsorbents featuring exposed metal sites, the spin-state transition mechanism enables **1** to bind CO selectively over more polarizable gas molecules such as CO_2.[19] For all pressures above the step pressure, **1** adsorbed more CO than CO_2 and demonstrated a stronger binding enthalpy of −66 kJ mol^{-1} compared to −23 kJ mol^{-1} for CO_2, indicating the potential for selective CO adsorption even in the presence of typically more strongly adsorbing species.

Because spin transitions are highly sensitive to changes in the ligand field of the transition metal[26] and even to subtle outer-sphere changes,[33] we hypothesized that simple electronic modifications to the linker could result in substantial changes in the adsorption properties. Therefore, we replaced $bbta^{2-}$ with $btdd^{2-}$ to form the isotypic metal–organic framework **2** (Figure 5.2b). This new linker results in subtle electronic differences in the iron environment owing to its ether moieties. Analogous to those observed in **1**, adsorption isotherms of CO in **2** display sharp steps, indicating a similar adsorption mechanism (Figure 5.4e). However, the step position at each temperature shifted considerably, from 170 mbar in **1** to 500 mbar in **2** at 25 °C. Other synthetic modifications to the triazolate ligand or to the bridging halide could be used to create systems with different step positions. Such tunability provides a means of customizing materials within this class of cooperative adsorbents, because the position of the adsorption step can be optimized for a given CO separation, dictated by the temperature and partial pressure of CO in a gas mixture. Moreover, by utilizing this tunability to further strengthen the ligand field at the iron(II) centers, it should be possible to realize analogous metal–organic frameworks exhibiting cooperative adsorption of other gas molecules that can act as strong field ligands, including acetylene, ethylene, propylene, and possibly even dinitrogen. Indeed, this new cooperative spin transition mechanism provides a potentially powerful means with which to tune an adsorbent so as to separate molecules efficiently by ligand field strength.

5.4. Conclusions and outlook

Our results demonstrate that new metal–organic frameworks can be created for the cooperative adsorption of a target molecule. By assembling structures wherein a selective binding event at one site will influence adsorption at neighboring sites connected within an extended network, this approach can in principle be applied to cooperative adsorption of other substrates for a wide variety of applications. Extension of this emerging family of cooperative adsorbents to the selective adsorption of other key industrial gases, such as N_2, O_2, ethylene, and propylene, stands to revolutionize the means by which energy-intensive gas separations are performed.

5.5. Acknowledgements

This research was supported through the Center for Gas Separations Relevant to Clean Energy Technologies, an Energy Frontier Research Center funded by the U.S. Department of Energy, Office of Science, Office of Basic Energy Sciences under Award DE-SC0001015. Powder X-ray diffraction data were collected at Beamline 11-BM and Beamline 17-BM at the Advanced Photon Source, a DoE Office of Science User Facility, operated by Argonne National Laboratory under Contract DE-AC02-06CH11357. The National Science Foundation provided graduate fellowship support.

5.6. References and supplementary information

(1) Perutz, M. F. *Mechanism of Cooperativity and Allosteric Regulation in Proteins*. Cambridge University Press: Cambridge, 1990.
(2) Perrella, M.; Di Cera, E. *J. Biol. Chem.* **1999**, *274*, 2605–2608.
(3) McDonald, T. M.; Mason, J. A.; Kong, X.; Bloch, E. D.; Gygi, D.; Dani, A.; Crocella, V.; Giordanino, F.; Odoh, S. O.; Drisdell, W.; Vlaisavljevich, B.; Dzubak, A. L.; Poloni, R.; Schnell, S. K.; Planas, N.; Lee, K.; Pascal, T.; Wan, L. F.; Prendergast, D.; Neaton, J. B.; Smit, B.; Kortright, J. B.; Gagliardi, L.; Bordiga, S.; Reimer, J. A.; Long, J. R. *Nature* **2015**, *519*, 303–308.
(4) Caskey, S. R.; Wong-Foy, A. G.; Matzger, A. J. *J. Am. Chem. Soc.* **2008**, *130*, 10870–10871.
(5) Sumida, K.; Rogow, D. L.; Mason, J. A.; McDonald, T. M.; Bloch, E. D.; Herm, Z. R.; Bae, T.-H.; Long, J. R. *Chem. Rev.* **2012**, *112*, 724–781.
(6) Herm, Z. R.; Bloch, E. D.; Long, J. R. *Chem. Mater.* **2014**, *26*, 323–338.
(7) Xiao, D. J.; Gonzalez, M. I.; Darago, L. E.; Vogiatzis, K. D.; Haldoupis, E.; Gagliardi, L.; Long, J. R. *J. Am. Chem. Soc.* **2016**, *138*, 7161–7170.
(8) Kahn, O.; Martinez, C. J. *Science* **1998**, *279*, 44–48.
(9) Niel, V.; Martinez-Agudo, J. M.; Munoz, M. C.; Gaspar, A. B.; Real, J. A. *Inorg. Chem.* **2001**, *40*, 3838–3839.
(10) Foucher, D. A.; Honeyman, C. H.; Nelson, J. M.; Tang, B. Z.; Manners, I. *Angew. Chem., Int. Ed.* **1993**, *32*, 1709–1711.
(11) Kerry, F. G. *Industrial Gas Handbook: Gas Separation and Purification*; CRC: Boca Raton, FL, 2007.
(12) Zhou, H. C.; Long, J. R.; Yaghi, O. M. *Chem. Rev*. **2012**, *112*, 673–674.
(13) Furukawa, H.; Cordova, K. E.; O'Keeffe, M.; Yaghi, O. M. *Science* **2013**, *341*, 123044.
(14) Li, J.-R.; Kuppler, R. J.; Zhou, H.-C. *Chem. Soc. Rev*. **2009**, *38*, 1477–1594.
(15) Schneeman, A.; Bon, V.; Schwelder, I.; Senkovska, I.; Kaskel, S.; Fisher, R. A. *Chem. Soc. Rev.* **2014**, *43*, 6062–6096.
(16) Serre, C.; Bourrelly, S.; Vimont, A.; Ramsahye, N. A.; Maurin, G.; Llewellyn, P. L.; Daturi, M.; Filinchuk, Y.; Leynaud, O.; Barnes, P.; Ferey, G. *Adv. Mater*. **2007**, *19*, 2246–2251.
(17) Walton, K. S.; Millward, A. R.; Dubbeldam, D.; Frost, H.; Low, J. J.; Yaghi, O. M.; Snurr, R. Q. *J. Am. Chem. Soc.* **2008**, *130*, 406–407.
(18) Benito-Garagorri, D.; Lagoja, I.; Veiros, L. F.; Kirchner, K. A. *Dalton Trans.* **2011**, *40*, 4778–4792.

(19) Reed, D. A.; Xiao, D. J.; Gonzalez, M. I.; Darago, L. E.; Herm, Z. R.; Grandjean, F.; Long, J. R. *J. Am. Chem. Soc.* **2016**, *138*, 5594–5602.
(20) Liao, P.-Q.; Li, X.-Y.; Bai, J.; He, C.-T.; Zhou, D.-D.; Zhang, W.-X.; Zhang, J.-P.; Chen, X.-M. *Chem. Eur. J.* **2014**, *20*, 11303–11307.
(21) Denysenko, D.; Grzywa, M.; Tonigold, M.; Streppel, B.; Krkljus, I.; Hirscher, M.; Mugnaioli, E.; Kolb, U.; Hanss, J.; Volkmer, D. *Chem. Eur. J.* **2011**, *17*, 1837–1848.
(22) Coelho, A. A. *J. Appl. Crystallogr.* **2003**, *36*, 86–95.
(23) Coelho, A. A. *TOPAS-Academic*, *Version 4.1*. Coelho Software, 2007.
(24) Liao, P.-Q.; Chen, H.; Zhou, D.-D.; Liu, S.-Y.; He, C.-T.; Rui, Z.; Ji, H.; Zhang, J.-P.; Chen, X.-M. *Energy Environ. Sci.* **2015**, *8*, 1011–1016.
(25) Reith, A. J.; Tulchinsky, Y.; Dinca, M. *J. Am. Chem. Soc.* **2016**, *138*, 9401–9404.
(26) Garcia, Y.; Niel, V.; Munoz, M. C.; Real, J. A. *Top. Curr. Chem.* **2004**, *233*, 229–257.
(27) Bloch, E. D.; Hudson, M. R.; Mason, J. A.; Chavan, S.; Crocella, V.; Howe, J. D.; Lee, K.; Dzubak, A. L.; Queen, W. L.; Zadrozny, J. M.; Geier, S. J.; Lin, L. C.; Gagliardi, L.; Smit, B.; Neaton, J. B.; Bordiga, S.; Brown, C. M.; Long, J. R. *J. Am. Chem. Soc*. **2014**, *136*, 10752–10761.
(28) International Energy Agency. *Global Action to Advance Carbon Capture and Storage: A Focus on Industrial Applications*. <http://www.iea.org/publications/freepublications/publication/CCS_Annex.pdf>. **2013**.
(29) Dutta, N. N.; Patil, G. S. *Gas. Sep. Purif.* **1995**, *9*, 277–283.
(30) Sato, H.; Kosaka, W.; Matsuda, R.; Hori, A.; Hijikata, Y.; Belosludov, R. V.; Sakaki, S.; Takata, M.; Kitagawa, S. *Science* **2014**, *343*, 167–170.
(31) Peng, J.; Xian, S.; Xiao, J.; Huang, Y.; Xia, Q.; Wang, H.; Li, Z. *Chem. Eng. J.* **2015**, *270*, 282–289.
(32) Air Products and Chemicals, Inc. Davis, R. A.; Nicholas, D. M.; Smith, D. D.; Wang, S.-I.; Wright, R. A. *Integrated reformer process for the production of carbon black*. U.S. Patent Number 5,011,670. 1991.
(33) Halder, G. J.; Kepert, C. J.; Moubaraki, B.; Murray, K. S.; Cashion, J. D. *Science*. **2002**, *298*, 1762–1765.
(34) Dollase, W. A. *J. Appl. Cryst*. **1986**, *19*, 267-272.
(35) Dassault Systèmes BIOVIA, *Materials Studio, Version 5.0*. Dassault Systèmes, 2009.
(36) Spek, A. L. *Acta Cryst.* **2009**, *D65*, 148-155.
(37) Myers, A. L.; Prausnitz, J. M. *AIChE J*. **1965**, *11*, 121−127.
(38) Bloch, E. D.; Murray, L. M.; Queen, W. L.; Chavan, S.; Maximoff, S. N.; Bigi, J. P.; Krishna, R.; Peterson, V. K.; Grandjean, F.; Long, G. J.; Smit, B.; Bordiga, S.; Brown, C. M.; Long, J. R. *J. Am. Chem. Soc.* **2011**, *133*, 14814–14822.

Supplementary Discussion

Structure solution and Rietveld refinement of $Fe_2Cl_2(bbta)$. The previously reported crystal structure of the isostructural $Mn_2Cl_2(bbta)$,[20] with Mn atoms replaced by Fe atoms, was used as a starting structural model for the Rietveld refinement. Prior to the refinement, precise unit cell parameters were obtained by Le Bail fitting implemented in TOPAS-Academic.[23] In the initial stages of the refinement, C–O, C–N and C–C distances were restricted with "soft" constraints, and the $bbta^{2-}$ ligand was constrained to be flat. Single refined isotropic thermal parameters were assigned to the Fe and Cl atoms, together with one single isotropic thermal parameter for all of the atoms of the $bbta^{2-}$ ligand. H atoms were placed on calculated positions. Thermal parameters, and sample and instrument parameters were fully refined together with the background parameters. Preferred orientation was detected and corrected with the March-Dollase formulation.[34] The calculated diffraction pattern for the final structural model of $Fe_2Cl_2(bbta)$ is in excellent agreement with the experimental diffraction pattern as seen in the Rietveld plot in Figure 5.S1 and crystallographic details in Table 5.S3.

Structure solution and Rietveld refinement of CO-dosed $Fe_2Cl_2(bbta)$. Precise unit cell parameters of the CO-dosed $Fe_2Cl_2(bbta)$ were obtained by Le Bail fitting. Using the refined structure of $Fe_2Cl_2(bbta)$ as a starting model, a Fourier difference map was calculated after a Rietveld refinement. Excess electron density was observed above the Fe centers at a distance expected for adsorbed CO. Additionally, excess electron density was observed directly above the Fe, suggesting that the Fe centers move slightly out of the equatorial ligand plane after CO dosing.

During of the refinement, the C–O, C–C, and C–N bond distances were restricted with "soft" constraints, and the $bbta^{2-}$ ligand was constrained to be flat. Single refined isotropic thermal parameters were assigned to the Fe atom, the Cl atom, the C atom of CO, and the O atom of CO. A single isotropic thermal parameter was assigned to all atoms of the $bbta^{2-}$ ligand. H atoms were placed on calculated positions. In the final stages of the refinement, the CO occupancy and thermal and unit cell parameters were fully refined with no constraints, convoluted with the sample and instrument parameters and Chebyshev background polynomials. As with the activated $Fe_2Cl_2(bbta)$ sample, the diffraction data required a preferred orientation correction in the March-Dollase formulation.[34] The calculated diffraction pattern for the final structural model of CO-dosed $Fe_2Cl_2(bbta)$ is in excellent agreement with the experimental diffraction pattern (Rietveld plot in Figure 5.S2 and figures-of-merit in Table 5.S4).

Rietveld refinement of $Fe_2Cl_2(bbta)$ Cycling Data. *In situ* powder X-ray diffraction were performed at APS Beamline 17-BM while a sample of $Fe_2Cl_2(bbta)$ sealed under 300 mbar of CO gas was cycled between the temperatures 273 K and 353 K. The sample was measured every minute for four cycles, with rates of change in temperature varying between 3 K/min and 6 K/min. Depending on the temperature during the course of the experiment, the sample switched between two distinct phases whose crystal structures are analogous to those refined for $Fe_2Cl_2(bbta)$ (at high temperatures) and CO-dosed $Fe_2Cl_2(bbta)$ (at low temperatures).

In order to monitor the quantitative phase change between the two crystal structures as a function of temperature, Rietveld refinements were performed on diffraction data collected during the cycling experiment. In these two-phase refinements, all atomic coordinates of the structural models of low-spin and high-spin phases ($Fe_2Cl_2(bbta)$ and CO-dosed $Fe_2Cl_2(bbta)$, respectively) were fixed. The sample and instrumental parameters, together with the Chebyshev background polynomials, the scale factors, and the weight fractions of the low-spin and high-

spin phases were refined for each pattern. To confirm the validity of the refinements, $R_{wp,}$ unit cell volumes, and unit cell volume errors for each pattern were extracted and plotted (Figures 5.S4-5.S5).

Structure solution and Rietveld refinement of Fe_2Cl_2(btdd). While crystalline, the powder X-ray diffraction pattern of Fe_2Cl_2(btdd) does not contain enough high-angle data to allow for *ab initio* methods of crystal structure solution. Therefore, the starting model was based on the refined crystal structure of Fe_2Cl_2(bbta). The symmetry of the initial Fe_2Cl_2(bbta) model was converted to P_1, and then, keeping the iron coordination sphere constant, the linker was extended from the original $bbta^{2-}$ to $btdd^{2-}$ in the program Materials Studio.[35] The structural model was then optimized using the Forcite module of Materials Studio. The resulting model was converted to the correct space group of *R*-3*m* by the ADDSYM module of PLATON[36] and was then used to perform a Rietveld refinement of the activated Fe_2Cl_2(btdd) powder pattern in TOPAS-Academic.

Precise unit cell parameters of Fe_2Cl_2(btdd) were first obtained by Le Bail fitting. In the initial stages of the refinement the $btdd^{2-}$ ligand itself was not refined, and the Fe and Cl atoms positions were varied freely, together with the isotropic thermal parameters for the Fe and Cl atoms and a single isotropic thermal parameter assigned to all atoms of the $btdd^{2-}$ ligand. Once the positions of the Fe and Cl atoms were determined, soft constraints were placed on all C–C, C–N, and C–O bond distances and angles and the atomic positions (with the exception of those for H). Thermal parameters, and sample and instrument parameters were fully refined together with the background parameters. The resulting calculated diffraction pattern for the final structural model of Fe_2Cl_2(btdd) is in excellent agreement with the experimental diffraction pattern (Rietveld plot shown on Figure 5.S7 and figures-of-merit given in Table 5.S5).

While the constraints on C–C, C–N, and C–O bond distances and angles could not be removed without resulting in chemically unreasonable ligand bond distances, an unconstrained refinement did not significantly alter the overall structure of the framework, confirming that the structural model obtained is a reasonable approximation of the average crystal structure of the compound.

Structure solution and Rietveld refinement of CO-dosed Fe_2Cl_2(btdd). Precise unit cell parameters of the CO-dosed Fe_2Cl_2(btdd) were first obtained by Le Bail fitting. Using the refined structure of Fe_2Cl_2(btdd) as a starting model, a Fourier difference map was calculated after a Rietveld refinement of the CO-dosed Fe_2Cl_2(btdd). Excess electron density was clearly observed above the Fe centers at a distance expected for adsorbed CO. The difference map was used as an initial guide for the placement of the C and O atoms of the adsorbed CO molecule before being optimized in later refinements.

The Fe and Cl atoms were allowed to refine freely, with separate isotropic thermal parameters assigned to the Fe atom, the Cl atom, the C atom of CO, and the O atom of CO. A separate isotropic thermal parameter was assigned to all atoms of the $btdd^{2-}$ ligand and refined, and the atom positions of the ligand were refined with "soft" constraints. Thermal parameters, and sample and instrument parameters were fully refined together with the background parameters. The calculated diffraction pattern for the final structural model of CO-dosed Fe_2Cl_2(btdd) is in excellent agreement with the experimental diffraction pattern (Rietveld plot shown on Figure 5.S8 and figures-of-merit given in Table 5.S6). Additionally, the structural model obtained is consistent with the crystal structure of CO-dosed Fe_2Cl_2(bbta).

Selectivity for CO adsorption. Selectivity for CO over H_2 and N_2 are presented as a simple selectivity parameter (*S*) in **1** by comparing the amount adsorbed at each gas (*q*) at a given

pressure (p) using Eqn 5.1 in each of the single component isotherms, with two gases a and b. The values for q were calculated by using the fit provided by the piecewise Langmuir-Freundlich equation (for CO) or single-site Langmuir equation (for H_2 and N_2).

$$S = \frac{q_\mathrm{a}/p_\mathrm{a}}{q_\mathrm{b}/p_\mathrm{b}} \tag{5.1}$$

While these values are indicative of a very selective separation, S is not necessarily the most accurate method, as the material after dosing with CO is a different material. Unfortunately, models that utilize competitive binding such as Ideal Adsorbed Solution Theory (IAST)[37] cannot be used here due to the phase change. In general, these adjusted values determined by IAST are significantly greater, meaning the numbers reported in this study should serve as a lower bound for adsorption selectivity. This presents an intriguing area for further study.

Isotherm fitting and isosteric heat of adsorption calculations. In order to calculate isosteric heats of adsorption, Q_st, as a function of CO loading, adsorption data for **1** and **2** was fit with a mathematical model. Due to the sharp step in many of the CO adsorption isotherms, a piecewise function (Eqn 5.2)[3] was employed to describe both the pre-step and post-step CO adsorption, n, at each temperature. Specifically, when the pressure, p, is less than the step pressure, p_step, at a given temperature, T, the isotherm is modeled using a single-site Langmuir-Freundlich equation where R is the ideal gas constant in J mol^{-1} K^{-1}, n_sat is the saturation capacity in mmol/g, S is the integral entropy of adsorption at saturation in units of R, H is the differential enthalpy of adsorption in kJ/mol, and v is the Freundlich parameter. When the p is greater than p_step, the isotherm is modeled using a dual-site Langmuir-Freundlich equation, with two adsorption sites a and b, for which p has been offset by p_step. The temperature dependence of p_step is described using the Clausius-Clapeyron relation (Eqn 5.3). Here, p_step is a function of the step pressure at an initial temperature, $p_\mathrm{step,T0}$, the initial temperature T_0, and the enthalpy of the phase transition that is associated with the step, H_step. The stepped CO adsorption isotherms of **1** and **2** collected at 20, 25, and 30 °C are fit simultaneously with one set of parameters for each sample. We note that there is a slight discontinuity when p is just above p_step and n is less than $n(p_\mathrm{step})$, but this does not significantly affect the isosteric heat of adsorption calculations. All parameters are listed in Table 5.S7.

$$n(p,T) = \begin{cases} \dfrac{n_{\mathrm{sat},1} e^{S_1} e^{-H_1/RT} p^{v_1}}{1 + e^{S_1} e^{-H_1/RT} p^{v_1}} \\ \dfrac{n_{\mathrm{sat,2a}} e^{S_\mathrm{2a}} e^{-H_\mathrm{2a}/RT} (p - p_\mathrm{step})^{v_\mathrm{2a}}}{1 + e^{S_\mathrm{2a}} e^{-H_\mathrm{2a}/RT} (p - p_\mathrm{step})^{v_\mathrm{2a}}} + \dfrac{n_{\mathrm{sat,2b}} e^{S_\mathrm{2b}} e^{-H_\mathrm{2b}/RT} (p - p_\mathrm{step})^{v_\mathrm{2b}}}{1 + e^{S_\mathrm{2b}} e^{-H_\mathrm{2b}/RT} (p - p_\mathrm{step})^{v_\mathrm{2b}}} \end{cases} \tag{5.2}$$

$$p_\mathrm{step}(T) = p_{\mathrm{step,T}_0} e^{\left(\frac{H_\mathrm{step}}{R}\right)\left(\frac{1}{T} - \frac{1}{T_0}\right)} \tag{5.3}$$

The isosteric heats of adsorption (Q_st) can be calculated by solving Eqn 2 for explicit values of n at a minimum of 3 temperatures, in this case 20, 25, and 30 °C. The isosteric heats of adsorption as a function of the amount of CO adsorbed can then be determined using the integrated form of the Clausius-Clapeyron equation (Eqn 5.4) by calculating the slope of ln(p) vs $1/T$ for each loading.

$$(\ln p)_n = \left(\frac{Q_{st}}{R}\right)\left(\frac{1}{T}\right) + C \quad (5.4)$$

Isotherms for H_2, N_2, and CO_2 were fit using standard Langmuir adsorption models shown in Eqn 5.5, from which Eqn 5.2 was derived, and in the case of CO_2 isotherms collected at 25, 35, and 45 °C were used to calculate isosteric heats of adsorption using Eqn 5.4. Additionally, for H_2 and N_2, n_{sat} was constrained to be 15 mmol/g, consistent with the saturation capacity as determined through the Langmuir surface area to accurately reflect selectivity values calculated from low-pressure isotherms. As shown in previous examples,[19,27] this saturation capacity has a large effect on the selectivity values observed. All parameters are listed in Table 5.S8. Note that for the calculated CO_2 parameters, the extremely linear isotherms were difficult to accurately fit with standard Langmuir isotherms, even when adding multiple, different adsorption sites. A possible explanation for this is the relatively weak interaction with the open, high-spin Fe^{II} site is similar to the strength of interaction elsewhere in the framework, such as on the pore walls, creating an arbitrarily large n_{sat}. However, this was not explored further. As such, the values are representative of the best mathematical fit for the data in order to extract useful information and not necessarily indicative of physically realizable parameters.

$$n = \frac{n_{sat} bp}{1+bp} \quad (5.5)$$

$$b = e^{-S} e^{\frac{H}{RT}} \quad (5.6)$$

Regeneration energy calculations. Regeneration energy values (E) of **1** were calculated from estimations of the latent and sensible heat contributions per kg of CO captured for a pure temperature swing adsorption process (no vacuum or inert gas purge), as shown in Eqn 5.7. Latent heat contributions were derived from the aforementioned calculated isosteric heats of adsorptions (Q_{st}) multiplied by the amount of CO released (q, in this case the working capacity). Sensible heat contributions were determined using heat capacities (C_p) determined by differential scanning calorimetry, and multiplied by temperature required for regeneration (ΔT). The regeneration energy was normalized per kg of CO captured by multiplying the resultant value by the mass of sample (m) needed to produce 1 kg CO, calculated using the working capacity.

$$E = m(-Q_{st}q + C_p \Delta T) \quad (5.7)$$

For regeneration temperatures, the desorption step pressure was extrapolated by using the Clausius-Clapeyron relation in Eqn 3, using the desorption step pressure as $p_{step,0}$ and the enthalpy associated with the phase transition, H_{step}, derived from the isosteric heat of adsorption.

Gas adsorption in Ni_2(dobdc) and Fe_2(dobdc). Working capacity measurements for Ni_2(dobdc) and Fe_2(dobdc) were derived using thermodynamic parameters calculated from multiple temperature CO adsorption isotherms previously reported.[27]

Infrared spectroscopy. Samples of **1** were exposed to various pressures of CO at 25 °C. A peak at 2157 cm^{-1} appears initially at pressures below 150 mbar, blue-shifted with respect to free CO. This feature is consistent previously reported examples that feature high-spin Fe^{II}–CO interactions.[27] Full conversion to low-spin Fe^{II} is expected upon raising the pressure past 150 mbar, and this peak is expected to lose intensity. However, instead it grows in intensity until 350 mbar and then begins to gradually lose intensity. This could be because conversion to low-spin

Fe^{II} is not complete, and as the gradual decrease in intensity suggests, the peak would eventually lose more intensity upon further increases in pressure. Incomplete activation before data collection could also cause domains of iron sites that are unable to transition to low-spin and that remain high-spin, presenting another potential source of error. Lastly, the heat provided by the IR beam might provide a slight amount of local heating, pushing the step pressure past the dosing pressure in a small amount of the sample, which would be expected to have the observed stretching frequency. Due to experimental limitations, these theories were not analyzed further. We acknowledge, however, that this could also be because the peak does not correspond to high-spin Fe^{II}–CO, and rather is CO bound to an impurity that was not detected by other spectroscopic methods or simply physisorbed CO on the framework.

The appearance of two, slightly different low-spin Fe^{II}–CO interactions is attributed to slight disorder of the CO molecules at 25 °C. This is visible in the large thermal parameter observed in the powder X-ray diffraction (Table S4). Additionally, incomplete activation or ambient solvent molecules that interfere during data collection may have contributed to the slightly different peak positions.

The interaction with CO is fully reversible at 25 °C. Figure 5.S18 shows several spectra collected upon a progressive decrease of the CO equilibrium pressure. In particular, in the 600-200 mbar pressure range, all bands due to the Fe^{II}–CO adducts (both high and low-spin), appear unchanged. When the pressure is lowered past 200 mbar (see green spectrum in Figure 5.S18), both signals from low-spin species (bands at 2048 and 2039 cm^{-1}) start to decrease significantly in intensity, whereas the component associated to the high spin adducts (2157 cm^{-1}) does not change. Finally, when the CO equilibrium pressure reaches 50 mbar (see orange spectrum in Figure 5.S18) and the 2048 and 2039 cm^{-1} components have almost disappeared, the band at 2157 cm^{-1} states to decrease in intensity. It is clear that the reversibility of both low and high-spin Fe^{II} IR components is not associated to the strength of the CO–Fe^{II} interactions but instead to the CO desorption behavior of this material.

Mössbauer spectroscopy. The 100 K spectra collected for the activated Fe_2Cl_2(bbta) shows two different iron sites (Figure 5.S19). We attribute this to ambient solvent occupying the open metal site during sample preparation or slight degrees of incomplete activation. Consistent with this, the respective areas of these two metal sites are present in different ratios in different preparations of the sample, even with using the same material. Additionally, preparation of the CO-dosed sample shows just one iron site, suggesting that weak solvent interactions are displaced by the carbon monoxide at low pressures.

Magnetic susceptibility. CO-dosed Fe_2Cl_2(bbta) displays a $\chi_M T$ at 300 K of 1.2 emu·K/mol, or 0.6 emu·K/mol Fe, while it is expected to be closer to 0 emu·K/mol. This observed residual magnetic moment is attributed to incomplete saturation of the iron sites during the course of the experiment, as this represents 17% of the $\chi_M T$ value at 300 K for the all high-spin Fe_2Cl_2(bbta) (6.9 emu·K/mol). This could be due to gas diffusion difficulties, as the powder to be dosed was compressed significantly and then immobilized with quartz wool to prevent torqueing during the measurement, instead of being a loose powder as is typically used during gas adsorption measurements. Additionally, ambient solvent may have occupied the iron sites during the preparation of the sample, which may also contribute to high-spin Fe^{II} sites. As the data broadly confirms what is expected, this was not explored further.

Table 5.S1. Unit cell parameters from powder X-ray diffraction.

	Temperature	Space Group	a (Å)	c (Å)	V (Å^3)
Fe_2Cl_2(bbta)	295 K	R–3m	25.1565(12)	8.2321(4)	4511.7(5)
CO•Fe_2Cl_2(bbta)	295 K	R–3m	23.9689(8)	8.0046(3)	3982.6(3)
Fe_2Cl_2(btdd)	298 K	R–3m	39.166(9)	8.1664(19)	10849(6)
CO•Fe_2Cl_2(btdd)	298 K	R–3m	38.082(5)	7.9951(9)	10041(3)

Table 5.S2. Selected bond distances.

	Fe_2Cl_2(bbta)	CO•Fe_2Cl_2(bbta)	Fe_2Cl_2(btdd)	CO•Fe_2Cl_2(btdd)
Fe–N1 (Å)	2.110(15)	1.972(5)	2.06(5)	2.00(3)
Fe–N2 (Å)	2.11(2)	1.987(9)	2.22(6)	2.11(6)
Fe–Cl (Å)	2.385(6)	2.259(4)	2.527(16)	2.409(10)
Fe–CO (Å)	–	1.76 (4)	–	1.84 (6)
C–O (Å)	–	1.18(4)	–	1.17(6)

Table 5.S3. Rietveld Refinement of Fe_2Cl_2(bbta). Values in parenthesis indicate one standard deviation from the parameter value. Temperature = 295 K, space group *R*–3m, *a* = 25.1565(12) Å, *c* = 8.2321(4) Å. Figures-of-merit (as defined by TOPAS): R_{wp} = 8.11%, R_p = 6.89%, R_{bragg} = 2.39%, GoF = 1.54.

atom	*x*	*y*	*z*	*multiplicity*	*occupancy*	U_{iso} (Å^2)
Fe	0.28877(19)	0.28877(19)	0	18	1	0.0534(18)
Cl	1/3	0.2438(4)	1/6	18	1	0.083(4)[a]
N1	0.2559(9)	0.3226(7)	0.3092 (18)	36	1	0.044(4)[a]
N2	0.2940(10)	1/3	1/3	18	1	0.044(4)[a]
C1	0.2100(8)	0.3238(5)	0.2516(8)	36	1	0.044(4)[a]
C2	0.1535(11)	0.307(1)	0.1730(17)	18	1	0.044(4)[a]
H1	0.143	0.287	0.057	18	1	0.044(4)[a]

[a]The thermal parameters for all of atoms of the $bbta^{2-}$ ligand were constrained to be equivalent.

Table 5.S4. Rietveld Refinement of CO•Fe_2Cl_2(bbta). Values in parenthesis indicate one standard deviation from the parameter value. Temperature = 295 K, space group *R*–3m, *a* = 23.9689(8) Å, *c* = 8.0046(3) Å. Figures-of-merit (as defined by TOPAS): R_{wp} = 7.43%, R_p = 5.85%, R_{bragg} = 1.70%, GoF = 1.34.

atom	*x*	*y*	*z*	*multiplicity*	*occupancy*	U_{iso} (Å^2)
Fe	0.28374(18)	0.28374(18)	0	18	1	0.0205(14)
Cl	1/3	0.2458(2)	1/6	18	1	0.030(2)
N1	0.2599(3)	0.3136(2)	0.2029(6)	36	1	0.010(3)[a]
N2	0.2999(3)	1/3	1/3	18	1	0.010(3)[a]
C1	0.2090(8)	0.3205(6)	0.2522(6)	36	1	0.010(3)[a]
C2	0.1530(9)	0.3059(8)	0.170(2)	18	1	0.010(3)[a]
H1	0.142	0.284	0.047	18	1	0.010(3)[a]
C	0.2097(14)	0.2097(14)	0	18	0.843(19)	0.0127(11)
O	0.1604(7)	0.1604(7)	0	18	0.843(19)	0.0367(8)

[a]The thermal parameters for all of atoms of the $bbta^{2-}$ ligand were constrained to be equivalent.

Table 5.S5. Rietveld refinement of Fe_2Cl_2(btdd). Values in parenthesis indicate one standard deviation from the parameter value. Temperature = 298 K, space group *R*–3m, *a* = 39.166(9) Å, *c* = 8.1664(19) Å. Figures-of-merit (as defined by TOPAS): R_{wp} = 4.83%, R_p = 3.27%, R_{Bragg} = 2.31%, GoF = 3.80.

atom	*x*	*y*	*z*	*multiplicity*	*occupancy*	U_{iso} (Å^2)
Fe	0.29850(15)	0.2985(3)	1/2	18	1	0.096(5)
Cl	0.2707(6)	1/3	1/3	18	1	0.127(11)
N1	0.3215(13)	0.287(2)	0.295(6)	36	1	0.108(9)[a]
N2	1/3	0.312(2)	1/6	18	1	0.108(9)[a]
C1	0.326(3)	0.256(4)	0.247(7)	36	1	0.108(9)[a]
C2	0.3181(18)	0.221(3)	0.328(8)	36	1	0.108(9)[a]
C3	0.326(3)	0.192(5)	0.248(9)	36	1	0.108(9)[a]
O1	0.3181(16)	0.159(3)	0.326(7)	36	1	0.108(9)[a]
H1	0.3064	0.215	0.452	36	1	0.108(9)[a]

[a]The thermal parameters for all of atoms of the btdd^{2-} ligand were constrained to be equivalent.

Table 5.S6. Rietveld refinement of CO•Fe_2Cl_2(btdd). Values in parenthesis indicate one standard deviation from the parameter value. Temperature = 298 K, space group *R*–3m, *a* = 38.082(5) Å, *c* = 7.9951(9) Å. Figures-of-merit (as defined by TOPAS): R_{wp} = 4.30%, R_p = 3.18%, R_{Bragg} = 1.61%, GoF = 3.43.

atom	*x*	*y*	*z*	*multiplicity*	*occupancy*	U_{iso} (Å^2)
Fe	0.2993(3)	0.2993(3)	1/2	18	1	0.082(5)
Cl	0.2726(4)	1/3	1/3	18	1	0.087(7)
N1	0.3200(9)	0.2866(7)	0.293(4)	36	1	0.075(6)[a]
N2	1/3	0.3120(15)	1/6	18	1	0.075(6)[a]
C1	0.3250(16)	0.2554(11)	0.246(4)	36	1	0.075(6)[a]
C2	0.3161(12)	0.2200(9)	0.331(6)	36	1	0.075(6)[a]
C3	0.3247(15)	0.1922(10)	0.249(4)	36	1	0.075(6)[a]
O1	0.3164(9)	0.1582(10)	0.329(5)	36	1	0.075(6)[a]
H1	0.303	0.214	0.456	36	1	0.075(6)[a]
C	0.2511(14)	0.2511(14)	1/2	18	1	0.03(2)
O	0.2204(4)	0.2204(4)	1/2	18	1	0.13(3)

[a]The thermal parameters for all of atoms of the btdd^{2-} ligand were constrained to be equivalent.

Table 5.S7. Langmuir and BET surface areas of Fe_2Cl_2(bbta) (**1**) and Fe_2Cl_2(btdd) (**2**). For Fe_2Cl_2(btdd), the pressure region chosen is consistent with analogous frameworks.[25]

Compound	$SA_{Langmuir}$ (m^2/g)	SA_{BET} (m^2/g)	slope	y-int	P_{low} (bar)	P_{high} (bar)	q_{sat} (mmol/g)	C
1	1342	1055	9.25E–2	3.11E–6	1.03E–3	1.45E–2	10.8	29693
2	3541	1897	5.13E–2	1.02E–4	7.78E–4	5.39E–2	19.5	503

Table 5.S8. CO adsorption parameters in Fe_2Cl_2(bbta) and Fe_2Cl_2(btdd) for the piecewise Langmuir-Freundlich equation (Eqns 5.2 and 5.3)

	Fe_2Cl_2(bbta)	Fe_2Cl_2(btdd)
$n_{sat,1}$ (mmol/g)	6.91	7.01
H_1 (–kJ/mol)	38.7	26.9
S_1 (–R)	16.1	12.6
v_1	1.07	0.986
$n_{sat,2a}$ (mmol/g)	2.91	1.68
H_{2a} (–kJ/mol)	19.9	$5.24*10^{-2}$
S_{2a} (–R)	5.69	$9.07*10^{-5}$
v_{2a}	0.599	0.714
$n_{sat,2b}$ (mmol/g)	3.13	2.77
H_{2b} (–kJ/mol)	260	149
S_{2b} (–R)	92.6	52.9
v_{2b}	3.64	2.79
H_{step} (–kJ/mol)	65.4	66.3
$p_{step,T0}$ (bar)	0.163	0.443
T_0 (K)	298.15	298.15

Table 5.S9. CO_2, H_2, and N_2 adsorption parameters in Fe_2Cl_2(bbta) for the single site Langmuir equation (Eqns 5.5 and 5.6). Note that the values are representative of the best mathematical fit for the data in order to extract useful information and not necessarily indicative of physically realizable parameters.

	H_2	N_2	CO_2
n_{sat} (mmol/g)	15.0	15.0	69.4
b	0.00584	0.0162	-
E (–kJ/mol)	-	-	23.2
S (–R)	-	-	11.9

Table 5.S10. Mössbauer parameters for Fe_2Cl_2(bbta) and CO-dosed Fe_2Cl_2(bbta) collected at 100 K. Note that for activated Fe_2Cl_2(bbta), the doublets were fit with asymmetric Γ parameters, as seen in other Fe^{II} square pyramidal metal–organic frameworks.[38] However, in this case these values were calculated to be symmetrical within error.

Sample	δ (mm/s)	ΔE_Q (mm/s)	Γ_L	Γ_R	Area (%)
Fe_2Cl_2BBTA - activated	1.084(2)	1.928(6)	0.408(11)	0.383(11)	69(2)
	1.088(4)	2.808(16)	0.390(23)	0.391(21)	31(2)
Fe_2Cl_2BBTA-CO-dosed	0.364(2)	0.989(4)	0.310(6)	0.310(6)	-

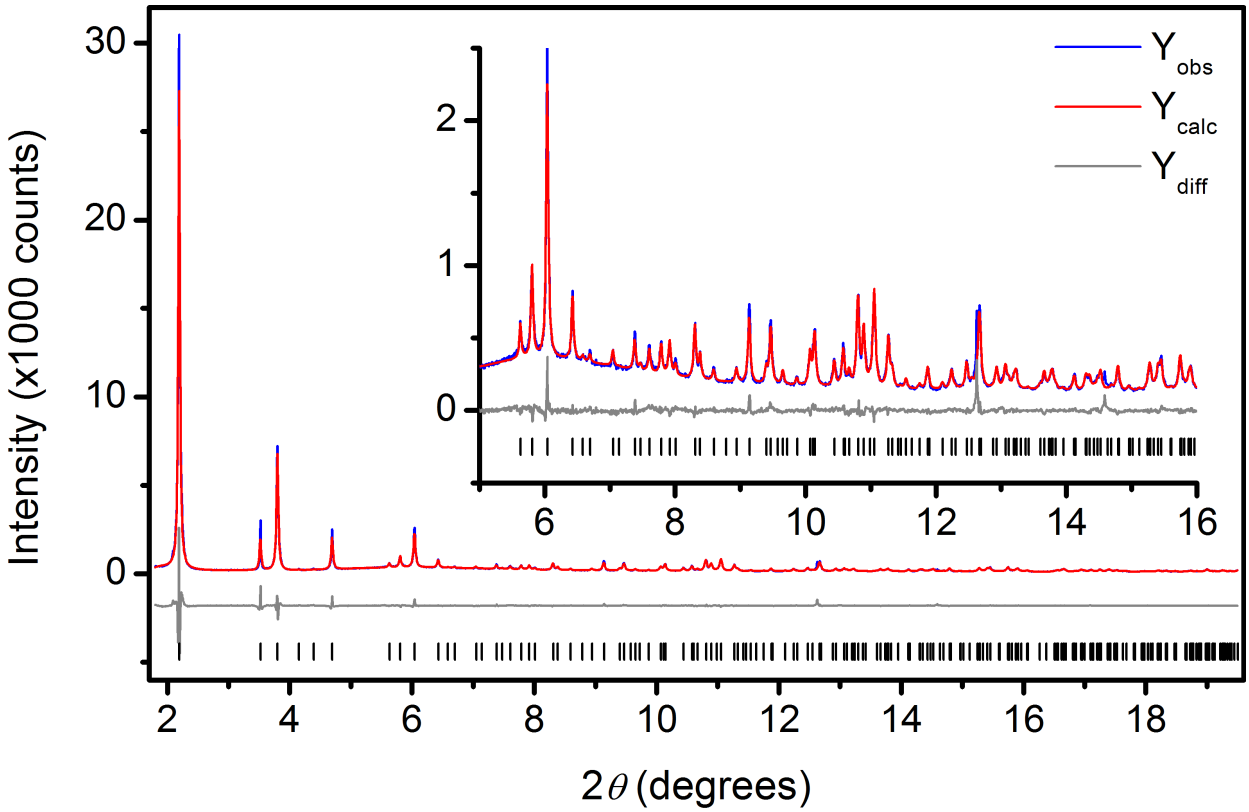

Figure 5.S1. Rietveld refinement of Fe_2Cl_2(bbta) under vacuum at 295 K from 1.8º to 19.5º. Blue and red lines represent the observed and calculated diffraction patterns, respectively. The gray line represents the difference between observed and calculated patterns, and the black tick marks indicate calculated Bragg peak positions. The inset shows the high angle region at a magnified scale. Figures-of-merit (as defined by TOPAS R_{wp} = 8.11%, R_p = 6.89%, R_{bragg} = 2.39%, GoF = 1.54. The wavelength was 0.458996 Å.

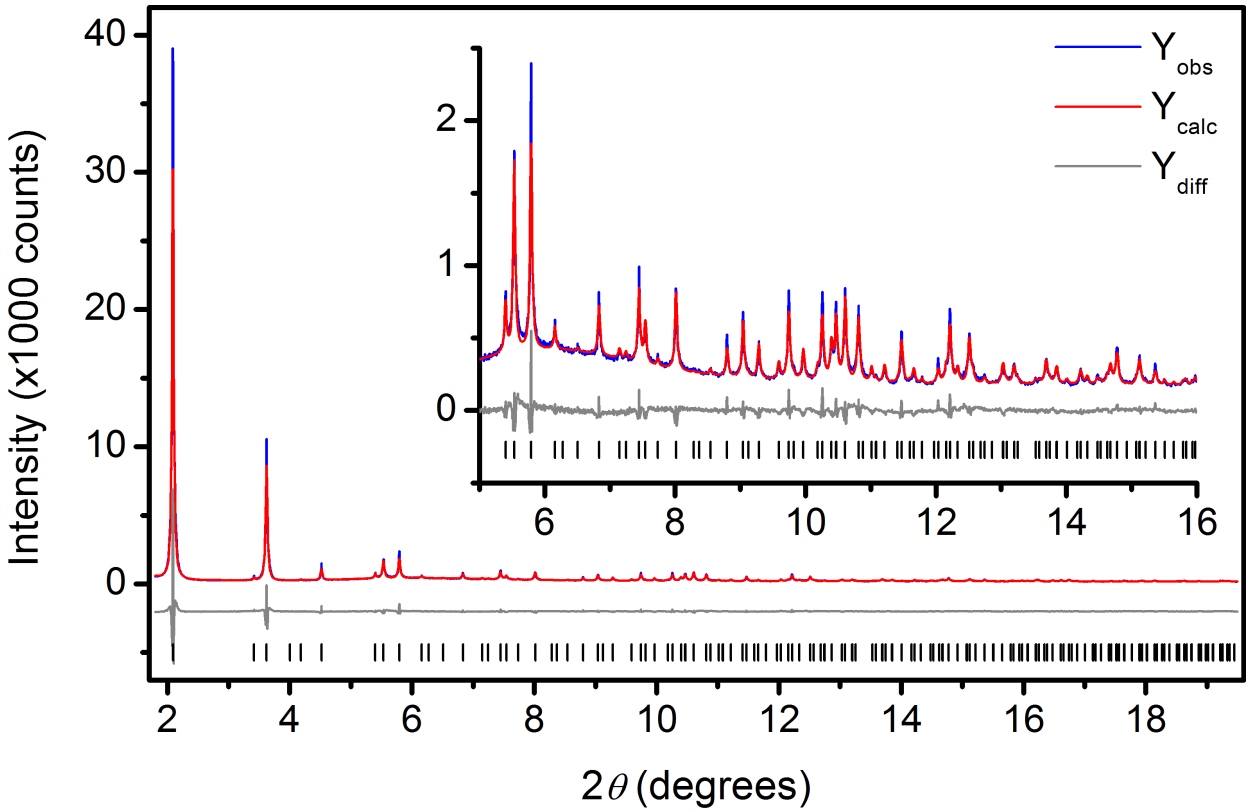

Figure 5.S2. Rietveld refinement of Fe_2Cl_2(bbta) dosed with CO at 295 K from 1.8º to 19.5º. Blue and red lines represent the observed and calculated diffraction patterns, respectively. The gray line represents the difference between observed and calculated patterns, and the black tick marks indicate calculated Bragg peak positions. The inset shows the high angle region at a magnified scale. Figures-of-merit (as defined by TOPAS): R_{wp} = 7.43%, R_p = 5.85%, R_{bragg} = 1.70%, GoF = 1.34. The wavelength was 0.458996 Å.

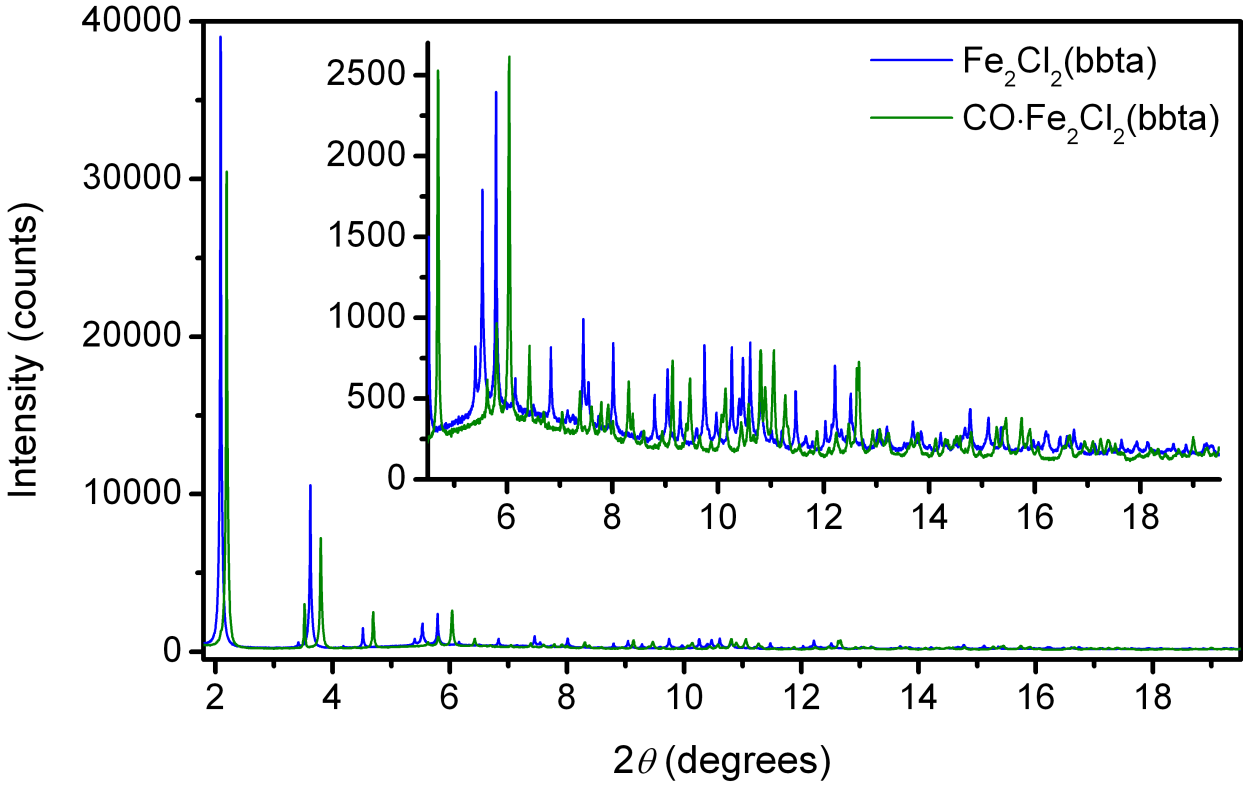

Figure 5.S3. Powder diffraction patterns for $Fe_2Cl_2(bbta)$ under vacuum (blue) and $Fe_2Cl_2(bbta)$ dosed with CO (green) are overlaid. Diffraction patterns were collected 295 K using a wavelength of 0.458996 Å.

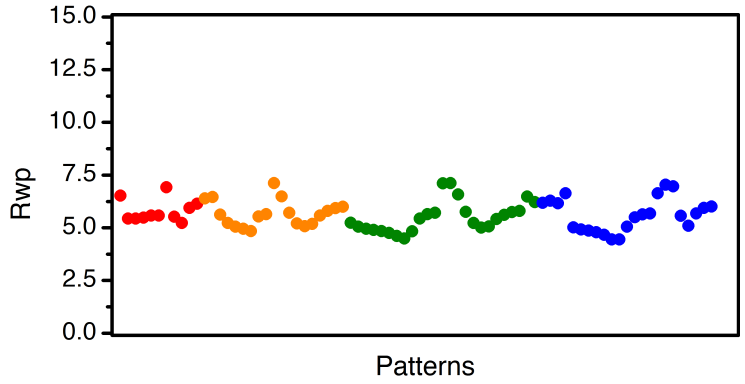

Figure 5.S4. R_{wp} values from each Rietveld refinement utilized in $Fe_2Cl_2(bbta)$ temperature cycling data, with data displayed in the order of measurement as temperature was cycled from high temperatures to low temperatures back to high temperatures within each cycle. Red, orange, green, and blue colors represent patterns from the first, second, third, and fourth cycles. Refinements with higher values for R_{wp} typically corresponded to patterns where the majority of the pattern was primarily one phase, making it difficult to get accurate strain and scaling parameters for the phase of lesser abundance. As a result, the higher R_{wp} values correspond to patterns in the beginning, middle, and end of each cycle (when small to nonexistent amounts of the low-spin, high-spin, and low-spin phases are present, respectively).

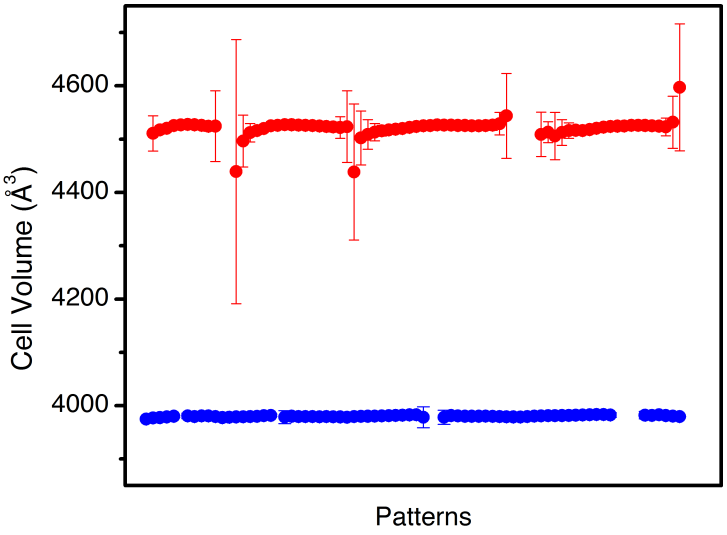

Figure 5.S5. Cell volumes extracted from each Rietveld refinement utilized in $Fe_2Cl_2(bbta)$ cycling data, displayed in order of measurement. Red symbols correspond to cell volumes determined by fitting the high spin $Fe_2Cl_2(bbta)$ structural model, whereas the blue symbols correspond to those determined by fitting the low spin $Fe_2Cl_2(bbta)$ structural model. Symbols with larger error bars are associated with refinement of patterns with <10% of that particular phase, which despite the error in the refined values still yielded reasonable values. As a result, these phases were included in the refinement.

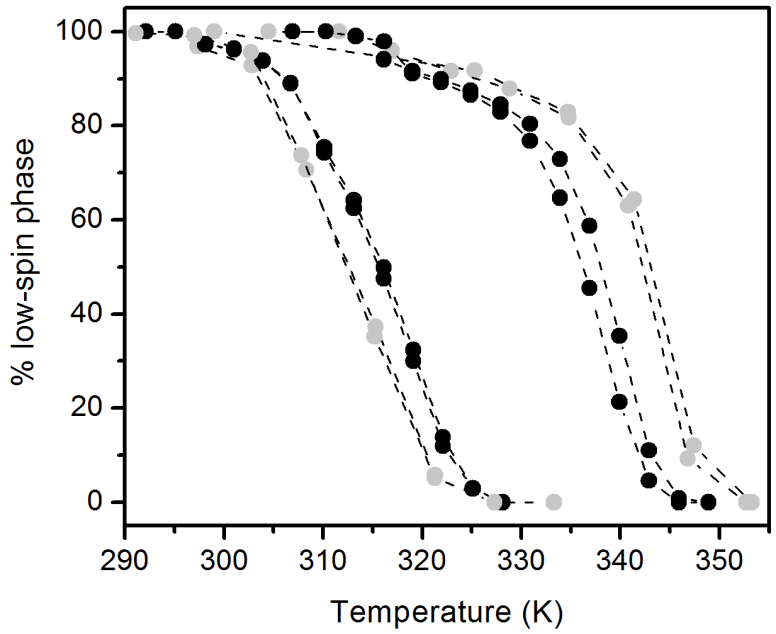

Figure 5.S6. Low-spin phase weight fraction extracted from each Rietveld refinement utilized in Fe_2Cl_2(bbta) cycling data, displayed versus average measurement temperature. Points connected by dotted lines were taken sequentially, going from low temperature to high temperature (following the higher curve) and high temperature to low temperature (following the lower curve) at a rate of 3 K/min (black circles) and 6 K/min (grey circles), with a diffraction pattern collected every minute. Error bars are plotted, but are within the symbols. As a result of differing scan speeds during different cycles, measurements taken at higher temperature cycling rates (grey circles) likely have greater error in their temperature values, visible in the scatter of the points visible in the plot.

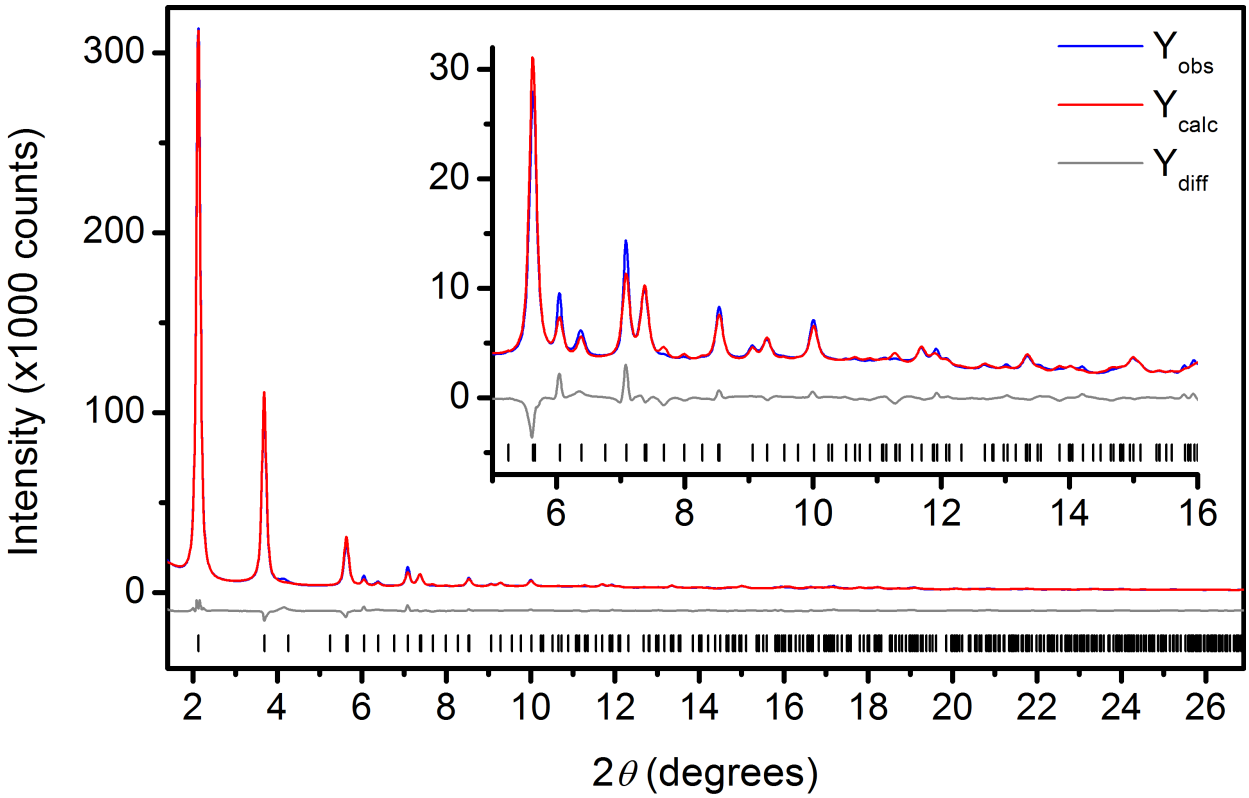

Figure 5.S7. Rietveld refinement of Fe_2Cl_2(btdd) under vacuum at 298 K from 1.4º to 27º. Blue and red lines represent the observed and calculated diffraction patterns, respectively. The gray line represents the difference between observed and calculated patterns, and the black tick marks indicate calculated Bragg peak positions. The inset shows the high angle region at a magnified scale. Figures-of-merit (as defined by TOPAS): R_{wp} = 4.83%, R_p = 3.27%, R_{Bragg} = 2.31%, GoF = 3.80. The wavelength was 0.727680 Å.

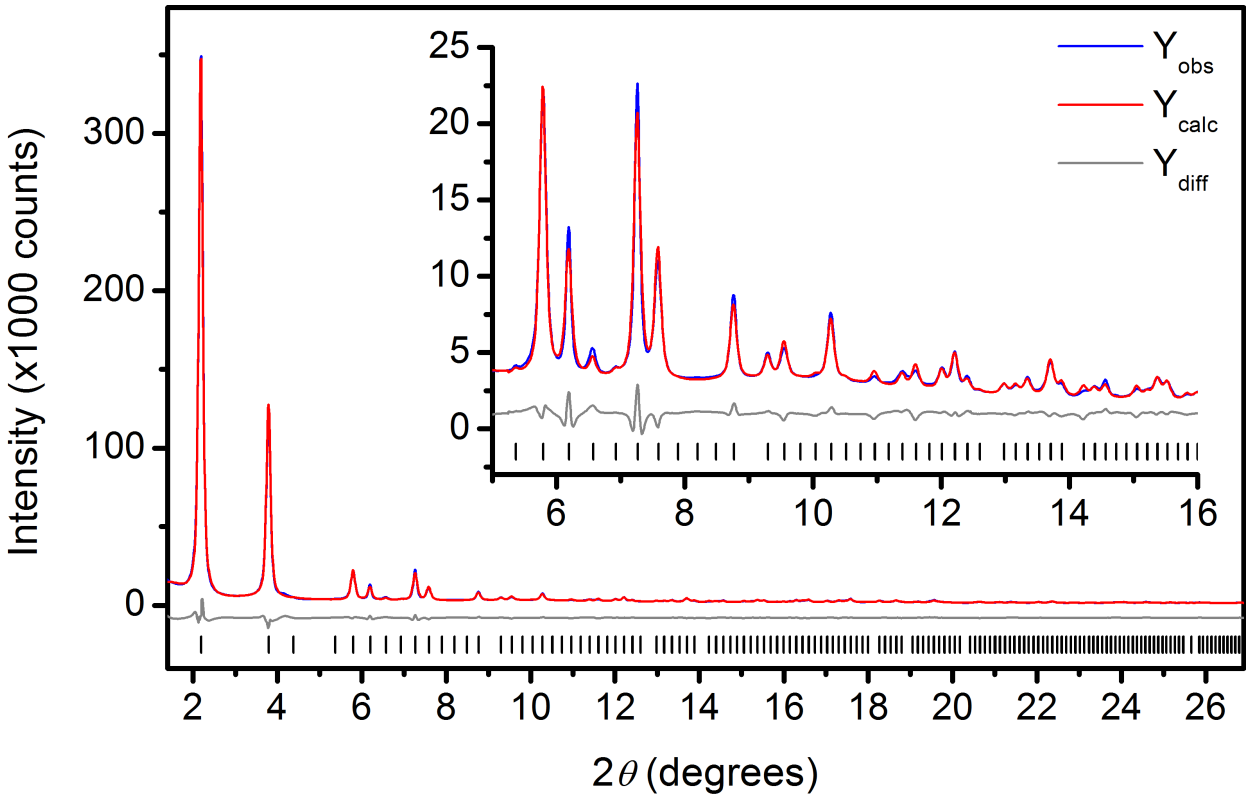

Figure 5.S8. Rietveld refinement of Fe_2Cl_2(btdd) dosed with CO at 298 K from 1.4º to 27º. Blue and red lines represent the observed and calculated diffraction patterns, respectively. The gray line represents the difference between observed and calculated patterns, and the black tick marks indicate calculated Bragg peak positions. The inset shows the high angle region at a magnified scale. Figures-of-merit (as defined by TOPAS): R_{wp} = 4.30%, R_p = 3.18%, R_{Bragg} = 1.61%, GoF = 3.43. The wavelength was 0.727680 Å.

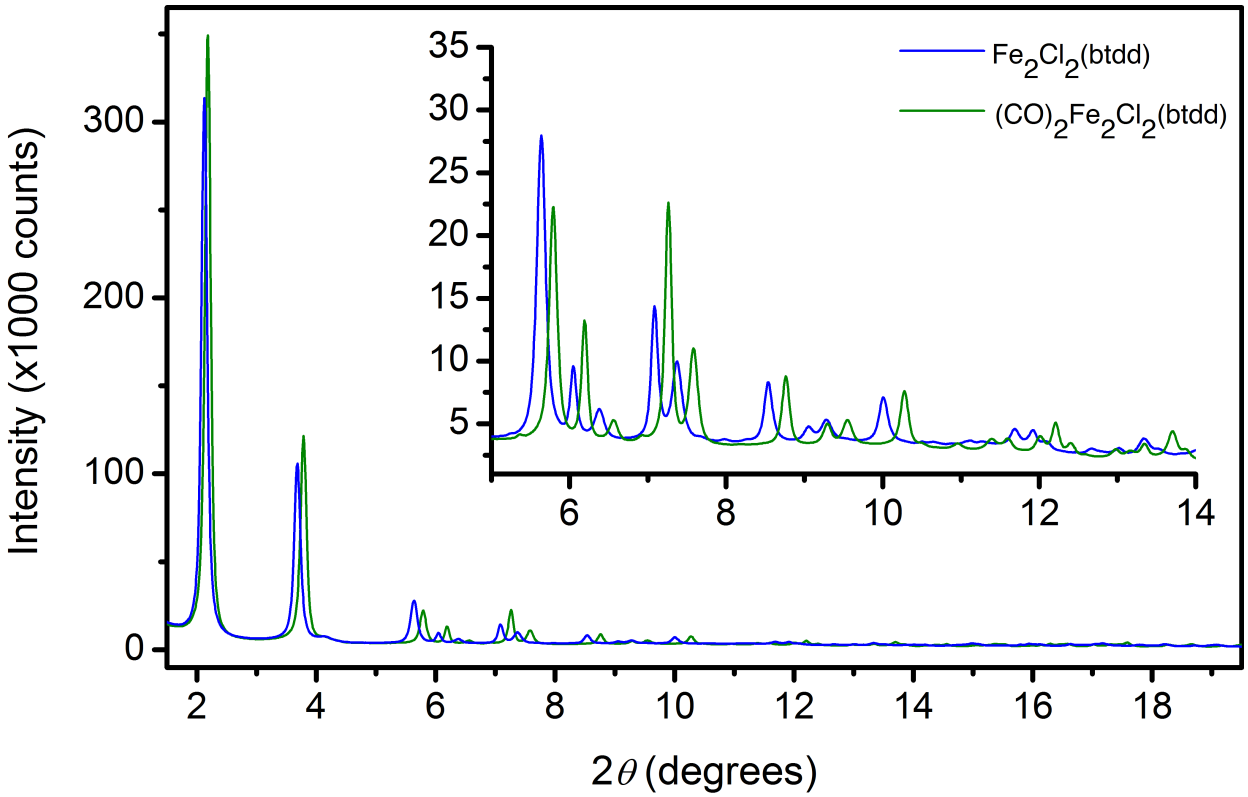

Figure 5.S9. Powder diffraction patterns for Fe_2Cl_2(btdd) under vacuum (blue) and Fe_2Cl_2(btdd) dosed with CO (green) are overlaid. Diffraction patterns were collected at 298 K using a wavelength of 0.72768 Å.

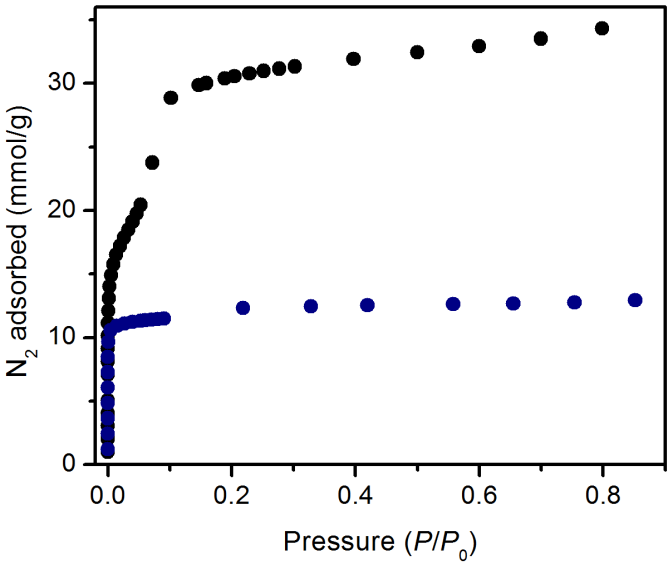

Figure 5.S10. N_2 adsorption isotherms collected at 77 K for Fe_2Cl_2(bbta) (blue) and Fe_2Cl_2(btdd) (black).

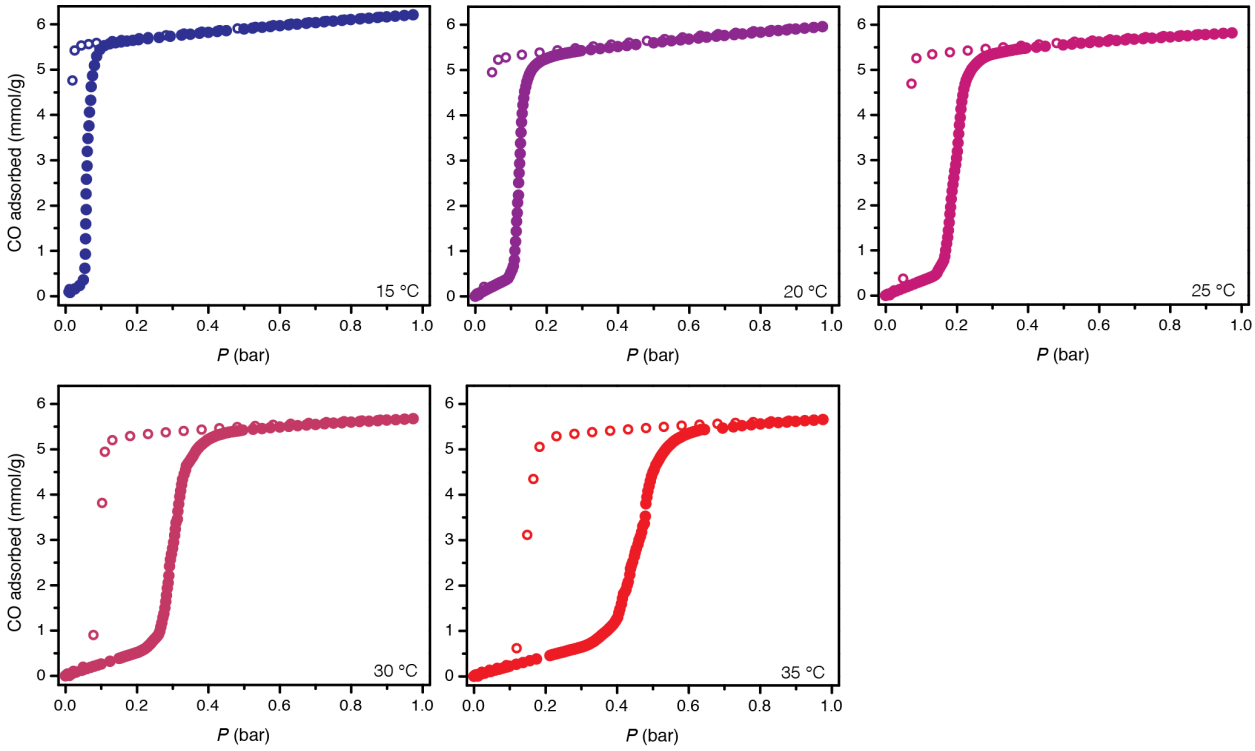

Figure 5.S11. CO adsorption (closed circles) and desorption (open circles) isotherms for Fe_2Cl_2(bbta) collected at various temperatures. Top (left to right): 15, 20, 25 °C. Bottom (left to right): 30, 35 °C.

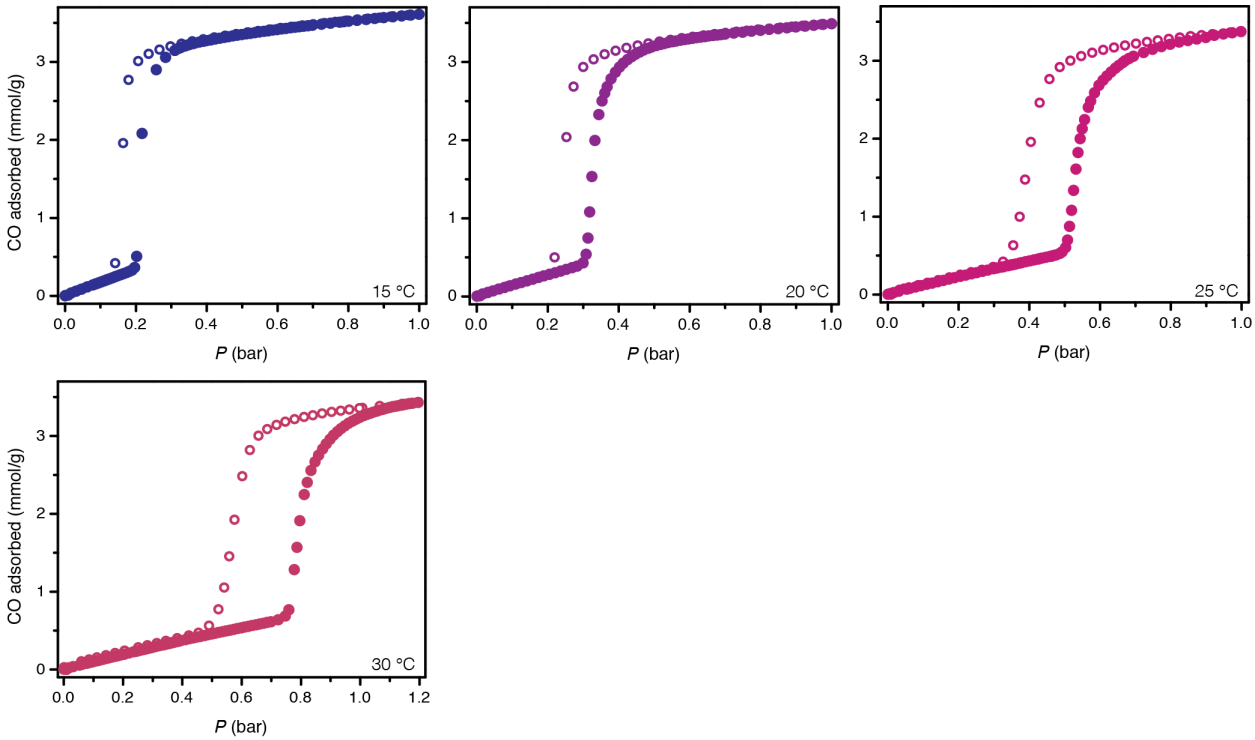

Figure 5.S12. CO adsorption (closed circles) and desorption (open circles) isotherms for Fe_2Cl_2(btdd) collected at various temperatures. Top (left to right): 15, 20, 25 °C. Bottom: 30 °C.

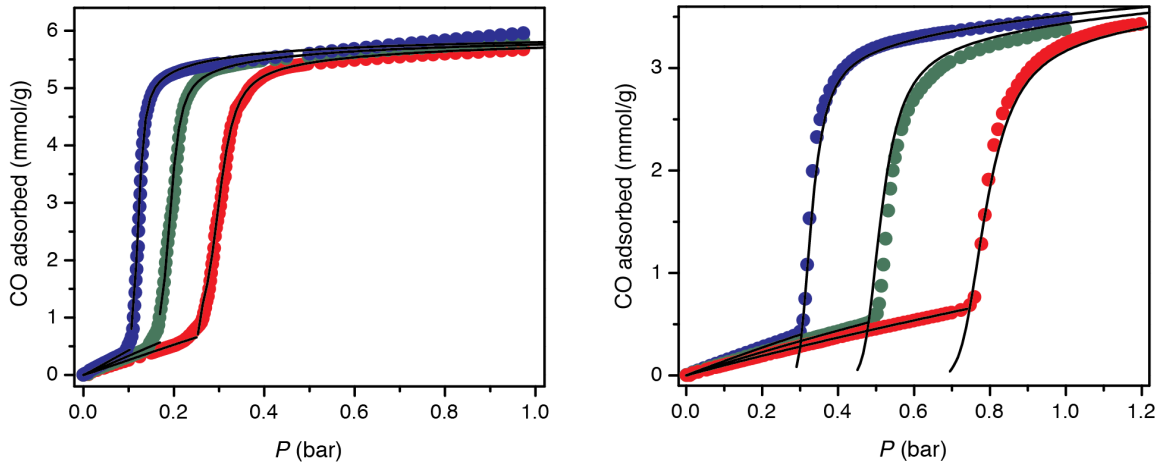

Figure 5.S13. CO adsorption isotherms for Fe_2Cl_2(bbta) (left) and Fe_2Cl_2(btdd) (right), collected at 20 (blue circles), 25 (green circles), and 30 °C (red circles), with black lines corresponding to a fit to a piecewise Langmuir-Freundlich equation (Eqn 5.2) with the parameters listed in Table 5.S8.

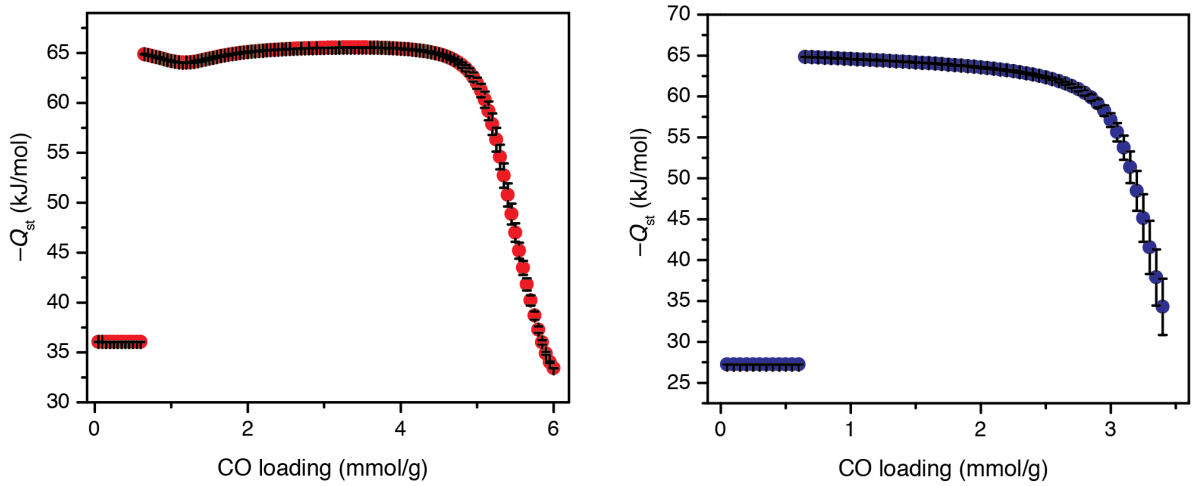

Figure 5.S14. Isosteric heats of CO adsorption ($-Q_{st}$) calculated using the Clausius-Clapeyron relation for Fe_2Cl_2(bbta) (left) and Fe_2Cl_2(btdd) (right), with error bars shown in black.

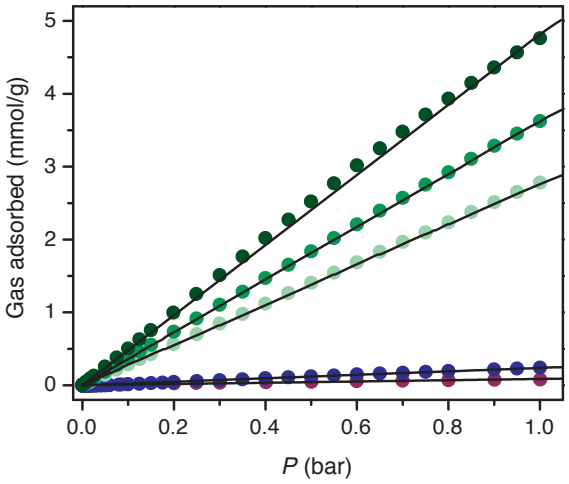

Figure 5.S15. CO_2 (green circles), N_2 (blue circles), and H_2 (purple circles) adsorption isotherms for Fe_2Cl_2(bbta) collected at 25 °C for H_2 and N_2, and (from light to dark) 25, 35, and 45 °C for CO_2, with black lines corresponding to a fit to a single-site Langmuir Equation (Eqn 5.5) with the parameters listed in Table 5.S9.

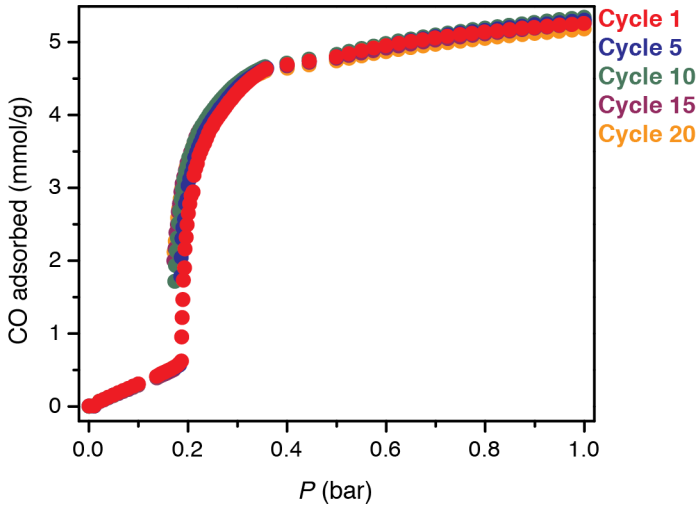

Figure 5.S16. CO cycling experiments conducted in Fe_2Cl_2(bbta) at 25 °C, with full CO adsorption isotherms collected during cycle 1, cycle 5, and every subsequent 5 cycles, shown here. For all other cycles, adsorption occurred at 1 bar for 30 min, while desorption occurred under dynamic vacuum for 1 hour.

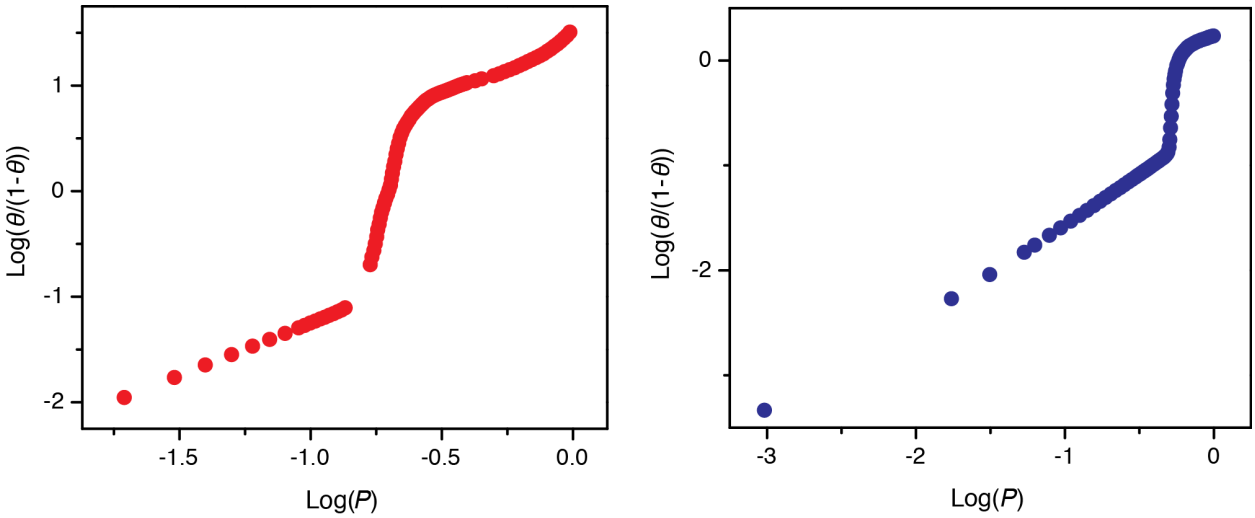

Figure 5.S17. Hill analysis of CO adsorption isotherms collected at 25 °C in Fe_2Cl_2(bbta) (left) and Fe_2Cl_2(btdd) (right).

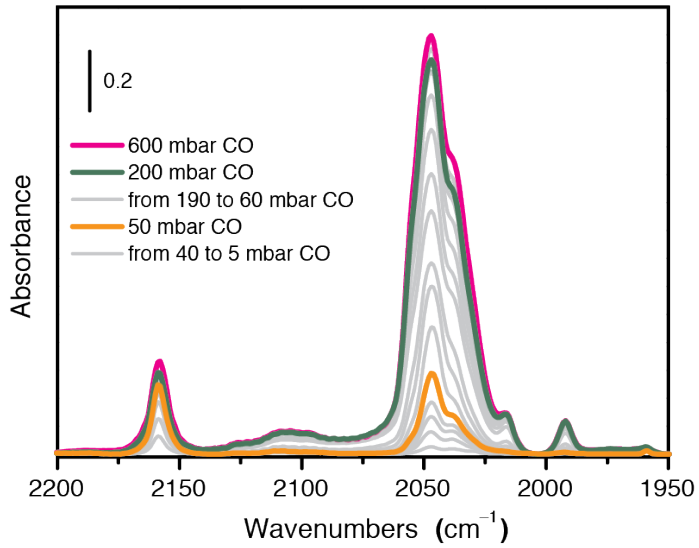

Figure 5.S18. Infrared data collected during desorption of CO in Fe_2Cl_2(bbta) at 25 °C

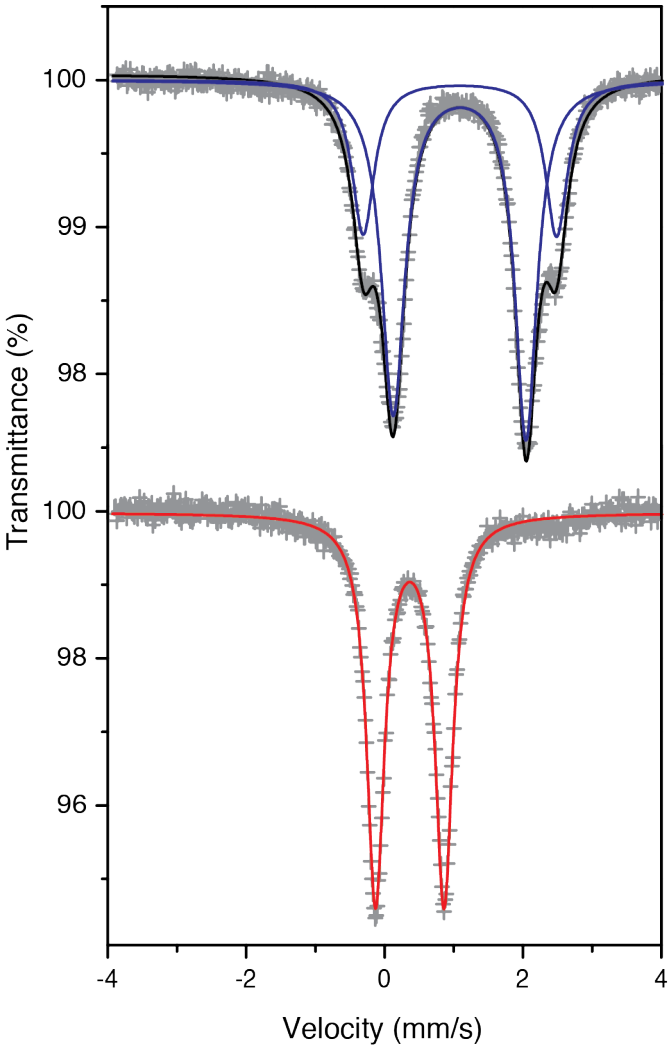

Figure 5.S19. Mössbauer spectra collected at 100 K for Fe_2Cl_2(bbta) (top) and CO-dosed Fe_2Cl_2(bbta) (bottom). In both spectra, the experimental data is shown in grey plusses, with blue doublets corresponding to high-spin Fe^{II} species and red doublets corresponding to low-spin Fe^{II} species. In the Fe_2Cl_2(bbta) spectra, the total fit is shown in black. Parameters for all spectra are shown in Table 5.S10.

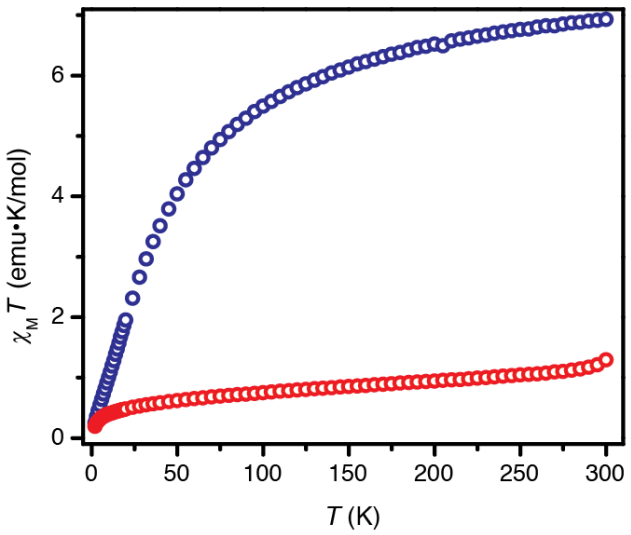

Figure 5.S20. Dc magnetic susceptibility times temperature data collected for $Fe_2Cl_2(bbta)$ (blue) and CO-dosed $Fe_2Cl_2(bbta)$ (red) collected at 1 T.

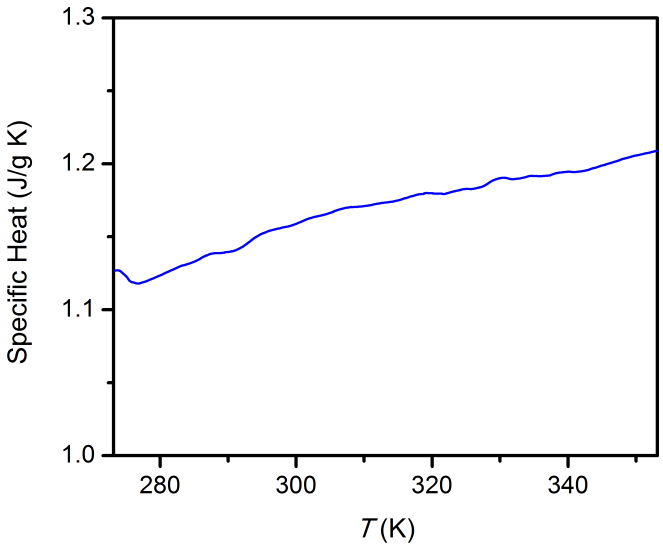

Figure 5.S21. Specific heat as a function of temperature for $Fe_2Cl_2(bbta)$.

Appendix A: Schematic of Organic Ligands

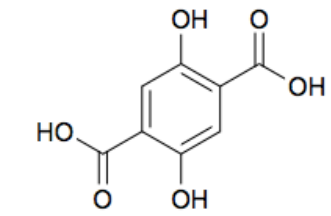

H_4dobdc

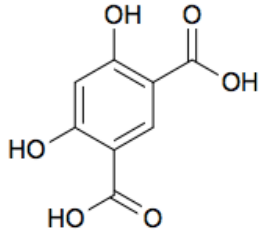

H_4(*m*-dobdc)

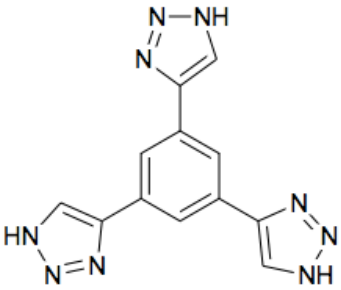

H_3BTTri

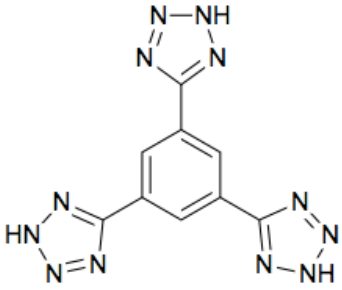

H_3BTT

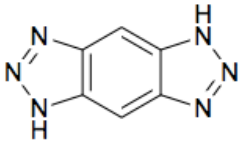

H_2bbta

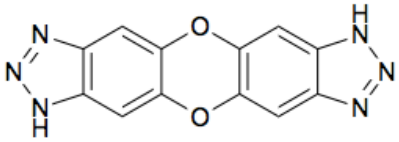

H_2btdd

Scheme A.1. Organic bridging ligands referenced in this thesis.